AN ABSTRACT OF THE THESIS OF

Charles T. Lewis for the degree of Master of Science in Geology presented on May 6, 2022.

Title: Rhyolitic Melt Production in the Midst of a Continental Arc Flare-Up - The Heterogenous Caspana Ignimbrite of the Altiplano-Puna Volcanic Complex of the Central Andes

Abstract approved: ____

Shanaka L. de Silva

The ~5 km^3, 4.54 to 4.09 Ma Caspana Ignimbrite of the Altiplano-Puna Volcanic Complex (APVC) of the Central Andes records the eruption of an andesite and two distinct rhyolitic magmas. It provides a unique opportunity to investigate the production of silicic magmas in a continental arc flare-up, where small volumes of magma rarely survive homogenization into the regional magmatic system that is dominated by supereruptions of monotonous dacitic ignimbrites.

The fall deposit and thin flow unit that record the first stage of the eruption (Phase 1) tapped a crystal-poor peraluminous rhyolite. The petrological and geochemical characteristics of Phase 1 are best explained by partial melting of- or reheating and melt extraction from a granodioritic intrusion. Phase 2 of the eruption records the emplacement of a more extensive flow unit with a crystal-poor, fayalite-bearing rhyolite and a porphyritic to glomeroporphyritic andesite containing abundant plagioclase-orthopyroxene-Fe-Ti oxide (norite) glomerocrysts. The isotopic composition of Phase 2 is significantly more “crustal” than Phase 1, indicating a separate petrogenetic path. The mineral assemblage of the noritic glomerocrysts and the observed trend between andesite and Phase 2 rhyolite are reproduced by rhyolite-MELTS based models.

P-T-H_2O estimates indicate that the main (Phase 2) reservoir resided between 400-200 MPa, with the andesite recording the deeper pressures and a temperature range of 1060 to 920 °C. Rhyolite phase equilibria predict an estimated temperature of ~775 °C and ~5 wt% H_2O. Pressures derived from phase equilibria indicate that the rhyolite was extracted directly from the noritic cumulate at ~340 MPa and stored at slightly shallower pressures (200-300 MPa) prior to eruption. The rhyolite-MELTS models reveal that latent-heat buffering during the extraction and storage process results in a shallow liquidus during the extensive crystallization that produced a noritic cumulate in equilibrium with a rhyodacitic residual liquid. Spikes in latent heat facilitated the segregation of the residual liquid, creating the pre-eruptive compositional gap of ~16 wt% SiO_2 between the andesite and the Phase 2 rhyolite.

Unlike typical APVC magmas, low fO_2 conditions in the andesite promoted cocrystallization of orthopyroxene and ilmenite in lieu of clinopyroxene and magnetite. This resulted in relatively high Fe concentrations in the rhyodacite and Phase 2 rhyolite. Combined with the co-crystallization of plagioclase, this low oxidation state forced high Fe^{2+}/Mg and Fe/Ca in the Phase 2 rhyolite, which promoted fayalite stability. The dominance of low Fe^{3+}/Fe^{Tot} and Fe-Ti oxide equilibria indicate low fO_2 (ΔFMQ 0 - ΔFMQ -1) conditions in the rhyolite indicate that the low oxidation state was inherited by the Phase 2 rhyolite from the andesite.

We propose that the serendipitous location on the periphery of the regional thermal anomaly of the Altiplano Puna Magma Body (APMB) permitted the small volume magma reservoir that fed the Caspana ignimbrite eruption to retain its heterogeneous character. This resulted in the record of rhyolitic liquids with disparate origins that evaded assimilation into the large dacite supereruption-feeding APMB. As such, the Caspana Ignimbrite provides a unique window into the multiscale processes that build long-lived continental silicic magma systems.

Rhyolitic Melt Production in the Midst of a Continental Arc Flare-Up - The Heterogenous Caspana Ignimbrite of the Altiplano-Puna Volcanic Complex of the Central Andes

By

Charles T. Lewis

A THESIS

submitted to

Oregon State University

in partial fulfillment of
the requirements for the
degree of

Master of Science

Presented May 6, 2022
Commencement June, 2022

Master of Science thesis of Charles T. Lewis presented on May 6, 2022

APPROVED:

Major Professor, representing Geology

Dean of the College of Earth, Ocean, and Atmospheric Sciences

Dean of the Graduate School

I understand that my thesis will become part of the permanent collection of Oregon State University libraries. My signature below authorizes release of my thesis to any reader upon request.

Charles T. Lewis, Author

ACKNOWLEDGEMENTS

"Nothing of me is original. I am the combined effort of everyone I've ever known". I first heard these words, written by Chuck Palahniuk, probably 13 years ago when I would have laughed in your face if you had told me I'd carry out an M.S. degree. They have never rung more true than they do when I try to compile the names of everyone that has contributed to my graduate school career.

My family has been invaluable over the last few years of my life. My mother has been steadfast in supporting each and every decision I've made, but has the uncanny ability to bring me back down to Earth when needed. I'll never repay her for what she has done for me. Dad, I will never understand your surety that I "can do anything I set my mind to" and I will always believe that is misplaced. However, the many lessons you've taught me over the years (with the help of Tim, Ron, Tonya, and my other "uncles") has given me the ability to stand as my own man in any situation. Kristin is, with no doubt, an irreplaceable figure in my life. I look up to you and your ability to handle anything in life. You have been teaching me about this life since I can remember, and I can only hope that you get something out of our siblinghood. Ride or die man. Chris, Tom, Seth. I know I cannot keep in touch with people to save my life and I'm sorry for that. In fact, I think Tom might be the only one of us that is (was) any good at it. You should know that my growth as a human being was catalyzed by you guys, and that I keep you in mind virtually always. All three of you significantly contributed to who I am today and I am certainly not capable of any of this without your influence. I hope you are (were) proud to call me your friend.

A number of scientists, academics, and teachers have put far more effort into me than I could have possibly imagined. Deron Carter undoubtedly altered the trajectory of my life and if I can do half of what you did for me for one other person, I will consider myself successful. I look up to you like you wouldn't believe. Chris Russo and Brain Haley introduced me to science and essentially put me in the saddle. I will always strive to be as instructive, intelligent, and downright cool as you guys. If CR and BH put me in the saddle, Jordan Lubbers loaded my saddle packs. Your mentorship has been vital to me both in and outside of science. Keep going man - you are the next big thing in this discipline. Shan and Dale, thank you for dragging me along and making this possible. Your patience is impeccable. We are about to do some cool science over the next few years. Well, I will try. You guys will though. To all my instructors at OSU, thank you.

I think Louie, Layla, and Natasha have seen me drink 850 cups of coffee while this thing was being written. I hope that our friendship strengthens in the coming years.

Most importantly, Katherine. I've been told by a number of people that when you know, you know. I had my doubts, but I now know that it is true. You changed the way I view the world around me. Because of you, I have had to re-evaluate how I feel about my existence and what I want from it. When life's circumstances left me spiritually shattered, you were there to turn my face back to the sun and begin healing. When I am angry that what I thought was a generally useful career path turns out to be driven by people with massive egos that love publications more than actually contributing to the world, you are the only person able to remind me that at least some of what I currently do is not entirely useless or futile for the people around me; that maybe I do good things people. I don't know what my future holds – you seem to think it involves science and I seem to think you're wrong – but I can't wait to see you there.

TABLE OF CONTENTS

TABLE OF CONTENTS (Continued)

Page

LIST OF FIGURES

LIST OF TABLES

LIST OF APPENDICES

LIST OF APPENDIX FIGURES

LIST OF APPENDIX TABLES

DEDICATION

To Mindy, and other students like her. May we understand life like you did.

1. Introduction

Discerning the details of how large continental silicic magma systems form is central to understanding the origin and evolution of the continental crust, mass balance in continental arc magmatism, the volcano-plutonic connection, catastrophic supereruptions, and a host of other important questions about crustal magmatism. Many such magma systems are dominated by "monotonous intermediate" bulk compositions (Hildreth, 1981; Best et al., 2016). These dacites or quartz latites consist of rhyolitic melts with high crystal contents (35-60%) and are commonly understood to be the inevitable products of long-lived thermochemical and thermomechanical histories that produce buffered, homogenized compositions (de Silva and Gregg, 2014; Caricchi and Blundy, 2015; Best et al., 2016). Powered and maintained by the often invisible hand of mafic recharge (e.g. Hildreth, 1981) it is clear that such long-lived systems have episodic and incremental histories (Coleman et al., 2004; de Silva and Gosnold, 2007; Lipman and Bachmann, 2015) that may be blurred and homogenized if the magmatic flux is high enough to promote homogenization over heterogeneity, particularly during flare-up conditions in continental arcs (e.g., de Silva et al., 2006; Huber et al., 2009; Best et al., 2016).

The extensive ignimbrite plateau of the Altiplano-Puna Volcanic Complex of the Central Andes (APVC; de Silva, 1989a) is the surface expression of protracted, focused volcanism that was generated during a period of high mantle flux (de Silva et al., 2006). This archetypal ignimbrite flare-up fostered the geophysically and petrochronologically imaged residual "batholith" known as the Altiplano-Puna Magma Body (APMB; Chmielowski et al., 1999; de Silva and Gosnold, 2007; Kern et al., 2016; Pritchard et al., 2018). Bulk compositions outside of 66-69 wt% SiO_2 on the APVC typically make up a few percent of the total erupted magma (de Silva, 1989b; Lindsay et al., 2001b; Schmitt et al., 2001; de Silva et al., 2006; Grocke et al., 2017a), but they provide valuable insights into the behavior of their magmatic reservoirs and the magmatic history of the APVC as a whole. Rhyolites on the APVC are dominantly derived by crystallization of parental magmas that are represented by less felsic compositions in their eruptive sequences and they have geochemical compositions that are dominated by assimilated continental crust. These mechanisms of evolved melt production typically cause the APVC rhyolites to have steeper REE patterns than their parental magmas (i.e., clinopyroxene and amphibole fractionation) and 'crustal' isotopic signatures. These geochemical characteristics provides valuable insight into the variety of melts that ultimately accumulate into- and segregate from this large continental silicic magmatic complex.

Strongly contrasting the typical APVC ignimbrite is the ~ 5km^3 Caspana ignimbrite that crops out near the periphery of the APVC (Figure 1; de Silva, 1991). The ignimbrite is notably heterogenous with two distinct rhyolites and an andesite found in outcrop, connoting a physical storage condition that is unlike the typical "monotonous intermediate" reservoirs that evacuated the large volume, crystal-rich dacites (de Silva and Wolff, 1995; Huber et al., 2012; de Silva and Gregg, 2014; Black and Andrews, 2020). Petrologically, the Caspana system defies the oxidized state that is typical of APVC dacites and, indeed, arc magmas in general (Kelley and Cottrell, 2009; Burns et al., 2020), because it was appropriate for a fayalite rhyolite and an andesite bearing noritic glomerocrysts. These unique features prompted the petrologic and geochemical study presented here, that captures the magmatic processes and physical storage conditions of the Caspana magmatic reservoir. The reconstruction of the Caspana system and its compositional gaps provide a new lens with which to investigate rarely preserved processes contributing to the massive APVC eruptions.

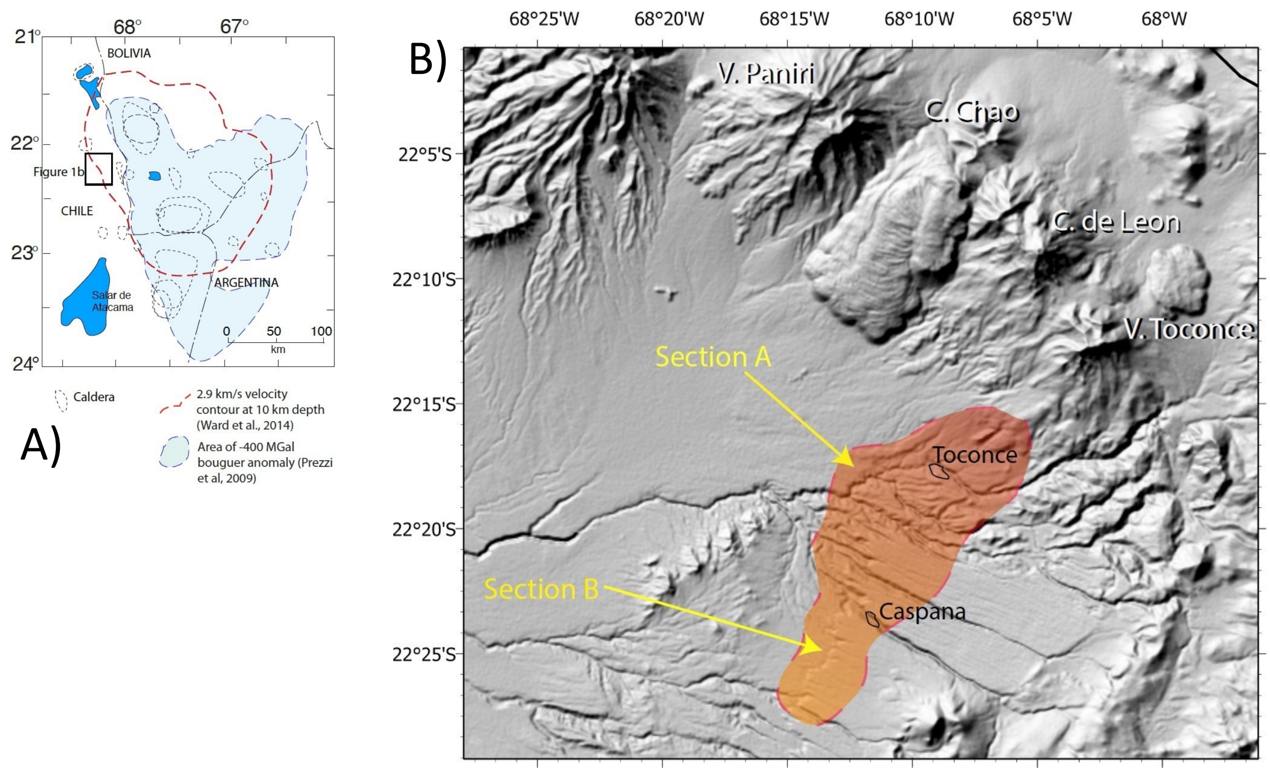

Figure 1: Location maps for the Caspana ignimbrite. A) Location of B) in relation to the subsurface geophysical anomalies of the Altiplano Puna Volcanic Complex (outlined). Surface projection of the AltiplanoPuna Magma Body (red dashed line; Ward et al., 2014) and the 400mGal Bouguer gravity anomaly (blue area) found by Prezzi et al. (2009) are shown. Caldera outlines modified from Kern et al. (2016). B) Shows the known distribution of the exposed Caspana ignimbrite. Volcanic centers of the Paniri-Toconce chain of volcanoes define the modern arc front in this part of N. Chile. Sites A and B correspond to the stratigraphic sections in Figure 2.

2. Geologic Setting

2.1 Geologic Background and Prior Work

Ignimbrites in the APVC are generally large volume monotonous dacites to rhyodacites that formed by the combination of crystal fractionation and crustal contamination (i.e. AFC) (de Silva, 1989a, 1989b; de Silva and Francis, 1989; Kay et al., 2010; Grocke et al., 2017a). In the Neogene between ~25-10 Ma, a relative flattening of the subduction angle occurred as the aseismic Juan Fernandez ridge was progressively subducted southwards beneath the South American Plate. This was followed by subsequent rollback on the subducting Nazca plate, resulting in arc-scale delamination of subcontinental lithospheric mantle (SCLM) and the ignition of a Central Andes-wide ignimbrite flare-up (Kay and Coira, 2009; Freymuth et al., 2015; Best et al., 2016; de Silva and Kay, 2018). In the ~21° to ~24°S segment of the arc, a crustal scale magmatic complex led to the development of an incrementally-constructed regional batholith (de Silva and Gosnold, 2007; Salisbury et al., 2011; Kern et al., 2016), the remnants of which is now detected as a seismic low-velocity zone known as the Altiplano-Puna Magma Body (APMB; Chmielowski et al., 1999; Ward et al., 2014; Prezzi et al., 2009; Pritchard et al., 2018). With an estimated depth range of 10 to 30 km and volume of >500,000 km^3, the APMB is interpreted as the parental source of the voluminous supereruptions of the APVC that ultimately erupted from upper crustal silicic magma chambers. Explosive activity during the Neogene ignimbrite flare up (de Silva et al., 2006; Kern et al., 2016) occurred in distinct pulses with peak episodes at ~8, 6, and 4 Ma. Since 4 Ma, volcanism in the APVC region appears to have returned to steady-state (i.e., background) activity (Burns et al., 2015; Tierney et al., 2016).

The APVC ignimbrites record a time of prodigious crustal magmatism when batholithic volumes of monotonous crustal magmas were the norm. In this context, the small volume (~5km^3) Caspana ignimbrite with its' strongly heterogeneous character stands out, particularly since it erupted during the last peak of the flare up (Kern et al., 2016). Prior case studies have found that many of the high silica magmas erupted on to the APVC are created dominantly by fractionation from the large volume dacites or andesites in the region (de Silva, 1991; Lindsay et al., 2001a; Schmitt et al., 2001; Grocke et al., 2017a). Isotopic compositions of these rhyolites and their parental magmas record significant crustal assimilation, with a 50:50 mix of mantle and regional basement compositions generally agreed upon (de Silva, 1989a; Aitcheson et al., 1995; Mamani et al., 2008, 2010; Kay et al., 2010). Importantly, the crystal cargo in all of these magmas record a high oxidation state and unchanging fO_2 within a given magmatic lineage (Grocke et al., 2016; Burns et al., 2020). For illustrative purposes and to emphasize the differences in rhyolite petrogenesis, the compositions of the low silica rhyolites found in the Tara ignimbrite (Grocke et al., 2017a) and the high silica rhyolites of the Alota ignimbrite (Salisbury et al., 2011; Kaiser, 2014) will be shown with the Caspana geochemical data.

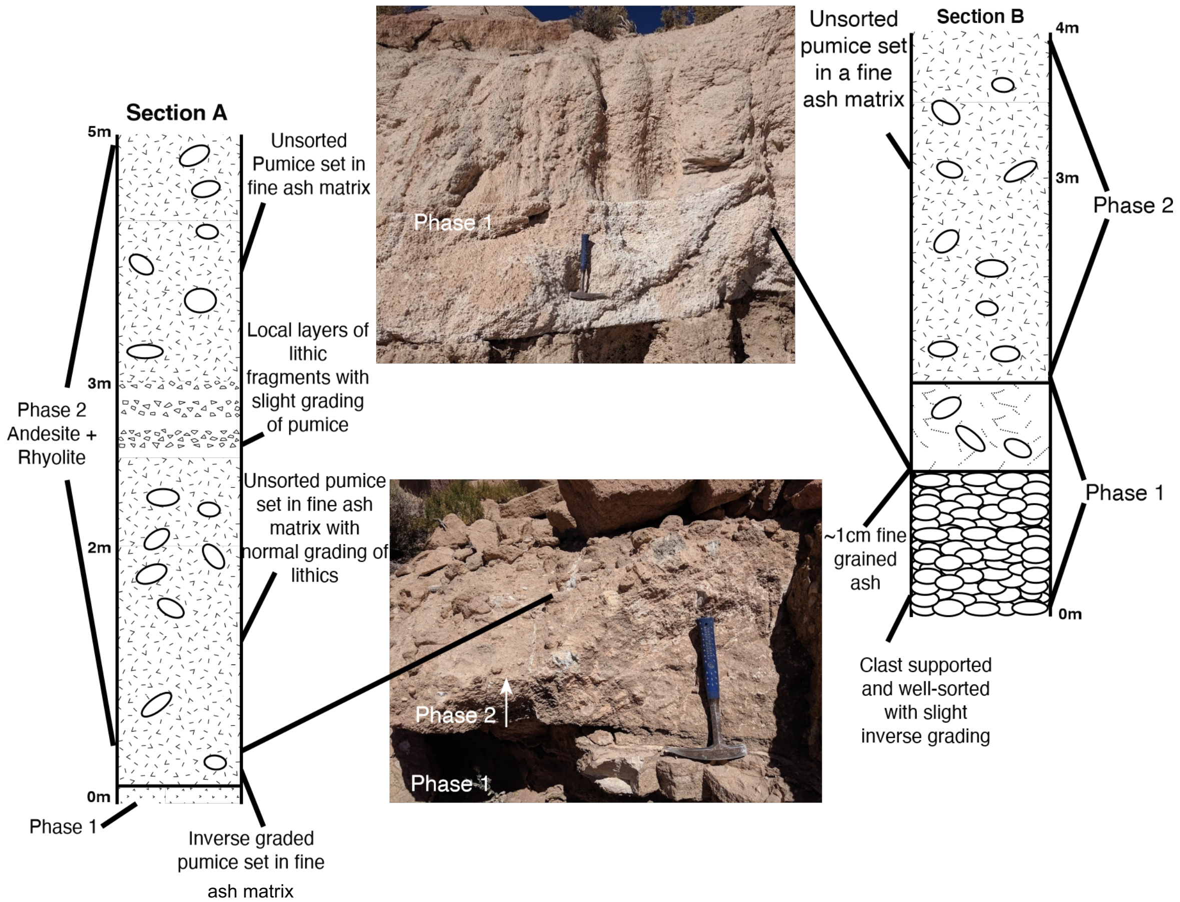

Figure 2: Graphic stratigraphic logs and photographs from the locations A and B on Figure 1B. Section A (left) is from a distal flow front of Phase 2 where andesite and the Phase 2 rhyolite clasts coexist. The flow unit contains local layers of lithics with very diffuse coarse-tail grading of pumice. Note the exposed sections of pumice in the lower flow unit (arrows) showing white (rhyolitic) and gray-black (andesitic) pumice. The area between the dashed white lines shows a thin reworked layer, below which is Phase 1. Section B (right) is more proximal. The section contains a plinian fallout deposit overlain by two pyroclastic flow deposits. Pumice from the plinian fallout and the immediately overlying thin flow unit have the same chemistry. The upper part of the section consists of Phase 2 rhyolite. Rock hammer for scale.

2.2 The Caspana Ignimbrite

The Caspana ignimbrite crops out in the Toconce-Caspana area of N. Chile (de Silva, 1989b; de Silva, 1991; Figure 1 ,2) and the age of the eruption is bracketed stratigraphically between the 4.09 Puripicar ignimbrite and the 4.54 Ma Linzor I ignimbrite. It's source vent(s) is/are thought to be buried beneath the younger Toconce and Leon volcanoes. de Silva (1991) first described the bimodal andesitic and rhyolitic juvenile clasts found in the ignimbrite, defining a large compositional gap. On the basis of reconnaissance bulk and mineral chemistry, an origin of the rhyolite by fractional crystallization of the andesite was proposed to have led to a small bimodal, zoned magma chamber.

We have resampled and reexamined the same exposures and sections introduced in de Silva (1991). The northern outcrops above the community of Toconce contain a rhyolitic plinian fallout of nearly aphyric pumice with occasional phenocrysts of plagioclase visible in hand specimen (Section B - Figure 2). There is a fine ash deposit on top of the fallout, that is in turn overlain by a distinct ~10 to 40cm flow unit that contains equally aphyric rhyolite. This sequence is collectively referred to as Phase 1. Above this lies several meters of massive ignimbrite containing the rhyolitic and andesitic pumices described by de Silva (1991), which are referred to herein as Phase 2. At the clast-rich flow front rhyolite and andesite pumice are largely mixed together with only hints of any internal stratigraphy (Section A, Figure 2) and overlie a basal ash that is equivalent to the basal plinian (Section B, Figure 2). The rhyolitic pumices in Phase 2 are distinct from those in Phase 1, as they have relatively higher crystallinity (~3-5%) and are substantially less fragile in hand sample. Phenocrysts in the Phase 2 rhyolite include plagioclase, biotite, and occasional yellow-green to amber colored olivine. The andesitic pumice in the Phase 2 ignimbrite has variable crystallinity from sample to sample that ranges from 2045%. In hand-sample the pumice displays plagioclase, orthopyroxene, and oxides.

3. Methodology

3.1 X-Ray Fluorescence and Inductively Coupled Plasma – Mass Spectrometry (ICP-MS)

Whole rock samples with the smallest amount of visible oxidation possible were selected for analysis. Those that contained oxidized surfaces were sawed or chipped off at Oregon State University to expose the innermost fresh face possible. Samples were crushed using steel plates in the jaw-crusher and grinded to a fine powder at OSU and processed at Washington State University using a ThermoARL AdvantXP for XRF analysis of major and some trace elements (HFSE) following the method of Johnson et al. (1999). REE and remaining trace elements were measured by ICP-MS on an Agilent 7700 Q-ICP-MS. LOI is high for some samples, so a subset of samples was re-run after washing in 1 molar HCl at OSU then sonicated and rinsed 3-5 times. The process was repeated until bubbles forming from reaction were no longer present; usually on the first wash. Results from XRF analysis on the digested samples show no systematic variation of CaO content from sample to sample (i.e., some are higher, some are lower) in the andesite and there is no change in rhyolite compositions. 1σ error bars of analysis from the tables of Johnson et al. (1999) are shown on major element graphs. For the whole rock error on trace elements, the quoted analytical precision of USGS standards is 5% RSD for the REE and less than 10% for all other trace elements. Repeat samples from 4 XRF runs from the WSU lab over the last few years have better precision than these reported values. Representative data from the Caspana ignimbrite are given in Table 1, with the full data set in Supplementary Table S1. Data measured by XRF from de Silva (1991) are denoted in tables where presented.

Table 1: Representative whole rock geochemistry

Unit	Phase 1 Rhyolite		Phase 2 Rhyolite		Andesite	
Sample	CH12022 - Dark		CH12021		CH12020(1)	
	Whole Rock	Glass	Whole Rock	Glass	Whole Rock$	Glass
SiO_2	73.79	73.59	75.21	75.72	59.95	68.70
TiO_2	0.20	0.16	0.09	0.08	0.72	0.44
Al_2O_3	15.46	14.83	12.86	13.52	20.91	16.10
FeO*	1.29	0.96	1.48	1.36	3.76	3.53
MnO	0.09	0.07	0.03	0.03	0.06	0.05
MgO	0.30	0.27	1.02	0.02	1.91	0.68
CaO	1.42	1.45	1.07	0.93	7.81	2.91
Na_2O	3.30	4.14	2.49	2.69	2.74	3.42
K_2O	4.10	4.30	5.74	5.54	2.00	3.86
P_2O_5	0.06	0.11	0.02	0.02	0.13	0.25
Cl	-	0.11	-	0.09	-	0.04
SO_3	-	0.02	-	0.01	-	0.02
Total	100.00	100.00	100.01	100.00	100.00	100.01
A/CNK	1.29	1.10	1.05	1.19	1.00	1.07
Mg#	29.30	33.82	55.13	2.83	47.50	25.40
La	39.3	45.8	39.8	41.7	25.2	41.5
Ce	76.7	82.2	81.0	84.5	49.9	77.8
Sm	5.4	6.3	7.9	8.4	4.7	7.8
Eu	1.1	1.2	0.8	0.7	1.5	1.3
Dy	3.8	4.4	7.7	8.4	4.0	6.8
Yb	1.8	2.2	3.6	4.4	1.8	3.7
Nb	15.3	19.1	12.6	14.6	9.7	14.8
Ba	970.8	1067.0	1140.3	1114.1	566.9	888.6
Y	19.7	25.6	40.1	46.9	20.2	43.4
Hf	4.7	6.2	4.6	4.4	3.8	6.8
Rb	129.3	149.3	174.0	200.0	71.5	124.8
Sr	212.9	229.2	118.0	102.4	513.1	323.2
Sc	3.2	10.4	9.7	16.4	12.0	21.4
Zr	146.5	198.4	125.7	107.3	138.7	280.0
$^{87}Sr/^{86}Sr$	0.70825		0.71129		0.71117	
$^{143}Nd/^{144}Nd$	0.51232		0.51210		0.51214	
$^{208}Pb/^{204}Pb$	38.796		38.871		38.850	
$^{207}Pb/^{204}Pb$	15.649		15.665		15.657	
$^{206}Pb/^{204}Pb$	18.814		18.763		18.745	

Totals are renormalized to 100% on anhydrous basis. * All Fe considered to be FeO. $Isotopic data listed from sample CH19C007. A/CNK: (Al_2O_3/101.96)/(CaO/56.08+Na_2O/61.98+K_2O/94.2). Errors on isotopic analyses, ICP-MS for whole rock, and LA-ICP-MS for glass discussed in text. Full data set including non-normalized values can be found in Supplementary Tables S1 and S2.

3.2 Thermal Ionization Mass Spectrometry (TIMS)

6 HCl digested samples (as in section 3.1) were analyzed for $^{87}Sr/^{86}Sr$, $^{143}Nd/^{144}Nd$, $^{208}Pb/^{204}Pb$, $^{207}Pb/^{204}Pb$, and $^{206}Pb/^{204}Pb$ analysis by thermal ionization mass spectrometry (TIMS) at New Mexico State University using the analytical methods highlighted in Ramos (1992). Analytical uncertainty is 0.000012, 0.001, 0.001, 0.002 for $^{87}Sr/^{86}Sr$, $^{208}Pb/^{204}Pb$, $^{207}Pb/^{204}Pb$, and $^{206}Pb/^{204}Pb$ (NBS 987 standard) and 0.00001 for $^{143}Nd/^{144}Nd$ (La Jolla standard). Representative data are given in Table 1, with the full data set in Supplementary Table S1.

3.3 Electron Probe Micro-Analysis (EPMA)

EPMA analysis was carried out in the Stanford Microchemical Analysis Facility (MAF) at Stanford University on a JEOL JXA-8230 SuperProbe. Major and minor element abundances in the silicate minerals (i.e., feldspar, pyroxene, fayalite, and biotite) were analyzed using an accelerating voltage of 15 keV, a 20 nA probe current, and a 3 μm spot size. On-peak count times ranged from 10-60 s and were optimized to achieve the desired counting statistics. Major element concentrations in the matrix glasses were measured using conditions similar to those used for the silicate minerals, except the spot size was increased to 10 μm to minimize alkali migration. In addition, Na migration was monitored during analyses and time-dependent intensity corrections were applied when applicable. In order to gain detailed information on minor and volatile element abundances (P, Fe, Mn, Ti, Cl, and S) in the glasses a second set of measurements were made at the same location(s) at higher probe currents and longer count times. This significantly decreases analytical uncertainties, reduces detection limit, and increases precision. Oxide phases were analyzed using a 20 keV accelerating voltage, 20 nA probe current, and focused 1 μm spot. On-peak count times ranged from 20-60 s. Full datasets are available in Supplementary Tables S2 to S7.

3.4 Laser Ablation – Inductively Coupled Mass Spectrometry (LA-ICPMS)

LA-ICPMS was conducted at the Keck Collaboratory at Oregon State University for trace element concentrations of silicate glasses that were mounted in epoxy and cleaned in an ultrasonic bath in ethanol and then DI. Methodology closely follows that outlined in Kent and Ungerer (2006). ^{43}Ca measured on BCR-2G was used as an internal standard and ATHO-G was run after every 15 analyses to check for consistency (e.g. instrument drift, clean lines). To reduce surface contamination, samples were initially ablated for ~3 seconds with a 160μm spot and given a brief washout period before measuring. Count times, dwell times, and the background interval for each analysis (taken prior to ablating) are 30, 0.01, and 12 seconds respectively. A 30 second washout time was used after each ablation period. The average 1σ of all analyses are shown on trace element plots and errors are propagated where trace element ratios are shown. Full datasets are available in Supplementary Tables S2 to S7.

3.5 Statistical Modelling: Two-Sample t-test, Kernel Density Estimates (KDE), and Polytopic Component Analysis (PCA)

Welch's two sample t-test is used below in conjunction with kernel density estimate (KDE) distributions to assess the existence of multiple phenocryst populations (Ramsey and Schaefer, 2013). The benefit of using Welch's t-test over a standard (student's) two sample ttest is the assumption that equal variance for two distinct samples is not required. Instead, the standard error of the t-statistic incorporates the standard deviation of both population distributions. The increase in standard error broadens the distributions, thereby increasing the probability that the true mean lies in the tails of the respective distributions. This causes Welch's two-sample t-test to be more resistant than the student's two sample t-test and it is well known that the t-test is robust against the normality assumption.

It is often effective to visualize data by stacking the distribution of each observation to create a density distriubtion. As pointed out by Vermeesch (2012) the commonly used probability density plots (PDPs) produce poor approximations to much geologic data. This is particularly true for data with large analytical uncertainties that cause the PDP to overemphasize more precise measurements. A PDP will also oversmooth a dataset if the sample size is large and undersmooth it if sample size is too low. The kernel density estimate (KDE) is constructed in a similar fashion, but the width of the i^{th} distribution can be determined by a constant value or the local data density. The resulting KDE is therefore not subject to over- or undersmoothing and better preserves the distribution of the measurements.

Principal component analysis (PCA) is a powerful tool that allows the data analyst to determine where a datset has the most variability. It is virtually always the case that the first two or three principal component (PCs) are those that should be considered, because principal components often become correlated with one another or lose interpretability beyond the third PC. The constructed linear combinations require some *a priori* knowledge and should correlate with the data in a predictable manner. The first principal component should correspond directly to its interpreted significance (i.e., its “real-world” meaning) and will contain most of the variance in the dataset. The second will usually account for most of the variability remaining. The validity of the linear combinations and their interpretations are assessed in two steps: 1) Regressing the linear combinations that are suggested by the first and second PC’s and 2) Analyzing the correlation between the residuals produced from the first two linear combinations vs. PC2. This allows the user to ensure that the variability associated with PC2 is being accounted for by the chosen linear combinations after ‘removing’ (regressing out) the variability that PC1 is already covering. In a likewise manner, the same can be done with PC3. In geologic studies it is common to use the suggested linear equations to create groups of data and visualize the vectors that are influencing their position on plots of PC1 vs PC2 (e.g., Pitcher et al., 2021).

<u>3.6 Mass Balance and Least Squares Regression</u>

The purpose of constructing a mass balance is to test if all parts of interest sum to their whole. For fractional crystallization this constitutes subtracting the chemical components constrained within each phase that is crystallizing from an observed magmatic composition to create a newly observed magmatic composition (Stormer and Nicholls, 1977). This is done by setting the mass of the of the newly derived magma equal to the amount of the i[th] oxide removed by the j[th] phase, giving the mass balance of the i[th] oxide:

$!_i + \sum_{j=1}^{n} a_{ij} X_j = F_i$ (1)

Where !! is the weight percent of each oxide, %!" is the mass fraction of the i[th] oxide in the j[th] phase, &" is the mass of each phase that is removed, and (! is the mass of the i[th] oxide in the new magma. Normalizing (! by the mass of the new magma (() and multiplying both (! and %!" by 100 gives the weight precent of each oxide in the newly derived magma ()!) and in each phase (+!"). Substituting these into (1) and considering the sum of !! and the total mass of the newly derived magma gives

$\sum_{j=1}^{n} \frac{b_{ij} X_j}{} = \frac{P_i}{} \big(100 + \sum_{\%((}$ %((#"$% &"/ − !! (2)

Or

$\sum_{j=1}^{n} u_{ij} X_j = D_i$ (3)

Where 1!" = &!%((-"*)! and 2! =)! − !!, forming a system of m equations for each oxide with n unknowns for the removed mass of each phase. The best fit masses are those that minimize the least squares:

$$S = \sum_{i=1}^{m}(g_i - D_i)^2 \quad (4)$$

Where 5! is the difference between the ith oxide in the starting composition and the newly derived magma.

Table 2: Petrographic features of Caspana pumice

Rock	Andesite	Phase 2 Rhyolite	Phase 1 Rhyolite
Crystallinity	35%	1-5%	0-2%
Vesicularity	40-50%	50-60%	50-60%
Groundmass	20-30%	35-45%	40-50%
Phases	Plag (75-80%)	Plag (80%)	Plag (>95%)
	Orthopyroxene (15-20%)	Biotite (10%)	Apatite (tr)
	Oxides (1-5%)	Fayalite (5%)	Zircon (tr)
	Apatite(1%)	Oxides (3%)	Muscovite (tr)
	Amphibole (tr)	Allanite (tr) Apatite (tr) Zircon (tr) Quartz (tr)	Titanite (tr)
Other Features	G2 Gloms-Plag + Opx + Ox (5-10%)	Allanite ~225 um	Mag > Ilm
	G1 Gloms- Plag gloms (15%) Ilm > Mag Xenoliths present	Ilm > Mag Xenoliths present	

4. Results

4.1 Petrography

4.1.1 Andesite Pumice

Andesite pumice in the Caspana ignimbrite is moderately crystalline (25-45 vol%), with a phase assemblage consisting of plagioclase (75-80%), enstatite (15-20%) and oxides (1-5%) in a groundmass of well vesiculated glass with ellipsoidal vesicles (~50%) (Table 2). Plagioclase is the dominant crystalline phase and occurs in a range of sizes (~100µm - 1.5mm) with an average size of ~1 mm. Texturally, plagioclase define a continuum of textures ranging from clear, concentrically zoned crystals with sharp rims, to crystals that are pervasively sieved (Figure 3). There are two texturally distinct populations of enstatite in the andesite pumice which can be easily differentiated by their crystal shapes and mineral inclusions (P1 and P2). P1 crystals range in size from ~0.5 to 1.5 mm, are more rounded, and have significantly more Fe-Ti oxide inclusions than P2 crystals. P2 crystals are roughly similar in size but are euhedral and contain minimal Fe-Ti oxide inclusions. The andesite pumice contains both ilmenite and magnetite. Ilmenite is far more abundant than magnetite and can occur as both a phenocryst and microphenocryst within the groundmass and within enstatite. In contrast, magnetite only occurs as microphenocrysts typically in enstatite or within glomerocrysts, and is always exsolved. There are also two distinct types of glomerocrysts present in the andesite pumice. One type (G1) is strictly plagioclase,

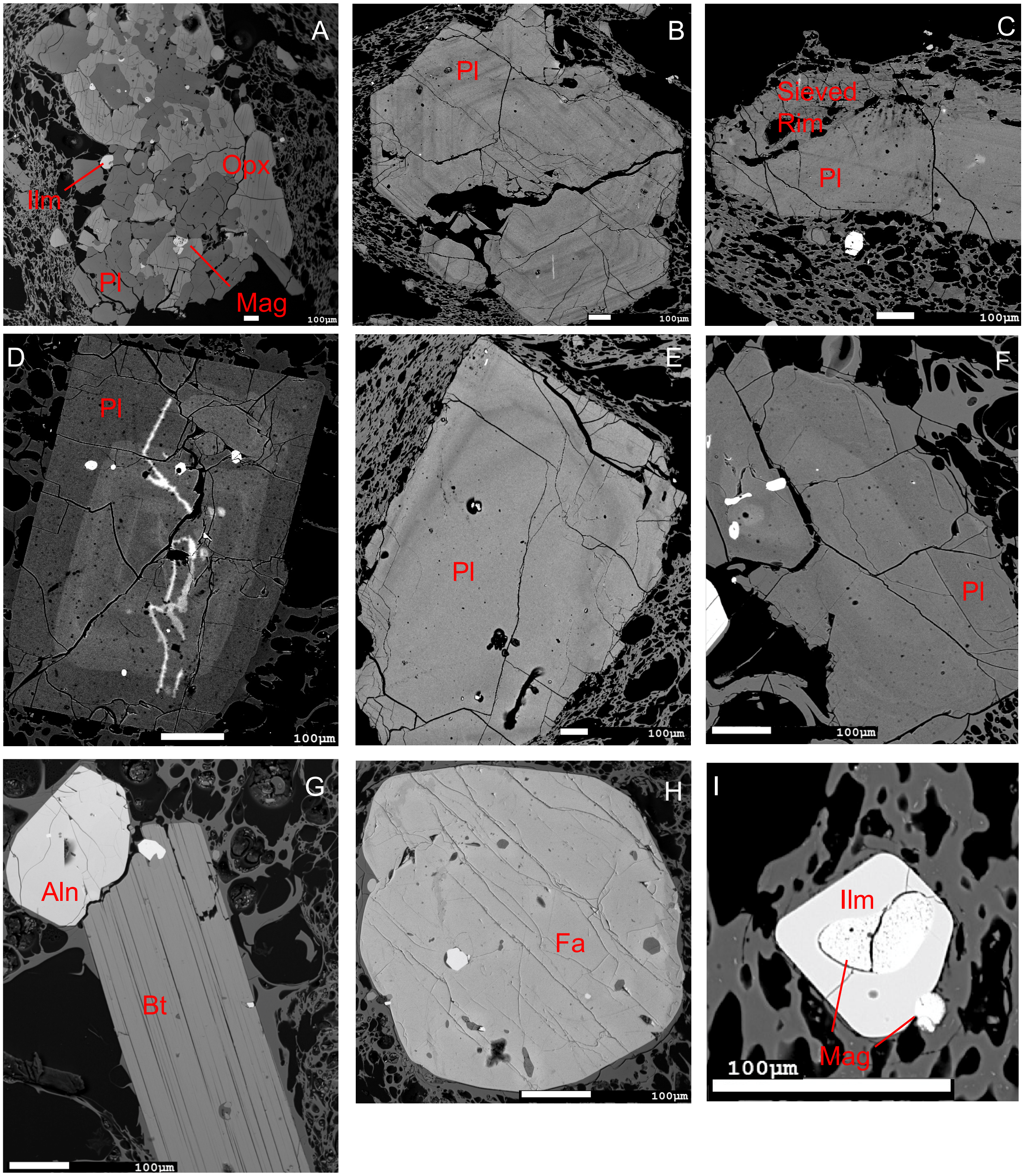

Figure 3: Backscattered electron images showing representative textures and crystalline phases from the Caspana ignimbrite units. A) G2 glomerocryst from the andesite. B, C, E) Representative plagioclase from the andesite pumice. D) Plagioclase from the Phase 1 rhyolite. Note the unmixing texture. F) Plagioclase from Phase 2 rhyolite. G) Biotite and allanite phenocrysts from the Phase 2 rhyolite. Allanite is surprisingly large in this rhyolite relative to other APVC rhyolites. H) Fayalite from Phase 2 rhyolite. I) Micro- phenocrysts of oxides from the andesite pumice. Magnetite is the exsolved phases occurring as an inclusion within, and adhering to, the larger ilmenite crystal.

whereas the other type (G2) is comprised of Plagioclase (Pl) + Orthopyroxene (Opx) + Ilmenite

(Ilm) + Magnetite (Mag). G1 glomerocrysts are more abundant and contain large, tabular concentrically zoned plagioclase. G2 glomerocrysts are dominantly orthopyroxene in the presence of more lath-like plagioclase than those found in G1 glomerocrysts. Ilmenite crystals are generally larger in G2 glomerocrysts and orthopyroxene can be heavily rounded at the edges. Amphibole is rare in the andesite pumice, occurring as a single phenocryst and as a single inclusion in opx. The andesite pumice also contains quartzofeldspathic xenoliths.

4.1.2 Rhyolite Pumice

There are two types of rhyolite pumice in the Caspana ignimbrite (herein referred to as Phase 1 and Phase 2) and both are crystal-poor (<1-5% vol.% crystals). The Phase 1 is the less crystalline of the two (+/- 1%). Phase 1 pumice in the plinian fallout can be entirely aphyric or contain <1% crystals by volume. Pumice that occurs in the flow unit just above the fallout has a crystallinity of ~1%. Feldspar is the most abundant mineral (~95%) in the Phase 1 rhyolite and frequently displays sharp rims and distinct, somewhat infrequent zoning boundaries. Microphenocrysts of oxides can be observed in thin-section and mineral separates as well as muscovite, and accessory zircon and titanite. Phase 1 rhyolite also contains small quartzofeldspathic xenoliths that contain quartz, feldspar, amphibole, oxides, +/- pyroxene and anhedral, micaceous material that bears semblance to restite. The quartzofeldspathic xenoliths are similar to those in the andesite. As previously stated, Phase 2 pumice are more crystal-rich (3-5%) and contain plagioclase (80%), fayalite (5%), biotite (10%), and ilmenite (3%) with accessory apatite and zircon. Phenocryst size allanite can be observed in thin section as well.
Magnetite is present but rare (<1%) and quartz was found in mineral separates.

4.2 Whole Rock Major and Trace Elements

Bulk rock analyses of the Caspana pumice (Table 1 and Supplementary Table S1) show that the system has clear calc-alkaline affinities. The three pumice types define three distinct compositional groups along a high-K calc-alkaline trend (Figure 4) with a large compositional gap between 60 and 74 wt.% SiO_2. Rhyodacitic glass from the andesite pumice (66-68% SiO_2) generally lies on a distinct trend between andesite and Phase 2 pumice in both major and trace element space (Figure 4, 5). The rhyodacite defines the termination of the trend of andesite pumice samples in FeO relative to MgO (Figure 5C). The FeO contents of the rhyodacite also exceeds the rest of the APVC pumice samples that have a comparable amount of MgO contents.

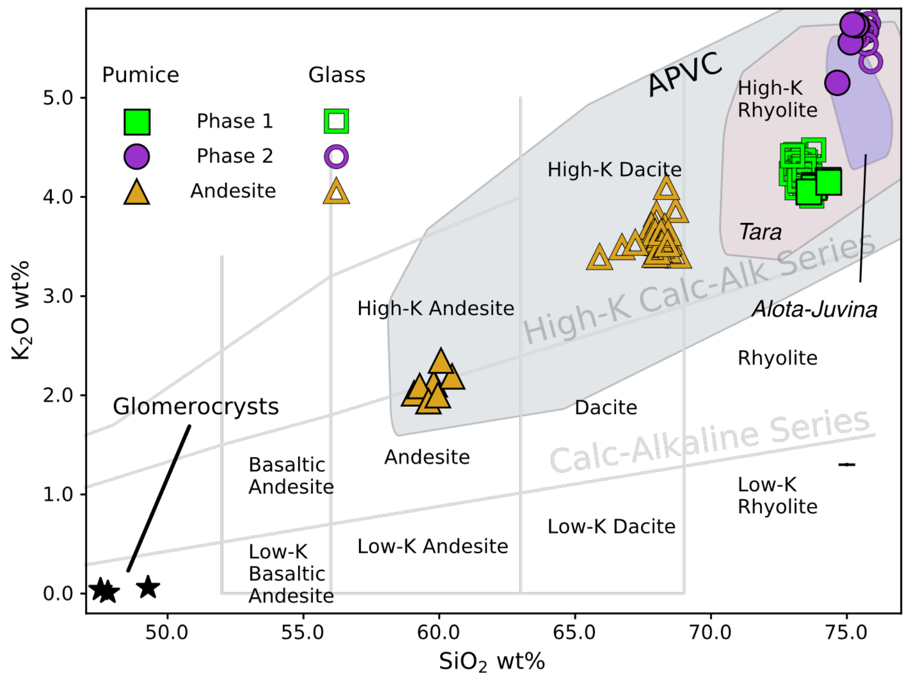

Figure 4: SiO_2 vs. K_2O bivariate diagram showing the lithological discrimination fields of Ewart et al. (1982). Diagram includes Caspana pumice types (filled symbols) and matrix glasses (empty symbols). Glomerocryst compositions of two G2 norite glomerocrysts (Plag + Opx + Oxides) and one G1 glomerocryst (Plag) are included. Compositions are based on mineral analyses and modal contents. The compositions of glomerocrysts, andesite, Phase 2 rhyolite, and their respective glasses lie on a straight line. Phase 1 falls below this line. Gray field outlines the data from APVC ignimbrites. Pink and blue field outlines the Tara and Alota-Juvina felsic pumices, respectively.

The Phase 1 rhyolite displays slightly lower SiO_2 and lower alkali concentrations than the Phase 2 rhyolite. Using Shand's index, the Phase 1 rhyolites are strongly peraluminous (A/CNK ~1.25, A/NK ~1.59), whereas the Phase 2 rhyolite and andesite are metaluminous to slightly peraluminous (Table 1), similar to other APVC magmas. By normalizing FeO with other major elements (i.e., CaO and MgO; herein referred to as Fe indices), the Phase 2 rhyolite pumice has considerably higher Fe indices relative to the Phase 1 rhyolite and the rest of the APVC rhyolites (Figure 5). The only other rhyolite that we know of that approaches these Feindices is the extremely evolved Alota-Juvina rhyolite (Salisbury et al., 2011; Kaiser, 2014). Phase 1 glasses (~73-74 wt.% SiO_2) have Fe indices (0.75-0.81 FeO/(FeO+MgO); Avg. 0.79) that are lower than the andesite (0.77-0.85 FeO/(FeO+MgO); Avg. 0.81) and always lower than the Phase 2 glasses (0.95-0.98 FeO/(FeO+MgO)). The Fe-indices of Phase 1 pumice and glass are commonly observed in APVC rhyolites and rhyodacites.

Trace element concentrations for the Caspana pumice and glasses presented in figures

5 and 6 reveal that Rb concentrations in the andesite are significantly lower than in the rhyolites (47-113 ppm). Chondrite-normalized trace element diagrams show typical arc affinity for all three pumice populations (i.e. Nb-Ta trough, negative Pb anomaly, enriched LILE) (Figure 6)

Figure 5: Major and trace element bivariate plots illustrating relationships between the bulk rock and glass compositions of the various components of the Caspana Ignimbrite. A to C) Fe-indices showing the distinct high FeO/MgO and FeO/CaO ratios in the Phase 2 rhyolite. Fe indices in matrix glass of each rhyolite trend in opposite directions. D) Sr vs Y; E) Rb-Nb and F) Rb-Y. Rb, like SiO_2, also displays a large compositional gap (~120ppm) with rhyodacitic glass lying in the center. There is a coherent positive trend between Phase 2 andesite and rhyolite in Rb-Y space and a negative trend in Sr-Eu space. Phase 1 does not share these characteristics. Fields as in Figure 4.

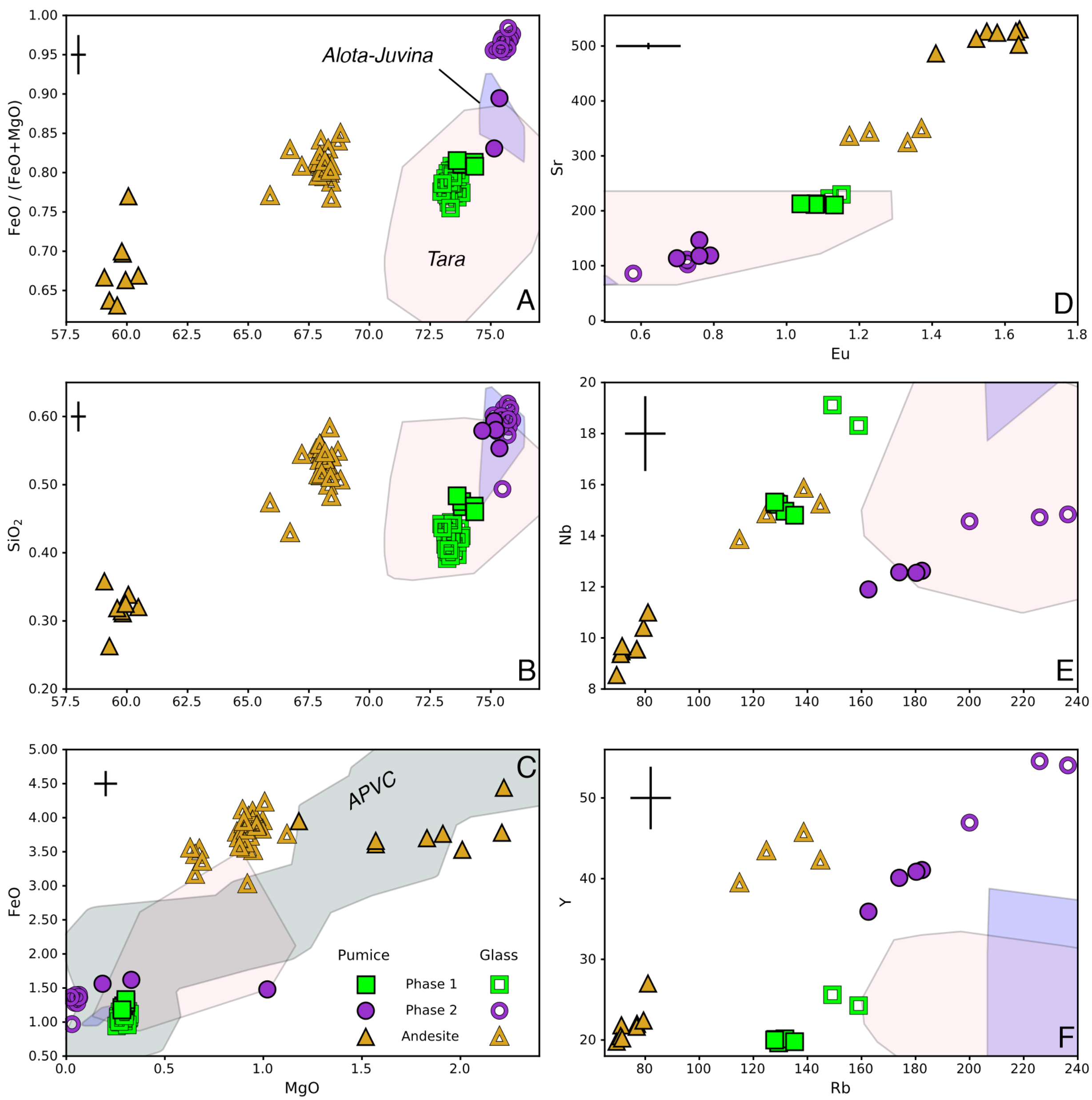

and all three have relatively high LREE/HREE ratios (8.9 - 14.9). The andesite pumices display either a flat or positive Eu anomaly (Figure 6). Both rhyolite pumices show negative Eu anomalies, but the anomaly is significantly more pronounced in the Phase 2 pumice. The Phase 2 pumice and the Alota-Juvina have comparable Eu anomalies and LREE/HREE ratios (Figure 6A). The Eu and Sr concentration of Phase 1 glasses are within error of the Phase 1 pumice (as is Ba),

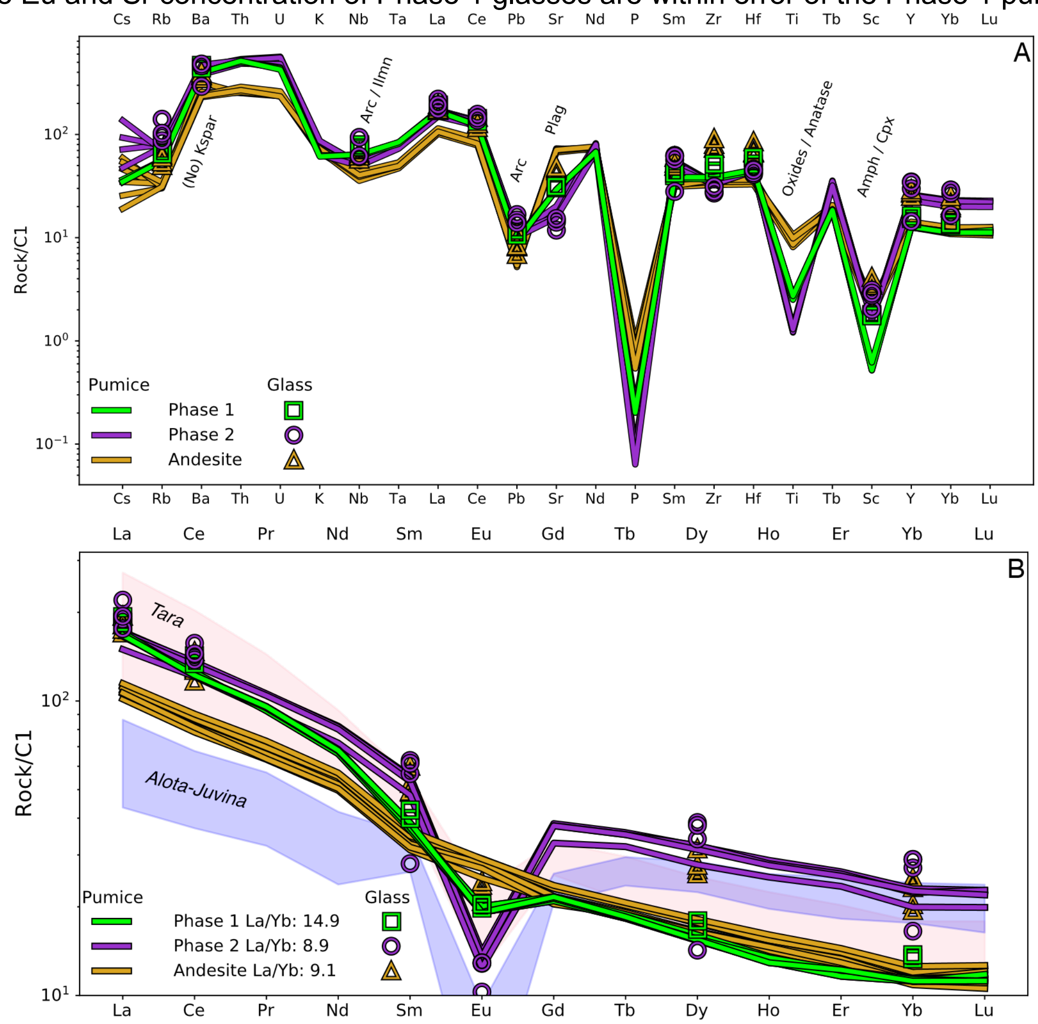

Figure 6: Multi Element "spider" diagrams illustrating trace element relationships in the Caspana Ignimbrite. Normalization values taken from McDonough and Sun (1995). A) C1 chondrite normalized trace element spider diagram. The Caspana compositions have characteristics typical of arc magmas including the Nb-Ta trough, enrichment in LILE, and depletions of elements compatible in minerals crystallized in hydrous/oxidized environments. Phase 1 is unlike the andesite and Phase 2 in its more stark Sc depletion. Zr and Hf are distinctly more fractionated from one another in phase 2 compared to phase 1. Concentrations of HFSE are substantially higher in Phase 2 than Phase 1. B) C1 Chondrite normalized diagram showing that the Phase 2 andesite has a flat or slight positive Eu anomaly whereas Phase 2 rhyolite has a large negative anomaly. The rhyodacitic glass from the andesite has a REE pattern overlapping the Phase 2 pumices. The Phase 2 rhyolite has higher HREE than the Phase 1 rhyolite (La/Yb 14.9 vs 8.9). Fields as in Figure 4.

whereas the Phase 2 glasses are depleted relative to their host pumice (Figure 5). Phase 2 pumice and rhyodacite glass both have higher concentrations of REE and Y than the Phase 1 pumice. The Phase 2 rhyolite pumice has similar to slightly lower Nb concentration than the rhyodacite and the two overlap one another in Y (Figure 5E, F).

The Phase 1 rhyolite has the largest Sc depletion and Dy/Dy* anomaly of all other compositions from the Caspana system (Figure 6, 7) and is more typical of APVC rhyolites. Interestingly, the crystallinity (mostly feldspar) and the amount of restite material in the Phase 1 rhyolite thin sections decreases down section, but the expected systematic change in trace element concentrations is not captured by matrix glass nor pumice data (i.e., Sr and Eu; Figure 5). Furthermore, zircon is readily found in the Phase 1 thin sections (and mineral separates), but Zr and Hf concentrations of matrix glass seem to indicate that the Zr saturation temperature was not attained for any prolonged timescale in the collected pumices (Figure 7).

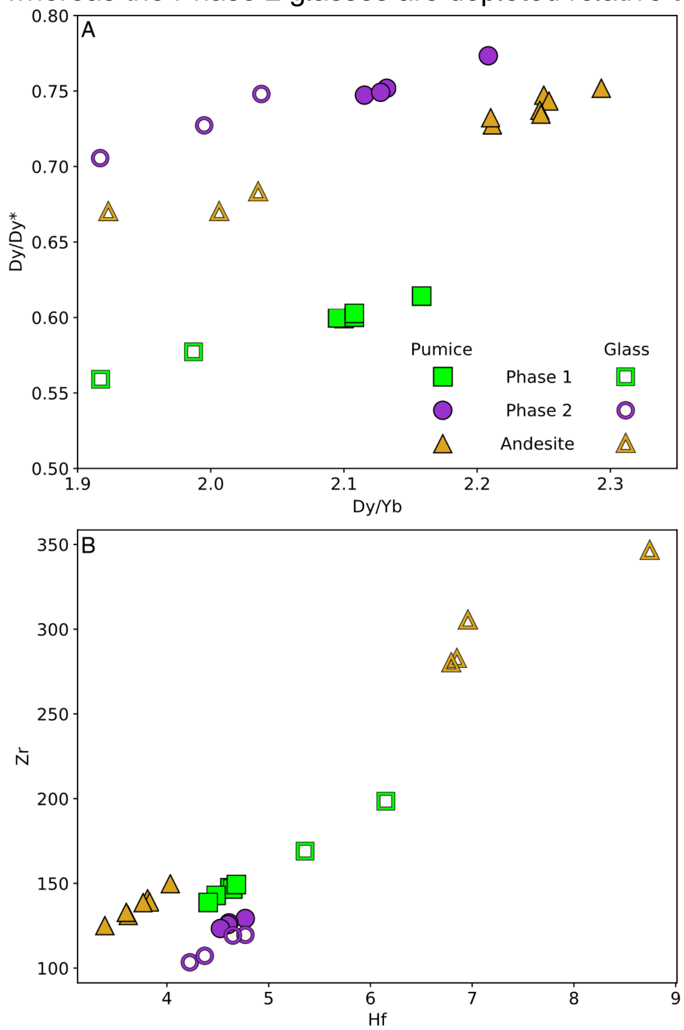

Figure 7: Bivariate diagrams of selected trace element concentrations from pumice samples and glass. A) Dy/Dy* (Davidson et al., 2013) of the Phase 1 rhyolite is lower than the Phase 2 rhyolite and andesite. The latter two are similar to one another and contain little to no amphibole or clinopyroxene (Table 2). B) Zr-Hf shows that both the Phase 2 andesite and the Phase 1 rhyolite have enriched Zr-Hf in glass relative to the pumice. Phase 2 rhyolite has the expected depletion in its glass based on typical arc magma Zr-saturation temperatures.

4.3 Whole Rock Isotopes

Broadly, the isotope ratios measured in the Caspana pumice are consistent with other ignimbrites in the APVC (Figure 8) (Lindsay et al., 2001a; Godoy et al., 2014, 2017; Grocke et al., 2017a). These isotopic ratios lie along the trend of a simplar AFC model (DePaolo, 1981) between mantle derived basalt and the most evolved samples within the Sierra de Moreno (SdM) metamorphic complex, which has been proposed as the local basement for this region of the arc (Godoy et al., 2014, 2017). Andesite pumice have $^{87}Sr/^{86}Sr$ and $^{143}Nd/^{144}Nd$ ratios that are indistinguishable from those measured in the Phase 2 rhyolite pumice (0.7112 and 0.5121 vs. 0.7113 & 0.5121, respectively) (Table 1; Figure 8A; Supplementary Table S1). The compositions are also close to one another in Pb isotope space ($^{207}Pb/^{204}Pb$ $^{208}Pb/^{204}Pb$-$^{206}Pb/^{204}Pb$) (Table 1; Figure 8; Supplementary Table S1). Compared to Phase 2, the Phase 1 rhyolite is significantly less radiogenic in $^{87}Sr/^{86}Sr$ (0.7081 – 0.7082) and variable in $^{143}Nd/^{144}Nd$ (0.5121 – 0.5123). Phase 1

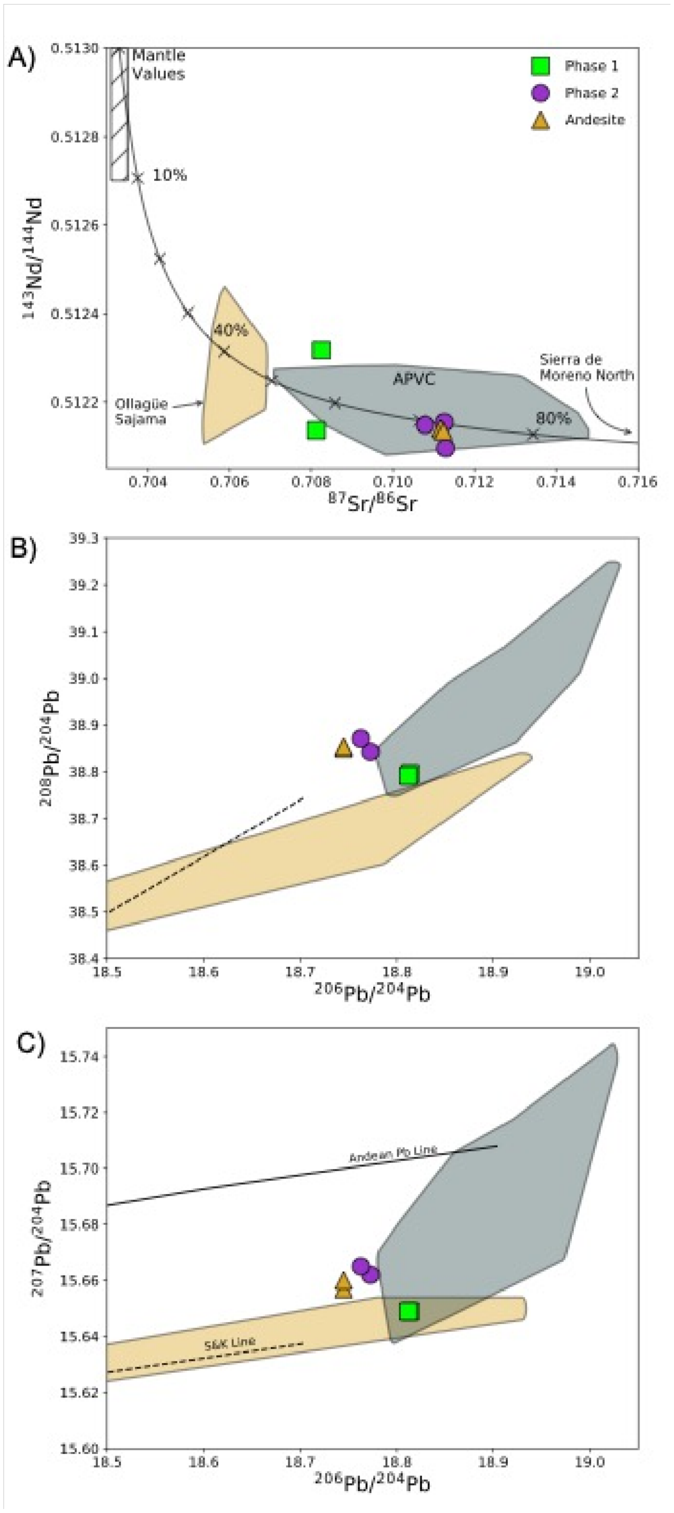

Figure 8: Radiogenic isotope variation diagrams showing samples from the Caspana system in context for various local and regional Central Andes and APVC relevant isotopic groups. A) The Phase 2 andesite and rhyolite have indistinguishable $^{87}Sr/^{86}Sr$ and $^{143}Nd/^{144}Nd$. Phase 1 has much less radiogenic $^{87}Sr/^{86}Sr$. Curve represents an AFC model (DePaolo, 1981; see Supplementary Table 8 for details) calculated using a mantle value of .703 and .513 for $^{87}Sr/^{86}Sr$ and $^{143}Nd/^{144}Nd$, respectively, following the findings of Mamani et al. (2010) and van Alderwerelt et al. (2021). Basement composition for the model is the Sierra de Moreno complex (e.g. Godoy et al., 2014, 2017). Fields for the APVC ignimbrites (bluegray field) and the arc parental magmas, represented by lavas from Ollague and Sajama volcanoes (tan field) are shown. B) $^{208}Pb/^{204}Pb$ vs $^{206}Pb/^{204}Pb$ and C) $^{207}Pb/^{204}Pb$ vs $^{206}Pb/^{204}Pb$ for the same data sets as in A. Andean Pb line (solid black line; Lucassen et al., 2002) and Stacey and Kramers line (dashed; Stacey and Kramers, 1975) shown for reference. Analytical errors are smaller than symbols. See text for further discussion.

rhyolite samples are within analytical error of one another in Pb isotopic composition (Figure 8C). These pumice have slightly lower $^{208}Pb/^{204}Pb$ and $^{207}Pb/^{204}Pb$ ratios, and slightly higher $^{206}Pb/^{206}Pb$ ratios than the Phase 2 rhyolite and andesite pumice but are well within the fields defined by other APVC ignimbrites.

Table 3: Representative feldspar analyses

Rock Type	Phase 1 Plinian		Phase 2 Rhyolite		Andesite		Andesite	
Crystal	CH12022_Fspar1		83070_Fspar4		CH120202_Fspar4		Glomerocryst	
Position	Core	Rim	Core	Rim	Core	Rim	Core	Rim
SiO_2	57.29	57.65	59.97	60.81	47.14	46.91	48.01	48.2
Al_2O_3	26.45	25.82	25.21	24.02	34	33.64	33.43	32.92
FeO	0.21	0.23	0.11	0.17	0.23	0.26	0.27	0.28
MgO	0.02	0.01	0	0	0.04	0.04	0.03	0.03
CaO	8.4	7.8	6.71	5.92	17.3	17.21	16.43	15.93
Na_2O	6.26	6.28	7.09	6.92	1.9	1.94	2.26	2.51
K_2O	0.44	0.51	0.73	1.05	0.07	0.11	0.11	0.14
Total	99.06	98.29	99.83	98.89	100.67	100.11	100.53	100
An	0.41	0.39	0.33	0.30	0.83	0.83	0.80	0.77
Ab	0.56	0.57	0.63	0.64	0.17	0.17	0.20	0.22
Or	0.03	0.03	0.04	0.06	0.00	0.01	0.01	0.01
Fe*/Al	0.006	0.006	0.003	0.005	0.005	0.005	0.006	0.006

Fe* represent total Fe. Fe/Al on cation basis. Full dataset in Supplementary Table S3.

4.4 Phase Chemistry

4.4.1 Plagioclase

Plagioclase phenocrysts in the andesite have a moderately broad range of ~An_{10} (An_{8676}) and little correlation between composition and texture (Figure 3B, 3C, 3E, 9; Table 3; Supplementary Table S3). The dominant mode in the distribution of all phenocrysts is at ~An_{82} (Figure 9C). This peak is defined by non-zoned phenocryst compositions, normally zoned cores, and reversely zoned rims. Kernel Density Estimates (KDEs) of core and rim An content from normally and reversely zoned phenocrysts are effectively mirrored distributions, though it should be noted that some normally zoned cores lie at low An content. The FeO concentration in andesite phenocryst cores and rims have a mode at ~0.24 wt%, though FeO on normally zoned phenocryst rims can be skewed up to ~0.35 wt% FeO. Like the phenocrysts in the andesite, G1 glomerocrysts have a tight distribution at ~An_{82} with a slight left skewness (Figure 9A). FeO concentration of G1 plagioclase are non-zoned and low (FeO 0.22-0.26 wt%). G2 plagioclase define the range of An and FeO contents (An_{88-76}; FeO 0.23-0.53) (Figure 9B). The distribution of An contents on G2 plagioclase rims are offset to lower An values than their cores, and overlap with with reversely zoned phenocryst cores, normally zoned phenocryst rims, and the subset of normally zoned phenocryst cores that is present at lower values of An. FeO of the G2 cores (mean ~0.29 wt%) is higher than that of G1 plagioclase and the phenocrysts, has a

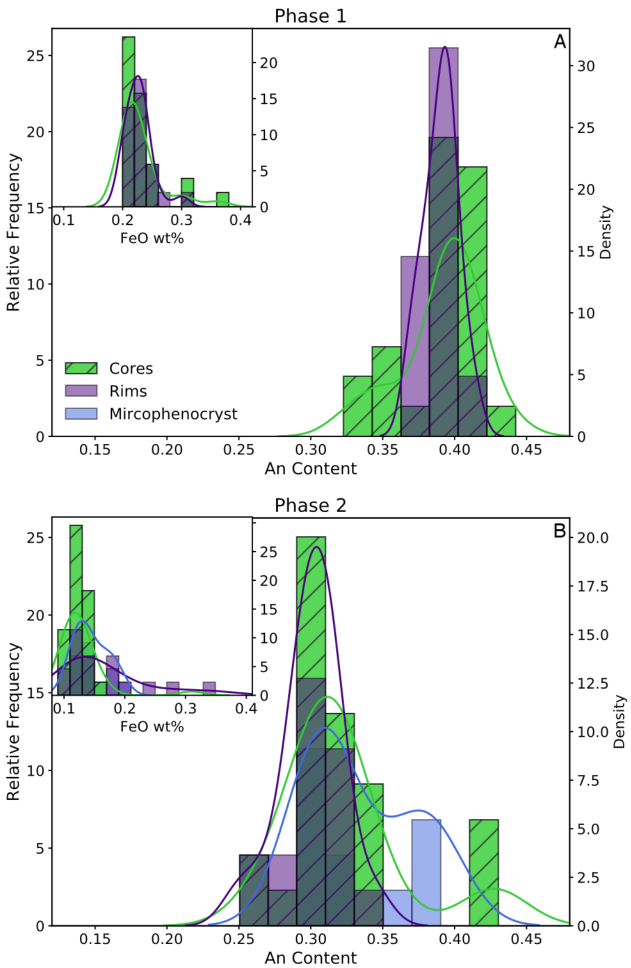

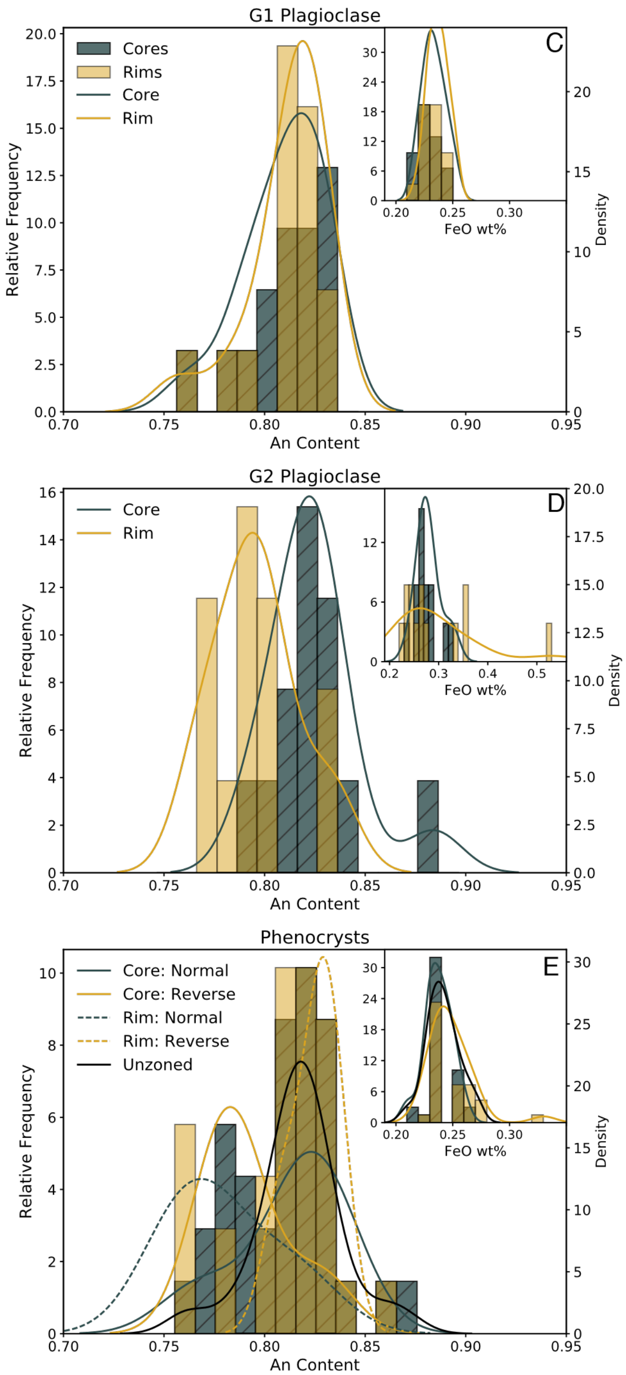

Figure 9: Histograms of plagioclase compositions from the Caspana Ignimbrite. A) Phase 1 rhyolite; B) Phase 2 Rhyolite. There is distinct right skewness in FeO in Phase 2 rhyolite phenocryst rims, similar to andesite G2 glomerocrysts and phenocrysts. Phase 2 has a prominent peak of cores and rims at ~An_{32} and another distinct subpopulation that shares compositions with Phase 1 (note right skewness). There is another population that has the same An contents as the andesite (not shown). C) G1 Glomerocrysts, D) G2 Glomerocrysts, E) Andesite Phenocrysts. There is a clear concordance in plagioclase compositions between the glomerocrysts and the phenocrysts. G2 rims and phenocrysts have similar and higher FeO content than G1 Plagioclase but extend to lower An values. KDEs of An content from normal and reversely zoned phenocrysts mimic the G2 glomerocryst core and rim distributions. Bin widths in distributions and kernel density estimates are fixed to propagated error through standards and analyses (~An_2).

broader distribution, and is offset slightly to the right.

The Phase 2 rhyolite has two distinct groupings of plagioclase, with two subpopulations in the lower An content group (Figure 9D). Excluding the high An plagioclase group in the Phase 2 rhyolite that are similar to plagioclase in the andesite, Welch's two-sample t-test shows that the two apparent subpopulations above and below An_{35} are indeed two separate populations (p~0.003, d.f.~10). The first subpopulation has anorthite contents ranging from An_{43-30} and FeO concentrations from 0.12-0.19 wt%. The second subpopulation of plagioclase in the Phase 2 rhyolite have slightly lower An contents but overlapping or higher FeO concentrations (An_{33-25}; FeO: 0.09-0.35 wt%, respectively). The crystals within this latter subpopulation are occasionally microphenocrysts but are more commonly cores to large concentrically zoned crystals (Figure 3F). Rim compositions of the concentrically zoned crystals overlap the first subpopulation. The other distinct type of plagioclase has high anorthite contents that overlap the andesite compositions. This group of plagioclase have similar FeO compositions to the andesite in the core (avg. 0.20 wt%) but rim FeO concentrations overlap the two low An plagioclase from the Phase 2 rhyolite (~0.14 wt%). PCA of plagioclase in the Phase 2 rhyolite show these systematic groupings as well and is given in the appendices.

Plagioclase from the Phase 1 rhyolite have An contents slightly higher than those observed in the Phase 2 rhyolite (An_{44-32}; avg. An_{39}) (Figure 9E). Most are non-zoned, although normal zoning is also found (Figure 3; Supplementary Table S3).

4.4.2 Orthopyroxene

There are two populations of orthopyroxene (opx) phenocrysts, P1 and P2, present in the andesite pumice (see section 4.1 for details). Data are presented in Table 4 and Supplementary Table S4. Both types of opx plot in the enstatite field (En_{65-49}). However, P1 opx are euhedral (P2 opx are subhedral) and have lower MgO, CaO, and Al_2O_3 concentrations than P2 opx (Figure 10). Orthopyroxene from glomerocrysts (G2 only) are also enstatite (Figure 3A). Some

Table 4: Representative pyroxene analyses

Rock Type	**Andesite**		**Andesite**	
Crystal	CH12020(2) Opx 1		CH12020(2) Opx 10	
Position	Core	Rim	Core	Rim
SiO_2	52.19	52.96	52.44	52.97
TiO_2	0.25	0.26	0.22	0.29
Al_2O_3*	1.23	1.14	1.25	1.39
FeO	23.57	24.26	21.76	21.31
MnO	0.46	0.52	0.47	0.42
MgO	19.87	20.16	21.66	21.67
CaO	1.30	1.19	1.27	1.31
NiO	-	0.07	-	0.04
Cr_2O_3	0.06	0.03	0.13	0.02
P_2O_5	0.00	-	-	-
Total	98.94	100.56	99.17	99.40
Mg #	0.60	0.60	0.64	0.60
En	0.58	0.58	0.62	0.58
Fs	39.33	39.82	35.59	39.03
Wo	2.73	2.45	2.61	2.62

Figure 10: Bivariate diagram of Al_2O_3 vs Mg# of orthopyroxene. P1 and P2 phenocrysts of opx have compositions that converge towards the glomerocryst compositions, which have approximately the mean Mg# of all grains, as indicated by the KDEs that have a Gaussian kernel at the margin of the plot. P1 phenocrysts have a steep decrease in Al with a decrease in Mg# and terminate at the inflection with the opx in glomerocrysts, where Al_2O_3 seems to no longer decrease at Mg# < 58.

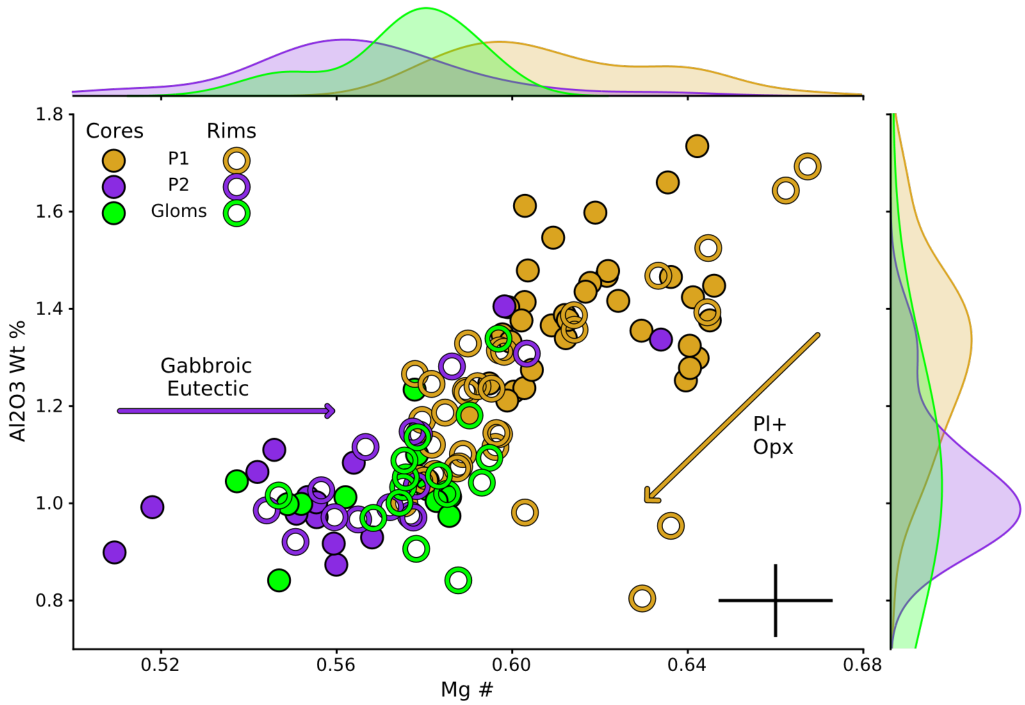

orthopyroxene from the glomerocrysts are compositionally similar to P2 phenocrysts. However, most G2 opx have distinctly higher Mg# with the same Al_2O_3 concentration of P1 phenocrysts and are thus intermediate between P1 and P2 phenocrysts. There are also orthopyroxene cores of high Al_2O_3 (~1.7-3 wt%), low CaO (0.7-1 wt%) with equivalent Mg# in glomerocrysts that are omitted in figure 10 for clarity but will be discussed below. A key observation is that P1 and P2 rims appear to converge on the intermediate compositions recorded in G2 opx glomerocrysts (Figure 10).

4.4.3 Oxides

Ilmenite and magnetite compositional data are presented in Table 5 and Supplementary Table S5. In the Caspana Phase 2 andesite, ilmenite is far more abundant than magnetite and occurs as both phenocrysts and microphenocrysts, whereas magnetite occurs strictly as microphenocrysts. There are no clear compositional distinctions between ilmenite phenocrysts and microphenocrysts. However, ilmenites define two compositionally distinct groups easily differentiated by FeO (reduced with the algorithm of Stormer (1983)), TiO_2, and V_2O_3 concentrations (Supplementary Figure S 1). The two groups have different TiO_2 and V_2O_3

Table 5: Representative oxide analyses

Rock Type	Andesite			Phase 2 Rhyolite			Phase 1 Plinian	
Crystal	007_ox6_cr1	0202_tp3_2	015_ox12_cr2	021plug5_tp5	021plug1_cr1	021plug3_rm2	009plug1_cr1	009plug2_rm2
Note	Low Ti	Glom	High Ti	Mt	Core	Rim	Core	Rim
SiO_2	0.03	0.01	0.01	0.09	0.01	0.02	0.04	0.02
TiO_2	48.57	50.62	50.87	16.66	49.18	48.34	5.34	4.38
Al_2O_3	0.14	0.19	0.21	1.97	0.09	0.08	3.10	2.04
FeO*	42.45	42.50	42.74	74.23	47.26	46.95	82.53	83.07
MnO	0.50	0.45	0.44	0.34	0.52	0.51	0.88	0.83
MgO	2.61	3.10	3.12	0.26	0.51	0.54	1.30	0.94
CaO	0.13	0.02	0.03	0.02	0.00	0.01	0.00	0.00
K_2O	0.03	0.02	0.00	0.01	0.01	0.02	0.01	0.02
Cr_2O_3	0.01	0.05	0.07	0.00	0.00	0.00	0.00	0.02
ZnO	0.03	0.08	0.00	0.22	0.00	0.03	0.24	0.31
V_2O_3	0.78	0.86	0.81	1.37	0.21	0.39	0.06	0.14
NiO	0.00	0.00	0.01	0.02	0.00	0.00	0.00	0.01
Total	95.26	97.89	98.20	95.16	97.76	96.88	93.46	91.78
Recalc Fe_2O_3	4.53	3.37	3.34	31.87	4.95	5.53	54.85	56.62
Recalc FeO	38.38	39.46	39.73	45.55	42.80	41.98	33.18	32.13
Total	95.74	98.23	98.63	98.39	98.29	97.44	99.00	97.45
% Usp	-	-	-	52.86	-	-	0.16	0.13
%Ilm	95.26	96.54	96.60	-	95.13	94.50	-	-

*Fe is reported as FeO. Recalcuations for Fe_2O_3, FeO, and mineral components are from the algorithm of Stormer (1983). Full dataset in Supplementary Table
S5

concentrations at a given FeO, defining two roughly linear arrays in FeO-TiO_2-space. Ilmenite inclusions found in the orthopyroxene belong to both the high and low Ti group.

Similar to the andesite, the Phase 2 rhyolite has far more ilmenite than magnetite. Compared to the andesite, these ilmenites are either slightly lower than or equivalent to the TiO_2 concentrations of the low Ti group in the andesite (TiO_2 48.3 – 49.7, Avg. 49.1 wt%) but have substantially more FeO (41.8-43.2, Avg. 42.7 wt%). Magnetite in the Phase 2 rhyolite are typically exsolved. The one un-exsolved magnetite found in Phase 2 has notably high Ti content of ~16-17% (Usp_{51}). This Ti-magnetite has the highest Ti composition of Ti-magnetite in rhyolite that we have found within the APVC, though we acknowledge that it is only a single grain. Phase 1 is different in that only magnetite was found and contains far less Ti content at Usp_{16}.

4.4.4 Fayalite

The Phase 2 rhyolite is an anomaly from the other lithologies in the Caspana ignimbrite because it contains fayalite (Figure 3H; Table 6 and Supplementary Table S6). Fayalite is * homogenous at ~Fa_{89}

Table 6: Representative fayalite analyses

Sample	**83070**	**83070**	**CH12021**	**CH12021**
Crystal	Fay_1_2	Fay_1_1	Fay_1_1	Fay_1_5
Position	Core	Rim	Core	Rim
SiO_2	30.10	29.89	30.14	30.83
TiO_2	n.d.	n.d.	n.d	n.d.
Al_2O_3	n.d.	n.d.	n.d.	0.13
FeO*	64.58	64.67	64.47	63.81
MnO	1.38	1.43	1.31	1.31
MgO	3.59	3.53	3.55	3.51
CaO	0.07	0.05	0.08	0.10
Cr_2O_3	-	0.01	-	-
P_2O_5	0.04	-	-	-
NiO	-	0.03	-	-
Total	99.75	99.58	99.56	99.70
Fo	0.09	0.09	0.09	0.09
Fa	0.89	0.89	0.89	0.89
Tp	0.02	0.02	0.02	0.02

($Fe_{90}Mg_8Mn_2Ca_{<<1}$) and we did not observe a textural or chemical relationship between fayalite and other phases in the unit (i.e., overgrowths of opx).

4.4.5 Biotite

Like fayalite, biotite can only be found in the Phase 2 pumice (Figure 3G). Biotite compositional data is presented in Table 7 and Supplementary Table S7. Data recalculations were done assuming 22 oxygens and are well into the annite - siderophyllite solid solution field based on the classification of Deer et al. (1992). Caspana biotites are homogenous with notably high Fe# (~77.5) and TiO_2 contents (5-6 wt%). The Fe concentrations are significant when compared to APVC ignimbrites and lavas (Supplementary Figure S2). The only unit in the APVC with comparable Fe# biotite is the poorly known 5.23 Ma Alota ignimbrite (Salisbury et al., 2011), which has comparable Fe indices (Figure 5). Biotite in the Phase 2 rhyolite has the highest Ti content of all biotite found in APVC ignimbrites (Supplementary Figure S2). As pointed out above, the Ti-magnetite in these pumices exhibits the same relationship.

Table 7: Representative biotite analysis

Sample	CH12021	CH12021	CH12021	CH12021	83070	83070
Crystal.Spot	1.2	1.4	2.3	2.4	1.2	1.3
SiO_2	33.43	33.80	33.44	33.60	33.53	33.78
TiO_2	5.29	5.26	5.28	5.35	5.32	5.26
Al_2O_3	14.21	14.42	14.24	14.24	14.25	14.30
FeO*	29.44	29.28	29.37	29.79	29.52	29.25
MnO	0.16	0.16	0.16	0.14	0.14	0.16
MgO	4.29	4.20	4.30	4.17	4.19	4.26
CaO	0.02	0.01	0.02	0.04	0.04	0.03
Na_2O	0.57	0.58	0.60	0.59	0.56	0.56
K_2O	9.07	9.15	8.96	8.92	8.89	9.07
Cl	0.27	0.26	0.26	0.26	0.25	0.25
Total	96.74	97.11	96.63	97.10	96.70	96.93
Al (apfu)	1.35	1.35	1.34	1.34	1.34	1.34
Fe/(Fe+Mg)	0.80	0.80	0.79	0.80	0.80	0.79

4.5 P-T-H_2O-fO_2 constraints

A variety of experimentally and theoretically calibrated phase equilibria models were used to constrain a suite of intensive parameters for the Caspana Ignimbrite magmas. These are summarized in Table 8.

4.5.1 Andesite

Storage pressures for the andesite were calculated using the rhyolite-MELTS based (rMELTS) plagioclase, pyroxene (+/- oxides) geobarometer (Harmon et al., 2018) under a range of water contents (4-10 wt%) and oxidation states (ΔFMQ – ΔFMQ -1) using rhyodacite matrix glass as input composition. There are two combinations of pressure, fO_2, and H_2O content that result in co-saturation of plagioclase and orthopyroxene with acceptably low residual temperatures (8°C; Table 8). The first is 400-450 MPa (Avg. 430 MPa), occurring at or close to water saturation (8-10 wt%) and at ΔFMQ – ΔFMQ -0.5. Under these conditions, the crystallization sequence is ilmenite -> magnetite -> plagioclase + orthopyroxene. The second is approximately normally distributed between 415-315 MPa (Avg. 366 Mpa) at undersaturated conditions (4-6 wt % H_2O) and at or below the FMQ buffer. The typical crystallization sequence is magnetite -> plagioclase + orthopyroxene -> ilmenite, but ilmenite occasionally joins magnetite before the equilibrium pair (Pl+Opx) depending on the glass composition that is used.

Equilibrium temperatures and water contents for the andesite were estimated using equations 24a and 25b of Putirka (2008). To assure plagioclase-liquid equilibrium,only $6_{-}^{.\&*.\#}$ values between 0.05-0.15for plagioclase rims and rhyodacite matrix glass were used for modeling purposes. Equilibrium temperature and water contents range from 915 – 956 °C (Avg. 933°C; 36°C Standard Error of the Estimate (SEE)) and 6.2 – 5.0 wt% H_2O (Avg. 5.5; 1.1 wt% SEE) when using an input pressure of 430 MPa. Changing the pressure to 350 MPa has a negligible effect on the output temperature and water contents (4°C and 0.01 wt%, respectively). To verify our results, we also estimated water contents using the plagioclase-liquid hygrometer of Waters and Lange (2015), which has been shown to be more accurate and have a smaller SEE (0.3 wt.%) than Putirka (2008). For model inputs, we assumed a pressure of 430 MPa, which is derived from r-MELTS barometry, and temperature from the Putirka (2008) plagioclaseliquid model. Although the Waters and Lange (2015) hygrometer is more accurate than the Putirka (2008) hygrometer and has a smaller SEE, we point out that it slightly underestimates water content compared to direct measurement (see Ulmer et al., 2018). Output water contents are 4.0 – 5.1 wt% H_2O (Avg. 4.3 wt%) and the estimated equilibrium anorthite composition (~An_{83}) agrees with observed compositions (Figure 9B, C, D). This equilibrium plagioclase composition is also predicted by r-MELTS models (An_{81}; see below). Interestingly, the water contents for the andesite agree with inferences for water content in mafic arc magmas globally (Kelley and Cottrell 2009; Plank et al. 2013).

The viability of the plagioclase-liquid temperature estimates was tested using the orthopyroxene-liquid thermobarometer of Putirka (2008; eqn. 28a/eqn. 29b). Temperatures were modeled assuming a pressure of 430 MPa (see r-MELTS outputs above) and water contents ranging from 3.5 – 6.5 wt%. Input compositions included rhyodacite matrix glass for the liquid component and orthopyroxene rims. Temperatures were calculated using equation 28a, as it yields the highest R^2 and lowest SEE when modeling hydrous and lower T systems (i.e., < ~1100 °C). Equation 29b was used for independently calculating equilibrium pressures because it relies on the enstatite-ferrosilite ($(Fe,Mg)_2Si_2O_6$) component rather than the jadeite ($NaAlSi_2O_6$) component. This is selected, because in the Caspana system the Na concentrations in the orthopyroxene approach the analytical detection limits resulting in unacceptably high uncertainties and glass may be altered. Orthopyroxene-glass equilibrium was

Table 8: Thermodynamic (PTX) estimates for Caspana magmas

	P (MPa)	T (°C) Est.	T (°C) Sat. / *a*Ti	ȟ	H_2O (wt%)	Method	Reference
Andesite	100-500	-	-	ˈFMQ	2 - 5	*Phase equilibria	Blatter & Carmichael (2001) Eggler (1979)
	390 Â 490	910 - 941	940	-	-	Opx - Liq	Putirka (2008)
	-	-	-	-	4 - 5.1	Plag - Liq	Water & Lange (2015)
	-	915 - 956	-	-	5.62	Plag Â Liq	Putirka (2008)
	415 - 315	-	-	FMQ	4 - 6	Thermodynamics	Harmon et al. (2018)
Phase 2 Rhyolite	200 Â 275 320-330^	-	-	-	-	Thermodynamics	Gualda & Ghiorso (2014, 2015)
	-	747	-	-1.5	-	Two Oxide	Lepage (2003); and references therein
	-	744 - 806	0.43	-1	-	Two Oxide	Ghiorso & Evans (2008)
	-	-	-	-	4.9 Â 5.7	Plag - Liq	Water & Lange (2015)
	-	787 - 805	-	-	-	Ol - Liq	Putirka (2008)
	-	-	780-804	-	-	Zr. Sat. Temp	Boehnke et al. (2013)
Phase 1 Rhyolite	210	834 - 850	865	-	4.8 Â 4.9	Plag - Liq	Putirka (2008)
	-	-	-	-	4.4 Â 5.1	Plag - Liq	Water & Lange (2015)
	-	-	834 - 850	-	-	Zr. Sat. Temp	Boehnke et al. (2013)

Representative PTX conditions calculated from models referenced here. *a*Ti and T(*sat*) expressed in same column where appropriate. *Phase stability is based on experimental evidence for petrologic conditions that promote crystallization of plagioclase+orthopyroxene+oxides >> amphibole + clinopyroxene.

^The ranges of 200-275 and 320-330 are the storage and extraction pressures, respectively (Gualda et al., 2019)

verified assuming a K_D(Fe-Mg) of 0.27 ± 0.3 (Roder and Emslie, 1970) and are displayed graphically following the methods of Rhodes et al. (1979; Supplementary Figure S3). The orthopyroxene-melt thermobarometer yields average temperatures of 910-941°C (range of 888950 °C; SEE: 39°C) and vary accordingly with the input water contents of 6.5 – 3.5 wt% H_2O. This range of water contents causes temperature to change less than the SEE of the model and are within error of the Putirka (2008) plagioclase-liquid model. The corresponding equilibrium pressure that is output from the Opx-liquid model agrees with the r-MELTS geobarometer with averages of 390 – 490 MPa (range of 350 – 550 MPa; SEE: 260MPa), which vary with the input water contents above. Changing the input pressure to 350 MPa causes the pressure and temperature outputs to change by < 0.01 MPa and 5°C. While these pressure ranges are far outside of acceptable constraints, it is important to note that the averages are in agreement with the (arguably) more accurate r-MELTS geobarometer.

4.5.2 Phase 2 Rhyolite

Matrix glass and bulk rock compositions from Phase 2 pumice were input into the rMELTS geobarometer (Gualda and Ghiorso, 2014, 2015) to estimate storage and extraction depth, respectively (Gualda et al., 2019). We exercise caution in presenting these results due to the potential for glass alteration affecting the pressure estimation (section 3.1; Pamukcu et al., 2015). Extraction pressures calculated using bulk rock compositions are ~330 MPa using 4 wt% H_2O and an oxidation state of ΔFMQ as input, which is just shy of the andesite storage pressure under the same petrologic conditions (~360 MPa). When using matrix glass as input in order to estimate storage pressure of the Phase 2 rhyolite, r-MELTS predicts the observed assemblage at slightly lower pressure (275-222 MPa; Avg. 235 MPa) using the same input water contents and at ΔFMQ – ΔFMQ-1. Only one glass composition predicts the equilibrium assemblage under fluid saturated conditions; the output pressure from the model is 200 MPa. Otherwise, increasing the water content puts sanidine on the liquidus for both matrix glass and bulk rock compositions, which is not observed in the Phase 2 rhyolite.

Equilibrium temperatures for the Phase 2 rhyolite were calculate using the olivine-liquid model of Putirka (2008). Equilibrium between olivine rims and matrix glasses were verified visually using the method of Rhodes et al (1979) Using an input pressure of 250 MPa (see previous paragraph for details) and water contents between 4 and 6 wt.% H_2O, calculated temperatures range from 787 – 805°C (Avg. 796°C; SEE 29°C). Changing the input pressure has a negligible effect on output temperature.

Equilibrium temperatures for the Phase 2 rhyolite were also estimated using compositions of coexisting magnetite-ilmenite pairs. As stated above, we were only able to find a single magnetite grain that was not exsolved. Additionally, we acknowledge that the magnetite ilmenite 'pairs' are not touching but simply coexisting and thus may not be in equilibrium. However, we attempted to verify this in-so-much as possible by using the equilibrium test of Bacon and Hirschmann (1988) for all possible pairs. We therefore view the temperature and oxidation state calculated by two-oxide equilibria with great speculation, but when integrated with the petrology of the Phase 2 rhyolite (ferrous-rich assemblage) and independent temperature estimates below, we also believe the results of oxythermometry presented here are informative. Temperatures calculated using the method of Ghiorso and Evans (2008) yields average temperatures of 774ºC (range of 744 - 806ºC) and aTi = 0.43. Using the recalculations of Stormer (1983) and Andersen and Lindsley (1985) gives slightly lower average T (747ºC). This latter method does not coincide well with other estimates and it is derived from a model that is calibrated on experiments that were conducted at irrelevant T-fO_2 conditions and is therefore not considered further. Zr saturation temperatures (Boehnke et al., 2013) of the Phase 2 glass lie within the temperatures estimated by the above methodology (780ºC).

These temperature estimates for the Phase 2 rhyolite are consistent with other fayalitebearing rhyolites and other high-silica rhyolites with anomalously high temperatures (Warshaw and Smith, 1988; Deering et al., 2010; Ghiorso and Gualda, 2013; Wolff et al., 2015).

Also significant is the low aTi, which is consistent with particularly high temperature felsic melts crystallizing ilmenite as the dominant oxide (Ghiorso and Gualda, 2013; Schiller and Finger, 2019). Importantly, the fayalite rhyolites studied throughout the literature lie on or below the FMQ buffer with moderate to high-water content at fluid saturated conditions (Mahood, 1981; Novak and Mahood, 1986; Macdonald et al., 1987; Warshaw and Smith, 1988; Chesner, 1998; Portnyagin et al., 2012). For this purpose, water contents were estimated using a plagioclaseglass hygrometer (Waters and Lange, 2015). This allows us to assess the potential dependence of a generally ferrous iron assemblage on water content and the inherent implications for explosive rhyolite volcanism. Using input temperature of 800 – 770 °C (above) as input to the Waters & Lange (2015) plagioclase-liquid hygrometer returns average water contents ranging from 4.9 – 5.7 wt% (Avg. 5.29 wt %; Table 8).

4.5.3 Phase 1 Rhyolite

Temperature, pressure, and water contents of the Phase 1 rhyolite were estimated using the plagioclase-liquid method of Putirka (2008) using matrix glass and plagioclase rims. All rims and liquid combinations are within the equilibrium exchange window of $6_{-}^{.\&*.\#}$ (0.05-0.15). The temperature and water contents are constrained between 834-850°C (Avg. 845°C; SEE: 36°C) and 4.8-4.9 wt% H_2O (Avg. 4.9 wt%; SEE: 1.1 wt%). The output pressure is always 210 MPa but the SEE (247 MPa) could put the magma on the surface or in the midcrust and is thus presented here with caution. The Waters and Lange (2015) hygrometer returns water contents of 4.4-5.1 wt% H_2O (Avg. 4.7 wt %; SEE: 0.3 wt%) using the range of temperatures output from the Putirka (2008) model. Varying the pressure input by 200 MPa results in a mere difference of ~0.1 wt%.

Zr saturation temperatures (Boehnke et al., 2013) of the glass are lower than temperatures estimated from plagioclase (808-829°C; Table 8), implying the magma should not be crystallizing abundant zircon.

4.5.4 Oxygen Fugacity

As the phase assemblages preserved in eruptive units at Caspana imply multiple oxidation environments (Table 2; Figure 3I; above). Therefore, understanding how oxidation changes throughout the eruption of the Caspana ignimbrite is paramount to understanding the physical and compositional evolution of the magmatic system.

Although there are no readily accessible mineral-mineral or mineral-melt systems in the Caspana andesite that allow for fO_2 to be estimated directly, the phase assemblage preserved in the andesite (plagioclase + orthopyroxene + FeTi oxide dominated) are consistent with experiments conducted on undersaturated andesites with moderate to high H_2O (2-5wt%) and fugacity at ~ΔFMQ (i.e., this assemblage will only crystallize at or below fO_2 ≤FMQ; Eggler, 1972; Blatter and Carmichael, 2001). This assemblage is also predicted by r-MELTS (above; below). Importantly, these oxygen fugacities are lower than those estimated for most of the other systems in the APVC (Lindsay et al., 2001a; Schmitt et al., 2001; Folkes et al., 2011; Grocke et al., 2017b).

Oxygen fugacities for the Phase 2 rhyolite were calculated on coexisting magnetiteilmenite pairs using the two-oxide method described above. The algorithm of Ghiorso and Evans (2008) yields an fO_2 for the Phase 2 rhyolite of approximately one log unit beneath the ΔFMQ buffer (-1.03).

We cannot place direct constraints on the oxygen fugacity of Phase 1 in order to identify if this part of the system shared the same fO_2 environment as Phase 2. However, the plagioclase in the Phase 1 rhyolite have Fe/Al ratios (Fe^{3+} substitutes for Al) that are notably higher compared to the Phase 2 rhyolite even though the FeO^{Tot} content is comparable between the two rhyolites (Figure 5). This is an agreement that the Fe content of plagioclase is potentially controlled by the oxygen fugacity of the system and not strictly on the melt composition (Tepley et al., 2013). In fact, Phase 1 plagioclase have Fe/Al equivalent to those in the andesite and other silicic magmas that have erupted in the APVC (Watts et al., 1999; Schmitt et al., 2001; Folkes et al., 2011; Grocke et al., 2017a, 2017b). Invoking this and the inferred phase equilibria (discussed below) leads us to believe that Phase 1 likely had an oxidation state at least a log unit higher than ΔFMQ; typical of APVC magmas with comparable Fe indices (Figure 5).

Given these constraints, it should be noted that the presence of ilmenite > magnetite and orthopyroxene >> clinopyroxene is the opposite of what is generally found in APVC intermediate magmas (Table 2; Burns et al., 2015; de Silva and Francis, 1989; Folkes et al., 2011; Grocke et al., 2017; Kaiser et al., 2017; Lindsay et al., 2001a), as is the presence of fayalite in rhyolite (Figure 3H). This implies significantly different petrologic conditions for the Caspana system, namely fO_2 and H_2O (Burns et al., 2020; Grocke et al., 2016; Kelley and Cottrell, 2009).

5. Discussion

Stratigraphic changes combined with bulk rock and mineral chemistry reveal that the Caspana ignimbrite eruption evacuated the most heterogeneous collection of magmas in any single known eruption from the APVC. This integrated dataset suggests that heterogenous magmatic systems can develop in proximity to a larger regional system under flare-up conditions that tend to promote homogeneity (e.g., de Silva et al., 2006). Below, the relationship between the Phase 1 and Phase 2 magmas and the large compositional gaps are examined with special interest paid to the only known occurrence of fayalite in the APVC. Based on this examination, we then draw comparative relationships between Caspana reservoir and its resident magmas with the rest of the APVC.

5.1 Production of the Phase 2 Rhyolite by Closed System Crystallization of Andesite

It is clear in the isotopic ratios that Caspana andesite and Phase 2 rhyolite are related by nearly closed system fractionation (Figure 8, Supplementary Figure S4). This is supported by high Fe indices in the Phase 2 rhyolite resulting from the fractionation of high An plagioclase and enstatite from the andesite (Figure 5). The elevated HREE in the Phase 2 rhyolite (Figure 6) also reflect an assemblage that is absent of clinopyroxene and/or abundant amphibole due to the low $6_{-3455/7455}$ of these minerals.

To model the relationship between the andesite and Phase 2 rhyolite, the Excel®-based software Magma Chamber Simulator (MCS; Bohrson et al., 2014, 2020) along with its rhyoliteMELTS major and trace element engines (Ghiorso and Sack, 1995; Spera et al., 2007; Gualda and Ghiorso, 2015) were used with relevant partition coefficients from the literature (Supplementary Table S9). For the purposes of modelling, wall rock assimilation is not considered because of the isotopic concordance of Phase 2. Based on the extraction and storage pressures estimated for the andesite and rhyolite, the isobaric MCS was run from 400200MPa using a 100MPa step in order to deal with the vertically extensive reservoir that is suggested by the phase equilibria. The chemical evolution at the deepest pressure (~400 MPa; section 4.6.1) uses the composition of andesite pumice. The input composition at the rhyolite extraction pressure (~300 MPa; section 4.6.2) is the liquid composition at 920°C, which is the equilibrium temperature of the G2 glomerocrysts and plagioclase (Table 8). While the error on the orthopyroxene-liquid temperature estimate is obviously large, the choice is supported by the fact that the composition turned out to coincide with the composition of rhyodacite glass when analyzing observed vs. modelled values (see below). The composition for the final step is chosen such that the composition is appropriate for modelling the final stages of liquid evolution with r-MELTS (i.e., version 1.1 instead of 1.2) and at the max temperature of the olivine-liquid thermometer (800°C + 29°C SEE). The composition at this temperature is rhyolite.

The best fit MCS models show that the major and trace element trends between the andesite and Phase 2 rhyolite can be produced via crystal fractionation (Figure 11 and Supplementary Figure S5) with initial water contents of 3-4 wt% H_2O and ΔFMQ-1 (Table 8) in the andesite. Higher and lower input water contents create a poor fit for the trend defined by pumice and glass at the estimated temperatures (Figure 12), as does higher fO_2. Significantly, rhyolite-MELTS predicts the crystallization sequence plagioclase +/- magnetite -> plagioclase + magnetite + ilmenite + orthopyroxene -> plagioclase + orthopyroxene + ilmenite (Table 9) in modal proportions that matched the observed G1 and G2 glomerocrysts. Interpreting the glomerocrysts as disaggregated remnants of cumulates (de Silva, 1989c; Ellis et al., 2014) leads to the apparent, near perfect closed-system fractionation between the Phase 2 lithologies

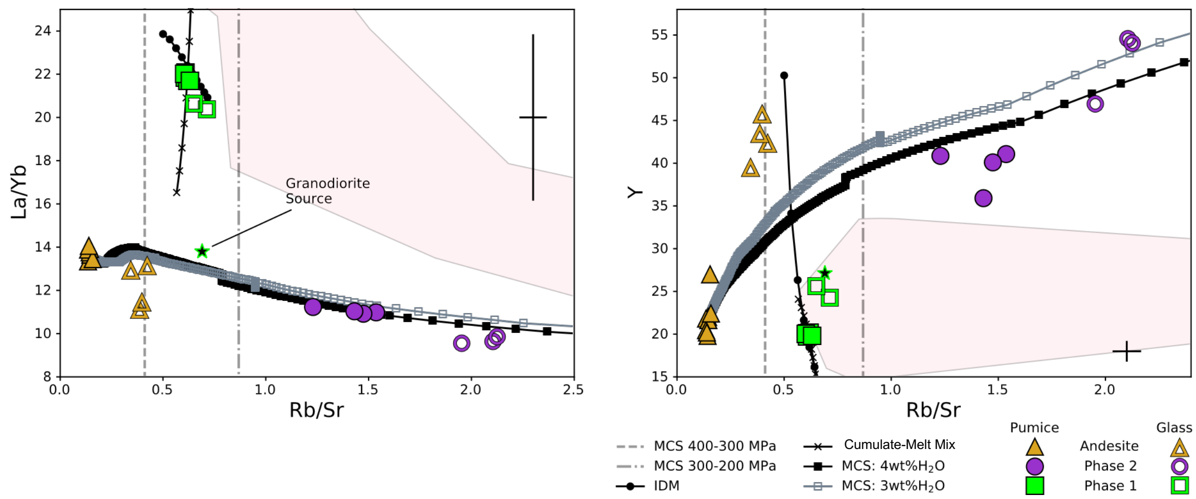

Figure 11: Graphs showing Magma Chamber Simulator and incongruent dynamic melting (IDM) models. A) La/Yb vs Rb/Sr; B) Y vs Rb/Sr. The observed assemblage of plagioclase + orthopyroxene + oxides are by far the dominant phases predicted by R-MELTS (Table 9). These models show that this assemblage can clearly create the Phase 2 rhyolite from the andesite by near closed system crystallization under initially H_2O undersaturated and 'low' fugacity conditions. The composition of the Phase 1 Rhyolite (Section 5.4) can be explained by recycling granodioritic material that has a composition similar to the rhyodacites and low silica rhyolites on the APVC. This is modelled as partial melting of an igneous protolith (IDM) or as a mix between a melted cumulate and resident melt (Cumulate-Melt mix). Gray vertical lines show where the MCS models were restarted at a new pressure. Additional figures are shown in Supplementary Figure S5 and modelling details are given in the text, Supplementary File S6, and Supplementary Table S10/11. Modal proportions of crystallized minerals from these models are shown in Table 9. Fields as in Figure 4. Alota-Juvina is more evolved than Phase 2 in Rb-Sr space and is not shown for clarity (c.f., Figure 5, 6).

that is readily reproduced with the simple lever principle in major element space (Figure 4, 5). While this is not a scientific breakthrough in any regard, observing it in the natural world should invoke some degree of bewilderment.

The thermodynamics (Table 8), phase chemistry, and cumulus textures (Figure 3) record the progressive cooling in the more mafic part of the system. At the highest pressures, plagioclase is predicted to be first on the liquidus at ~1050 – 1100°C, followed by orthopyroxene and magnetite saturation at ~1000°C (Figure 13). These orthopyroxenes have high-Al due to high pressure and are thus represented by the P1 phenocrysts that are were co-crystallizing with plagioclase (Figure 10). This co-crystallizing assemblage remained saturated all the way through the crystallization sequence in this hydrous, low fO_2 environment, driving up the

Feindices that lead to fayalite stability (Figure 5, 10; see below). Ilmenite then saturates at the same temperature estimated by equilibrium temperature of orthopyroxene (~930°C).

In the second, lower pressure step of the thermodynamic models, the crystallization sequence is similar except that magnetite is first on the liquidus (Figure 12) and the various phases saturate at temperatures within error of what is estimated by phase equilibria (Figure 12; Table 8). The stability of this assemblage through the crystallization sequence allowed the large glomerocrysts (Figure 3A) to grow in the upper reaches of the reservoir as cooling progressed. The low Al and En contents of orthopyroxene in G2 glomerocrysts and P2 phenocrysts (Figure 10) that record lower temperature and pressure than the P1 phenocrysts (Martel et al. 1999) provide further support for this interpretation of the glomerocrysts. The dominant equilibrium state during liquid evolution and formation of the noritic cumulate is clearly recorded by the convergence of P1 and P2 phenocryst rims towards the glomerocryst compositions (Figure 10). Plagioclase in the G2 glomerocrysts provide further support that the glomerocrysts were critical in the final stages of liquid evolution (Figure 9B). These plagioclase have rim An contents that are offset to low An values, as do reversely zoned phenocrysts cores and the subset of normally zoned phenocrysts (Figure 9B,C). The more lath-like texture of G2 plagioclase than their counterparts (Figure 3A,B,E) also suggests that they were the plagioclase growing where thermal gradients were highest (e.g., de Silva, 1989c) and when orthopyroxene was already saturated in the advanced stages of crystallization (Figure 11, 12).

The switch from magnetite to ilmenite as the dominant oxide is recorded in the FeO content in the rims of the G2 glomerocrysts and reversely zoned phenocrysts (Figure 3I; 9 B,C). As these plagioclase grew, Fe^{3+} became progressively more available and oxidation state increased with changing pressure. That is, Fe^{3+}/Fe^{tot} was probably controlled by a decrease in pressure (Kress and Carmichael, 1991) and the crystallizing assemblage (Cottrell and Kelley, 2011; and references therein) though it was probably only a local process given that the andesite and the Phase 2 rhyolite share a low oxidation state.

The dominance of ilmenite during advanced stages of crystallization is also reflected in the ilmenite chemistry (Supplementary Figure 1). Ilmenite become progressively more enriched in TiO2 and V2O3 as the glomerocrysts continued to grow. Following Buddington and Lindsley (1964) and Ghiorso and Evans (2008) we interpret the low TiO_2 and V_2O_3 ilmenite to be the result of crystallization in the presence of Ti-magnetite (now exsolved), which is predicted by rMELTS to be first on the liquidus (Table 9). Transition from magnetite to ilmenite dominance also agrees with the high aTi recorded in the mineral chemistry of the residual, Phase 2 rhyolite (i.e., biotite and Ti-magnetite). We propose this to be a more consistent interpretation than an alternative where ilmenite is introduced by recharging magma.

It is clear that in the Caspana system the liquid line of descent (LLD) associated with fractionation of rhyolite was controlled by crystallization

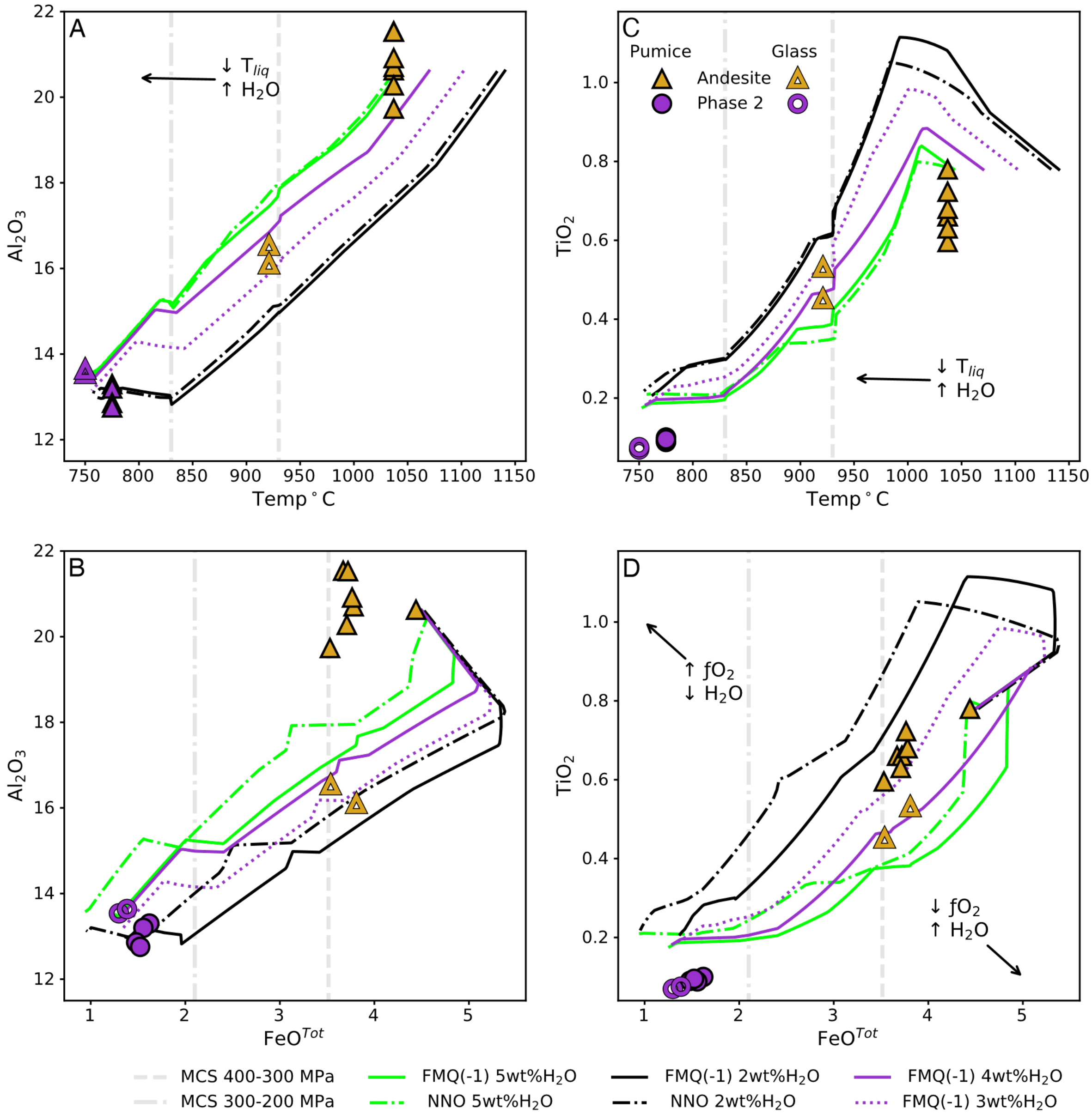

Figure 12: R-MELTS/MCS modelled LLDs using the same pumice sample (CH19C007) with variable inputs of H_2O concentration and different $ƒO_2$ buffers plotted with glass and pumice in major element space. Percentages refer to initial H_2O input in the andesite starting composition. Increasing amounts of H_2O causes the crystallization interval to happen over a shorter temperature range, indicating that water has the dominant control on the LLD. Lowering the $ƒO_2$ at equivalent water concentrations creates a residual liquid that fractionates to lower values of TiO_2 due to increasing amounts of ilmenite. No trend with 'low' water content (~2% input) creates a residual liquid in agreement with pumice samples or matrix glass of the andesite and Phase 2 rhyolite. The best fit models are found within 3 to 4% H_2O input. Grey dashed vertical lines as in Figure 11 - see Table 9, Supplementary File S7 and Table S9 and S10 for further details.

of FeTi oxides (e.g., Toplis and Carroll, 1996; Morse, 2011). This dataset, however, does not

Table 9: MCS/r-MELTS input compositions and model output assemblages.
Table shows representative input compositions and intensive parameters (PT-H_2O) of MCS models. Modal percentages are the outputs from the model based on the r-MELTS algorithm. Each column shows the input composition for the respective pressure 'step'. R-MELTS was set to version 1.2 for modelling mafic-intermediate compositions and version 1.1 for modeling eutectoid (Qtz + Feldspar) compositions, as kindly directed by Dr. Ghiorso on the r-MELTS website and outlined in Gualda et al (2012) and Ghiorso and Gualda (2015). Full table of all model inputs, outputs and explanation are given in text and Supplementary File 1, Figures 12 and 13.

H_2O	**3 wt%**			**4 wt%**		
r-MELTS version	1.2	1.2	1.1	1.2	1.2	1.1
P (MPa)	400	300	200	400	300	200
T start	1100	950	856	1100	980	846
T End	760	750	740	760	748	740
T increment	2	2	2	2	2	2
T stop*	930.15	830.22	-	929.92	830.92	-
SiO_2	57.31	64.09	68.02	56.76	62.13	66.51
TiO_2	0.76	0.56	0.25	0.75	0.50	0.20
Al_2O_3	20.02	15.38	13.28	19.82	16.27	13.86
Fe_2O_3	0.56	0.47	0.33	0.56	0.49	0.34
Cr_2O_3	0.00	0.00	0.00	0.00	0.00	0.00
FeO	3.81	3.11	1.90	3.77	3.28	1.92
MnO	0.07	0.12	0.14	0.07	0.10	0.13
MgO	2.15	0.87	0.37	2.13	1.13	0.44
NiO	0.00	0.00	0.00	0.00	0.00	0.00
CoO	0.00	0.00	0.00	0.00	0.00	0.00
CaO	7.73	4.25	3.00	7.65	4.51	2.89
Na_2O	2.49	2.63	2.32	2.47	2.77	2.58
K_2O	1.96	3.33	4.17	1.94	2.93	3.86
P_2O5	0.23	0.40	0.51	0.23	0.35	0.47
H_2O	2.91	4.78	5.70	3.85	5.53	6.81
	Modal Percentages from r-MELTS outputs					
Plag	78	78	35	75	77	43
Mag	2	3	1	2	3	1
Opx	17	16	3	16	18	6
Cpx	2	-	1	7	-	-
Ilm	1	3	1	-	2	-
Fay	-	-	1	-	-	1
Qtz	-	-	32	-	-	28
San	-	-	26	-	-	21

explain the lack of a compositional continuum in either bulk rock (Figure 4, 5, 6, 11) or mineral chemistry (Figure 9, 10) that would be inevitable during the physical process that would accompany fractional crystallization sensu stricto. In fact, it requires some other physical mechanism to explain the apparent shallow liquidus in Phase 2 (de Silva, 1991; and references therein). It is worthwhile to point out that when orthopyroxene and ilmenite saturate at 300MPa, the liquid composition is rhyodacite to rhyolite with the initial input water contents of 3-4 wt%.

5.2 In-situ Crystallization in Gabbronoritic Mush Controls Caspana's Shallow Liquidus

Compositional gaps have been identified in volcanic systems in virtually every tectonic environment with fractionation proposed as a dominant mechanism for their presence (Daly, 1925; Brophy, 1991; Dufek and Bachmann, 2010). The compositional gap of ~16% SiO_2 between the andesite and Phase 2 rhyolite bulk compositions is one of the more extreme within global compilations by Brophy (1991) and Dufek and Bachmann (2010) and warrants consideration. A comparison of the modelled LLDs above naturally show that the liquidus temperatures are negatively correlated with initial water content (Figure 12). The result of this is a decrease in the temperature interval required for crystallization from andesite to rhyolite (Figure 12 and Supplementary File 7). The low fO_2 of this system specifically would increase plagioclase stability as opposed to amphibole at liquidus temperatures (Martel et al., 1999), validating the comparisons of r-MELTS models in the absence of amphibole with high water content in the melt. Overall then, it seems then that high water content will serve to lower the liquidus temperature while also decreasing the temperature interval required for fractionation in both low (here) and high (Grove and Donnelly-Nolan, 1986; Brophy et al., 2011) fO_2 systems. de Silva (1991) suggested that a shallow liquidus between andesite and rhyolite was responsible for the compositional gap present in the Caspana system. Similar conclusions have been made for the well-established gap at the Medicine Lake system where rhyolite is directly related to its gabbroic cumulate (Brophy et al., 2011; Grove and Donnelly-Nolan, 1986). The lack of a compositional continuum is, however, difficult to reconcile by classic models such as purely convection and growth of a solidification front (Bachmann and Bergantz, 2004; and references therein), especially when considering the locked rheological state of the crystal mush represented by the G2 glomerocrysts. Instead, compositional gaps have been hypothesized to develop by interstitial melt extraction due to settling and compaction at crystallinities that are approaching (or at) rheological lock up (~40-70%; Dufek and Bachmann, 2010; Bachman and Bergantz, 2004). An eruptible volume of evolved interstitial melt can be released from these porous media by compaction and settling so long as the latent heat of crystallization can dominate the heat budget and make crystallization temporarily unfavorable (i.e., latent:sensible heat >1; Dufek and Bachman, 2010). Indeed, textural observations suggest that significant crystallization events, particularly from FeTi oxides, can temporarily halt textural maturity in Pl+Pyx dominated mushes and allow for efficient, rapid melt extraction of evolved interstitial melt (Holness et al., 2007, 2011). The effect of latent heat buffering in the Caspana system is tested with r-MELTS using the same inputs as the MCS models described in section 5.1 and utilizing the method described in detail by Sliwinski et al. (2015).

In the 400 MPa step, a latent heat spike is brought on by orthopyroxene saturation but the latent/sensible heat is <1 and thus below the threshold where crystallization is no longer favored and in-situ melt would be released (e.g., Morse, 2011) (Figure 13). The crystallinity is also not above the threshold where the probability of melt extraction by channelization and compaction is non-negligible (40%) (Dufek and Bachmann, 2010; Bachmann and Bergantz, 2004). At 300 MPa the latent heat spike is brought on by orthopyroxene and, even though minor, ilmenite contributes some buffering during the fractional latent heat dissipation of orthopyroxene. The temperatures at which ilmenite and orthopyroxene saturation occur at 300

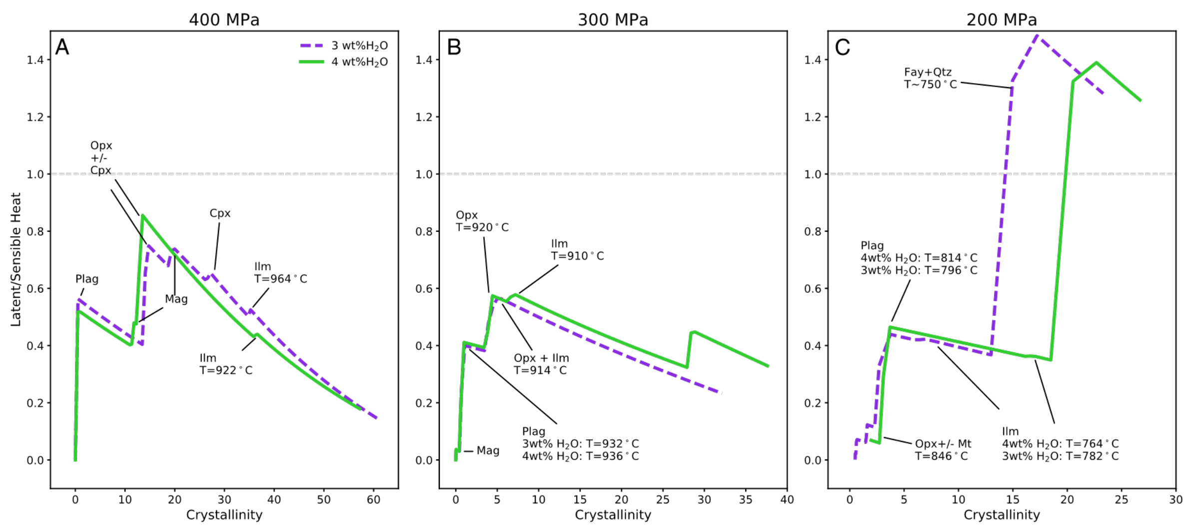

Figure 13: Latent/Sensible Heat vs Crystallinity plots from r-MELTS model results to test if and where extraction from proposed 'mush' material may occur. Two separate trends represent the same input water contents in Figure 11 (3 and 4 wt%). These models use the same inputs as the MCS models shown in Figures 11 and 12. Extraction of the interstitial liquid is favored when the Latent/Sensible Heat is >1 (e.g. Morse, 2011). See Table 9 and Supplementary Table S9 for supporting details.

MPa are within a few degrees of ilmenite saturation at 400 MPa, collectively pushing the latent:sensible heat >1 and putting the crystallinity within range of probable melt extraction from a ‘mushy’ system with local channel development (e.g. Dufek and Bachmann, 2010).

The liquid composition at the crystallinity where latent heat released by crystallization favors melt extraction is rhyodacitic to rhyolitic and quickly evolves to the Phase 2 rhyolite composition (Figure 11). The paucity of continuous mineral and bulk rock compositions in the

Caspana system is well-explained by in-situ crystallization that is temporarily suspended by latent heat buffering and subsequent interstitial melt extraction. Importantly, the control that FeTi oxides exert on the system is significant for both the LLD and the heat budget (Figure 12, 13), which is consistent with observed plutonic equivalents of the gabbronoritic glomerocrysts (Holness et al., 2007, 2011). With respect to the expansive APVC and its many ignimbrites, this mechanism has obvious implications for efficient, rapid rhyolite production from either small volume, short-lived systems (e.g., Schmitt et al., 2011) or large volume, long-lived systems that are subjected to recharge (Lindsay et al., 2001a; Folkes et al., 2013; Grocke et al., 2017b).

5.3 Petrologic Conditions Explain Fayalite Rhyolite in the APVC

The occurrence of fayalite in rhyolitic magmas has been documented for well over a century (Iddings, 1885), however the conditions that lead to its saturation and the cocrystallizing mineral assemblages appear to be quite varied (Bacon et al., 1981; Mahood, 1981; Novak and Mahood, 1986; Macdonald et al., 1987; Warshaw and Smith, 1988; Jónasson, 1994; Lowenstern et al., 1997; Chesner, 1998; Portnyagin et al., 2012; Holness et al., 2019; Rooyakkers et al., 2021). Warshaw and Smith (1988) originally proposed that fayalite is stable due to cations influencing the oxidation state of the melt. Specifically, FeO/CaO correlates negatively with Fe^{3+}/Fe^{2+} due to increased amounts of alkaline Earth metals disrupting the melt structure and oxidizing multivalent ions. Fe^{2+}/Mg must also be high, as the Mg component of the melt must be sufficiently low to allow an Fe^{2+} enriched mineral (fayalite) to be stable instead of an Mg rich mineral (orthopyroxene). This latter inference is supported by textural evidence that shows fayalite develops orthopyroxene overgrowths during pronounced perturbations (i.e., recharge) to a volcanic system (Portnyagin et al., 2012; Troch et al., 2017; Chiaro, 2019). Both of these cation ratios are proxied by the Fe-indices in Figure 5. As far as we know, none of the other known ignimbrites containing high silica rhyolites in the APVC (Toconao, Alota-Juvina, Talabre; Carcoté; Lindsay et al., 2001a; Salisbury et al., 2011) are known to have fayalite in them except for the Caspana Phase 2 rhyolite. The Phase 2 rhyolite also has the highest Feindices that we know of in the APVC (Figure 5) and relatively flat REE patterns at high overall concentrations (Figure 6). This provides us with an opportunity to investigate the petrology of the Caspana andesite and Phase 2 rhyolite with respect to the plethora of well-studied APVC ignimbrites that are derived from the APMB.

Rhyolite-MELTS modelling supports the crystallization of high An plagioclase and enstatite in the 'low' oxidation state ($fO_2 \leq \Delta$FMQ) from a parental andesite (Eggler, 1972; Blatter and Carmichael, 2001) as the cause of the high Fe-indices in the Phase 2 rhyolite

(Figure 5). Additionally, we have shown that the relative amounts of magnetite and ilmenite in the MCS runs are controlled by low $ƒO_2$ with little correlation of H_2O (Figure 12; Supplementary File S7), and the pressures and water contents of the Phase 2 rhyolite (Table 8) indicate that it was saturated (Newman and Lowenstern, 2002; their Fig. 2). These constraints demonstrate that the reduced mineral assemblage of the Caspana system (Table 2) and the appearance of fayalite in high-Si rhyolite (Figure 3H) is apparently not controlled by H_2O, but solely low $ƒO_2$. In fact, increasing the water content would only serve to increase the olivine stability field and promote fayalite stability (Portnyagin et al., 2012; and references therein).

The presence of hydrous, ferrous rich phases (annite, allanite) provides further evidence for a high water, low $ƒO_2$ environment (Table 2, 8; Figure 3G; Supplementary Figure S2). The nearly linear REE trends defined by the andesite pumice, rhyodacite glass, and Phase 2 pumice are consistent with fractionation of Pl+Opx+Ilm, with the exception of La and Ce (Figure 13), which can likely be attributed to crystallization of hydrous allanite. Indeed, the abnormally large size of allanite (for APVC ignimbrites) is likely the result of early saturation brought on by the low $ƒO_2$ (Table 2, Figure 3; Vlach and Gualda, 2007). Given that the phase has no correlation with REE concentration of host rocks (Vlach and Gualda, 2007), it may be that the low oxidation state promoted allanite stability due to a high Ce^{3+}/Ce^{4+}. The positive or flat Eu anomaly in the andesite pumice samples (Figure 6) also imply a residual liquid with a rather steep negative Eu anomaly, as observed in the Phase 2 rhyolite. These characteristics are rare or unobserved in APVC magmas, adding more support to the interpretation that the oxidation state at least partially controlled REE partitioning while plagioclase was on the liquidus (i.e., high Eu^{2+}/Eu^{tot}).

While providing decent first order assessments of the system, the parental assemblage in the andesite and melt structure still does not explain why the Phase 2 rhyolite and andesite are carrying reduced assemblages in an arc setting where magmas should be oxidized by either mantle source properties (Kelley and Cottrell, 2009) or crystallization during stalling in the lower crust (Ulmer et al., 2018). This leaves 3 possibilities for the reduced state of the magma: 1) crystallization induced reduction from the parental basalt, 2) degassing induced reduction (Kelley and Cottrell, 2012), and 3) a source that has an oxygen fugacity lower than expected. The Caspana andesite is currently one of the most mafic andesites measured in the APVC (Figure 4) and should be crystallizing abundant magnetite and have an oxidation state significantly higher than it does (Blatter et al., 2013; Ulmer et al., 2018; Burns et al., 2020) at these pressures and the observed degree of evolution from parental basalt. Thus, significant crystallization of magnetite causing reduction in the andesite can be ruled out. It has also been shown that the magnitude of reduction that can occur during degassing of most APVC magmas is too small to explain the oxidation state of the Caspana system (Grocke et al., 2016) and models suggest that that fO_2 is too high for graphite stability. Rather, multiple studies have found that fO_2 remains the same within a given magmatic lineage in the APVC (Burns et al., 2020; Grocke et al., 2016). The Phase 2 rhyolite and the gabbronorite cumulate formed during its fractionation bear obvious semblance to the relatively reduced fayalite rhyolites and gabbro forming basalts discussed by Frost and Frost (1997) that are produced by mixing of primary mantle melts and partially melted, igneous rocks in the lower crust during periods of high heat advection. This model is consistent with the crustal foundering and the development of lower crustal MASH zones (Hildreth and Moorbath, 1988) thought to have taken place during the Neogene ignimbrite flare-up in the APVC prior to adiabatic ascent into the upper crust (Kay and Coira, 2009; Burns et al., 2020). It is beyond the scope of this paper to directly address the lower crust and mantle, but it is clear that the fO_2 of the Caspana system was governed by its mantle source, or, its lineage has a significant contribution from partial melts of mafic igneous rocks in the lower crust. Given the well-established evidence for extensive assimilation of crust that effectively filters out mantle source characteristics in the Central Andes (Davidson et al., 1991; Kay et al., 2010) we prefer the latter alternative.

5.4 Recycling Intermediate-Silicic Compositions Produces the Phase 1 Rhyolite

The outlier isotopic composition, peraluminous character, (Table 1; Figure 8), and excursions in major and trace element space (Figure 5) show that the Phase 1 rhyolite cannot be genetically related to the andesite and Phase 2 rhyolite. The FeO content of the Phase 1 glass is also appreciably lower than the rhyodacitic glass from the Phase 2 andesite and within error of the Phase 2 Rhyolite glass, indicating that the high Fe/Al ratio of Phase 1 plagioclase (Table 3) is the result of a high oxidation state rather than the Fe content in the melt (Toplis and Carroll, 1996; Tepley et al., 2013). The Phase 1 rhyolite is similar to the peraluminous, garnet bearing Coyaguayma rhyolites of Caffe et al. (2012), but has some important differences. The Coyaguayma rhyolites, apparently derived from ~30% contamination of metasedimentary rocks into dacitic melt, have Pb isotopic compositions slightly more radiogenic than the Phase 2 rhyolite and are more peraluminous (A/CNK > 1.3; Table 1). These strongly peraluminous (SP) are also substantially more fractionated (Sr ~55ppm and Ba ~65ppm) and have notable differences in isotopic composition and mineral assemblages (i.e., sillimanite and garnet). Given these differences, it is unlikely that the Phase 2 rhyolite is an extension of these SP rhyolites that resided and isobarically cooled in the midcrust while assimilating metasedimentary rocks prior to eruption. Another potential source is partial melting of the low-grade metasedimentary rocks that are occasionally found as xenoliths in the APVC east calderas (Ort et al., 1996; Kay et al., 2010; Caffe et al., 2012), which could explain the Nd isotopic disequilibria (Figure 9; Ayres and Harris, 1997; Wolf et al., 2019), but the Sr isotopic composition of Phase 1 is far too low. It has also been proposed that the rapid fractionation of andesitic liquid when intrudied into the base of the previously emplaced magma reservoir may produce some of the rhyolitic magmas observed in the APVC (Schmitt et al., 2001). However, the only evidence for mafic recharge is the andesite that fractionated to form the Phase 2 rhyolite (Figure 5, 10, 11). This model is not applicable to the Caspana system, as our data indicates that fractionation of the andesite was not rapid and instead occurred over multiple kilometers during the ascent and subsequent cooling of the andesite. This model also relies on bulk density and viscosity contrasts that have been shown insufficient to explain an eruptive sequence that is initiated by a recharging magma unless the intruding melt was already less dense than resident mafic magma when recharge occurred (Carrara et al., 2020).

In the light of the weaknesses and inconsistencies of the alternatives above, we propose a partial melting origin for the Phase 1 rhyolite. Experimental results have found that peraluminous rhyolitic melts similar to the Phase 1 rhyolite can be formed by melting of granodiorites (Patiño Douce, 1997) or amphibolites and gneisses (Patiño Douce and Beard, 1995). Plagioclase in the Phase 1 rhyolite occasionally have 'veins' of high An content (Figure 3D) that are indicative of unmixing during prolonged cooling below the solidus (e.g., Alling, 1932), providing direct textural evidence for some relation to a slow cooling igneous body. Equilibrium temperatures between glass and the rims of these plagioclase are higher than the Zr saturation temperatures (Table 8) indicating that zircon would not be stable prior to eruption. Combining these temperature constraints with the increase of Zr-Hf concentration of glass relative to juvenile pumice clasts (Figure 8), clearly shows that the zircon in thin section was being introduced back into the melt prior to eruption. A parallel argument can be made for plagioclase, given that Sr and Eu concentrations of the glass that are within error of bulk rock compositions (Figure 5D). These data and lines of evidence suggest that the Phase 1 rhyolite can be formed by partial melting of granodiorite or cumulate melting. These processes will be explored further later in this section.

We build on the interpretation that the uppermost crust in the APVC has a large component of granodioritic intrusions (de Silva et al., 1994; Tierney et al., 2016) like that recorded in co-magmatic xenoliths at the Pastos Grandes caldera to the north of the Caspana outcrops (Watts et al., 1999; Kaiser et al., 2017). Some remnant cumulate mush within the upper crust is also reasonable to consider. Various groups of Ordovician granitoids with similar geochemistry to the PGI also contribute to the local basement (Lucassen et al., 1999, 2001). Cogenetic xenoliths and pumices found in the Pastos Grandes Ignimbrite (PGI) thus have the geochemical composition that can explain the petrogenesis of the Phase 1 rhyolite by either of the proposed methods. Notably, these xenoliths broadly have the composition of low silica rhyolites and rhyodacites in the APVC (Figure 11).

Least squares residual models (LSQ) using the open-source version of the program Igpet (Stormer and Nicholls, 1978; Carr and Gazel, 2017) were used to test the viability of the petrogenetic models (Supplementary Table S10, S11). Results of the LSQ for both fractional crystallization and batch melting are the same since the test is simply to derive the fit of one composition from another based on mass balance, except for the amount of melt remaining (F). For the melting case, F becomes the amount of protolith left after melting and 1-F is the amount of melt produced. Least squares results are satisfactory for the granodiorite (F=0.353, R^2 = 0.236) in major element space (Supplementary Table S10). To reconcile the complexities associated with phase changes during partial melting, the incongruent dynamic melting (IDM) model of Zou and Reid (2001) was employed to model changes in trace element concentration. For the case of cumulate melting and prolonged melt presence, the same LSQ model is used and the cumulate material is partially melted using the fractional melting equation (Shaw, 1970; Wolff et al., 2020). This cumulate melt is then mixed with the pumice clasts from the PGI using the common mixing equation, as these would represent the liquid dominated portion of the

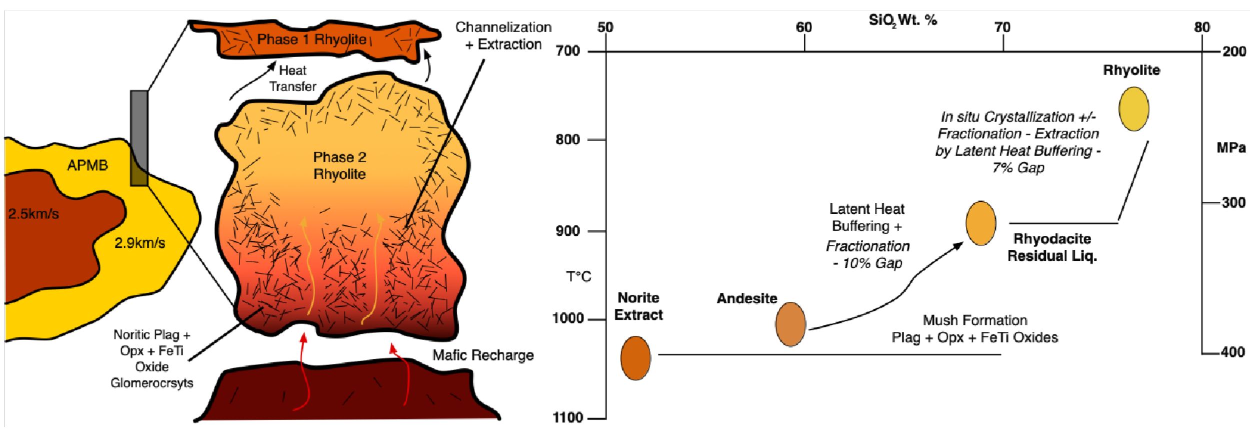

Figure 14: Schematic of the A) Temperature-composition path and B) pre-eruptive magma dynamics of the Caspana magma system. The location of the system is at the edge of the APMB shown here by the velocity contours of Ward et al. (2014). In A) the progressive crystallization of the andesite and formation of a mush. The cumulate extract is represented by the noritic glomerocrysts and the residual liquid is the rhyodacite glass. This process is shown to occur over a relatively narrow temperature range (latent heat buffering) at pressures of 400-300MPa, generating a pronounced compositional gap. Extraction of the residual liquid happens when latent/sensible heat exceeds 1 between 300-200 MPa and further fractionation magnifies the compositional gap, creating an eruptible volume of high Si rhyolite (a eutectoid composition). Dashed line in B) represents a change in local basement from deeper Sierra de Moreno complex to upper remnant granodiorite intrusions.

reservoir. Parameters, partition coefficients appropriate for rhyolitic melts, and a full explanation of these models are given in Supplementary Table S10.

In both models, Fe-Mg minerals, feldspars, and quartz (granodiorite) undergo melting and in the IDM case these minerals react to form residual titanite + clinopyroxene and partial melt. The depletion in Fe indices in the glass can be easily reconciled considering that biotite would be introduced to the melt concomitantly with quartz and progressive melting would eventually introduce clinopyroxene (cpx) and more Mg-rich hydrous minerals (e.g., amphibole). Evidence for cpx or amphibole at the source is indicated clearly by the severe Sc depletion (Figure 6) and low Dy/Dy* values (Figure 7), as these would behave compatibly in the protolith. The results of the trace element models (Figure 11) show that either mechanism proposed here can explain the geochemistry of the Phase 1 rhyolite in trace element space. Thus, re-melting remnant plutonic protolith from previous eruptions onto the APVC, or, melting of a cumulate material in the presence of felsic melt can produce the Phase 1 rhyolite. Again, this model is presented here as our current best effort, to be tested if better constraints on the upper crust in this area become available.

5.5 The Architecture of the Caspana Reservoir

The emerging evidence of a system that consisted of a variety of magmas instead of voluminous monotonous intermediates that typify the APVC solicits some discussion on its relevance. At the edge of the APMB, beneath the Caspana area, seismic velocity models speed up (Ward et al., 2014), indicating that the crust is less thermally softened and riven with melts as it is in the rest of the APVC where storage and homogenization in large dacitic reservoirs are promoted (de Silva and Gosnold, 2007; de Silva and Gregg, 2014). The cooler conditions on the periphery of the APMB would therefore limit the prolific assimilation and homogenization that characterizes most other APVC felsic magmas.

While broadly consistent with regional compositions, the isotopic signatures of Phase 1 and Phase 2 also support that these magmas remained discrete during storage (Figure 9). Kay et al. (2010) pointed out that there is general agreement that isotopic diversity is generated in the low- to mid crust where D_{Sr} is ≤ 1 (e.g., de Silva et al., 2006). AFC calculations based on DePaolo (1981) and Aitcheson and Forrest (1994) suggest that 50-60% assimilation of a Sierra de Moreno gneiss (following Godoy et al., 2017) into a primitive mantle derived basalt (Davidson et al., 1991; Mamani et al., 2010; van Alderwerelt et al., 2021) are required to account for the isotopic composition of Phase 2 (Supplementary Table S8). Meanwhile, the Sr and Nd isotopic compositions of Phase 1 are less evolved and more similar to the lavas that have erupted from local edifices that typify the modern arc (Figure 1). The Phase 1 magma was able to maintain relatively low isotopic compositions by eluding the significantly contaminated APMB (GonzálezMaurel et al., 2019). In effect, the locale of the Caspana system at the edge of the APVC/APMB facilitated its heterogeneity and ability to host magmas of different lineage in discrete batches.

The physical storage conditions that limited any homogenization are described herein.

The norite mush represented by the G1 and G2 glomerocrysts and the Phase 2 rhyolite are parallel to a variety of cumulates that have been shown to be responsible for the fractionation of high silica rhyolites (Ellis and Wolff, 2012; Ellis et al., 2013, 2014; Troch et al., 2017), in agreement with observations of plutonic rocks that show the crystallization of cumulates is an efficient mechanism for the production of felsic magma (Tavazzani et al., 2020). For the case of the Caspana system and its regional context, the small volume reservoir would crystallize faster than its typical APVC counterparts (e.g., de Silva and Wolff, 1995), producing a dense cumulate at the margins that may have limited introduction of assimilated material, allowing the system to remain closed (Figure 14). Latent heat produced by crystallization of the Pl + Opx + FeTi Oxides was high enough to either induce partial melting of country rock (e.g., Grove et al., 1997) or remobilize a discrete batch of remnant dacitic magma from prior eruptions (e.g., Godoy et al., 2019). This process of dense crystallization synchronously produced a rhyolites by reheating (Phase 1) and crystallization (Phase 2). As ilmenite came on the liquidus with orthopyroxene, latent heat buffering allowed an eruptible volume of Phase 2 rhyolite to be accumulated at the roof after extraction from the cumulate. The crystal-poor rhyolites have a rheology that does not require pre-eruptive homogenization like the crystal-rich, large volume APVC dacites (Huber et al., 2009, 2012), which allowed each rhyolite to retain its primary geochemical signature. However, some plagioclase phenocrysts found in Phase 2 rhyolite pumices clearly grew under the thermodynamic conditions appropriate to Phase 1 and some of the Phase 2 microlites are intermediary (Figure 15). These plagioclase are the product of cryptic mixing either before eruption and/or periodically on long time scales (de Silva et al., 2008).

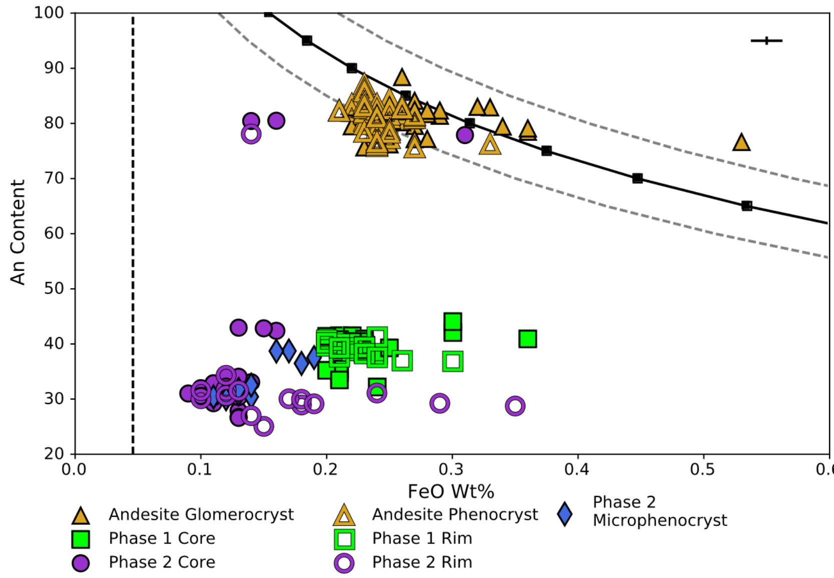

Figure 15: Bivariate plot of An vs FeO from plagioclase in the Caspana pumices. Microphenocryst and some phenocryst compositions of the Phase 2 rhyolite indicate that the two rhyolites mixed with one another prior to eruption but remained mostly discrete during their lifetime.. Curved black line is the calculated equilibrium melt composition for a magma crystallizing plagioclase of AnX composition (represented by the squares) at the FeO content (Table 1) and temperature (Table 8) of the andesite in this study. Andesite glomerocryst and phenocryst compositions are mostly concordant and lie along the equilibrium line. Gray dashed lines are the 1σ error of the model. Regression from Bindeman et al. (1998). Black vertical line shows the detection limit.

The dense cumulate framework and rhyodacitic liquid that make up the andesitic portion of the chamber does, however, require thorough disaggregation to be erupted. The mirrored distributions of normally and reversely zoned plagioclase phenocrysts in the andesite (Figure 9C) attest to mixing of similar mafic liquid prior to eruption, as do high Mg-Al rims on P1 orthopyroxene (Figure 10). Meanwhile, the An contents of cores and rims on normally zoned plagioclase phenocrysts in the andesite coincide with the of cores and rims on G2 plagioclase from glomerocrysts (Figure 8), indicating prolonged cooling and in-situ crystallization of the fractionates in the upper portion of the reservoir as discussed in section 5.1. Presumably, the shearing and perturbation exerted on the mush during the recharge event that is indicated by the data helped induce eruption, as is commonly found in silicic magma.

6. Concluding Summary

The ~5 km^3, 4.56 to 4.09 Ma Caspana Ignimbrite of the Altiplano-Puna Volcanic Complex (APVC) of the Central Andes records the eruption of an andesite and two distinct rhyolitic magmas from a vertically heterogeneous reservoir established between 400-200 MPa.

The first erupted magma (Phase 1) was a crystal-poor peraluminous (A/CNK >1.2) rhyolite that was produced by either partial melting of granodiorite or melt extraction from a granodiorite mush in the upper reaches of the reservoir. The subsequent, main stage of the eruption (Phase 2) tapped a crystal-poor slightly peraluminous fayalite-bearing rhyolite and an undersaturated, low fO_2 (≤ ΔFMQ) crystal-rich andesite that exhibits more "crustal" isotopic characteristics than Phase 1. Rhyolite-MELTS based models indicates that one of rhyolites (the Phase 2 rhyolite) is derived from the andesite by extensive crystallization of an assemblage represented by the abundant noritic glomerocrysts in the andesite.

The large (16 wt% SiO_2) compositional gap recorded in the main Phase 2 reservoir is proposed to be the result of pre-eruptive segregation of the rhyodacitic residual melts from a gabbroic (norite) mush. Latent-heat buffering produced during in-situ crystallization of silicic melt within the gabbronoritic cumulate imposed a shallow liquidus, causing efficient production of rhyodacitic melt. Spikes in latent heat facilitated the segregation of this rhyodacitic residual liquid that further fractionated to produce high-SiO_2 rhyolite. The hydrous, low fO_2 conditions promoted ilmenite stability instead of magnetite, causing an enrichment of FeO relative to the rest of the APVC during in-situ crystallization. These petrologic conditions caused high Fe^{2+}/Mg and Fe/Ca by keeping high An plagioclase (~An_{83}) and enstatite (Mg# ~58) leading to saturation of fayalite in the Phase 2 rhyolite (Warshaw and Smith, 1988) – unique in the APVC. Estimates of pressure and water contents suggest that the Phase 2 rhyolite was saturated and that fayalite stability has no dependence on-, and is probably enhanced by, high water content (Toplis and Carroll, 1996; Portnyagin et al., 2012).

The Caspana ignimbrite records km^3-scale compositional heterogeneity of diverse origin and a singular magmatic evolution within a regional magmatic complex that is dominated by monotony. This rare record is attributed to the development of the Caspana magma system on the cooler periphery of the regional upper crustal magmatic reservoir - the Altiplano Puna Magma Body - where the Caspana magmas fortuitously escaped being mixed into the APMB and the APVC magmatic system. As such, this small volume ignimbrite provides a unique window into the multiscale processes that build large silicic magma systems.

References

Aitcheson, S.J., and Forrest, A.H., 1994, Quantification of crustal contamination in open magmatic systems: Journal of Petrology, v. 35, p. 461–488, doi:10.1093/petrology/35.2.461.

Aitcheson, S.J., Harmon, R.S., Moorbath, S., Schneider, A., Soler, P., Soria-Escalante, E., Steele, G., Swainbank, I., and Worner, G., 1995, Pb isotopes define basement domains of the Altiplano, central Andes: Geology, v. 23, p. 555–558, doi:10.1130/00917613(1995)023<0555:PIDBDO>2.3.CO;2.

Alling, H. L., 1932, Perthites: The American Mineralogist, v.17, p.43-65, http://www.minsocam.org/ammin/AM17/AM17_43.pdf

Andersen, D.J., Lindsley, D.H., 1985, New (and final) models for the Ti-magnetite/ilmenite geothermometer and oxygen barometer (abs.): EOS, 66, 416

Ayres, M., and Harris, N., 1997, REE fractionation and Nd-isotope disequilibrium during crustal anatexis: Constraints from Himalayan leucogranites: Chemical Geology, v. 139, p. 249–269, doi:10.1016/S0009-2541(97)00038-7.

Bachmann, O., and Bergantz, G.W., 2004, On the origin of crystal-poor rhyolites: Extracted from batholithic crystal mushes: Journal of Petrology, v. 45, p. 1565–1582, doi:10.1093/petrology/egh019.

Bachmann, O., Dungan, M.A., and Bussy, F., 2005, Insights into shallow magmatic processes in large silicic magma bodies: The trace element record in the Fish Canyon magma body, Colorado: Contributions to Mineralogy and Petrology, v. 149, p. 338–349, doi:10.1007/s00410-005-0653-z. 816

Bacon, C.R., and Druitt, T.H., 1988, Compositional evolution of the zoned calcalkaline magma chamber of Mount Mazama, Crater Lake, Oregon: Contributions to Mineralogy and Petrology, v. 98, p. 224–256, doi:10.1007/BF00402114.

Bacon, C.R., and Hirschmann, M.M., 1988, Mg/Mn partitioning as a test for equilibrium between coexisting Fe-Ti oxides: American Mineralogist, v. 73, p. 57–61.

Bacon, C.R., Macdonald, R., Smith, R.L., and Baedecker, P.A., 1981, Pleistocene High-Silica Rhyolites of the Coso Volcanic Field , Inyo County , California progress has been made in understanding the genesis erupted between ago within the range and local of silicic magmas through detailed study of the products of basaltic: v. 86, p. 10223–10241.

Bea, F., Pereira, M.D., and Stroh, A., 1994, Mineral/leucosome trace-element partitioning in a peraluminous migmatite (a laser ablation-ICP-MS study): Chemical Geology, v. 117, p. 291–312, 823 doi:10.1016/0009-2541(94)90133-3.

Benito-Garcia, R., Lopez-Ruiz, J., 1992, Mineralogical changes of the residual solid and traceelement fractionation during partial incongruent melting. Geochimica et Cosmochimica Acta v. 56, p. 3705-826 3710, doi:10.1016/0016-7037(92)90163-d

Best, M.G., Christiansen, E.H., de Silva, S., and Lipman, P.W., 2016, Slab-rollback ignimbrite flareups in the southern Great Basin and other Cenozoic American arcs: A distinct style of arc volcanism: Geosphere, v. 12, p. 1097–1135, doi:10.1130/GES01285.1.

Black, B.A., and Andrews, B.J., 2020, Petrologic imaging of the architecture of magma reservoirs feeding caldera-forming eruptions: Earth and Planetary Science Letters, v. 552, p. 116572, doi:10.1016/j.epsl.2020.116572.

Blatter, D.L., and Carmichael, I.S.E., 2001, Hydrous phase equilibria of a Mexican high-silica andesite: A candidate for a mantle origin? Geochimica et Cosmochimica Acta, v. 65, p. 4043–4065, doi:10.1016/S0016-7037(01)00708-6.

Blatter, D.L., Sisson, T.W., and Hankins, W. Ben, 2013, Crystallization of oxidized, moderately hydrous arc basalt at mid- to lower-crustal pressures: Implications for andesite genesis: Contributions to Mineralogy and Petrology, v. 166, p. 861–886, doi:10.1007/s00410-0130920-3.

Boehnke, P., Watson, E.B., Trail, D., Harrison, T.M., and Schmitt, A.K., 2013, Zircon saturation re-revisited: Chemical Geology, v. 351, p. 324–334, doi:10.1016/j.chemgeo.2013.05.028.

Bohrson, W.A., Spera, F.J., Ghiorso, M.S., Brown, G.A., Creamer, J.B., and Mayfield, A., 2014, Thermodynamic model for energy-constrained open-system evolution of crustal magma bodies undergoing simultaneous recharge, assimilation and crystallization: The magma chamber simulator: Journal of Petrology, v. 55, p. 1685–1717, doi:10.1093/petrology/egu036.

Bohrson, W.A., Spera, F.J., Heinonen, J.S., Brown, G.A., Scruggs, M.A., Adams, J. V., Takach, M.K., Zeff, G., and Suikkanen, E., 2020, Diagnosing open-system magmatic processes using the Magma Chamber Simulator (MCS): part I—major elements and phase equilibria: Contributions to Mineralogy and Petrology, v. 175, p. 1–29, doi:10.1007/s00410-02001722-z.

Brophy, J.G., 1991, Composition gaps, critical crystallinity, and fractional crystallization in orogenic (calc-alkaline) magmatic systems: Contributions to Mineralogy and Petrology, v. 109, p. 173–182, doi:10.1007/BF00306477.

Brophy, J.G., Ota, T., Kunihro, T., Tsujimori, T., and Nakamura, E., 2011, In situ ion-microprobe determination of trace element partition coefficients for hornblende, plagioclase, orthopyroxene, and apatite in equilibrium with natural rhyolitic glass, Little Glass Mountain Rhyolite, California: American Mineralogist, v. 96, p. 1838–1850, doi:10.2138/am.2011.3857.

Buddington, A.F., and Lindsley, D.H., 1964, Iron-titanium oxide minerals and synthetic equivalents: Journal of Petrology, v. 5, p. 310–357, doi:10.1093/petrology/5.2.310.

Burns, D.H., de Silva, S.L., Tepley, F.J., and Schmitt, A.K., 2020, Chasing the mantle: Deciphering cryptic mantle signals through Earth's thickest continental magmatic arc: Earth and Planetary Science Letters, v. 531, p. 115985, doi:10.1016/j.epsl.2019.115985.

Burns, D.H., de Silva, S.L., Tepley, F., Schmitt, A.K., and Loewen, M.W., 2015, Recording the transition from flare-up to steady-state arc magmatism at the Purico-Chascon volcanic complex, northern Chile: Earth and Planetary Science Letters, v. 422, p. 75–86, doi:10.1016/j.epsl.2015.04.002.

Caffe, P.J., Trumbull, R.B., and Siebel, W., 2012, Petrology of the Coyaguayma ignimbrite, northern Puna of Argentina: Origin and evolution of a peraluminous high-SiO 2 rhyolite magma: Lithos, v. 134–135, p. 179–200, doi:10.1016/j.lithos.2011.12.013.

Caricchi, L., and Blundy, J., 2015, Experimental petrology of monotonous intermediate magmas: Geological Society Special Publication, v. 422, p. 105–130, doi:10.1144/SP422.9.

Carr, M.J., and Gazel, E., 2017, Igpet software for modeling igneous processes: examples of application using the open educational version: Mineralogy and Petrology, v. 111, p. 283–289, doi:10.1007/s00710-016-0473-z.

Chesner, C.A., 1998, Petrogenesis of the Toba Tuffs, Sumatra, Indonesia: Journal of Petrology, v. 39, p. 397–438, doi:10.1093/petroj/39.3.397.

Chiaro, G.R., 2019, Multiple Magma Bodies: Understanding the pre-eruptive architecture and magmatic processes of supereruptions based on textural, mineralogical, and geochemical features of fiamme from the Ora Ignimbrite (Permian, Italy), http://scioteca.caf.com/bitstream/handle/123456789/1091/RED2017-Eng-8ene.pdf?sequence=12&isAllowed=y%0Ahttp://dx.doi.org/10.1016/j.regsciurbeco.2008.06.005%0Ahttps://www.researchgate.net/publication/305320484_SISTEM_PEMBETUNGAN_TERPUSAT_STRATEGI_MELESTARI.

Chmielowski, J., Zandt, G., and Haberland, C., 1999, The central Andean Altiplano-Puna magma body: Geophysical Research Letters, v. 26, p. 783–786, doi:10.1029/1999GL900078.

Coleman, D.S., Gray, W., and Glazner, A.F., 2004, Rethinking the emplacement and evolution of zoned plutons: Geochronologic evidence for incremental assembly of the Tuolumne Intrusive Suite, California: Geology, v. 32, p. 433–436, doi:10.1130/G20220.1.

Cottrell, E., and Kelley, K.A., 2011, The oxidation state of Fe in MORB glasses and the oxygen fugacity of the upper mantle: Earth and Planetary Science Letters, v. 305, p. 270–282, doi:10.1016/j.epsl.2011.03.014.

Daly, B.R.A., 1925, The Geology of Ascension Island: Proceedings of the American Academy of Arts and Sciences, v. 60, p. 3–80, https://www.jstor.org/stable/25130043.

Davidson, J.P., Harmon, R.S., and Wörner, G., 1991, The source of central Andean magmas; Some considerations: Special Paper of the Geological Society of America, v. 265, p. 233–243, doi:10.1130/SPE265-p233.

Davidson, J.P., Turner, S., Plank, T., 2013, Dy/Dy*: Variations Arising from Mantle Sources and Petrogenetic Processes: Journal of Petrology, v. 54, p. 525-537, https://doi.org/10.1093/petrology/egs076

Deer, W., Howie, R., Zussman, J., 1992, An Introduction to the Rock forming Minerals: (2nd ed.), Longman, London

Deering, C.D., Gravley, D.M., Vogel, T.A., Cole, J.W., and Leonard, G.S., 2010, Origins of coldwet-oxidizing to hot-dry-reducing rhyolite magma cycles and distribution in the Taupo Volcanic Zone, New Zealand: Contributions to Mineralogy and Petrology, v. 160, p. 609–629, doi:10.1007/s00410-010-0496-0.

DePaolo, D.J., 1981, Trace element and isotopc effects of combined wallrock assimilation and fractional crystallization: Earth and Planetary Science Letters, v. 53, p. 189–202.

de Silva, S.L., 1989a, Altiplano-Puna volcanic complex of the central Andes: Geology, v. 17, p. 1102–1106, doi:10.1130/0091-7613(1989)017<1102:APVCOT>2.3.CO;2. de Silva, S.L., 1989b, Geochronology and stratigraphy of the ignimbrites from the 21 ° 30’ S to 23 ° 30’ S portion of the Central Andes of Northern Chile.: , p. 93–131. de Silva, S.L., 1991, Style of zoning in central Andean ignimbrites; Insights into magma chamber processes: Geological Society Special Publication, p. 217–232.

de Silva, S.L., 1989c, The origin and significance of crystal rich inclusions in pumices from two Chilean ignimbrites: Geological Magazine, v. 126, p. 159–175, doi:10.1017/S0016756800006300.

de Silva, S.L., and Francis, P.W., 1989, Correlation of large ignimbrites - Two case studies from the Central Andes of northern Chile: Journal of Volcanology and Geothermal Research, v. 37, p. 133–149.

de Silva, S.L., and Gosnold, W.D., 2007, Episodic construction of batholiths: Insights from the spatiotemporal development of an ignimbrite flare-up: Journal of Volcanology and Geothermal Research, v. 167, p. 320–335, doi:10.1016/j.jvolgeores.2007.07.015. de Silva, S.L., and Gregg, P.M., 2014, Thermomechanical feedbacks in magmatic systems: Implications for growth, longevity, and evolution of large caldera-forming magma reservoirs and their supereruptions: Journal of Volcanology and Geothermal Research, v. 282, p. 77–91, doi:10.1016/j.jvolgeores.2014.06.001.

de Silva, S., and Kay, S.M., 2018, Turning up the heat: High-flux magmatism in the central andes: Elements, v. 14, p. 245–250, doi:10.2138/gselements.14.4.245.

de Silva, S., Salas, G., and Schubring, S., 2008, Triggering explosive eruptions-The case for silicic magma recharge at Huaynaputina, southern Peru: Geology, v. 36, p. 387–390, doi:10.1130/G24380A.1.

de Silva, S.L., Self, S., Francis, P.W., Drake, R.E., and Ramirez R., C., 1994, Effusive silicic volcanism in the Central Andes: the Chao dacite and other young lavas of the AltiplanoPuna volcanic complex: Journal of Geophysical Research, v. 99, p. 805–825, doi:10.1029/94jb00652.

de Silva, S.L., and Wolff, J.A., 1995, Zoned magma chambers: the influence of magma chamber geometry on sidewall convective fractionation: Journal of Volcanology and Geothermal Research, v. 65, p. 111–118, doi:10.1016/0377-0273(94)00105-P. de Silva, S., Zandt, G., Trumbull, R., Viramonte, J.G., Salas, G., and Jiménez, N., 2006, Large ignimbrite eruptions and volcano-tectonic depressions in the Central Andes: A thermomechanical perspective: Geological Society Special Publication, v. 269, p. 47–63, doi:10.1144/GSL.SP.2006.269.01.04.

Dufek, J., and Bachmann, O., 2010, Quantum magmatism: Magmatic compositional gaps generated by melt-crystal dynamics: Geology, v. 38, p. 687–690, doi:10.1130/G30831.1.

Dunn, T., and Sen, C., 1994, Mineral/matrix partition coefficients for orthopyroxene, plagioclase, and olivine in basaltic to andesitic systems: A combined analytical and experimental study: 910 Geochimica et Cosmochimica Acta, v. 58, p. 717–733, doi:10.1016/0016-7037(94)90501-0.

Eggler, D.H., 1972, Water-saturated and undersaturated melting relations in a Paricutin andesite and an estimate of water content in the natural magma: Contributions to Mineralogy and Petrology, v. 34, p. 261–271, doi:10.1007/BF00373757.

Ellis, B.S., Bachmann, O., and Wolff, J.A., 2014, Cumulate fragments in silicic ignimbrites: The case of the Snake River Plain: Geology, v. 42, p. 431–434, doi:10.1130/G35399.1.

Ellis, B.S., and Wolff, J.A., 2012, Complex storage of rhyolite in the central Snake River Plain: Journal of Volcanology and Geothermal Research, v. 211–212, p. 1–11, doi:10.1016/j.jvolgeores.2011.10.002.

Ellis, B.S., Wolff, J.A., Boroughs, S., Mark, D.F., Starkel, W.A., and Bonnichsen, B., 2013, Rhyolitic volcanism of the central Snake River Plain: A review: Bulletin of Volcanology, v. 75, p. 1–19, doi:10.1007/s00445-013-0745-y.

Ewart, A., 1982, The mineralogy and petrology of Tertiary-Recent orogenic volcanic rocks: with special reference to the andesitic-basaltic compositional range. Andesites: Orogenic andesites and related rocks. v. 1, p. 25-98, ISBN: 978-0471280347

Ewart, A., and Griffin, W.L., 1994, Application of proton-microprobe data to trace-element partitioning in volcanic rocks: Chemical Geology, v. 117, p. 251–284, doi:10.1016/00092541(94)90131-7.

Folkes, C.B., de Silva, S.L., Bindeman, I.N., and Cas, R.A.F., 2013, Tectonic and climate history influence the geochemistry of large-volume silicic magmas: New δ18O data from the Central Andes with comparison to N America and Kamchatka: Journal of Volcanology and Geothermal Research, v. 262, p. 90–103, doi:10.1016/j.jvolgeores.2013.05.014.

Folkes, C.B., de Silva, S.L., Wright, H.M., and Cas, R.A.F., 2011, Geochemical homogeneity of a long-lived, large silicic system; evidence from the Cerro Galán caldera, NW Argentina: Bulletin of Volcanology, v. 73, p. 1455–1486, doi:10.1007/s00445-011-0511-y.

Freymuth, H., Brandmeier, M., and Wörner, G., 2015, The origin and crust/mantle mass balance of Central Andean ignimbrite magmatism constrained by oxygen and strontium isotopes and erupted volumes: Contributions to Mineralogy and Petrology, v. 169, p. 1– 24, doi:10.1007/s00410-015-1152-5.

Frost, C.D., and Frost, B.R., 1997, Reduced rapakivi-type granites: The tholeiite connection: Geology, v. 25, p. 647–650, doi:10.1130/0091-7613(1997)025<0647:RRTGTT>2.3.CO;2.

Ghiorso, M.S., and Evans, B.W., 2008, Thermodynamics of rhombohedral oxide solid solutions and a revision of the Fe-Ti two-oxide geothermometer and oxygen-barometer: American Journal of Science, v. 308, p. 957–1039, doi:10.2475/09.2008.01.

Ghiorso, M.S., and Gualda, G.A.R., 2013, A method for estimating the activity of titania in magmatic liquids from the compositions of coexisting rhombohedral and cubic irontitanium oxides: Contributions to Mineralogy and Petrology, v. 165, p. 73–81, doi:10.1007/s00410-012-0792-y.

Ghiorso, M.S., and Sack, R.O., 1995, Chemical mass transfer in magmatic processes IV. A revised and internally consistent thermodynamic model for the interpolation and extrapolation of liquid-solid equilibria in magmatic systems at elevated temperatures and pressures: Contributions to Mineralogy and Petrology, v. 119, p. 197–212, doi:10.1007/BF00307281.

Godoy, B., Taussi, M., González-Maurel, O., Renzulli, A., Hernández-Prat, L., le Roux, P., Morata, D., and Menzies, A., 2019, Linking the mafic volcanism with the magmatic stages during the last 1 Ma in the main volcanic arc of the Altiplano-Puna Volcanic Complex (Central Andes): Journal of South American Earth Sciences, v. 95, p. 102295, doi:10.1016/j.jsames.2019.102295.

Godoy, B., Wörner, G., Kojima, S., Aguilera, F., Simon, K., and Hartmann, G., 2014, Lowpressure evolution of arc magmas in thickened crust: The San Pedro-Linzor volcanic chain, Central Andes, Northern Chile: Journal of South American Earth Sciences, v. 52, p. 24–42, doi:10.1016/j.jsames.2014.02.004.

Godoy, B., Wörner, G., Le Roux, P., de Silva, S., Parada, M.Á., Kojima, S., González-Maurel, O., Morata, D., Polanco, E., and Martínez, P., 2017, Sr- and Nd- isotope variations along the Pleistocene San Pedro – Linzor volcanic chain, N. Chile: Tracking the influence of the upper crustal Altiplano-Puna Magma Body: Journal of Volcanology and Geothermal Research, v. 341, p. 172–186, doi:10.1016/j.jvolgeores.2017.05.030.

González-Maurel, O., le Roux, P., Godoy, B., Troll, V.R., Deegan, F.M., and Menzies, A., 2019, The great escape: Petrogenesis of low-silica volcanism of Pliocene to Quaternary age associated with the Altiplano-Puna Volcanic Complex of northern Chile (21°10′-22°50′S): Lithos, v. 346–347, doi:10.1016/j.lithos.2019.105162.

Green, T.H., and Pearson, N.J., 1987, An experimental study of Nb and Ta partitioning between Ti-rich minerals and silicate liquids at high pressure and temperature: Geochimica et Cosmochimica Acta, v. 51, p. 55–62, doi:10.1016/0016-7037(87)90006-8.

Grocke, S.B., Andrews, B.J., and de Silva, S.L., 2017a, Experimental and petrological constraints on long-term magma dynamics and post-climactic eruptions at the Cerro Galán caldera system, NW Argentina: Journal of Volcanology and Geothermal Research, v. 347, p. 296–311, doi:10.1016/j.jvolgeores.2017.09.021.

Grocke, S.B., Cottrell, E., de Silva, S., and Kelley, K.A., 2016, The role of crustal and eruptive processes versus source variations in controlling the oxidation state of iron in Central Andean magmas: Earth and Planetary Science Letters, v. 440, p. 92–104, doi:10.1016/j.epsl.2016.01.026.

Grocke, S.B., de Silva, S.L., Iriarte, R., Lindsay, J.M., and Cottrell, E., 2017b, Catastrophic Caldera-Forming (CCF) monotonous silicic magma reservoirs: Geochemical and petrological constraints on heterogeneity, magma dynamics, and eruption dynamics of the 3.49Ma Tara supereruption, Guacha II Caldera, SW Bolivia: Journal of Petrology, v. 58, p. 227–260, doi:10.1093/petrology/egx012.

Grove, T.L., and Donnelly-Nolan, J.M., 1986, The evolultion of young silicic lavas at Medicine Lake Volcano, California: Implications for the origin of compositional gaps in calc-alkaline series lavas: Contributions to Mineralogy and Petrology, v. 92, p. 281–302.

Grove, T.L., Donnelly-Nolan, J.M., and Housh, T., 1997, Magmatic processes that generated the rhyolite of Glass Mountain, Medicine Lake volcano, N. California: Contributions to Mineralogy and Petrology, v. 127, p. 205–223, doi:10.1007/s004100050276.

Gualda, G.A.R., and Ghiorso, M.S., 2015, Gualda et al (2015) G3 MELTS for Excel and rhyolite: , p. 315–324, doi:10.1002/2014GC005545.Received.

Gualda, G.A.R., and Ghiorso, M.S., 2014, Phase-equilibrium geobarometers for silicic rocks based on rhyolite-MELTS. Part 1: Principles, procedures, and evaluation of the method: Contributions to Mineralogy and Petrology, v. 168, p. 1–17, doi:10.1007/s00410-0141033-3.

Gualda, G.A.R., Gravley, D.M., Deering, C.D., and Ghiorso, M.S., 2019, Magma extraction pressures and the architecture of volcanic plumbing systems: Earth and Planetary Science Letters, v. 522, p. 118–124, doi:10.1016/j.epsl.2019.06.020.

Harmon, L.J., Cowlyn, J., Gualda, G.A.R., and Ghiorso, M.S., 2018, Phase-equilibrium geobarometers for silicic rocks based on rhyolite-MELTS. Part 4: Plagioclase, orthopyroxene, clinopyroxene, glass geobarometer, and application to Mt. Ruapehu, New Zealand: Contributions to Mineralogy and Petrology, v. 173, p. 1–20, doi:10.1007/s00410017-1428-z.

Hildreth, W., 1981, Gradients in silicic magma chambers: implications for lithospheric magmatism.: v. 86, 10153–10192 p., doi:10.1029/JB086iB11p10153.

Hildreth, W., and Moorbath, S., 1988, Crustal contributions to arc magmatism in the Andes of Central Chile: Contributions to Mineralogy and Petrology, v. 98, p. 455–489, doi:10.1007/BF00372365.

Holness, M.B., Stock, M.J., and Geist, D., 2019, Magma chambers versus mush zones: Constraining the architecture of sub-volcanic plumbing systems from microstructural analysis of crystalline enclaves: Philosophical Transactions of the Royal Society A: Mathematical, Physical and Engineering Sciences, v. 377, doi:10.1098/rsta.2018.0006.

Holness, M.B., Stripp, G., Humphreys, M.C.S., Veksler, I. V., Nielsen, T.F.D., and Tegner, C., 2011, Silicate liquid immiscibility within the crystal mush: late-stage magmatic microstructures in the skaergaard intrusion, east greenland: Journal of Petrology, v. 52, p. 175–222, doi:10.1093/petrology/egq077.

Holness, M.B., Tegner, C., Nielsen, T.F.D., Stripp, G., and Morse, S.A., 2007, A textural record of solidification and cooling in the skaergaard intrusion, East Greenland: Journal of Petrology, v. 48, p. 2359–2377, doi:10.1093/petrology/egm064.

Huber, C., Bachmann, O., and Dufek, J., 2012, Crystal-poor versus crystal-rich ignimbrites: A competition between stirring and reactivation: Geology, v. 40, p. 115–118, doi:10.1130/G32425.1.

Huber, C., Bachmann, O., and Manga, M., 2009, Homogenization processes in silicic magma chambers by stirring and mushification (latent heat buffering): Earth and Planetary Science Letters, v. 283, p. 38–47, doi:10.1016/j.epsl.2009.03.029.

Iddings, J.P., 1885, On the occurrence of Fayalite in the lithophyses of obsidian and rhyolite in the Yellowstone National Park: American Journal of Science, v. 30, p. 58.

Johnson, D.M., Hooper, P.R., and Conrey, R.M., 1999, XRF Analysis of Rocks and Minerals for Major and Trace Elements on a Single Low Dilution Li-tetraborate Fused Bead: JCPDSInternational Centre for Diffraction Data, p. 843–867.

Jónasson, K., 1994, Rhyolite volcanism in the Krafla central volcano, north-east Iceland: Bulletin of Volcanology, v. 56, p. 516–528, doi:10.1007/BF00302832.

Kaiser, J.F., 2014, Understanding Large Resurgent Calderas and Associated Magma Systems: The Pastos Grandes Caldera Complex, Southwest Bolivia: Oregon State University.

Kaiser, J.F., de Silva, S., Schmitt, A.K., Economos, R., and Sunagua, M., 2017, Million-year melt–presence in monotonous intermediate magma for a volcanic–plutonic assemblage in the Central Andes: Contrasting histories of crystal-rich and crystal-poor super-sized silicic magmas: Earth and Planetary Science Letters, v. 457, p. 73–86, doi:10.1016/j.epsl.2016.09.048.

Kay, S.M., and Coira, B.L., 2009, Shallowing and steepening subduction zones, continental lithospheric loss, magmatism, and crustal flow under the Central Andean Altiplano-Puna Plateau: v. 204, 229–259 p., doi:10.1130/2009.1204(11).

Kay, S.M., Coira, B.L., Caffe, P.J., and Chen, C.H., 2010, Regional chemical diversity, crustal and mantle sources and evolution of central Andean Puna plateau ignimbrites: Journal of Volcanology and Geothermal Research, v. 198, p. 81–111, doi:10.1016/j.jvolgeores.2010.08.013.

Kelley, K.A., and Cottrell, E., 2012, The influence of magmatic differentiation on the oxidation state of Fe in a basaltic arc magma: Earth and Planetary Science Letters, v. 329–330, p. 109–121, doi:10.1016/j.epsl.2012.02.010.

Kelley, K.A., and Cottrell, E., 2009, Water and the oxidation state of subduction zone magmas: Science, v. 325, p. 605–607, doi:10.1126/science.1174156.

Kent, A.J.R., and Ungerer, C.A., 2006, Analysis of light lithophile elements (Li, Be, B) by laser ablation ICP-MS: Comparison between magnetic sector and quadrupole ICP-MS: American Mineralogist, v. 91, p. 1401–1411, doi:10.2138/am.2006.2030.

Kern, J.M., de Silva, S.L., Schmitt, A.K., Kaiser, J.F., Iriarte, A.R., and Economos, R., 2016, Geochronological imaging of an episodically constructed subvolcanic batholith: U-Pb in zircon chronochemistry of the Altiplano-Puna Volcanic Complex of the Central Andes: Geosphere, v. 12, p. 1054–1077, doi:10.1130/GES01258.1.

Kress, V.C., and Carmichael, I.S.E., 1991, The compressibility of silicate liquids containing Fe2O3 and the effect of composition, temperature, oxygen fugacity and pressure on their redox states: Contributions to Mineralogy and Petrology, v. 108, p. 82–92.

Lepage, L.D., 2003, ILMAT: An Excel worksheet for ilmenite-magnetite geothermometry and geobarometry: Computers and Geosciences, v. 29, p. 673–678, doi:10.1016/S00983004(03)00042-6.

Lindsay, J.M., Schmitt, A.K., Trumbull, R.B., de Silva, S.L., Siebel, W., and Emmermann, R., 2001a, Magmatic Evolution of the La Pacana Caldera System, Central Andes, Chile: Compositional Variation of Two Cogenetic, Large-Volume Felsic Ignimbrites: Journal of Petrology, v. 42, p. 459–486, doi:10.1093/petrology/42.3.459.

Lindsay, J.M., de Silva, S., Trumbull, R., Emmermann, R., and Wemmer, K., 2001b, La Pacana caldera, N. Chile: A re-evaluation of the stratigraphy and volcanology of one of the world's largest resurgent calderas: Journal of Volcanology and Geothermal Research, v. 106, p. 145–173, doi:10.1016/S0377-0273(00)00270-5.

Lipman, P.W., and Bachmann, O., 2015, Ignimbrites to batholiths: Integrating perspectives from geological, geophysical, and geochronological data: Geosphere, v. 11, p. 705–743, doi:10.1130/GES01091.1.

Lowenstern, J.B., Clynne, M.A., and Bullen, T.D., 1997, Comagmatic A-type granophyre and rhyolite from the Alid volcanic center, eritrea, northeast Africa: Journal of Petrology, v. 38, p. 1707–1721, doi:10.1093/petroj/38.12.1707.

Lucassen, F., Becchio, R., Harmon, R., Kasemann, S., Franz, G., Trumbull, R., Wilke, H.G., Romer, R.L., and Dulski, P., 2001, Composition and density model of the continental crust at an active continental margin - The Central Andes between 21° and 27°S: Tectonophysics, v. 341, p. 195–223, doi:10.1016/S0040-1951(01)00188-3.

Lucassen, F., Franz, G., Thirlwall, M.F., and Mezger, K., 1999, Crustal recycling of metamorphic basement: Late Palaeozoic granitoids of Northern Chile (~22°S). Implications for the composition of the Andean crust: Journal of Petrology, v. 40, p. 1527–1551, doi:10.1093/petroj/40.10.1527.

Lucassen, F., Harmon, R., Franz, G., Romer, R.L., Becchio, R., and Siebel, W., 2002, Lead evolution of the Pre-Mesozoic crust in the Central Andes (18-27°): Progressive homogenisation of Pb: Chemical Geology, v. 186, p. 183–197, doi:10.1016/S00092541(01)00407-7.

Luhr, J.F., and Carmichael, I.S.E., 1980, The Colima Volcanic complex, Mexico - I. Post caldera andesites from Volcán Colima: Contributions to Mineralogy and Petrology, v.71, p. 343–372, doi:10.1007/BF00374707.

Macdonald, R., Davies, G.R., Bliss, C.M., Leat, P.T., Bailey, D.K., and Smith, R.L., 1987, Geochemistry of High-silica Perhalkaline Rhyolites, Naivasha, Kenya Rift Valley: Journal of Petrology1, v. 28, p. 979–1008, doi:0022-3530.

Mahood, G.A., 1981, A summary of the geology and petrology of the Sierra La Primavera, Jalisco, Mexico.: Journal of Geophysical Research, v. 86, p. 10137–10152, doi:10.1029/JB086iB11p10137.

Mamani, M., Tassara, A., and Wörner, G., 2008, Composition and structural control of crustal domains in the central Andes: Geochemistry, Geophysics, Geosystems, v. 9, doi:10.1029/2007GC001925.

Mamani, M., Wörner, G., and Sempere, T., 2010, Geochemical variations in igneous rocks of the Central Andean orocline (13°S to 18°S): Tracing crustal thickening and magma generation through time and space: Bulletin of the Geological Society of America, v. 122, p. 162–182, doi:10.1130/B26538.1.

Martel, C., Pichavant, M., Holtz, F., and Scaillet, B., 1999, Effects of fO2 and H2O on andesite phase relations between 2 and 4 kbar: Journal of Geophysical Research, v. 104, p. 29453–29470.

McDonough, W.F., and Sun, S. s., 1995, The composition of the Earth: Chemical Geology, v. 120, p. 223–253, doi:10.1016/0009-2541(94)00140-4.
Michael, P.J., 1988, Partition coefficients for rare earth elements in mafic minerals of high silica rhyolites: The importance of accessory mineral inclusions: Geochimica et Cosmochimica Acta, v. 52, p. 275–282.
Morse, S.A., 2011, The fractional latent heat of crystallizing magmas: American Mineralogist, v. 96, p. 682–689, doi:10.2138/am.2011.3613.
Nagasawa, H., 1973, Rare-earth distribution in alkali rocks from Oki-Dogo Island, Japan: Contributions to Mineralogy and Petrology, v. 39, p. 301–308, doi:10.1007/BF00376470.
Nicholls, I.A., and Harris, K.L., 1980, Experimental rare earth element partition coefficients for garnet, clinopyroxene and amphibole coexisting with andesitic and basaltic liquids: Geochimica et 1073 Cosmochimica Acta, v. 44, p. 287–308, doi:10.1016/00167037(80)90138-6.
Nielsen, R.L., and Beard, J.S., 2000, Magnetite-melt HFSE partitioning: Chemical Geology, v. 164, p. 21–34, doi:10.1016/S0009-2541(99)00139-4.
Nielsen, R.L., Gallahan, W.E., and Newberger, F., 1992, Experimentally determined mineralmelt partition coefficients for Sc, Y and REE for olivine, orthopyroxene, pigeonite, magnetite, and ilmenite: Contributions to Mineralogy and Petrology, v. 110, p. 488–499.
Newman, S., and Lowenstern, J.B., 2002, VOLATILECALC: A silicate melt-H2O-CO2 solution model written in Visual Basic for excel: Computers and Geosciences, v. 28, p. 597–604, doi:10.1016/S0098-3004(01)00081-4.
Novak, S.W., and Mahood, G.A., 1986, Rise and fall of a basalt-trachyte-rhyolite magma system at the Kane Springs Wash Caldera, Nevada: Contributions to Mineralogy and Petrology, v. 94, p. 352–373.
Ort, M.H., Coira, B.L., and Mazzoni, M.M., 1996, Generation of a crust-mantle magma mixture: Magma sources and contamination at Cerro Panizos, central Andes: Contributions to Mineralogy and Petrology, v. 123, p. 308–322, doi:10.1007/s004100050158.
Padilla, A.J., and Gualda, G.A.R., 2016, Crystal-melt elemental partitioning in silicic magmatic systems: An example from the Peach Spring Tuff high-silica rhyolite, Southwest USA: Chemical Geology, v. 440, p. 326–344, doi:10.1016/j.chemgeo.2016.07.004.
Pamukcu, A.S., Gualda, G.A.R., Ghiorso, M.S., Miller, C.F., and McCracken, R.G., 2015, Phase-equilibrium geobarometers for silicic rocks based on rhyolite-MELTS—Part 3: Application to the Peach Spring Tuff (Arizona–California–Nevada, USA): Contributions to Mineralogy and Petrology, v. 169, doi:10.1007/s00410-015-1122-y.
Patiño Douce, A.E., 1997, Generation of metaluminous A-type granites by low-pressure melting of calc-alkaline granitoids: Geology, v. 25, p. 743–746, doi:10.1130/00917613(1997)025<0743:GOMATG>2.3.CO;2.
Patiño Douce, A.E., and Beard, J.S., 1995, Dehydration-melting of Biotite Gneiss and Quartz Amphibolite from 3 to 15 kbar: Journal of Petrology, v. 36.
Pitcher, B. W., Kent, A. J. R. & Grunder, A. L. (2021). Tephrochronology of North America's most recent arc-sourced ignimbrite flare-up: The Deschutes Formation of the Central Oregon Cascades. Journal of Volcanology and Geothermal Research. Elsevier B.V. 412.
Plank, T., Kelley, K.A., Zimmer, M.M., Hauri, E.H., and Wallace, P.J., 2013, Why do mafic arc magmas contain ~4wt% water on average? Earth and Planetary Science Letters, v. 364, p. 168–179, doi:10.1016/j.epsl.2012.11.044.
Portnyagin, M., Hoernle, K., Storm, S., Mironov, N., van den Bogaard, C., and Botcharnikov, R., 2012, H2O-rich melt inclusions in fayalitic olivine from Hekla volcano: Implications for phase relationships in silicic systems and driving forces of explosive volcanism on Iceland: Earth and Planetary Science Letters, v. 357–358, p. 337–346, doi:10.1016/j.epsl.2012.09.047.

Prezzi, C.B., Götze, H.J., and Schmidt, S., 2009, 3D density model of the Central Andes: Physics of the 1104 Earth and Planetary Interiors, v. 177, p. 217–234, doi:10.1016/j.pepi.2009.09.004.

Pritchard, M.E. et al., 2018, Synthesis: PLUTONS: Investigating the relationship between pluton growth and volcanism in the Central Andes: Geosphere, v. 14, p. 954–982, doi:10.1130/GES01578.1.

Prowatke, S., and Klemme, S., 2005, Effect of melt composition on the partitioning of trace elements between titanite and silicate melt: Geochimica et Cosmochimica Acta, v. 69, p. 695–709, doi:10.1016/j.gca.2004.06.037.

Putirka, K.D., 2005, Igneous thermometers and barometers based on plagioclase + liquid equilibria: Tests of some existing models and new calibrations: American Mineralogist, v. 90, p. 336–346, 1112 doi:10.2138/am.2005.1449.

Putirka, K.D., 2008, Thermometers and barometers for volcanic systems: Reviews in Mineralogy and Geochemistry, v. 69, p. 61–120, doi:10.2138/rmg.2008.69.3.

Ramos, F.C., 1992, Isotope Geology of the Metamorphic Core of the Central Grouse Creek Mountains, Box Elder County, Utah: University of California, Los Angeles.

Ramsey, F. L. and Schafer, D. W. (2013). The Statistical Sleuth: A Course in Methods of Data Analysis. Boston: Brooks/Cole ISBN13: 978-1133490678

Reid, F., 1983, Origin of the rhyolitic rocks of the taupo volcanic zone, New Zealand: Journal of Volcanology and Geothermal Research, v. 15, p. 315–338, doi:10.1016/03770273(83)90105-1.

Rhodes, J.M., Dungan, M.A., Blanchard, D.P., and Long, P.E., 1979, Magma mixing at mid ocean ridges: Evidence from basalts drilled near 22° N on the Mid-Atlantic Ridge: Tectonophysics, v. 55, p. 35–61, doi:10.1016/0040-1951(79)90334-2.

Roeder, P.L., and Emslie, R.F., 1970, Olivine-Liquid Equilibrium: Contributions to Mineralogy and Petrology, v. 29, p. 275–289, doi:10.1007/BF00371276.

Rooyakkers, S.M., Stix, J., Berlo, K., Petrelli, M., Hampton, R.L., Barker, S.J., and Morgavi, D., 2021, The Origin of Rhyolitic Magmas at Krafla Central Volcano (Iceland): Journal of Petrology, v. 62, p. 1–80, doi:10.1093/petrology/egab064.

Salisbury, M.J., Jicha, B.R., de Silva, S.L., Singer, B.S., Jiménez, N.C., and Ort, M.H., 2011, 40Ar/39Ar chronostratigraphy of Altiplano-Puna volcanic complex ignimbrites reveals the development of a major magmatic province: Bulletin of the Geological Society of America, v. 123, p. 821–840, doi:10.1130/B30280.1.

Schiller, D., and Finger, F., 2019, Application of Ti-in-zircon thermometry to granite studies: problems and possible solutions: Contributions to Mineralogy and Petrology, v. 174, p. 1–16, doi:10.1007/s00410-019-1585-3.

Schmitt, A.K., de Silva, S.L., Trumbull, R.B., and Emmermann, R., 2001, Magma evolution in the Purico ignimbrite complex, northern Chile: Evidence for zoning of a dacitic magma by injection of rhyolitic melts following mafic recharge: Contributions to Mineralogy and Petrology, v. 140, p. 680–700, doi:10.1007/s004100000214.

Schmitt, A.K., Danišík, M., Evans, N. J., Siebel, W., Kiemele, E., Aydin, F., Harvey, J. C., 2011, Acigöl rhyolite field, Central Anatolia (part 1): high-resolution dating of eruption episodes and zircon growth rates: Contributions to Mineralogy and Petrology, v. 162, p. 1215-1231, https://doi.org/10.1007/s00410-011-0648-x

Schnetzler, C.C., and Philpotts, J.A., 1970, Partition coefficients of rare-earth elements between igneous matrix material and rock-forming mineral phenocrysts-II: Geochimica et Cosmochimica Acta, v. 34, p. 331–340.

Sisson, T.W., 1991, Pyroxene-high silica rhyolite trace element partition coefficients measured by ion microprobe: Geochimica et Cosmochimica Acta, v. 55, p. 1575–1585, doi:10.1016/0016-1136 7037(91)90129-S.

Shaw, D.M., 1970, Trace element fractionation during anatexis: Geochimica et Cosmochimica Acta, v. 34, p. 237–243, doi:10.1016/0016-7037(70)90009-8.

Sliwinski, J.T., Bachmann, O., Ellis, B.S., Dávila-Harris, P., Nelson, B.K., and Dufek, J., 2015, Eruption of shallow crystal cumulates during explosive phonolitic eruptions on Tenerife, Canary Islands: Journal of Petrology, v. 56, p. 2173–2194, doi:10.1093/petrology/egv068.

Spera, F.J., Bohrson, W.A., Till, C.B., and Ghiorso, M.S., 2007, Partitioning of trace elements among coexisting crystals, melt, and supercritical fluid during isobaric crystallization and melting: American Mineralogist, v. 92, p. 1881–1898, doi:10.2138/am.2007.2326.

Stormer, J.C., 1983, The effects of recalculation on estimates of temperature and oxygen fugacity from analyses of multicomponent iron-titanium oxides.: American Mineralogist, v. 68, p. 586–594.

Stormer, J.J.C., and Nicholls, J., 1978, XLFRAC: A program for the interactive testing of magmatic differentiation models: Computers and Geosciences, v. 4, p. 143–149.

Tavazzani, L., Peres, S., Sinigoi, S., Demarchi, G., Economos, R.C., and Quick, J.E., 2020, Timescales and mechanisms of crystal-mush rejuvenation and melt extraction recorded in Permian plutonic and volcanic rocks of the Sesia Magmatic System (southern Alps, Italy): Journal of Petrology, v. 61, doi:10.1093/petrology/egaa049.

Tepley, F.J., de Silva, S., and Salas, G., 2013, Magma dynamics and petrological evolution leading to thevei 5 2000 BP Eruption of EL mistivolcano, southern Peru: Journal of Petrology, v. 54, p. 2033–2065, doi:10.1093/petrology/egt040.

Tierney, C.R., Schmitt, A.K., Lovera, O.M., and de Silva, S.L., 2016, Voluminous plutonism during volcanic quiescence revealed by thermochemical modeling of zircon: Geology, v. 44, p. 683–686, doi:10.1130/G37968.1.

Toplis, M.J., and Carroll, M.R., 1996, Differentiation of ferro-basaltic magmas under conditions open and closed to oxygen: Implications for the skaergaard intrusion and other natural systems: Journal of Petrology, v. 37, p. 837–858, doi:10.1093/petrology/37.4.837.

Troch, J., Ellis, B.S., Mark, D.F., Bindeman, I.N., Kent, A.J.R., Guillong, M., and Bachmann, O., 2017, Rhyolite generation prior to a yellowstone supereruption: Insights from the Island Park-Mount Jackson rhyolite series: Journal of Petrology, v. 58, p. 29–52, doi:10.1093/petrology/egw071.

Ulmer, P., Kaegi, R., and Müntener, O., 2018, Experimentally derived intermediate to silica-rich arc magmas by fractional and equilibrium crystallization at 1·0 GPa: An evaluation of phase relationships, compositions, liquid lines of descent and oxygen fugacity: Journal of Petrology, v. 59, p. 11–58, doi:10.1093/petrology/egy017.

van Alderwerelt, B., Ukstins, I.A., and Ramos, F.C., 2021, Sr isotopes and geochemistry of Cerro Overo maar provide a unique window into arc magma genesis in the Central Volcanic Zone of the Andes: Lithos, v. 386–387, p. 105978, doi:10.1016/j.lithos.2021.105978.

Vermeesch, P. (2012). On the visualisation of detrital age distributions. Chemical Geology. Elsevier B.V. 312–313, 190–194.

Vlach, S.R.F., and Gualda, G.A.R., 2007, Allanite and chevkinite in A-type granites and syenites of the Graciosa Province, southern Brazil: Lithos, v. 97, p. 98–121, doi:10.1016/j.lithos.2006.12.003.

Ward, K.M., Zandt, G., Beck, S.L., Christensen, D.H., and McFarlin, H., 2014, Seismic imaging of the magmatic underpinnings beneath the Altiplano-Puna volcanic complex from the joint inversion of surface wave dispersion and receiver functions: Earth and Planetary Science Letters, v. 404, p. 43–53, doi:10.1016/j.epsl.2014.07.022.

Warshaw, C.M., and Smith, R.L., 1988, Pyroxenes and fayalites in the Bandelier Tuff, New Mexico: temperatures and comparison with other rhyolites: American Mineralogist, v. 73, p. 1025–1037, doi:0003-004X.

Waters, L.E., and Lange, R.A., 2015, An updated calibration of the plagioclase-liquid hygrometer-thermometer applicable to basalts through rhyolites: American Mineralogist, v. 100, p. 2172–2184, doi:10.2138/am-2015-5232.

Watts, R.B., de Silva, S.L., Jimenez De Rios, G., and Croudace, I., 1999, Effusive eruption of viscous silicic magma triggered and driven by recharge: A case study of the Cerro Chascon-Runtu Jarita Dome Complex in Southwest Bolivia: Bulletin of Volcanology, v. 61, p. 241–264, doi:10.1007/s004450050274.

Wolf, M., Romer, R.L., and Glodny, J., 2019, Isotope disequilibrium during partial melting of metasedimentary rocks: Geochimica et Cosmochimica Acta, v. 257, p. 163–183, doi:10.1016/j.gca.2019.05.008.

Wolff, J.A., Ellis, B.S., Ramos, F.C., Starkel, W.A., Boroughs, S., Olin, P.H., and Bachmann, O., 2015, Remelting of cumulates as a process for producing chemical zoning in silicic tuffs: A comparison of cool, wet and hot, dry rhyolitic magma systems: Lithos, v. 236–237, p. 275–286, doi:10.1016/j.lithos.2015.09.002.

Wolff, J.A., Forni, F., Ellis, B.S., and Szymanowski, D., 2020, Europium and barium enrichments in compositionally zoned felsic tuffs: A smoking gun for the origin of chemical and physical gradients by cumulate melting: Earth and Planetary Science Letters, v. 540, p. 116251, doi:10.1016/j.epsl.2020.116251.

Zou, H., and Reid, M.R., 2001, Quantitative modeling of trace element fractionation during incongruent dynamic melting: Geochimica et Cosmochimica Acta, v. 65, p. 153–162, doi:10.1016/S0016-7037(00)00505-6.

Appendix I: Supplementary Figures and PCA outputs

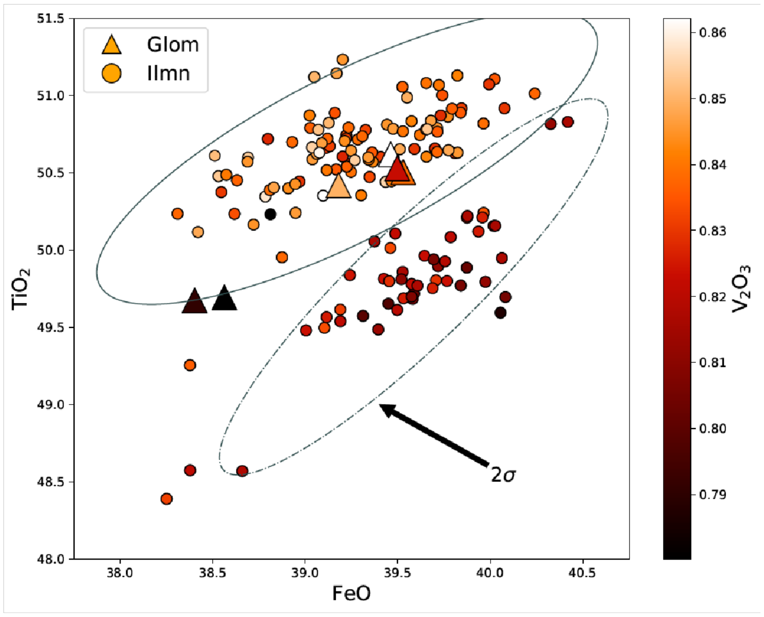

Supplementary Figure S1: Ilmenite compositions from the andesite. X-axis is recalculated ferrous iron content. The ellipse shows a 2SD confidence of data in the low Ti and high Ti group in TiO2-FeO space. V is clearly correlated with an increase in Ti. Glomerocrysts are triangles. All other data are phenocrysts, microphenocrysts, and inclusions in other minerals.

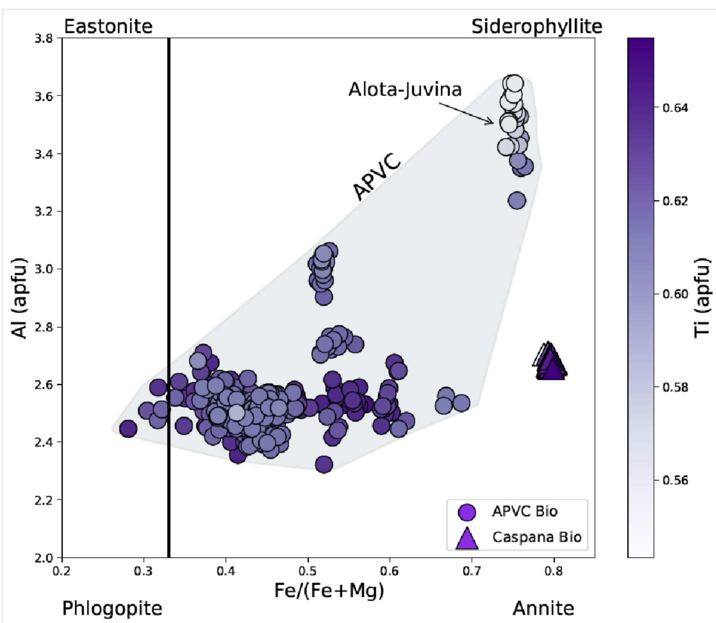

Supplementary Figure S2: Biotite from phase 2 (triangles) and the APVC (gray field, circles) shown using the classification of Deer et al. (1992). All data recalculated assuming 22 oxygens and all Fe as ferrous. Like the Ti-magnetite found in phase 2, biotite from the Caspana also is anomalously high in TiO2 relative to other APVC ignimbrite and has substantially high Fe#. The Alota-Juvina rhyolites that have characteristics similar to phase 2 (Figure 5) crystallized high Fe biotite as well; unlike other APVC rhyolites with lower Fe indices.

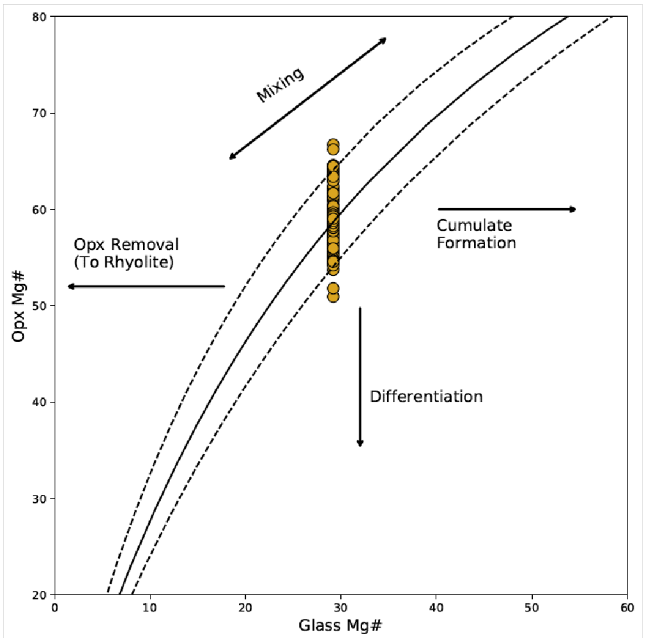

Supplementary Figure S3: Opx Mg# vs. Mg# of rhyodacitic glass on a cation basis (after Rhodes et al., 1979). Glass is average of all analyses and have a range of Mg# 24-35, a similar range to the pumice (Figure 12) with a 1SD of 2.5 from two samples. The sample that contains the lower Mg# is somewhat distinct from the other as noted here and seen clearly in Figure 12.

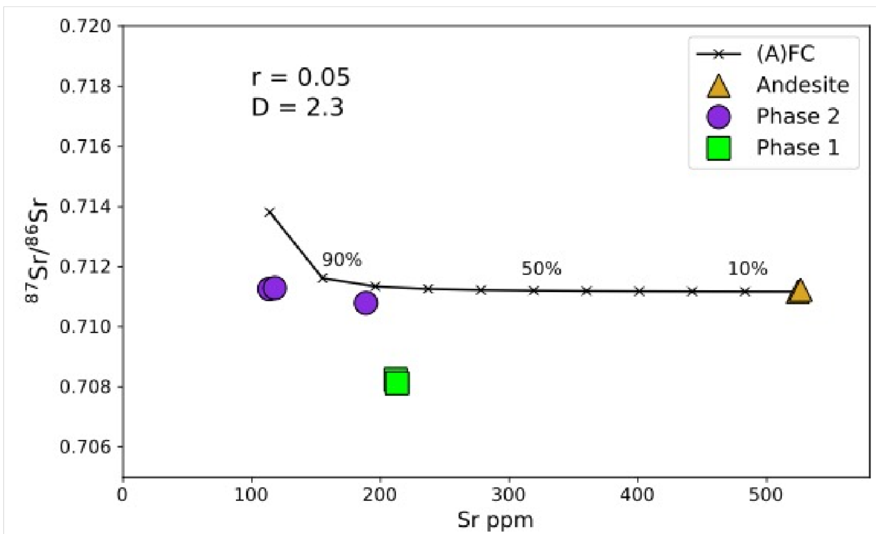

Supplementary Figure S4: 87Sr/86Sr vs Sr concentration of pumices with isotopic evolution model of DePaolo (1981). Model shows that the Phase 2 rhyolite can be derived from the andesite by near closed system fractionation on the basis of isoptic constraints using local basement (Sierra de Moreno) as a possible upper crustal contaminant. Trend requires DSr >1, consistent with upper crustal processes. Phase 1 lies off-trend. Model details can be found in Supplementary Table S8

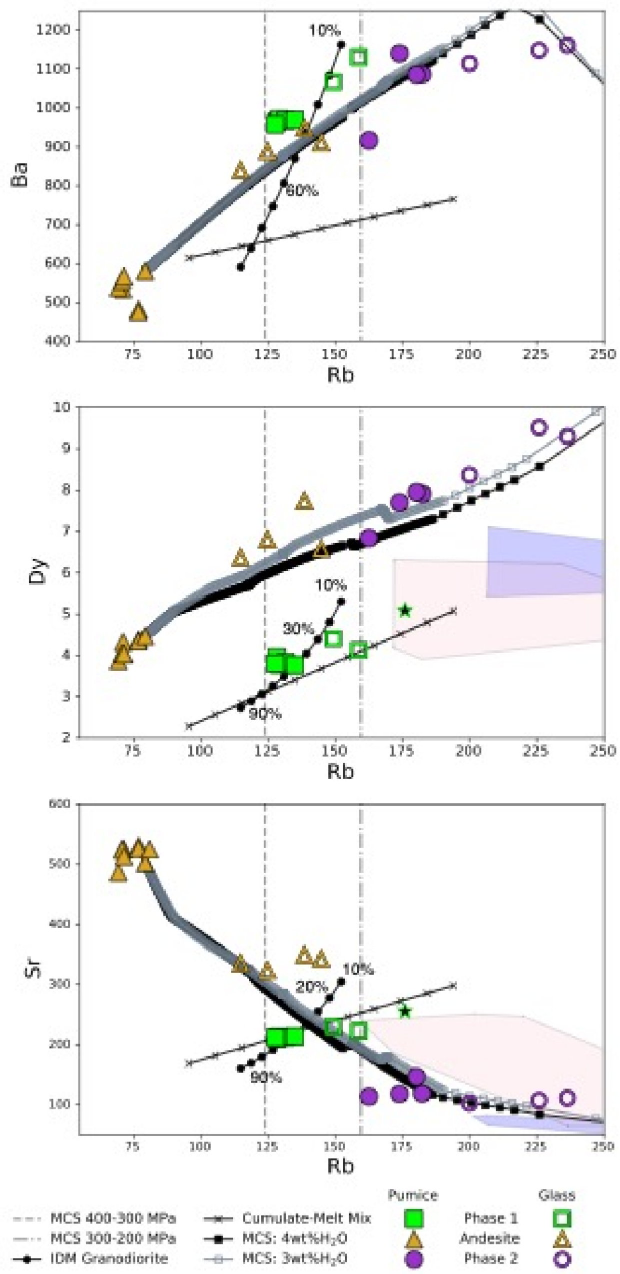

Supplementary Figure S5: Supplement to Figure 11 in the text. Graphs showing additional MCS models, IDM melting models of granodiorite, and a mixing line between cumulate and resident melt (seee text for details). Gray vertical lines show where the MCS models were restarted at a new pressure. The observed assemblage is dominant in the r-MELTS backed models with some caveats described in the text and in this supplementary file.

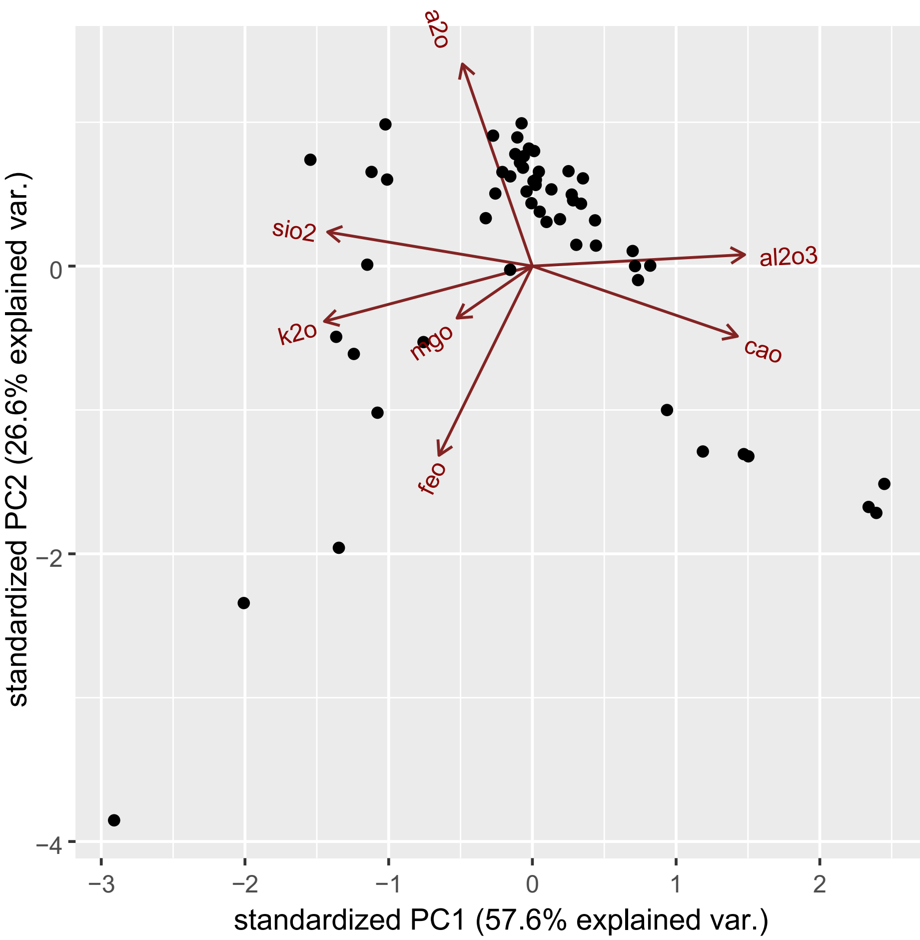

a2o
sio2
al2o3
k2o
mgo
cao
feo
standardized PC2 (26.6% explained var.)
standardized PC1 (57.6% explained var.)
0
−2
−4
−3
−2
−1
0
1
2

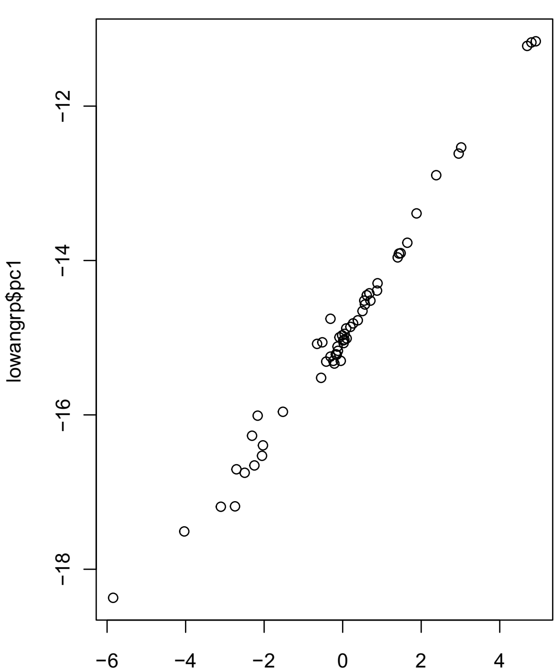

lowangrp$pc1
−12
−14
−16
−18
−6
−4
−2
0
2
4

plagpr$x[, 1]

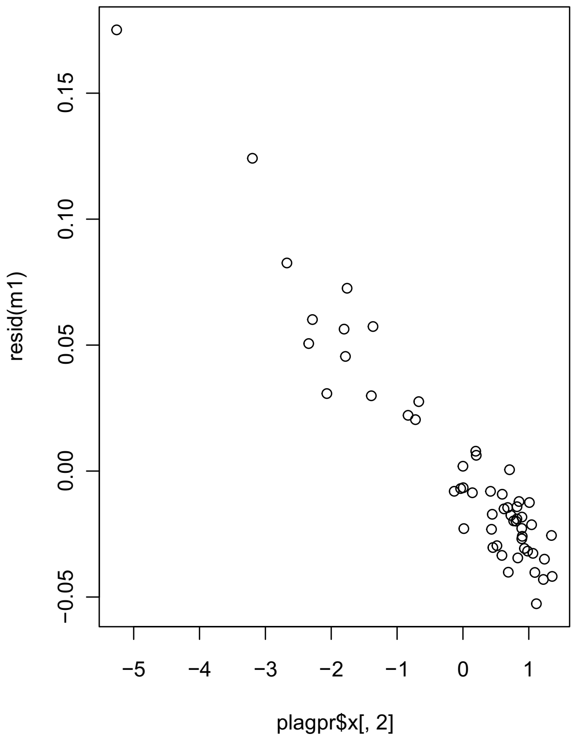
resid(m1)
0.15
0.10
0.05
0.00
−0.05
−5
−4
−3
−2
−1
0
1
plagpr$x[, 2]

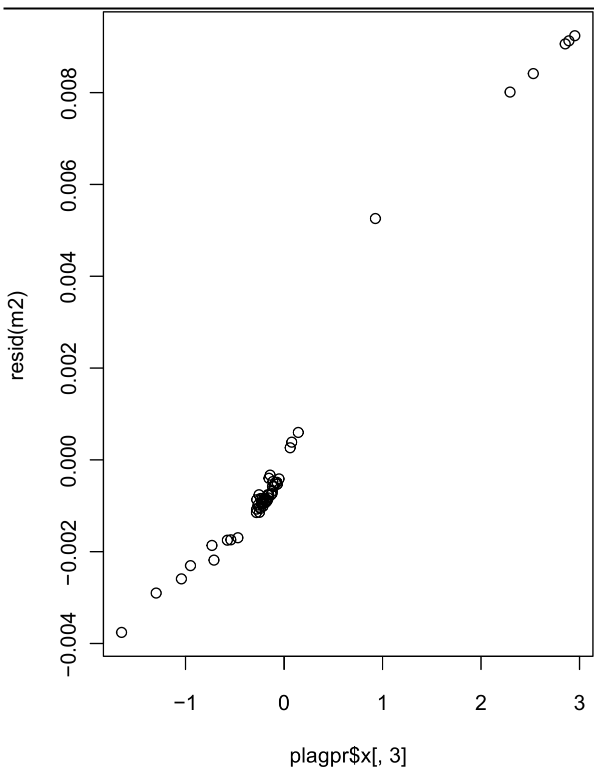
resid(m2)
0.008
0.006
0.004
0.002
0.000
−0.002
−0.004
−1
0
1
2
3
plagpr$x[, 3]

Variables

Loading	cao	k2o	sio2	al2o3	na2o	mgo	feo
PC1	0.468	-0.475	-0.468	0.485	-0.16	-0.172	-0.213
PC2	-0.236	-0.186	0.115	0.038	0.679	-0.175	-0.636
PC3	0.033	-0.093	-0.108	0.075	0.094	0.968	-0.165
PC4	-0.195	0.098	-0.796	-0.55	0.005	-0.05	-0.114
PC5	0.008	0.266	0.187	-0.085	-0.618	-0.008	-0.71
PC6	-0.076	-0.789	0.261	-0.502	-0.226	0.022	0.028
PC7	0.825	0.168	0.137	-0.443	0.267	-0.001	-0.071

Suggested Linear Models

Loading	Model	Tangible Interpretation
PC1	(CaO+Al2O3)/2 - (SiO2+K2O)/2	An Content / Feldpsar Category
PC2	FeO	Trace Element represeting fO2
PC3	MgO	Trace Element representing Magma

Appendix II: Magma Chamber Simulator and r-MELTS Modelling Details

To deal with the 200MPa pressure change (Table 7) the model was run in three steps (following Heinonen et al. (2019)) between 400-200 MPa with a 100MPa change. Assuming that ƒO2 remained more or less constant in the system (e.g Kress and Carmichael, 1991; Grocke et al., 2016), the Fe3+/Fetot was reset to adhere to our estimated value of ΔFMQ-1 (Table 8) at each step. ƒO2 was allowed to equilibrate with temperature change and thus crystallization during each run. The following sequence was followed:

1) Step 1 was done using major elements from one of the andesite samples 2) Step 2 was started using the major element composition that was present at the estimated temperature from the orthopyroxene-liquid (~930°C) in Step 1.

3) Step 3 began where composition was well into the dacite field at temperatures (830 °C) and compositions where the appropriate rhyolite-MELTS model (version 1.1) could be used to model fractionation to rhyolite.

4) For the purposes of keeping plots that compare LLD's in major element space coherent (see below) the beginning of the LLD at 300 and 200 MPa are removed and a full plot is shown below. This initial sequence, removed in Figure 13, is an artifact of resetting Fe2+/Fetot to keep the isobaric computer model in agreement with petrologic observations and our current understanding of oxygen fugacity (e.g., Kress and Carmichael, 1991).

To elaborate, the relationships of P-T-Fe3+/Fetot-ƒO2 is calibrated on thermodynamic and compressibility criteria as follows: Temperature 1/Fe3+/Fetot, Pressure 1/Fe3+/Fetot, and ƒO2 Fe3+/Fetot. So, taking the Fe2O3/FeOtot output from a model of higher pressure and inputting it into a lower pressure isobaric model while keeping ƒO2 constant causes an increase in the Fe3+/Fetot that must be accounted for. At the start of each of these models the FeO content increases until magnetite, usually the first phase on the liquidus, saturates and begins to decrease Fe2O3/FeOtot and FeOtot. The crystallization of magnetite and the decrease in temperature cause the Fe2O3/FeOtot in the MCS models to re-equilibrate back to the values that were present at the end of the preceding MCS model (below). Modal percentages of each of these models are given in Supplementary Table S1.

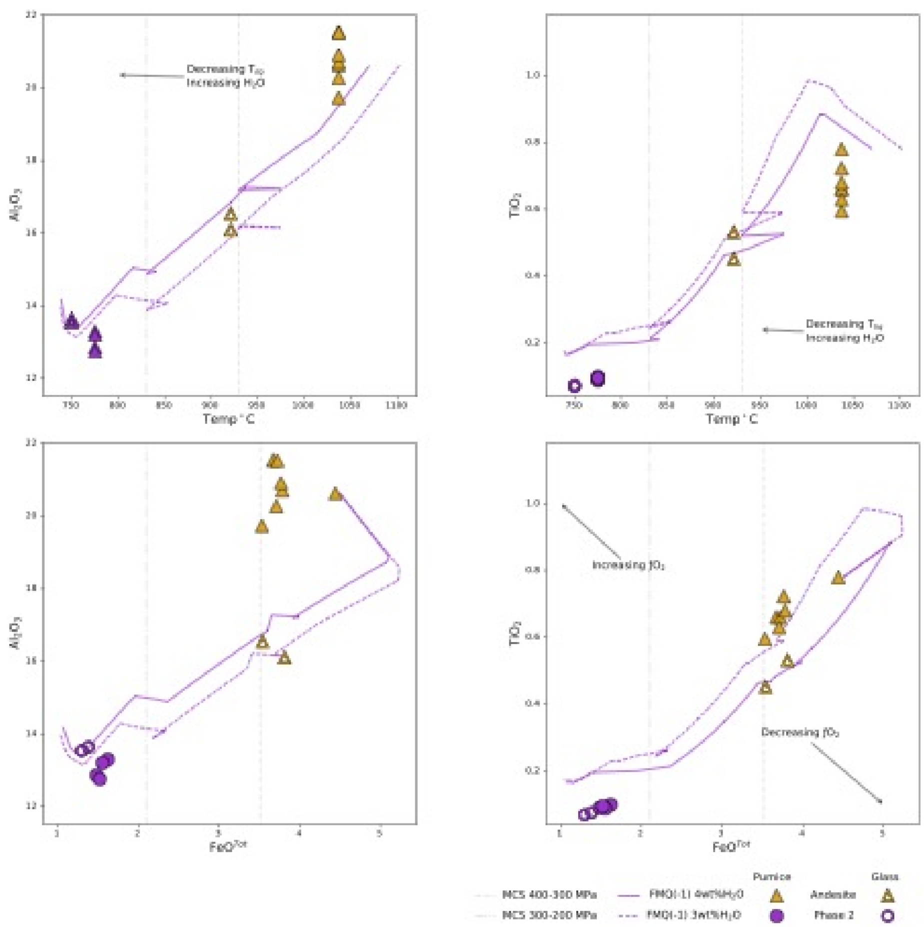

Supplementary Figure S6 showing the LLDs of interest as adjunct to figure 12 in the text. The artifacts of the modelling process that are the result of adhering to well-known geologic processes (i.e., relatively constant fO_2) are shown here. The drastic changes in melt major element content at high degrees of crystallinity in r-MELTS models, which don't seem to be naturally observed in rhyolites (i.e., stark decreases in SiO_2 during crystallization, etc.) are also shown. See Figure 12, Table 9, S9, S10 for further details. Grey vertical lines are as on Figure 11 and 12.

D Values	Opx	Spinel	Feldspar	Rhm-Oxide	Cpx	Qtz	Ol
Sc	4.3/1110/26/740	2.5/1110/10.65/740	0.01/1110/0.466/740	10/1110/18.5/740		0.000001	8.65
V	1.335/1110/5.8/740	31.35/1110/63/740	0.27/1110/0.281/740		3.15/1110/8.25/725	0.000001	0.0000001
Rb	0.01/1110/0.005/740	0.15/1110/0.05/740	0.16/1110/0.02/740	0.01/1110/0.05/740	0.07/1110/0.01/740	0.000001	0.0000001
Sr	0.01/1110/0.008/740	0.11/1110/0.01/740	2.2/1110/6/740	0.01/1110/0.415/740	0.28/1110/0.25/740	0.000001	0.0000001
Y	0.46/1110/0.4/740	0.64/1110/0.09/740	0.066/1110/0.07/740	0.00045/1110/0.09/740	2.4/1110/4.8/740	0.000001	0.0000001
Nb	0.78/1110/0.005/740	0.11/1110/1.2/740	0.0265/1110/0.01/740	4.6/1110/1.2/740	2.1/1110/0.009/740	0.000001	0.0000001
Ba	0.1/1110/0.005/740	0.26/1110/0.005/740	0.27/1110/0.5/740	0.01/1110/0.005/740	0.1/1110/0.01/740	0.000001	0.0000001
La	0.26/1110/10.8/740	0.335/1110/21.5/740	0.2171/1110/0.3/740	0.01/1110/1.31/740	0.28/1110/0.2/740	0.000001	12.19
Ce	0.31/1110/12.3/740	0.27/1110/17.85/740	0.1785/1110/0.2/740	0.01/1110/1.19/740	0.47/1110/0.5/740	0.000001	10.665
Nd	0.049/1110/14/740	0.4/1110/12.5/740	0.09/1110/0.15/740	0.01/1110/0.96/740	0.86/1110/2/740	0.000001	7.385
Sm	0.46/1110/8.985/740	0.42/1110/8.315/740	0.1145/1110/0.1/740	0.01/1110/0.684/740	0.6/1110/4/740	0.000001	4.448
Eu	0.245/1110/3.9/740	0.32/1110/4.05/740	1.12545/1110/4.685/740	0.01/1110/0.4/740	1.1/1110/4.8/740	0.000001	2.945
Dy	0.5485/1110/6.8/740	0.51/1110/0.09/740	0.1515/1110/0.02/740	0.01/1110/0.37/740	1.5/1110/5/740	0.000001	2.1
Yb	0.77/1110/2.1/740	0.49/1110/0.09/740	0.16/1110/0.01/740	0.01/1110/0.55/740	2/1110/3.8/740	0.000001	1.425
Pb	0.29/1110/0.009/740	2.9/1110/0.1/740	0.61/1110/0.4/740	0.1/1110/0.1/740	0.515/1110/0.03/740	0.000001	0.0000001

Format for D values: DAnd / High Temp / DRhy / Low Temp. D values are interpolated at each temperature step between

Mineral/Fluid partition coefficients set to 10000 in appropriate models where fluid exsolved

Apatite and Kspar on the liquidus at the last few temperature steps in the MCS models. Their effect on the liquid composition is negligible and they are ignored

Garnet is set as an excluded phase for all models

Sources - End Temp

	Opx	Spinel	Feldspar	Rhm-Oxide	Cpx	Qtz	Ol
Sc	Sisson (1991)	Mahood and Hildreth (1983)	Padilla and Guala (2016)	Mahood and Hildreth (1983)	Bacon and Druitt (1988)	Assumed	Michael 1988
V	Sisson (1991)	Reid (1983)	Padilla and Guala (2016)	Microprobe / LA-ICPMS	Sisson (1991)	Assumed	Luhr and Carmichael (1980)
Rb	Streck (unpublished)	Streck (unpublished)	Streck (unpublished)	Streck (unpublished)	Streck (unpublished)	Assumed	Assumed
Sr	Streck (unpublished)	Bacon and Druitt (1988)	Streck (unpublished)	Bacon and Druitt (1988)	Streck (unpublished)	Assumed	Assumed
Y	Streck (unpublished)	Streck (unpublished)	Streck (unpublished)	Streck (unpublished)	Streck (unpublished)	Assumed	Assumed
Nb	Streck (unpublished)	Streck (unpublished)	Streck (unpublished)	Streck (unpublished)	Streck (unpublished)	Assumed	Assumed
Ba	Streck (unpublished)	Streck (unpublished)	Streck (unpublished)	Streck (unpublished)	Streck (unpublished)	Assumed	Assumed
La	Mahood and Hildreth (1983)	Mahood and Hildreth (1983)	Streck (unpublished)	Mahood and Hildreth (1983)	Streck (unpublished)	Assumed	Mahood and Hildreth (1983)
Ce	Mahood and Hildreth (1983)	Mahood and Hildreth (1983)	Streck (unpublished)	Mahood and Hildreth (1983)	Streck (unpublished)	Assumed	Mahood and Hildreth (1983)
Nd	Mahood and Hildreth (1983)	Mahood and Hildreth (1983)	Streck (unpublished)	Mahood and Hildreth (1983)	Streck (unpublished)	Assumed	Mahood and Hildreth (1983)
Sm	Mahood and Hildreth (1983)	Mahood and Hildreth (1983)	Streck (unpublished)	Mahood and Hildreth (1983)	Streck (unpublished)	Assumed	Mahood and Hildreth (1983)
Eu	Mahood and Hildreth (1983)	Mahood and Hildreth (1983)	Streck and Grunder (1997)	Mahood and Hildreth (1983)	Streck (unpublished)	Assumed	Mahood and Hildreth (1983)
Dy	Mahood and Hildreth (1983)	Streck (unpublished)	Bachman et al. (2005)	Mahood and Hildreth (1983)	Streck (unpublished)	Assumed	Mahood and Hildreth (1983)
Yb	Mahood and Hildreth (1983)	Streck (unpublished)	Bachman et al. (2005)	Mahood and Hildreth (1983)	Streck (unpublished)	Assumed	Mahood and Hildreth (1983)
Pb	Streck (unpublished)	Streck (unpublished)	Streck (unpublished)	Streck (unpublished)	Streck (unpublished)	Assumed	Assumed

Sources - Start Temp

	Opx	Spinel	Feldspar	Rhm-Oxide	Cpx
Sc	Bacon and Druitt (1988)	Luhr and Carmichael (1980)	Bacon and Druitt (1988)	Bacon and Druitt (1988)	Bacon and Druitt (1988)
V	Luhr and Carmichael (1980)	Luhr and Carmichael (1980)	Luhr and Carmichael (1980)	Microprobe / LA-ICPMS	Luhr and Carmichael (1980)
Rb	Bacon and Druitt (1988)	Ewart and Griffin (1994)	Ewart and Griffin (1994)	Bacon and Druitt (1988)	Philpotts and Schnetzler (1970)
Sr	Bacon and Druitt (1988)	Ewart and Griffin (1994)	Nagasawa (1973)	Bacon and Druitt (1988)	Ewart and Griffin (1994)
Y	Ewart and Griffin (1994)	Ewart and Griffin (1994)	Ewart and Griffin (1994)	Nielsen et al. (1992)	Ewart and Griffin (1994)
Nb	Ewart and Griffin (1994)	Nielsen and Beard (2000)	Dunn and Sen (1994)	Green and Pearson (1987)	Ewart and Griffin (1994)
Ba	Bacon and Druitt (1988)	Luhr and Carmichael (1980)	Bacon and Druitt (1988)	Bacon and Druitt (1988)	Bacon and Druitt (1988)
La	Bacon and Druitt (1988)	Luhr and Carmichael (1980)	Fujimaki et al. (1984)	Bacon and Druitt (1988)	Bacon and Druitt (1988)
Ce	Bacon and Druitt (1988)	Luhr and Carmichael (1980)	Fujimaki et al. (1984)	Bacon and Druitt (1988)	Bacon and Druitt (1988)
Nd	Schnetzler and Philpotts (197)	Luhr and Carmichael (1980)	Fujimaki et al. (1984)	Bacon and Druitt (1988)	Nicholls and Harris (1980)
Sm	Bacon and Druitt (1988)	Luhr and Carmichael (1980)	Schnetzler and Philpotts (197)	Bacon and Druitt (1988)	Bacon and Druitt (1988)
Eu	Luhr and Carmichael (1980)	Luhr and Carmichael (1980)	Fujimaki et al. (1984)	Bacon and Druitt (1988)	Bacon and Druitt (1988)
Dy	Schnetzler and Philpotts (197)	Luhr and Carmichael (1980)	Schnetzler and Philpotts (197)	Bacon and Druitt (1988)	Luhr and Carmichael (1980)
Yb	Bacon and Druitt (1988)	Luhr and Carmichael (1980)	Reid (1983)	Bacon and Druitt (1988)	Luhr and Carmichael (1980)
Pb	Dunn and Senn (1994)	Luhr and Carmichael (1980)	Ewart and Griffin (1994)	Streck (unpublished)	Ewart and Griffin (1994)

Inputs for Models in Figure 13

	2 wt% H2O			3 wt%			4 wt%		
r-MELTS version	1.2	1.2	1.1	1.2	1.2	1.1	1.2	1.2	1.1
P (MPa)	400	300	200	400	300	200	400	300	200
T start	1100	950	875	1100	950	856	1100	980	846
T End	760	750	740	760	750	740	760	748	740
T increment	2	2	2	2	2	2	2	2	2
T stop*	930.43	830.41	-	930.15	830.22	-	929.92	830.92	-
fO_2	ΔFMQ (-1)	ΔFMQ (-1)	ΔFMQ (-1)	ΔFMQ (-1)	ΔFMQ (-1)	ΔFMQ (-1)	ΔFMQ (-1)	ΔFMQ (-1)	ΔFMQ (-1)
SiO2	57.87	66.45	70.24	57.31	64.09	68.02	56.76	62.13	66.51
TiO2	0.76	0.65	0.31	0.76	0.56	0.25	0.75	0.50	0.20
Al2O3	20.21	14.39	12.43	20.02	15.38	13.28	19.82	16.27	13.86
Fe2O3	0.57	0.45	0.30	0.56	0.47	0.33	0.56	0.49	0.34
Cr2O3	0.00	0.00	0.00	0.00	0.00	0.00	0.00	0.00	0.00
FeO	3.84	2.93	1.75	3.81	3.11	1.90	3.77	3.28	1.92
MnO	0.07	0.13	0.16	0.07	0.12	0.14	0.07	0.10	0.13
MgO	2.18	0.60	0.24	2.15	0.87	0.37	2.13	1.13	0.44
NiO	0.00	0.00	0.00	0.00	0.00	0.00	0.00	0.00	0.00
CoO	0.00	0.00	0.00	0.00	0.00	0.00	0.00	0.00	0.00
CaO	7.80	4.03	3.04	7.73	4.25	3.00	7.65	4.51	2.89
Na2O	2.52	2.28	1.83	2.49	2.63	2.32	2.47	2.77	2.58
K2O	1.98	3.85	4.69	1.96	3.33	4.17	1.94	2.93	3.86
P2O5	0.24	0.47	0.58	0.23	0.40	0.51	0.23	0.35	0.47
H2O	1.96	3.78	4.44	2.91	4.78	5.70	3.85	5.53	6.81
Modal Percentages from r-MELTS outputs									
Plag	80	78	32	78	78	35	75	77	43
Mag	17	4	1	2	4	1	2	3	1
Opx	2	15	2	17	16	3	16	18	6
Cpx	1	3	5	3	-	1	7	-	-
Ilm	-	-	1	1	3	0	-	2	0
Fay	-	-	1	-	-	1	-	-	1
Qtz	-	-	38	-	-	32	-	-	28
San	-	-	19	-	-	26	-	-	21
Apa	-	-	-	-	-	0	-	-	-

**Temperature at which the output was taken for the next step. Modal percentages correspond to this temperature*

		wt%			wt% H2O			wt%
1.2	1.2	1.1	1.2	1.2	1.1	1.2	1.2	1.1
400	300	200	400	300	200	400	300	200
1100	950	846	1160	950	860	1050	950	860
760	748	740	800	800	740	800	800	740
2	2	2	5	5	5	5	5	5
930.77	831.04	-	931.83	832.5	-	929.73	829.23	-
ΔFMQ (-1)	ΔFMQ (-1)	ΔFMQ (-1)	NNO	NNO	NNO	NNO	NNO	NNO
56.22	60.65	66.05	59.23863737	67.58679383	71.53611857	57.54596588	61.73536598	66.14
0.74	0.40	0.19	0.617279959	0.710481669	0.334840695	0.59964194	0.376727548	0.21
19.63	16.74	14.01	19.86427146	13.68845794	11.50647104	19.29667425	16.0084695	13.47
0.55	0.51	0.34	0.720946478	0.639672866	0.367103449	0.723355365	0.722145056	0.44
0.00	0.00	0.00	0	0	0	0	0	0.00
3.73	3.38	1.93	2.984128769	2.102353746	0.987580582	2.87815715	2.467938935	1.28
0.07	0.09	0.13	0.059704127	0.11119203	0.131373759	0.057998155	0.079077397	0.10
2.11	1.36	0.47	1.791123815	0.686309862	0.346167351	1.739944647	1.394259693	0.69
0.00	0.00	0.00	0	0	0	0	0	0.00
0.00	0.00	0.00	0	0	0	0	0	0.00
7.58	4.84	2.84	7.690701127	4.025805788	3.049318303	7.470948765	4.743167448	3.01
2.45	2.78	2.70	2.732222769	2.393419671	1.894481351	2.654152851	2.904255246	2.83
1.92	2.68	3.74	2.155420184	3.972053895	4.824298091	2.093831693	2.834080629	3.70
0.23	0.32	0.45	0.186195922	0.354369937	0.435839668	0.180875602	0.246614254	0.32
4.76	6.24	7.14	1.959368022	3.729088772	4.586407149	4.758453703	6.487898314	7.80
73	76	55	84	80	18	80	77	39
2	3	1	2	5	<1	3	5	1
14	20	8	13	11	-	10	16	3
11	-	-	<1	-	5	7	2	3
-	1	<1	<1	4	<1	-	<1	<1
-	-	<1	-	-	<1	-		-
-	-	24	-	-	39	-	-	28
-	-	12	-	-	36	-	-	24
-	-	-	-	-	<1	-	-	-

Appendix III: Supplementary Field Descriptions

The Caspana ignimbrite, crops out in the Toconce-Caspana area of N. Chile (de Silva, 1989; de Silva, 1991; Figure 1,2). The age of the eruption is bracketed stratigraphically between 4.09 and 4.54 Ma. It's source vent(s) is/are thought to be buried beneath the younger Toconce and Leon volcanoes. de Silva (1991) found that the ignimbrite was bimodal containing both andesitic and rhyolitic juvenile clasts, defining a large compositional gap. On the basis of reconnaissance bulk and mineral chemistry, an origin of the rhyolite by fractional crystallization of the andesite was proposed to have led to a small bimodal, zoned magma chamber. We have resampled and reexamined the same exposures and sections introduced in de Silva (1991). The northern outcrops above the community of Toconce contain a rhyolitic plinian fallout of nearly aphyric pumice with occasional phenocrysts of feldspar in hand specimen (Section B - Figure 2). There is a fine ash on top of the fallout, that is in turn overlain by a distinct ~10 to 40cm flow unit that contains equally aphyric rhyolite. This sequence is collectively referred to as Phase 1. Above this lies several meters of massive ignimbrite that is referred to herein as Phase 2. Phase 2 also contains rhyolitic pumice. However, these are distinct from the pumice in Phase 1 as they have obviously higher, yet still very low crystallinity (~3-5%) and are substantially less fragile in hand-sample. Phenocrysts in pumice from Phase 2 include plagioclase and biotite, with occasional yellow-green olivine. The top of the section is eroded and has lava and colluvium from Volcan Toconce on top. Between this location and the community of Toconce, the ignimbrite fills deep narrow canyons carved into the underlying Toconce formation (5.56 – 6.65 Ma). Throughout this area a distinct orange hue dominates the ignimbrite.

To the south of Toconce, around Caspana and to the south and east, the Caspana Ignimbrite is capped by the extensive 4.09 Ma Puripicar ignimbrite. These outcrops contain a more complete section of dominantly Phase 2. The upper parts of the stratigraphy record the appearance of andesite pumice. At the distal flow front (Figure 2, Section A), a basal ash (equivalent to the basal Plinian in Section B) is overlain by a thin 5-10 cm reworked layer above which lies ~ 5 meters of massive ignimbrite. The center of the massive unit includes a crudely laminated facies that contains rhyolitic pumice with a higher crystal content of up to 5 volume %. Several pumice rafts attest to progressive aggradation of the deposit in several pulses. These rafts contain successively more andesitic clasts up-sequence. At the clast-rich flow front rhyolite and andesite pumice are largely mixed together with only hints of any internal stratigraphy (Figure 2).

The andesitic pumice in the Phase 2 ignimbrite has variable crystallinity from sample to sample that ranges from 20-45%. In hand-sample the pumice has plagioclase, orthopyroxene, and oxides readily identifiable. Andesite pumice textures vary from highly oxidized, lower crystallinity porphyritic pumices found in the upper flow unit to glomeroporphyritic, higher crystallinity black to gray pumices in the lower flow unit. These latter pumices can occur in the upper flow unit but not nearly as often and are more vesiculated than their counterparts, with round to oblate vesicles.

In the distal outcrops south of Caspana, a thick sequence of lake sediments occurs between the Caspana and the overlying Puripicar ignimbrite. Significant penetration of carbonate veins and coatings were seen in some of the distal outcrops. We were careful in our selection of pumice samples and treated them accordingly (see text).

Appendix IV: IDM Modelling Details / IDM and Mixing Tables

The incongruent dynamic melting (IDM) equations of Zou and Reid (2001) allot the calculation of residual melt in a scenario where minerals in the protolith contribute to both melt and new minerals formed during reaction. The appendix of Zou and Reid (2001) highlights the mass balance and necessary calculations well and there is an example provided in table S10. D values and proportions of minerals taking place in the melting reaction in this example are assumed constant in order to honor the least squares modelling. To the authors knowledge, there are no well tested models regarding the porosity (Φ) at which melt begins migrating in an upper crustal granitoid, but mantle values are known to be quite low and that is adopted here. The plethora of upper crustal xenoliths with small porosities that erupt with silicic magmas supports the assumed value (0.001) in the equation. Changing the value up to 10%, where buoyancy differences would certainly begin occurring, have negligible effects on the result. As noted in the text, the hypothetical protolith used is a granitoid that is typical of APVC magmatism and was shown to be co-genetic with the erupted dacite in which it was found

(Watts et al., 1999; Kaiser, 2014; Kaiser et al., 2017). The modal proportion of minerals in the protolith, required for the bulk partitioning as the protolith minerals are introduced to melt, is taken from Kaiser (2014). The modal proportion of the minerals introduced into melt and new minerals is estimated from least squares (Carr and Gazel, 2017).

The new minerals created during the melting reaction and reaction abundances are inferred from a variety of prior works. First, melting granodiorites and tonalites produces plagioclase with An contents similar to the phase 1 plagioclase that clearly has a prolonged history dur to slight unmixing (verified by spot analysis; Figure 3) in the experiments of Patino-Douce (1995). The melt fractions produced are quite high (20-40%) at low pressure and temperatures are within range of the andesite. However, these experiments were run 1 log unit below the FMQ buffer and produced Opx > Cpx. This is not in agreement with APVC magmas nor is it in agreement with the geochemical signature in phase 1 (Figure 6). We can argue based on prior works and, somewhat ironically, the MCS models for the andesite-phase 2 lineage to say that higher $fO2$ will produce Cpx > Opx, especially if the rhyolite was at fluid saturation (also seen in r-MELTS models) and was releasing its fluids into surrounding wallrock by Darcy flow. Additional melting experiments on synthetic biotite gneiss are also enlightening and produce high melt fraction, peraluminous rhyolites at temperatures and pressures relevant in this study (Patino Douce and Beard, 1995). These experiments also produced opx > cpx, though the starting phase assemblage does not have amphibole nor clinopyroxene, both of which are abundant in the APVC. Nevertheless, the inferred masses for melt fraction vs residuum here is in agreement with these experiments as well as others (see Benito-Garcia and Lopez-Ruiz, 1992) and geochemical relationships (Reid, 1983) support these masses for the upper crustal reaction here.

Regarding the specific minerals produced, the presence of titanite in phase 1 and the xenoliths found give leverage on the ability to infer what they may be, as does geochemistry (Figure 6). Titanite stability is relatively low in temperatures (Wones, 1989; Xirouchakis and Lindsley, 1998) and often involves clinopyroxene and amphibole during an ox-redox reaction. During heating and the introduction of water through dehydration of biotite and amphibole +/- fluid from the sub-adjacent reservoir, the reaction would proceed through clinopyroxene to titanite favored in the experiments of Xirouchakis and Lindsley (1998) if fugacity is the same; which it probably is not and that is again acknowledged here.

Parent	**Sample**	**SiO2**	**TiO2**	**Al2O3**	**FeO**	**MnO**	**MgO**	**CaO**	***10***	**Na2O**	**K2O**	**P2O5**	**NiO**	**Cr2O3**
Daughter	**BOL12017A** 69.89 0.39 15.2 **CH19C009** 73.6 0.2 15.78				2.51	0.05	1.01	2.48		3.24	5.13	0.1	0	0
	Quartz	100	0	0	1.33	0.09	0.3	1.42		3.18	4.05	0.05	0	0
	Magnetite	0	0	0	0	0	0	0		0	0	0	0	0
	Kspar	64.51	0	19.55	100	0	0	0		0	0	0	0	0
	Plag	58.88	0	26.64	0.06	0	0	0.17		2.2	13.15	0	0	0
	Biotite	37.05	4.05	13.81	0	0.17	0	0		7.51	6.66	0.69	0	0
	Hornblende	44.92	1.23	8.63 *Default wt.*	0	17.58	0.26	13.2		0.04	0.33	9.25	0	0
	was used for the igpet model. NiO and Cr2O3 are ignored				0	16.64	0.64	11.89		11.97	1.36	1.1	0	0

	SiO2	**TiO2**	**Al2O3**	**FeO**	**MnO**	**MgO**	**CaO**	**Na2O**	**K2O**	**P2O5**	**NiO**	**Cr2O3**
Calc	70	0.23	15.69	2.53	0.07	1.05	2.47	2.88	5.05	0.02	0	0
Diff*wt	0.04	0.17	0.24	0.02	0.02	0.04	0.01	0.36	0.07	0.08	0	0
ΣR^2	0.236											
F	0.353											

Mineral	**Mode from LSQ**	**Mode in source**	Mode Obeying Products
Quartz	23	11	34.96
Magnetite	1.1	2	1.672
Kspar 38 36 57.76 **Plag** 26.4 36 40.128			
Biotite	3.3	10	5.016
Hornblende	8.3	5	12.616
	100	100	152.152

Input Trace Elements and D Values and IDM Setup

Example for Rb

Assuming the Reaction: Modal minerals -> 1.0 melt + 0.02 titanite + 0.5 Cpx (Assumptions 3-5)

Steps	***6***	***7***		***8***			***9***				***11***	***12***
	p_i	**Σalpha^**	**t_{liq}**	**t_{ttn}**	**t_{cpx}**	**D values**	**Σbeta ti*Ki**	**Di**	**D0**	**pi* Ki**	**theta + pialpha)**	**Q0**
Quartz	0.23	0.621	1.610305958	0.032206119	0.805152979	1E-10	0.008534622	1.1E-11		2.3E-11	0.56557	0.406287165
Magnetite	0.011					0.05		0.001	1.0396	0.00055		
Kspar	0.38					0.7		0.252		0.266		
Plag	0.264					0.235		0.0846		0.06204		
Biotite	0.033					6.98		0.698		0.23034		
Hornblende	0.083					0.08		0.004		0.00664		
Titanite						0.015				0		
Cpx						0.01						

13			***14***	***15***
Φ	**Source [Rb]**	**F**	**X**	**[Rb] liq**
0.001	163	1	1	114.8541842
		0.9	0.8998999	118.7734186
		0.8	0.7997998	122.7559712
		0.7	0.6996997	126.8004562
		0.6	0.5995996	130.9055778
		0.5	0.499499499	135.0701209
		0.4	0.399399399	139.2929424
		0.3	0.299299299	143.5729644
		0.2	0.199199199	147.9091676
		0.1	0.099099099	152.3005866

^Minerals thought to be taking place in reaction

D values

	Rb	**Y**	**La**	**Sr**	**Ba**	**Eu**	**Dy**	**Yb**	**Sm**	**V**
Quartz	1E-10	1E-10	1E-10	1E-10	1E-10	1E-10	1E-10	1E-10	1E-10	1E-10
Magnetite	0.05	0.03	0.22	0.01	0.005	0.13	0.09	0.09	0.1	130
Kspar	0.7	0.05	0.138	0.77	1	2.33	0.77	0.64	0.42	0.22
Plag	0.235	0.02	0.307	1.25	0.19	2	0.07	0.07	0.1	0.281
Biotite	6.98	0.03	0.021	0.6	0.59	0.05	0.02	0.12	0.01	79.5
Hornblende	0.08	4	1.04	0.442	0.08	4.8	11	3.3	8.1	31
Titanite 0.015 344 **Cpx** 0.01 4.8			75	0.904	0.01	6.85	5.33	183	20.4	214
			0.2	3.285	0.01	4.8	5	3.8	3.6	14

Source Concentrations

	Rb	**Y**	**La**	**Sr**	**Ba**	**Eu**	**Dy**	**Yb**	**Sm**	**V**
[]	163	29.12	34.36	273	613	0.83	5.08	2.49	5.68	85
Sample^	CC9317a	JFKBOL12-017B	JFKBOL12-017B	JFKBOL12-017A	CC9317	JFKBOL12-024B	CC9317	CC9317	CC9317	CC9317

^All samples are plutonic clasts analyzed by Kaiser (2014), Kaiser et al. (2017), or Watts et al. (1999)

	Rb	**Y**	**La**	**Sr**	**Ba**	**Eu**	**Dy**	**Yb**	**Sm**	**V**
Quartz	Assumed	Assumed	Assumed	Assumed	Assumed	Assumed	Assumed	Assumed	Assumed	Assumed
Magnetite	Streck (unpublished)	Bachman et al. (2005)	Streck and Grunder (1997)	Bacon and Druitt (1988)	Streck (unpublished)	Streck and Grunder (1997)	Streck (unpublished)	Streck (unpublished)	Bachman et al. (2005)	Reid (1983)
Kspar	Bachman et al. (2005)	Streck (unpublished)	Streck (unpublished)	Bea et al. (1994)	Mahood and Hildreth 1983	Padilla and Gualda (2016)	Bea et al. (1994)	Bea et al. (1994)	Bea et al. (1994)	Bea et al. (1994)
Plag	Streck and Grunder (1997)	Bachman et al. (2005)	Padilla and Gualda (2016)	Bea et al. (1994)	Bea et al. (1994)	Assumed	Streck (unpublished)	Streck (unpublished)	Bachman et al. (2005)	Padilla and Gualda (2016)
Biotite	Bea et al. (1994)	Streck unpub	Padilla and Gualda (2016)	Streck (unpublished)	Bea et al. (1994)	Bea et al. (1994)	Streck (unpublished)	Bea et al. (1994)	Bachman et al. (2005)	Bea et al. (1994)
Hornblende	Streck (unpublished)	Streck (unpublished)	Padilla and Gualda (2016)	Padilla and Gualda (2016)	Bachman et al. (2005)	Streck (unpublished)	Padilla and Gualda (2016)	Streck (unpublished)	Padilla and Gualda (2016	Padilla and Gualda (2016)
Titanite	Padilla and Gualda (2016)	Padilla and Gualda (2016)	Padilla and Gualda (2016)	Padilla and Gualda (2016)	Bachman et al. (2005) Streck (unpublished)	Tiepolo et al. (2002)	Tiepolo et al. (2002)	Padilla and Gualda (2016	owatke and Klemme (200	Padilla and Gualda (2016)
Cpx	Streck (unpublished)	Streck (unpublished)	Streck (unpublished)	Sisson (1991)		Streck (unpublished)	Streck (unpublished)			
								Streck (unpublished)	Sisson (1991)	Sisson (1991)

The trace element modelling used for the phase 1 rhyolite consists of least squares modelling (LSQ; Carr and Gazel, 2017) and the incongruent dynamic melting equations of Zou and Reid (2001). The steps to do this are given as follows and equations from Zou and Reid (2001) are noted in the table to the left. The reader is encouraged to explore the appendix as well.

1. Use the fractional crystallization model in the program Igpet to estimate the modal proportion of minerals required to go from the major element composition of the granodioritic protolith (Watts et al., 1999; Kaiser et al., 2017) to the observed major element composition of phase 1.
   - This is a fractional crytallization model and the resulting F is the amount of melt left over. Equivalently, the amount of minerals required to go from the 'parent' to the 'daughter' is 1-F. The F value in the melting models described by Zou and Reid (2001) is the degree of melting (i.e., proportion of minerals added to melt). Because of this, the correct F in the models below are 1-F in the mass balance obtained from least squares.
   - This modal proportion is considered the modal proportion of minerals introduced to melt, not the mineralogy of the protolith (see below).

2. Estimate a modal proportion of the protolith. This was estimated in thin section by Kaiser (2014).

3. Model Assumptions - Minerals: Titanite was found in mineral separates and there are marked HFSE depletions in agreement with clinopyroxene being in the residuum. Clinopyroxene is apparently frequently involved in titanite formation (Wones, 1989; Xirouchakis and Lindsley, 1988) and melting experiments on granodiorites and tonalites frequently have clinopyroxene in the residuum (Patino-Douce, 1995; Patino-Douce and Beard, 1995). This is also the dominant pyroxene in APVC dacites. These are considered to be products in the reaction along with melt.

4. Model Assumptions - Proportions: There is agreement in low melt:residuum masses found in natural settings, with proportions of residuum often being >0.6 (for example: Reid, 1983). These proportions are also reflected in the experimental work cited above. Here we have assumed abundant melt:residuum of 1:0.52 (~65% melt) based on phase diagrams as lower pressure seems to give more melt at the temperatures of interest here in the experiments above and the requirement for eruptible volumes to be created. The modal proportions of minerals from the least squares models are considered to be the reactant minerals, which is not the same as the protolith.

5. Model Assumptions - Equations: The equations of Zou and Reid (2001) can accomadate changing D values and a changing mass fraction of the i'th mineral. D values are assumed to be constant here and mass fraction of minerals contributed to the melt is assumed not to change during melting.

6. Calculate p_i: The modal propotions estimated by LSQ must be multiplied by 1.52 to obey the sum of the products of (1.0 melt + 0.5 cpx + 0.02 titanite). Renormalizing for the calculation, however, puts everything back on a scale of 100.

7. Calculate $\sum_\alpha p_i$: Sum the modal proporiton of incongruent (contriubting to both melt and product minerals). K-feldspar is not considered to contribute to product minerals. Plagioclase is considered to contribute to product minerals due to the high CaO content that would contribute to Cpx.

8. Calculate t_i and t_l : Mass fractions of incongruent minerals converted to product mineral i and liquid, respectively.

9. Calculate $\sum_\beta t_i K_i$: This is effectively the bulk distribution coefficient of the product minerals

10. Calculate D_0: The ever familiar bulk distribution coefficient of the protolith before melting and melt extraction. This is why you need to know the modal proportion in the protolith.

11. Calculate $\sum_\alpha t_i K_i$: The effective bulk D of minerals contributing to product melt once melting has initiated. This is P_0

12. Calculate Q_0: This is the key parameter in differentiating congruent and incongruent dynamic melting. If $Q_0 = P_0$, we arrive at equations describing congruent melting.

13. Find Φ. This is the value for porosity in the protolith as melting is occurring. This value is more studied for the mantle and there are no well tested estimates for average porosites of upper crustal protoliths. However, it seems that the plethora of xenoliths that are erupted with silicic magmas, such as those from which the composition was used as starting material here, are quite low. As such, we assume that melt is able to begin migrating at relatively low porosity so long as the dihedral angle allots this. We thus follow Zou and Reid (2001) and others in assuming 0.001.

14. Calculate X: This is the amount of melt allotted to be extracted and is related to F (the degree of melting) by Φ.

15. and finally, C_L: The concentration of trace element *i* in the extracted melt.

Fractional (Disequilibrium) Melting Model

	proportion	D_i								
qtz	30.9	1.00E-10	1.00E-10	1.00E-10	1.00E-10	1.00E-10	1.00E-10	1.00E-10	1.00E-10	1.00E-10
mag		0.05	0.09	0.22	0.01	0.005	0.13	0.09	0.09	0.11
kspar	15	0.391	0.05	0.082	5.6	1	2.33	0.024	0.02	0.02
plag	40	0.018	0.011	0.3	6	0.5	3.36	0.07	0.07	0.1
bio	13.1	1.57	0.047	0.021	0.307	0.59	0.15	0.02	0.04	0.01
hbl	33.2	0.012	4	1.04	0.442	0.08	4.8	4.8	4.6	4
	0.309	3.09E-11	3.09E-11	3.09E-11	3.09E-11	3.09E-11	3.09E-11	3.09E-11	3.09E-11	3.09E-11
	0	0.00E+00	0.00E+00	0.00E+00	0.00E+00	0.00E+00	0.00E+00	0.00E+00	0.00E+00	0.00E+00
	0.15	5.87E-02	7.50E-03	1.23E-02	8.40E-01	1.50E-01	3.50E-01	3.60E-03	3.00E-03	3.00E-03
	0.4	7.20E-03	4.40E-03	1.20E-01	2.40E+00	2.00E-01	1.34E+00	2.80E-02	2.80E-02	4.00E-02
	0.131	2.06E-01	6.16E-03	2.75E-03	4.02E-02	7.73E-02	1.97E-02	2.62E-03	5.24E-03	1.31E-03
	0.332	3.98E-03	1.33E+00	3.45E-01	1.47E-01	2.66E-02	1.59E+00	1.59E+00	1.53E+00	1.33E+00
D_bulk		2.76E-01	1.35E+00	4.80E-01	3.43E+00	4.54E-01	3.31E+00	1.63E+00	1.56E+00	1.37E+00
C_0		163	27.13	34.36	354	613	0.81	5.08	2.49	5.68

F Rb Y La Sr Ba Eu Dy Yb Sm

1 0.5 0.00#DIV/0! 0.00#DIV/0! 0.00#DIV/0!#DIV/0!#DIV/0!#DIV/0!
0.9 0.45 1.39 36.43 5.92 527.58 84.56 1.22 7.58 3.65 7.73 0.8 0.4
8.59 30.48 12.54 322.93 194.73 0.75 5.81 2.84 6.41 0.7 0.35 24.95 27.47
19.45 242.32 317.20 0.57 4.97 2.46 5.74 0.6 0.3 53.16 25.51 26.54 197.66
448.41 0.46 4.44 2.22 5.31 0.5 0.25 95.60 24.09 33.79 168.77 586.54 0.40
4.08 2.04 5.00

0.4	0.2										
154.41	22.98	231.59	22.09	48.63	132.98	879.31	0.31	3.58	1.81	4.56	
41.16	148.32										
730.44	0.35	3.80	1.91	4.75							
0.3	0.15										
0.2	0.1	329.01	21.35	56.19	120.98	1032.59	0.29	3.40	1.73	4.40	
0.1	0.05	448.47	20.71	63.83	111.30	1189.83	0.26	3.25	1.65	4.26 0	0
	591.64	20.16	71.53	103.30	1350.67	0.24	3.12	1.59	4.14		

		JFKBOL12-00	JFKBOL12-00	JFKBOL10-01	SALB06-037	JFKBOL10-01	CRT07-BOL27	JFKBOL10-00	JFKBOL12-00	CRT07-BOL27
	JFKBOL10-00	194.05	14.35	44.656	298	765.62	1.01762	3.04101	1.49353	5.252555
1		194.1	14.4	44.7	298.0	765.6	1.0	3.0	1.5	5.3
0.9		184.2	15.3	43.6	285.1	747.7	1.0	3.1	1.5	5.2
0.8		174.4	16.3	42.5	272.2	729.8	0.9	3.2	1.6	5.2
0.7		164.5	17.3	41.4	259.2	711.9	0.8	3.4	1.7	5.2
0.6		154.7	18.2	40.3	246.3	694.0	0.8	3.5	1.7	5.1
0.5		144.8	19.2	39.2	233.4	676.1	0.7	3.6	1.8	5.1
0.4		135.0	20.2	38.1	220.5	658.2	0.6	3.7	1.8	5.1
0.3		125.1	21.2	37.1	207.5	640.3	0.6	3.8	1.9	5.1
0.2		115.3	22.1	36.0	194.6	622.4	0.5	3.9	1.9	5.0
0.1		105.4	23.1	34.9	181.7	604.4	0.5	4.0	2.0	5.0
0		95.6	24.1	33.8	168.8	586.5	0.4	4.1	2.0	5.0

Appendix V: Data Tables and Isotopic Models

XRF - Acid Washed 10% HCl

*Some samples were new and some were re-runs to check for pervasive contamination

XRF														
Unnormalized														
Sample	CH19C006-CL	CH19C002-CL	CH19C003-CL	CH19C007-CL	CH19C009-CL	84014-Caspana	84015-Dark	84015-Light	83070	84015-Dark®	CH12020 (2)	CH12021	CH12022-light	CH12022-dark
SiO2	57.66	69.93	70.63	58.54	68.79	72.26	58.28	57.60	70.73	58.26	53.65	71.76	69.31	69.44
TiO2	0.66	0.17	0.17	0.61	0.19	0.10	0.63	0.76	0.08	0.63	0.54	0.08	0.18	0.19
Al2O3	20.03	14.17	13.87	19.63	14.75	12.79	20.64	20.11	12.44	20.64	17.86	12.27	14.74	14.55
FeO*	3.66	1.15	1.12	3.59	1.24	1.56	3.52	4.33	1.48	3.56	3.20	1.41	1.17	1.21
MnO	0.06	0.08	0.08	0.06	0.08	0.03	0.06	0.07	0.03	0.06	0.06	0.03	0.08	0.08
MgO	2.14	0.27	0.27	1.77	0.28	0.32	1.53	2.16	0.34	1.53	1.89	0.97	0.27	0.28
CaO	7.82	1.30	1.31	7.60	1.32	1.06	7.78	7.77	1.19	7.78	11.49	1.02	1.33	1.33
Na2O	2.65	3.07	3.57	2.70	2.97	2.67	2.71	2.51	3.01	2.72	2.35	2.37	2.92	3.11
K2O	1.87	3.92	3.95	2.13	3.79	5.35	2.06	1.97	5.40	2.06	1.89	5.48	3.86	3.85
P2O5	0.19	0.05	0.05	0.18	0.05	0.02	0.20	0.23	0.02	0.20	0.18	0.02	0.05	0.05
Total	96.74	94.10	95.02	96.81	93.47	96.16	97.40	97.52	94.72	97.44	93.11	95.41	93.91	94.11
LOI %	2.66	5.51	4.41	2.53	5.94	3.37	2.20	2.13	4.38	2.20	6.45	4.06	5.81	5.45
Normalized														
SiO2	59.60	74.31	74.33	60.47	73.60	75.14	59.83	59.07	74.67	59.79	57.62	75.21	73.80	73.79
TiO2	0.68	0.18	0.18	0.63	0.20	0.10	0.65	0.78	0.09	0.65	0.58	0.09	0.20	0.20
Al2O3	20.71	15.05	14.59	20.28	15.78	13.30	21.19	20.63	13.13	21.18	19.18	12.86	15.70	15.46
FeO*	3.78	1.22	1.18	3.70	1.33	1.62	3.61	4.44	1.56	3.66	3.43	1.48	1.24	1.29
MnO	0.06	0.09	0.09	0.06	0.09	0.04	0.06	0.07	0.04	0.06	0.07	0.03	0.08	0.09
MgO	2.21	0.28	0.28	1.83	0.30	0.33	1.57	2.22	0.35	1.57	2.03	1.02	0.29	0.30
CaO	8.08	1.38	1.38	7.85	1.42	1.11	7.99	7.96	1.26	7.98	12.34	1.07	1.41	1.42
Na2O	2.74	3.26	3.76	2.79	3.18	2.78	2.79	2.57	3.17	2.79	2.52	2.49	3.11	3.30
K2O	1.94	4.17	4.15	2.19	4.05	5.56	2.11	2.02	5.70	2.12	2.03	5.74	4.12	4.10
P2O5	0.20	0.05	0.05	0.19	0.05	0.02	0.20	0.24	0.02	0.20	0.19	0.02	0.05	0.06
Total	100.00	100.00	100.00	100.00	100.00	100.00	100.00	100.00	100.00	100.00	100.00	100.00	100.00	100.00
Ni	0.00	0.59	0.05	0.00	0.40	2.39	2.54	3.98	1.29	3.41	2.64	2.49	1.40	1.40
Cr	51.86	62.91	40.34	54.53	44.65	61.99	10.85	19.15	4.46	10.68	12.39	6.07	4.19	4.24
Sc	12.61	3.66	3.47	12.64	3.81	10.52	12.84	13.63	9.41	11.88	11.14	9.75	3.69	3.59
V	91.90	5.05	6.58	76.91	6.58	6.54	86.76	114.13	6.24	86.11	76.96	4.13	6.68	8.03
Ba	549.68	940.70	939.31	576.30	930.90	1056.49	565.06	759.53	1050.84	567.37	618.09	1099.97	940.04	954.16
Rb	69.77	131.73	135.22	79.56	127.46	182.06	77.61	71.27	178.72	77.23	69.13	171.60	129.47	130.25
Sr	526.68	215.33	216.46	505.61	215.28	120.95	530.04	529.84	145.18	530.52	485.06	117.16	215.36	215.46
Zr	132.58	140.99	138.12	150.15	147.29	128.90	139.85	130.17	124.96	140.96	124.09	123.22	147.07	145.52
Y	20.93	19.80	20.25	22.24	19.95	41.15	21.79	21.79	39.85	21.85	19.45	40.00	20.40	19.25
Nb	8.77	14.65	14.21	10.15	15.05	12.17	9.45	9.20	12.13	9.67	8.41	11.79	15.01	14.81
Ga	20.39	16.73	15.99	20.60	16.29	17.61	22.59	21.44	16.83	21.20	19.25	16.47	16.86	16.31
Cu	15.07	4.65	3.42	9.45	4.65	6.63	4.53	5.47	15.74	4.61	11.09	11.54	4.04	11.32
Zn	65.01	66.78	65.93	67.01	66.53	68.73	64.58	73.03	67.17	64.21	85.77	91.99	66.48	67.13
Pb	13.79	23.02	23.17	14.48	22.97	27.18	13.98	12.14	26.78	14.09	13.98	27.21	22.94	24.24
La	23.25	38.12	37.37	27.96	40.99	40.90	25.52	25.02	38.51	26.41	22.89	38.66	38.46	37.01
Ce	49.35	69.80	72.81	54.92	71.97	79.16	55.72	51.09	79.10	52.13	48.80	75.87	70.35	73.80
Th	7.29	13.46	13.46	8.06	14.36	14.96	7.11	7.76	14.75	7.87	6.92	14.38	14.10	14.20
Nd	23.15	29.21	28.02	26.07	30.29	35.90	26.37	23.68	35.89	24.91	22.59	34.38	30.85	28.83
U	2.41	3.47	3.17	3.18	3.22	4.89	3.23	2.39	4.65	2.25	1.89	3.88	3.19	3.39
						112.29		47.90						
LAICPMS														
La ppm	25.09	39.61	38.78	27.18	39.66	40.75	26.58	25.62	40.44	26.35	24.08	39.75	40.42	39.31
Ce ppm	50.34	74.80	75.42	55.36	74.94	82.76	53.95	51.33	83.20	53.25	48.06	81.02	75.15	76.74
Pr ppm	6.12	8.79	8.62	6.78	8.87	9.79	6.54	6.29	9.82	6.45	5.88	9.68	8.89	8.60
Nd ppm	23.78	30.92	30.30	26.03	31.07	37.54	25.14	24.50	37.26	25.34	22.72	36.65	31.30	30.26
Sm ppm	4.84	5.51	5.37	5.36	5.71	8.22	5.16	5.09	8.15	5.15	4.62	7.90	5.62	5.39
Eu ppm	1.58	1.08	1.04	1.64	1.08	0.79	1.64	1.55	0.76	1.63	1.41	0.76	1.13	1.08
Gd ppm	4.32	4.25	4.20	4.71	4.30	7.63	4.68	4.59	7.51	4.60	4.18	7.50	4.31	4.17
Tb ppm	0.69	0.66	0.66	0.75	0.67	1.29	0.73	0.74	1.27	0.73	0.66	1.27	0.68	0.66
Dy ppm	4.06	3.83	3.77	4.47	3.80	7.91	4.38	4.32	7.95	4.35	3.87	7.70	3.95	3.78
Ho ppm	0.80	0.73	0.72	0.88	0.71	1.57	0.84	0.84	1.53	0.84	0.77	1.51	0.74	0.71
Er ppm	2.13	1.95	1.95	2.31	1.96	4.21	2.21	2.19	4.14	2.24	2.03	4.07	1.93	1.86
Tm ppm	0.29	0.29	0.28	0.32	0.28	0.62	0.31	0.32	0.60	0.32	0.30	0.59	0.30	0.28
Yb ppm	1.81	1.83	1.79	2.02	1.80	3.71	1.91	1.92	3.60	1.93	1.75	3.64	1.83	1.80
Lu ppm	0.27	0.28	0.28	0.31	0.28	0.56	0.30	0.30	0.56	0.31	0.26	0.54	0.28	0.29
Ba ppm	554.84	967.93	969.50	580.76	957.47	1086.75	573.63	769.90	1085.57	567.64	622.53	1140.31	964.84	970.78
Th ppm	7.47	14.54	14.10	8.39	14.98	15.57	8.04	7.31	15.37	7.91	7.33	15.20	14.90	14.73
Nb ppm	9.37	14.96	14.81	10.40	15.32	12.63	9.55	9.48	12.55	9.56	8.55	12.57	15.27	15.25
Y ppm	20.47	20.18	19.81	22.42	20.01	41.07	22.00	21.82	40.86	21.65	19.80	40.10	20.12	19.71
Hf ppm	3.60	4.49	4.41	4.03	4.68	4.77	3.81	3.62	4.61	3.83	3.39	4.60	4.62	4.65
Ta ppm	0.67	1.10	1.06	0.73	1.14	1.08	0.69	0.68	1.06	0.69	0.64	1.06	1.14	1.12
U ppm	1.74	3.23	3.26	1.93	3.14	4.19	1.89	1.74	4.13	1.86	1.80	4.11	3.30	3.25
Pb ppm	14.02	23.14	22.71	14.59	23.00	27.88	13.89	12.84	27.04	13.65	13.58	27.81	22.77	24.15
Rb ppm	70.90	131.57	135.04	79.36	127.73	182.37	76.93	71.19	180.28	76.84	69.41	173.95	128.28	129.25
Cs ppm	11.28	6.56	6.78	10.22	6.61	13.62	6.81	8.76	17.70	6.60	4.87	9.03	6.59	6.96
Sr ppm	524.09	212.62	213.64	502.30	211.89	118.70	530.33	526.28	146.61	526.19	486.54	117.97	210.69	212.91
Sc ppm	12.05	3.08	3.21	12.65	3.67	9.84	12.09	13.54	9.74	11.88	10.28	9.66	3.07	3.17
Zr ppm	132.91	142.74	138.88	149.82	149.20	129.29	140.95	131.08	126.71	139.00	125.10	125.72	147.23	146.48

84014	CH19C006	84015	83070	CH19C005	CH12022	CH12020(1)	CH19C009
72.38	58.21	57.73	72.48	69.94	69.53	58.25	68.94
0.10	0.66	0.74	0.09	0.09	0.19	0.70	0.21
12.90	19.42	21.26	12.70	11.95	14.67	20.32	14.96
1.62	3.61	3.81	1.50	1.43	1.17	3.66	1.29
0.03	0.06	0.06	0.03	0.03	0.08	0.06	0.08
0.28	2.68	1.52	0.18	2.37	0.25	1.86	0.28
1.09	7.27	8.20	1.03	1.04	1.29	7.59	1.32
2.69	2.45	2.73	2.66	2.01	3.07	2.66	3.02
5.29	1.88	1.87	5.51	4.83	3.82	1.94	3.81
0.02	0.13	0.13	0.02	0.01	0.05	0.13	0.05
96.40	96.36	98.03	96.18	93.68	94.12	97.18	93.95
3.43	3.50	1.76	3.52	6.02	5.69	2.65	5.69
Normalized							
75.08	60.41	58.88	75.36	74.65	73.88	59.95	73.38
0.11	0.68	0.75	0.09	0.10	0.20	0.72	0.22
13.38	20.16	21.69	13.20	12.76	15.59	20.91	15.92
1.68	3.74	3.88	1.56	1.52	1.24	3.76	1.37
0.04	0.06	0.06	0.03	0.03	0.09	0.06	0.08
0.29	2.78	1.55	0.18	2.52	0.26	1.91	0.30
1.13	7.54	8.36	1.07	1.11	1.37	7.81	1.40
2.79	2.54	2.79	2.76	2.15	3.27	2.74	3.21
5.49	1.95	1.90	5.73	5.15	4.06	2.00	4.06
0.02	0.14	0.13	0.02	0.02	0.05	0.13	0.05
100.00	100.00	100.00	100.00	100.00	100.00	100.00	100.00
6.58	2.25	1.39	0.20	0.00	3.46	1.86	0.83
9.43	10.53	12.30	3.40	2.67	3.96	9.29	4.83
10.26	11.72	13.57	10.17	9.33	3.39	12.14	4.50
7.97	91.32	100.63	3.70	7.00	6.92	94.06	8.93
1061.62	522.86	533.85	1068.71	901.40	938.30	562.60	924.46
179.00	70.31	69.52	182.14	165.72	129.43	72.77	128.96
122.99	500.34	543.17	136.96	116.17	211.78	521.18	220.33
138.32	134.06	132.68	130.57	125.68	147.59	139.23	151.75
40.96	19.40	19.63	40.96	35.37	19.40	20.23	20.69
12.34	8.94	9.05	12.47	11.37	15.14	9.29	15.23
17.01	19.77	21.66	16.58	15.63	16.04	21.26	16.19
3.81	9.30	4.61	1.80	3.70	4.03	8.06	5.50
70.94	64.50	66.67	67.01	63.37	64.96	79.83	65.25
26.87	12.74	12.84	26.85	24.93	22.21	13.03	21.58
40.21	23.58	23.52	41.50	34.70	39.34	26.20	41.49
82.62	47.52	48.32	82.20	72.80	72.10	48.66	75.32
14.65	7.14	7.46	15.14	13.50	14.60	7.07	14.16
37.11	20.93	22.89	36.27	32.40	30.88	22.96	31.90
4.14	1.79	2.69	4.74	3.70	3.03	1.99	3.17
	LAICPMS						
41.10	24.06	24.36	41.76	35.47	39.06	25.24	41.27
83.31	48.27	48.64	84.32	74.22	75.07	49.94	76.58
9.86	5.70	5.81	9.83	8.66	8.50	5.90	8.99
37.52	21.87	22.35	38.00	32.88	30.19	23.03	32.22
8.11	4.55	4.54	8.35	7.09	5.67	4.72	5.74
0.77	1.46	1.57	0.76	0.70	1.07	1.52	1.13
7.57	4.05	4.01	7.55	6.55	4.24	4.07	4.49
1.27	0.64	0.66	1.30	1.16	0.65	0.68	0.69
7.92	3.92	3.90	8.00	6.84	3.74	4.03	3.99
1.56	0.74	0.77	1.58	1.38	0.73	0.80	0.75
4.30	2.03	2.04	4.23	3.76	1.96	2.07	2.06
0.59	0.28	0.28	0.59	0.53	0.28	0.28	0.29
3.62	1.61	1.76	3.58	3.21	1.76	1.79	1.72
0.53	0.28	0.27	0.58	0.49	0.28	0.28	0.29
1082.40	527.16	533.55	1086.27	916.75	958.53	566.91	949.29
15.49	7.28	7.25	15.88	14.08	14.87	7.79	14.70
12.71	9.13	9.45	12.61	11.90	15.00	9.68	15.25
40.27	19.42	19.37	40.89	35.91	19.63	20.19	20.28
4.88	3.58	3.57	4.63	4.53	4.56	3.77	4.75
1.07	0.69	0.68	1.04	0.99	1.13	0.67	1.14
4.26	1.70	1.78	4.25	3.55	3.13	1.73	3.22
28.22	13.12	12.83	27.60	25.11	22.65	13.33	22.35

177.06	69.40	68.34	177.39	162.57	127.31	71.45	127.64
12.01	11.68	3.36	17.32	25.97	6.62	3.63	7.30
120.38	487.89	532.96	133.11	113.63	207.07	513.11	213.27

10.22 11.87 13.15 10.13 9.40 3.22 12.02 3.66 136.10 131.90 130.95 126.99 123.40 144.34 138.65 150.19

TIMS - Isotopic Analyses

	Analyses							
	CH19C005	CH19C006	CH19C009	CH12022	CH12021	84015	84015*	84014*
87Sr/86Sr	0.711258	0.711168	0.708247	0.708122	0.711289	0.711231	0.71114	0.71079
143Nd/144Nd	0.512154	0.51214	0.512317	0.512136	0.512096	0.512134	0.512127	0.512148
206Pb/204Pb	18.773	18.745	18.814	18.812	18.763	18.745 15.66		
207Pb/204Pb	15.662 38.843	15.657	15.649 38.796	15.649 38.791	15.665 38.871	38.854		
208Pb/204Pb		38.85						

	Error					
	CH19C005	CH19C006	CH19C009	CH12022	CH12021	84015
87Sr/86Sr	0.000016	0.000008	0.000013	0.000009	0.000010	0.000008
143Nd/144Nd	0.000005	0.000005	0.000007	0.000006	0.000012	0.000006
206Pb/204Pb	0.001	0.002	0.001	0.001	0.002	0.001
207Pb/204Pb	0.001 0.002	0.001 0.003	0.001 0.002	0.001 0.002	0.002 0.003	0.001 0.003
208Pb/204Pb						

Standards

	87Sr/86Sr	Error
NBS987	0.710291	0.000012
	0.710293	0.000012

	143Nd/144Nd	Error
La Jolla	0.512111	0.00001
	0.512116	0.000009
	0.512103	0.00001
	0.512115	0.000008

206Pb/204Pb	Error	207Pb/204Pb	Error	208Pb/204Pb	
16.93	0.001	15.482	0.001	36.667	0.002
16.929	0.001	15.482	0.001	36.667	0.002 0.002
16.93	0.001	15.483	0.001	36.672	

** from de Silva (1991)*

Unormalized - EPMA														
Sample	Rock	SiO2	TiO2	Al2O3	FeO	MnO	MgO	CaO	Na2O	K2O	P2O5	Cl	SO3	Total
CH12022_Glass1	Phase 1	70.24	0.15	14.15	0.92	0.07	0.26	1.38	3.95	4.11	0.10	0.11	0.02	95.47
CH12022_Glass2	Phase 1	69.93	0.16	14.29	1.07	0.04	0.28	1.39	3.84	3.98	0.08	0.10	0.04	95.21
CH12022_Glass4	Phase 1	70.11	0.18	14.30	1.10	0.09	0.26	1.40	3.72	4.17	0.09	0.10	0.04	95.56
CH12022_Glass21	Phase 1	69.97	0.17	14.25	1.01	0.12	0.30	1.36	4.10	4.12	0.02	0.12	0.04	95.55
CH12022_Glass30	Phase 1	69.84	0.16	14.35	1.02	0.03	0.25	1.43	3.61	4.13	0.11	0.11	0.02	95.07
CH12022_Glass33	Phase 1	69.84	0.19	14.34	0.96	0.07	0.26	1.36	3.97	4.23	0.17	0.10	0.03	95.53
CH12022_Glass40	Phase 1	69.69	0.16	14.30	1.03	0.08	0.25	1.42	3.69	4.14	0.14	0.11	0.05	95.06
CH12022_Glass41	Phase 1	70.19	0.18	14.41	0.92	0.06	0.28	1.40	3.62	4.05	0.11	0.10	0.04	95.37
CH12022_glass3	Phase 1	70.08	0.17	14.53	1.07	0.08	0.27	1.38	3.46	3.81	0.09	0.11	0.03	95.07
CH19C002_Glass2	Phase 1	70.15	0.15	14.39	1.01	0.06	0.27	1.41	3.76	4.05	0.06	0.12	0.04	95.48
CH19C002_Glass7	Phase 1	70.27	0.16	14.58	1.07	0.11	0.29	1.41	3.66	4.05	0.09	0.11	0.00	95.83
CH19C002_Glass8	Phase 1	70.16	0.17	14.47	1.05	0.05	0.29	1.36	3.70	4.09	0.07	0.10	0.03	95.57
CH19C002_Glass9	Phase 1	69.58	0.17	14.39	1.07	0.10	0.27	1.38	3.79	4.09	0.10	0.11	0.01	95.06
CH19C002_Glass10	Phase 1	69.97	0.16	14.51	0.97	0.11	0.27	1.41	3.74	3.92	0.08	0.11	0.02	95.26
CH19C002_Glass11	Phase 1	70.10	0.16	14.62	0.97	0.07	0.28	1.32	3.04	4.25	0.09	0.11	0.03	95.03
CH19C002_Glass12	Phase 1	69.95	0.18	14.42	1.04	0.07	0.28	1.31	3.67	4.16	0.11	0.09	0.02	95.31
CH19C002_Glass13	Phase 1	70.27	0.20	14.72	0.90	0.13	0.24	1.40	3.86	4.02	0.13	0.10	0.03	96.00
CH19C002_Glass14	Phase 1	69.49	0.17	14.40	1.01	0.07	0.27	1.34	4.00	4.12	0.08	0.10	0.00	95.06
CH19C002_Glass16	Phase 1	70.33	0.17	14.29	1.03	0.06	0.27	1.45	3.70	4.02	0.12	0.10	0.01	95.54
CH19C002_Glass17	Phase 1	70.23	0.17	14.67	0.95	0.04	0.30	1.41	3.75	4.07	0.14	0.10	0.03	95.86
CH19C002_Glass18	Phase 1	69.83	0.16	14.47	1.10	0.07	0.30	1.41	3.72	4.04	0.15	0.11	0.03	95.39
CH19C002_Glass19	Phase 1	70.15	0.17	14.49	1.04	0.08	0.28	1.38	3.82	4.06	0.10	0.11	0.02	95.69
CH19C002_Glass20	Phase 1	69.93	0.16	14.67	1.03	0.08	0.30	1.50	3.72	3.91	0.15	0.10	0.01	95.58
CH19C002_Glass21	Phase 1	70.42	0.17	14.57	1.03	0.03	0.27	1.39	3.90	3.99	0.07	0.10	0.03	95.99
CH19C002_Glass22	Phase 1	70.20	0.13	14.47	1.08	0.09	0.27	1.34	3.92	4.00	0.06	0.11	0.03	95.71
CH19C002_Glass23	Phase 1	70.63	0.19	14.56	1.03	0.10	0.28	1.39	3.80	4.11	0.07	0.10	0.02	96.28
CH19C002_Glass24	Phase 1	69.99	0.18	14.67	1.07	0.08	0.31	1.35	3.99	4.06	0.10	0.11	0.03	95.93
CH19C002_Glass25	Phase 1	70.39	0.15	14.38	1.00	0.11	0.25	1.37	3.68	3.91	0.14	0.11	-0.01	95.48
CH19C002_Glass26	Phase 1	69.96	0.15	14.46	0.91	0.13	0.30	1.40	3.94	4.03	0.02	0.10	0.02	95.42
CH19C002_Glass27	Phase 1	70.27	0.17	14.67	0.96	0.08	0.26	1.42	3.91	3.99	0.07	0.10	0.03	95.92
CH19C002_Glass28	Phase 1	69.94	0.16	14.34	1.11	0.08	0.28	1.40	3.64	4.10	0.07	0.11	0.02	95.25
CH19C002_Glass29	Phase 1	70.23	0.17	14.41	1.10	0.06	0.29	1.40	3.73	4.09	0.09	0.10	0.00	95.66
CH19C002_Glass30	Phase 1	70.00	0.17	14.57	1.05	0.07	0.28	1.35	3.96	4.23	0.09	0.09	0.02	95.89
83070_glass1	Phase 2	72.61	0.07	13.13	1.31	0.03	0.03	0.89	2.36	5.13	0.04	0.09	0.00	95.69
83070_glass5	Phase 2	72.92	0.07	13.11	1.32	0.01	0.05	0.89	2.65	5.55	0.02	0.08	0.00	96.67
83070_glass6	Phase 2	73.30	0.07	12.96	1.32	0.03	0.06	0.84	2.44	5.89	0.03	0.10	0.01	97.04
83070_glass7	Phase 2	73.03	0.07	13.01	1.29	0.02	0.05	0.80	2.47	5.63	0.02	0.08	0.00	96.47
83070_carbglass5	Phase 2	73.20	0.07	12.93	1.28	0.02	0.04	0.82	2.53	5.55	0.03	0.08	0.01	96.57
83070_carbglass6	Phase 2	71.64	0.06	12.87	1.30	0.03	0.06	0.95	2.36	5.81	0.03	0.09	0.01	95.20
83070_carbglass7	Phase 2	72.88	0.07	13.00	1.23	0.03	0.04	0.88	2.52	5.46	0.03	0.08	0.00	96.23
83070_carbglass9	Phase 2	72.73	0.04	13.11	0.93	0.05	0.03	0.96	2.54	5.46	0.03	0.47	0.02	96.36
83070_carbglass10	Phase 2	74.67	0.07	13.37	1.26	0.03	0.06	0.94	2.50	5.60	0.06	0.09	0.00	98.65
CH12021_glass1	Phase 2	71.45	0.07	13.07	1.33	0.02	0.06	0.88	2.17	5.82	0.03	0.23	0.00	95.12
CH12021_glass2	Phase 2	72.20	0.07	12.99	1.34	0.04	0.04	0.89	2.67	5.38	0.01	0.08	0.00	95.72
CH12021_glass3	Phase 2	72.34	0.07	13.09	1.31	0.04	0.06	0.92	2.49	5.49	0.02	0.09	0.01	95.93
CH12021_glass5	Phase 2	72.06	0.07	12.87	1.30	0.03	0.02	0.88	2.56	5.28	0.02	0.09	0.01	95.17
CH19C007_glass11	Andesite	66.85	0.43	15.67	3.44	0.05	0.66	2.83	3.33	3.76	0.25	0.04	0.02	97.33
CH19C007_glass14	Andesite	66.36	0.44	15.94	3.37	0.05	0.64	3.21	3.54	3.73	0.28	0.04	0.00	97.61
CH19C007_glass15	Andesite	65.32	0.45	14.80	3.77	0.07	0.95	2.70	3.23	3.91	0.28	0.06	0.01	95.57
CH19C007_glass16	Andesite	65.22	0.43	17.21	3.09	0.07	0.64	4.12	3.19	3.41	0.33	0.05	0.00	97.77
CH19C007_glass19	Andesite	67.04	0.42	16.25	3.46	0.11	0.61	3.37	2.64	3.32	0.16	0.05	0.02	97.45
CH19C007_glass21	Andesite	66.55	0.45	15.80	3.27	0.09	0.67	3.29	3.38	3.60	0.32	0.05	0.01	97.46
CH19C007_glass28	Andesite	64.93	0.45	17.01	3.70	0.03	1.10	4.12	3.58	3.34	0.24	0.04	0.00	98.54
CH12020-2_glass2	Andesite	65.59	0.53	15.37	3.68	0.04	0.95	3.19	2.97	3.47	0.40	0.05	0.01	96.26

CH12020-2_glass3	Andesite	65.12	0.47	15.44	3.34	0.06	0.90	3.08	3.02	3.29	0.32	0.09	0.04	95.18
CH12020-2_glass4	Andesite	65.21	0.54	15.35	3.68	0.08	0.86	3.08	3.20	3.54	0.38	0.05	0.01	95.99
CH12020-2_glass7	Andesite	65.26	0.55	15.53	3.62	0.04	0.83	3.12	3.00	3.46	0.37	0.05	0.03	95.84
CH12020-2_glass8	Andesite	65.15	0.52	15.40	3.55	0.06	0.84	3.02	2.83	3.37	0.38	0.05	0.02	95.19
CH12020-2_glass9	Andesite	64.99	0.54	15.52	3.84	0.05	0.89	3.12	2.87	3.54	0.40	0.06	0.02	95.84
CH12020-2_glass10	Andesite	65.13	0.54	15.38	3.88	0.06	0.91	3.08	2.97	3.38	0.38	0.06	0.02	95.79
CH12020-2_glass11	Andesite	65.45	0.54	15.50	3.81	0.06	0.91	3.19	2.99	3.28	0.39	0.06	0.02	96.21
CH12020-2_glass12	Andesite	65.18	0.53	15.41	3.91	0.07	0.91	3.17	2.78	3.38	0.38	0.07	0.02	95.80
CH12020-2_glass13	Andesite	65.19	0.54	15.38	3.72	0.06	0.93	3.21	2.99	3.32	0.38	0.05	0.01	95.76
CH12020-2_glass14	Andesite	65.48	0.53	15.50	3.76	0.06	0.87	3.27	3.14	3.29	0.41	0.06	0.01	96.38
CH12020-2_glass15	Andesite	65.49	0.54	15.46	3.55	0.06	0.84	3.15	2.94	3.45	0.38	0.05	0.01	95.91
CH12020-2_glass18	Andesite	65.38	0.53	15.42	3.57	0.07	0.89	3.18	3.10	3.43	0.37	0.05	0.02	96.02
CH12020-2_glass19	Andesite	64.92	0.52	15.61	3.39	0.06	0.87	3.21	3.08	3.48	0.40	0.06	0.03	95.62
CH12020-2_glass20	Andesite	65.34	0.51	15.43	3.47	0.06	0.87	3.10	3.04	3.48	0.34	0.07	0.03	95.76
CH12020_carbglass1	Andesite	65.10	0.54	15.28	3.94	0.05	0.86	3.11	3.01	3.48	0.37	0.06	0.02	95.81
CH12020_carbglass2	Andesite	64.41	0.56	15.30	4.05	0.06	0.96	3.39	3.24	3.39	0.39	0.07	0.03	95.83
CH12020_carbglass3	Andesite	65.53	0.53	15.46	3.67	0.06	0.88	3.17	2.93	3.47	0.37	0.06	0.03	96.14
CH12020_carbglass4	Andesite	65.15	0.24	15.36	3.70	0.05	0.92	3.48	3.10	3.30	0.41	0.03	0.02	95.76
CH12020_carbglass6	Andesite	65.33	0.35	15.10	2.89	0.05	0.88	3.10	3.08	3.47	0.27	0.95	0.01	95.48
CH12020_carbglass8	Andesite	65.61	0.53	15.36	3.79	0.06	0.87	3.15	2.93	3.50	0.39	0.06	0.02	96.25
CH12020_carbglass9	Andesite	66.02	0.52	15.56	3.44	0.07	0.85	3.31	2.85	3.40	0.43	0.06	0.02	96.54

Normalized - EPMA - Anhydrous

Sample	Rock	SiO2	TiO2	Al2O3	FeO	MnO	MgO	CaO	Na2O	K2O	P2O5	Total
CH12022_Glass1	Phase 1	73.67	0.16	14.84	0.96	0.07	0.28	1.45	4.15	4.31	0.11	100.00
CH12022_Glass2	Phase 1	73.56	0.17	15.03	1.13	0.05	0.30	1.46	4.04	4.18	0.09	100.00
CH12022_Glass4	Phase 1	73.47	0.19	14.99	1.15	0.09	0.27	1.46	3.90	4.37	0.09	100.00
CH12022_Glass21	Phase 1	73.34	0.17	14.94	1.06	0.13	0.32	1.43	4.29	4.31	0.02	100.00
CH12022_Glass30	Phase 1	73.56	0.17	15.12	1.08	0.03	0.27	1.50	3.81	4.35	0.11	100.00
CH12022_Glass33	Phase 1	73.21	0.20	15.03	1.00	0.08	0.28	1.43	4.16	4.43	0.18	100.00
CH12022_Glass40	Phase 1	73.44	0.17	15.07	1.08	0.08	0.27	1.49	3.89	4.36	0.15	100.00
CH12022_Glass41	Phase 1	73.71	0.19	15.13	0.97	0.07	0.29	1.47	3.80	4.26	0.11	100.00
CH12022_glass3	Phase 1	73.82	0.18	15.31	1.12	0.08	0.28	1.46	3.64	4.01	0.09	100.00
CH19C002_Glass2	Phase 1	73.59	0.16	15.10	1.06	0.07	0.28	1.48	3.95	4.25	0.06	100.00
CH19C002_Glass7	Phase 1	73.42	0.17	15.24	1.12	0.12	0.30	1.48	3.82	4.23	0.10	100.00
CH19C002_Glass8	Phase 1	73.52	0.18	15.17	1.10	0.06	0.31	1.43	3.88	4.28	0.08	100.00
CH19C002_Glass9	Phase 1	73.30	0.18	15.16	1.13	0.10	0.28	1.45	3.99	4.30	0.10	100.00
CH19C002_Glass10	Phase 1	73.55	0.17	15.25	1.02	0.12	0.29	1.48	3.93	4.12	0.09	100.00
CH19C002_Glass11	Phase 1	73.87	0.16	15.40	1.02	0.08	0.30	1.39	3.20	4.48	0.10	100.00
CH19C002_Glass12	Phase 1	73.49	0.19	15.15	1.10	0.07	0.30	1.38	3.86	4.37	0.11	100.00
CH19C002_Glass13	Phase 1	73.29	0.20	15.36	0.94	0.13	0.25	1.46	4.03	4.20	0.13	100.00
CH19C002_Glass14	Phase 1	73.19	0.18	15.17	1.07	0.07	0.28	1.41	4.21	4.34	0.09	100.00
CH19C002_Glass16	Phase 1	73.70	0.18	14.98	1.08	0.07	0.28	1.52	3.87	4.21	0.12	100.00
CH19C002_Glass17	Phase 1	73.36	0.18	15.33	0.99	0.04	0.31	1.48	3.92	4.26	0.14	100.00
CH19C002_Glass18	Phase 1	73.31	0.17	15.19	1.16	0.07	0.31	1.48	3.90	4.24	0.16	100.00
CH19C002_Glass19	Phase 1	73.41	0.18	15.16	1.08	0.08	0.29	1.44	3.99	4.25	0.11	100.00
CH19C002_Glass20	Phase 1	73.26	0.17	15.37	1.08	0.08	0.32	1.58	3.90	4.10	0.16	100.00
CH19C002_Glass21	Phase 1	73.47	0.18	15.20	1.08	0.04	0.28	1.45	4.07	4.16	0.08	100.00
CH19C002_Glass22	Phase 1	73.46	0.14	15.14	1.13	0.10	0.28	1.41	4.11	4.19	0.06	100.00
CH19C002_Glass23	Phase 1	73.45	0.19	15.14	1.07	0.11	0.29	1.45	3.95	4.28	0.08	100.00
CH19C002_Glass24	Phase 1	73.06	0.19	15.31	1.11	0.08	0.32	1.40	4.16	4.24	0.11	100.00
CH19C002_Glass25	Phase 1	73.80	0.16	15.07	1.05	0.12	0.26	1.44	3.86	4.10	0.14	100.00
CH19C002_Glass26	Phase 1	73.42	0.16	15.18	0.96	0.14	0.31	1.46	4.14	4.23	0.02	100.00
CH19C002_Glass27	Phase 1	73.36	0.18	15.31	1.01	0.08	0.27	1.48	4.08	4.16	0.07	100.00
CH19C002_Glass28	Phase 1	73.53	0.17	15.08	1.17	0.09	0.30	1.47	3.82	4.31	0.08	100.00
CH19C002_Glass29	Phase 1	73.49	0.17	15.08	1.16	0.07	0.30	1.46	3.90	4.28	0.09	100.00
CH19C002_Glass30	Phase 1	73.09	0.18	15.21	1.09	0.07	0.30	1.41	4.13	4.42	0.10	100.00
83070_glass1	Phase 2	75.95	0.08	13.73	1.37	0.03	0.03	0.93	2.47	5.37	0.04	100.00
83070_glass5	Phase 2	75.50	0.07	13.57	1.37	0.01	0.05	0.92	2.74	5.74	0.02	100.00
83070_glass6	Phase 2	75.61	0.07	13.37	1.36	0.03	0.07	0.86	2.52	6.08	0.03	100.00
83070_glass7	Phase 2	75.76	0.08	13.50	1.34	0.02	0.05	0.83	2.56	5.84	0.02	100.00
83070_carbglass5	Phase 2	75.87	0.07	13.40	1.33	0.03	0.04	0.85	2.62	5.75	0.03	100.00
83070_carbglass6	Phase 2	75.32	0.07	13.53	1.37	0.03	0.06	1.00	2.49	6.10	0.03	100.00
83070_carbglass7	Phase 2	75.80	0.08	13.52	1.28	0.03	0.04	0.91	2.63	5.68	0.03	100.00
83070_carbglass9	Phase 2	75.87	0.04	13.67	0.97	0.05	0.03	1.00	2.65	5.69	0.03	100.00
83070_carbglass10	Phase 2	75.76	0.07	13.56	1.28	0.03	0.06	0.96	2.54	5.68	0.06	100.00
CH12021_glass1	Phase 2	75.29	0.08	13.77	1.40	0.02	0.06	0.93	2.28	6.14	0.03	100.00
CH12021_glass2	Phase 2	75.50	0.08	13.59	1.40	0.04	0.05	0.93	2.79	5.62	0.01	100.00
CH12021_glass3	Phase 2	75.48	0.07	13.66	1.37	0.04	0.06	0.97	2.60	5.73	0.02	100.00
CH12021_glass5	Phase 2	75.79	0.08	13.54	1.37	0.03	0.02	0.93	2.69	5.55	0.02	100.00
CH19C007_glass11	Andesite	68.73	0.44	16.11	3.54	0.05	0.68	2.91	3.42	3.87	0.25	100.00
CH19C007_glass14	Andesite	68.01	0.45	16.34	3.45	0.06	0.65	3.29	3.63	3.82	0.29	100.00
CH19C007_glass15	Andesite	68.40	0.47	15.49	3.95	0.08	1.00	2.83	3.39	4.10	0.30	100.00
CH19C007_glass16	Andesite	66.75	0.44	17.61	3.16	0.07	0.65	4.21	3.26	3.49	0.34	100.00
CH19C007_glass19	Andesite	68.84	0.44	16.69	3.55	0.11	0.63	3.46	2.71	3.41	0.16	100.00
CH19C007_glass21	Andesite	68.33	0.46	16.22	3.36	0.09	0.69	3.37	3.47	3.69	0.32	100.00
CH19C007_glass28	Andesite	65.92	0.45	17.27	3.75	0.03	1.12	4.19	3.64	3.39	0.25	100.00
CH12020-2_glass2	Andesite	68.18	0.55	15.98	3.83	0.04	0.99	3.31	3.08	3.61	0.42	100.00

CH12020-2_glass3	Andesite	68.51	0.49	16.25	3.52	0.06	0.95	3.25	3.18	3.46	0.34	100.00
CH12020-2_glass4	Andesite	67.98	0.56	16.00	3.84	0.08	0.89	3.21	3.34	3.70	0.40	100.00
CH12020-2_glass7	Andesite	68.15	0.57	16.21	3.78	0.05	0.87	3.25	3.13	3.61	0.38	100.00
CH12020-2_glass8	Andesite	68.49	0.55	16.19	3.73	0.07	0.88	3.17	2.98	3.54	0.40	100.00
CH12020-2_glass9	Andesite	67.86	0.56	16.21	4.01	0.06	0.93	3.26	2.99	3.70	0.42	100.00
CH12020-2_glass10	Andesite	68.05	0.56	16.07	4.06	0.07	0.95	3.22	3.10	3.54	0.39	100.00
CH12020-2_glass11	Andesite	68.08	0.56	16.13	3.97	0.07	0.95	3.32	3.11	3.41	0.40	100.00
CH12020-2_glass12	Andesite	68.10	0.55	16.10	4.09	0.07	0.95	3.31	2.90	3.53	0.40	100.00
CH12020-2_glass13	Andesite	68.12	0.56	16.07	3.88	0.06	0.97	3.35	3.13	3.47	0.40	100.00
CH12020-2_glass14	Andesite	67.99	0.55	16.09	3.91	0.06	0.90	3.40	3.27	3.41	0.43	100.00
CH12020-2_glass15	Andesite	68.33	0.56	16.13	3.70	0.07	0.88	3.29	3.07	3.60	0.39	100.00
CH12020-2_glass18	Andesite	68.14	0.55	16.07	3.72	0.07	0.93	3.31	3.23	3.57	0.39	100.00
CH12020-2_glass19	Andesite	67.95	0.54	16.34	3.55	0.07	0.91	3.36	3.22	3.64	0.41	100.00
CH12020-2_glass20	Andesite	68.31	0.54	16.13	3.63	0.06	0.91	3.24	3.18	3.64	0.36	100.00
CH12020_carbglass1	Andesite	68.01	0.56	15.96	4.11	0.05	0.90	3.25	3.14	3.63	0.39	100.00
CH12020_carbglass2	Andesite	67.28	0.58	15.98	4.23	0.06	1.01	3.55	3.38	3.54	0.41	100.00
CH12020_carbglass3	Andesite	68.22	0.55	16.09	3.82	0.06	0.91	3.30	3.05	3.62	0.39	100.00
CH12020_carbglass4	Andesite	68.06	0.25	16.05	3.87	0.06	0.97	3.64	3.24	3.45	0.43	100.00
CH12020_carbglass6	Andesite	69.12	0.37	15.98	3.05	0.05	0.93	3.28	3.26	3.67	0.28	100.00
CH12020_carbglass8	Andesite	68.21	0.55	15.97	3.94	0.06	0.90	3.27	3.05	3.63	0.41	100.00
CH12020_carbglass9	Andesite	68.45	0.54	16.13	3.57	0.07	0.88	3.43	2.96	3.52	0.44	100.00

Standards

Comment	K2O	CaO	SiO2	Al2O3	Na2O	MgO	P2O5	FeO	MnO	TiO2	Cl	SO3	Total
RLS132.	4.71	0.09	75.55	11.65	5.00	0.07	-0.07	2.13	0.16	0.22	0.17	0.01	99.67
RLS132.	4.86	0.13	75.84	11.63	4.72	0.05	0.04	2.11	0.16	0.19	0.18	0.02	99.89
RLS132.	4.68	0.15	75.79	11.48	4.81	0.04	-0.03	1.97	0.11	0.18	0.19	0.01	99.34
RLS132.	4.78	0.14	75.44	11.73	4.90	0.07	-0.08	2.10	0.14	0.20	0.18	0.01	99.57
RLS132.	4.78	0.11	75.36	11.45	4.66	0.05	-0.05	1.99	0.16	0.18	0.18	0.03	98.86
RLS132.	4.76	0.12	75.94	11.79	4.62	0.04	0.03	1.89	0.14	0.17	0.18	0.02	99.66
RLS132.	4.77	0.11	75.56	11.79	4.91	0.07	-0.06	2.17	0.15	0.21	0.18	0.02	99.83
RLS132.	4.75	0.13	76.33	11.80	3.94	0.09	-0.07	1.95	0.15	0.19	0.18	0.01	99.43
RLS132.	4.72	0.12	75.61	11.71	5.29	0.06	-0.01	2.00	0.20	0.19	0.19	0.02	100.05
RLS132.	4.66	0.11	75.33	11.86	4.68	0.06	0.01	2.23	0.13	0.19	0.19	0.04	99.45
Avg	4.75	0.12	75.67	11.69	4.75	0.06	-0.03	2.06	0.15	0.19	0.18	0.02	99.58
2SD	0.11	0.04	0.62	0.28	0.69	0.03	0.09	0.22	0.05	0.03	0.01	0.02	
VG568.	5.44	0.45	77.09	12.42	3.80	0.02	0.00	1.20	0.04	0.09	0.11	0.00	100.62
VG568.	5.39	0.46	77.17	12.46	3.70	0.03	-0.06	0.91	0.01	0.08	0.10	0.01	100.24
VG568.	5.31	0.46	76.87	12.44	3.47	0.01	0.06	1.07	0.04	0.07	0.11	0.00	99.89
Avg	5.38	0.46	77.05	12.44	3.66	0.02	0.00	1.06	0.03	0.08	0.11	0.00	100.25
2SD	0.13	0.01	0.31	0.04	0.34	0.02	0.12	0.29	0.03	0.02	0.01	0.01	

Average Glass LAICPMS

Sample	Spot	Rocktype	Sc	V	Rb	Sr	Y	Zr	Nb	Ba	La	Ce	Sm	Eu	Dy	Yb	Hf	Pb
84014	All	Phase 2	18.41	0.94	225.82	107.67	54.78	119.98	14.71	1142.86	45.05	85.45	9.25	0.72	9.56	4.68	4.79	35.07
83070	All	Phase 2	11.92	4.70	323.26	85.82	22.53	103.43	22.50	704.61	52.18	96.32	4.15	0.58	3.51	2.66	4.23	41.41
CH12021	All	Phase 2	16.44	1.19	199.97	102.41	46.94	107.26	14.57	1114.10	41.72	84.48	8.39	0.73	8.37	4.37	4.37	36.66
CH19C005	All	Phase 2	17.15	1.27	236.36	111.24	54.05	119.25	14.84	1161.06	45.97	88.79	9.09	0.73	9.30	4.66	4.65	34.40
CH19C003	All	Phase 1	10.74	3.77	158.85	222.48	24.28	169.00	18.31	1130.29	43.85	87.33	5.93	1.12	4.13	2.15	5.36	29.34
CH19C009	All	Phase 1	10.42	3.89	149.30	229.23	25.62	198.44	19.11	1066.98	45.79	82.17	6.32	1.15	4.41	2.22	6.15	26.26
CH19C007	All	Andesite	24.32	50.93	138.60	348.87	45.67	346.39	15.84	948.13	45.95	89.97	8.88	1.37	7.74	4.02	8.74	20.59
CH12020_1	All	Andesite	20.43	54.72	114.85	334.63	39.42	282.59	13.83	839.42	40.35	71.53	7.30	1.17	6.37	3.13	6.85	16.97
83069	All	Andesite	20.66	55.84	144.79	342.21	42.24	305.30	15.23	910.90	42.95	79.00	7.25	1.23	6.57	3.28	6.96	28.07
CH12020_2	All	Andesite	21.36	58.77	124.82	323.22	43.39	279.99	14.84	888.56	41.49	77.81	7.76	1.33	6.80	3.74	6.79	20.10

Spots LAICPMS

Sample	Spot	Rocktype	Si	Ca	Sc	V	Rb	Sr	Y	Zr	Nb	Ba	La	Ce	Sm	Eu	Dy	Yb	Hf	Pb
84014	84014_gl1	Phase 2	385464.94	6575.19	17.87	0.89	226.86	102.06	51.29	114.33	14.91	1229.35	44.47	89.93	9.97	0.83	8.83	4.53	4.51	39.80
84014	84014_gl2	Phase 2	358562.31	6575.19	18.45	0.93	210.20	102.42	52.25	114.53	13.69	1105.66	45.97	85.19	9.39	0.89	9.29	4.75	5.43	33.68
84014	84014_gl3	Phase 2	332205.40	6575.19	16.95	0.81	208.39	101.42	49.77	111.52	13.82	986.94	39.89	73.42	5.00	0.42	8.14	4.68	4.03	28.73
84014	84014_gl4	Phase 2	365481.27	6575.19	19.02	0.00	214.42	110.50	58.22	122.07	13.84	1164.38	45.39	82.98	10.80	0.65	9.48	4.45	5.32	31.68
84014	84014_gl5	Phase 2	382790.06	6575.19	18.97	1.09	264.08	117.93	55.11	123.91	15.98	1191.27	45.12	90.43	11.52	0.68	9.76	4.84	4.36	34.00
84014	84014_gl6	Phase 2	343746.44	6575.19	17.15	0.49	203.98	100.51	53.93	119.42	13.71	1066.26	42.22	80.33	9.31	0.77	9.74	4.48	4.28	30.91
84014	84014_gl7	Phase 2	375203.23	6575.19	19.62	1.75	235.04	112.76	61.21	120.67	15.89	1170.87	48.12	92.09	9.88	0.65	11.11	4.74	5.09	34.08
84014	84014_gl8	Phase 2	316168.73	6575.19	17.15	0.73	187.94	99.46	52.83	116.79	13.94	1094.20	44.39	77.03	9.22	0.76	8.03	4.35	4.42	26.98
84014	84014_gl9	Phase 2	362650.18	6575.19	18.40	0.75	230.32	111.71	48.78	121.22	13.12	1088.46	42.32	84.72	8.28	0.79	8.28	4.62	4.62	34.23
84014	84014_gl10	Phase 2	360226.16	6575.19	18.30	0.70	225.16	109.23	53.13	116.38	15.32	1225.43	47.51	88.24	9.48	0.70	9.62	4.99	5.40	38.15
84014	84014_gl11	Phase 2	362972.62	6575.19	18.46	0.96	235.57	106.35	55.65	117.35	16.02	1179.65	46.37	89.94	9.75	0.68	10.33	4.61	5.07	41.98
84014	84014_gl12	Phase 2	391180.10	6575.19	18.34	0.87	246.12	116.63	50.48	119.21	14.69	1230.69	44.71	89.36	9.01	0.86	8.64	4.68	4.68	42.08
84014	84014_gl13	Phase 2	322762.20	6575.19	18.03	0.82	190.58	96.79	50.91	112.50	14.19	1091.40	41.52	86.14	8.07	0.73	10.75	4.09	4.30	30.57
84014	84014_gl13	Phase 2	347340.22	6575.19	18.35	1.11	214.76	99.07	51.46	115.39	13.74	1055.15	42.52	81.00	9.57	0.69	9.14	4.28	5.08	33.61
84014	84014_gl14	Phase 2	419469.71	6575.19	19.65	1.76	282.31	115.20	64.39	120.55	16.77	1282.09	47.84	84.08	8.84	0.83	10.29	4.75	4.67	48.61
84014	84014_gl15	Phase 2	379969.81	6575.19	19.35	1.31	238.49	115.04	63.64	148.24	15.97	1210.39	51.88	96.88	10.67	0.66	10.80	5.87	5.05	36.76
83070	83070_gl2	Phase 2	430960.85	6575.19	12.36	5.79	313.03	83.92	21.33	101.39	23.03	682.15	52.11	97.25	3.98	0.56	3.21	2.40	4.12	42.81
83070	83070_gl3	Phase 2	451616.69	6575.19	13.86	5.28	347.12	83.87	23.39	105.43	24.55	739.56	52.50	105.00	4.00	0.55	3.53	2.75	4.15	45.65
83070	83070_gl4	Phase 2	503283.94	6575.19	14.04	5.30	391.14	84.72	22.80	106.29	25.35	701.28	57.42	105.02	4.50	0.52	4.20	2.93	4.45	46.97
83070	83070_gl5	Phase 2	457621.22	6575.19	12.87	4.65	348.25	88.12	24.65	109.12	24.02	779.76	56.57	104.21	4.96	0.61	3.41	2.89	3.77	44.46
83070	83070_gl6	Phase 2	454768.43	6575.19	11.87	4.67	345.06	90.42	21.59	101.61	24.23	733.18	50.36	99.63	4.53	0.58	3.65	2.73	4.42	49.37
83070	83070_gl7	Phase 2	407898.34	6575.19	11.79	4.95	308.99	75.86	20.51	96.51	21.42	634.92	50.70	92.50	3.86	0.57	3.13	2.74	4.31	38.32
83070	83070_gl10	Phase 2	370610.31	6575.19	10.32	4.08	286.49	91.38	26.08	116.67	21.01	720.99	54.09	92.02	4.67	0.74	3.78	3.03	4.61	33.50
83070	83070_gl11	Phase 2	451683.72	6575.19	11.68	4.29	319.82	87.97	22.59	104.05	22.94	712.13	52.24	94.30	4.22	0.61	3.44	2.71	4.38	42.10
83070	83070_gl12	Phase 2	466634.39	6575.19	12.51	5.05	345.92	86.95	24.22	105.28	24.08	754.48	55.55	103.69	4.29	0.62	3.98	2.70	4.14	42.98
83070	83070_gl14	Phase 2	423051.20	6575.19	11.72	4.41	321.74	88.88	22.62	106.88	21.85	735.04	53.44	100.43	3.72	0.61	3.44	2.68	4.42	39.75
83070	83070_gl15	Phase 2	397949.57	6575.19	11.87	4.35	319.73	82.66	21.65	104.81	21.79	713.55	52.92	95.45	3.84	0.48	3.34	2.62	4.34	38.84
83070	83070_gl16	Phase 2	321190.23	6575.19	8.18	3.63	231.86	85.16	18.91	83.13	15.75	548.32	38.20	66.38	3.21	0.49	2.97	1.76	3.60	32.23
CH12021	CH12021_gl1	Phase 2	377405.97	6718.12	17.57	1.37	227.41	100.91	45.17	102.02	14.49	1021.82	46.07	81.28	7.84	0.60	7.97	3.98	4.24	66.00
CH12021	CH12021_gl2	Phase 2	422735.84	6718.12	18.60	1.09	220.80	102.95	48.09	107.90	16.45	1202.48	43.18	91.44	8.64	0.66	8.65	4.86	4.67	36.26
CH12021	CH12021_gl3	Phase 2	307079.77	6718.12	14.42	1.30	176.92	112.68	50.17	110.16	12.82	1022.67	41.94	73.72	8.92	0.68	9.33	4.80	3.96	30.73
CH12021	CH12021_gl4	Phase 2	338573.30	6718.12	17.10	1.41	231.94	110.05	52.26	118.44	14.97	1105.94	43.00	81.73	9.56	0.71	8.61	4.26	4.88	41.12
CH12021	CH12021_gl5	Phase 2	257106.60	6718.12	13.15	1.42	171.31	108.08	34.15	98.08	12.11	762.89	29.37	53.92	6.92	0.67	6.75	2.94	3.24	23.38
CH12021	CH12021_gl6	Phase 2	281609.46	6718.12	16.27	2.34	200.77	131.04	50.39	112.81	12.82	1020.98	43.15	74.98	5.90	0.76	8.41	4.06	4.29	26.07
CH12021	CH12021_gl7	Phase 2	303530.19	6718.12	14.28	0.87	194.04	81.71	36.83	84.81	12.59	1029.93	35.98	81.21	7.43	0.65	6.48	3.52	3.83	38.70
CH12021	CH12021_gl8	Phase 2	384027.81	6718.12	17.08	0.73	202.03	94.81	46.67	105.03	16.01	1207.69	42.83	92.17	9.11	0.75	7.94	4.67	4.71	38.55
CH12021	CH12021_gl9	Phase 2	366273.15	6718.12	17.48	0.81	194.25	98.16	50.17	112.79	16.40	1247.04	44.09	95.63	9.44	0.78	8.64	4.42	4.78	35.58
CH12021	CH12021_gl10	Phase 2	336514.04	6718.12	16.12	1.89	188.93	108.45	55.53	121.67	12.55	1177.14	46.48	78.41	9.87	0.70	9.89	5.50	5.04	30.29
CH12021	CH12021_gl11	Phase 2	360480.81	6718.12	16.49	0.69	191.74	93.74	45.22	104.23	15.41	1158.67	41.87	95.74	8.15	0.86	8.45	4.62	4.54	35.98

CH12021	CH12021_gl12	Phase 2	386764.69	6718.12	17.68	0.90	210.14	95.59	47.25	109.89	16.90	1286.63	42.11	101.92	8.39	0.82	8.84	4.83	4.33	37.98
CH12021	CH12021_gl13	Phase 2	374468.59	6718.12	17.46	0.65	189.31	93.15	48.36	106.54	15.86	1239.45	42.27	96.03	8.89	0.84	8.82	4.31	4.31	35.97
CH19C005	CH19C005_gl1	Phase 2	376735.36	7146.94	18.07	1.01	306.58	114.55	53.14	118.69	13.21	1057.87	43.78	79.53	8.77	0.52	8.00	4.66	4.55	34.47
CH19C005	CH19C005_gl2	Phase 2	347015.56	7146.94	16.02	1.23	270.86	116.70	59.38	122.78	15.50	1206.49	47.09	90.93	9.78	0.83	9.45	4.85	4.74	37.26
CH19C005	CH19C005_gl3	Phase 2	368459.73	7146.94	17.80	1.53	228.19	98.47	50.69	107.65	16.70	1190.35	42.32	93.81	8.86	0.65	9.62	5.36	4.28	43.63
CH19C005	CH19C005_gl4	Phase 2	273648.15	7146.94	16.89	0.27	186.94	114.73	56.06	125.22	13.82	1224.84	48.15	88.18	8.14	0.92	9.00	3.43	3.53	22.13
CH19C005	CH19C005_gl5	Phase 2	351930.52	7146.94	17.46	0.99	241.84	108.69	58.56	126.96	14.95	1197.01	51.46	88.90	10.24	1.06	10.40	4.45	4.95	29.45
CH19C005	CH19C005_gl6	Phase 2	301669.38	7146.94	15.95	0.39	201.00	105.31	55.90	120.50	14.87	1108.38	47.88	84.12	9.46	0.60	10.52	4.96	4.94	25.59
CH19C005	CH19C005_gl7	Phase 2	381897.33	7146.94	20.06	0.88	253.54	111.24	54.67	122.02	15.94	1189.32	47.56	91.84	9.27	0.68	9.14	5.47	4.81	39.95
CH19C005	CH19C005_gl8	Phase 2	282514.49	7146.94	15.48	1.78	247.17	118.90	38.51	84.27	12.50	821.26	32.07	57.91	8.41	0.61	5.78	3.40	4.14	23.87
CH19C005	CH19C005_gl9	Phase 2	361592.40	7146.94	15.69	1.65	205.74	108.80	51.13	110.97	14.99	1203.56	44.05	91.56	7.26	0.79	8.42	4.78	4.77	40.99
CH19C005	CH19C005_gl10	Phase 2	351565.08	7146.94	18.27	1.14	233.95	122.77	58.13	130.29	15.00	1227.16	49.94	91.04	9.61	0.62	9.81	4.96	4.79	34.71
CH19C005	CH19C005_gl11	Phase 2	373550.53	7146.94	18.64	2.87	281.65	119.96	60.93	157.05	16.59	1237.54	51.56	107.36	7.80	0.67	14.63	3.41	4.24	39.86
CH19C005	CH19C005_gl12	Phase 2	451435.81	7146.94	17.44	1.97	313.55	132.26	62.49	130.84	13.28	1172.73	49.16	95.06	9.92	1.16	6.25	5.50	5.17	34.36
CH19C005	CH19C005_gl13	Phase 2	318102.03	7146.94	16.25	1.41	187.61	102.45	48.18	110.08	16.38	1275.32	45.41	99.03	9.34	0.72	8.87	4.67	4.27	38.06
CH19C005	CH19C005_gl14	Phase 2	450223.92	7146.94	19.28	1.26	244.22	104.09	50.48	115.39	18.14	1305.67	47.07	104.96	10.25	0.69	9.18	5.16	5.67	47.46
CH19C005	CH19C005_gl15	Phase 2	364991.60	7146.94	17.36	1.12	210.26	113.74	52.79	117.27	16.28	1228.05	45.91	90.20	10.06	0.89	10.77	4.94	5.18	41.46
CH19C005	CH19C005_gl16	Phase 2	296826.25	7146.94	14.23	1.18	204.39	103.35	45.15	109.23	11.42	943.28	41.62	69.81	6.10	0.30	7.20	3.77	3.66	22.84
CH19C005	CH19C005_gl17	Phase 2	284755.33	7146.94	16.65	0.92	200.59	95.02	62.65	118.05	12.66	1149.12	46.46	85.16	11.36	0.63	11.09	5.49	5.33	28.72
CH19C003	CH19C003_gl1	Phase 1	365732.96	10291.60	11.46	3.55	162.31	213.31	21.91	151.35	17.89	1084.94	40.57	88.28	5.68	1.11	3.75	1.53	5.47	32.16
CH19C003	CH19C003_gl2	Phase 1	398949.39	10291.60	12.95	4.68	178.42	203.09	22.12	163.48	18.76	1160.66	45.29	86.38	6.36	1.29	4.42	2.04	5.64	38.78
CH19C003	CH19C003_gl3	Phase 1	361036.47	10291.60	11.77	3.64	159.93	223.98	24.46	166.26	17.77	1131.03	46.10	87.71	6.82	1.08	4.06	2.14	5.17	26.97
CH19C003	CH19C003_gl4	Phase 1	331838.02	10291.60	10.33	3.46	132.76	198.23	23.24	171.40	14.31	960.17	43.23	75.47	5.43	0.83	3.77	2.02	5.11	25.53
CH19C003	CH19C003_gl5	Phase 1	374732.99	10291.60	10.15	3.75	161.15	217.77	23.42	162.28	19.22	1151.25	42.42	92.38	6.07	1.03	4.26	1.86	4.70	29.24
CH19C003	CH19C003_gl6	Phase 1	395868.80	10291.60	12.62	3.96	183.41	229.14	24.22	162.55	20.45	1183.10	44.21	99.19	5.32	1.33	4.04	2.24	4.88	29.12
CH19C003	CH19C003_gl7	Phase 1	323937.08	10291.60	9.76	3.68	145.62	220.90	28.08	192.99	17.11	1080.46	45.07	84.78	6.79	1.07	5.02	3.21	6.17	27.69
CH19C003	CH19C003_gl8	Phase 1	353839.88	10291.60	10.50	4.30	153.01	222.03	24.45	170.06	18.51	1109.76	43.07	84.45	6.39	1.15	4.76	2.59	6.08	28.44
CH19C003	CH19C003_gl9	Phase 1	344067.64	10291.60	9.61	3.48	148.54	276.06	27.14	185.07	17.16	1391.41	46.21	81.96	5.58	1.43	4.20	2.10	5.98	30.78
CH19C003	CH19C003_gl10	Phase 1	372968.11	10291.60	9.81	3.64	148.57	245.47	27.66	194.71	18.69	1146.98	50.03	88.32	5.70	1.20	4.52	2.28	5.48	33.89
CH19C003	CH19C003_gl11	Phase 1	363229.92	10291.60	10.37	4.02	162.76	218.77	22.14	151.57	18.77	1092.97	39.18	89.02	6.18	1.11	3.00	1.92	4.97	28.44
CH19C003	CH19C003_gl12	Phase 1	341392.59	10291.60	9.88	3.69	149.87	224.27	23.69	168.69	17.74	1100.54	45.13	83.38	5.91	1.07	3.98	1.99	5.41	25.50
CH19C003	CH19C003_gl13	Phase 1	393460.78	10291.60	10.81	3.67	168.73	227.35	22.91	166.56	18.84	1168.44	43.32	88.27	5.54	1.08	4.02	2.09	5.07	28.72
CH19C003	CH19C003_gl14	Phase 1	376499.91	10291.60	11.09	4.04	165.25	201.58	23.49	153.72	20.67	1137.46	43.27	93.81	5.74	0.88	3.52	2.20	5.29	29.00
CH19C003	CH19C003_gl16	Phase 1	359505.34	10291.60	9.99	3.06	162.46	215.29	25.32	174.32	18.70	1055.21	40.68	86.61	5.41	1.11	4.56	2.06	4.94	25.83
CH19C009	CH19C009_gl1	Phase 1	348153.62	10363.06	8.99	3.35	146.22	234.49	26.16	195.23	18.44	1068.12	43.07	81.30	5.77	1.54	4.33	1.97	5.72	30.57
CH19C009	CH19C009_gl2	Phase 1	347190.63	10363.06	11.04	3.96	151.16	225.73	29.53	212.30	19.86	1120.49	53.63	81.91	8.63	1.33	5.56	2.40	6.08	25.21
CH19C009	CH19C009_gl3	Phase 1	364289.46	10363.06	10.14	3.52	151.06	232.89	26.35	186.90	18.85	1139.79	46.64	83.04	7.19	1.26	4.48	2.22	7.02	28.92
CH19C009	CH19C009_gl4	Phase 1	398024.19	10363.06	11.86	4.08	161.46	239.31	29.91	250.53	20.18	1113.23	54.35	83.96	6.63	1.06	5.11	2.28	6.80	23.06
CH19C009	CH19C009_gl5	Phase 1	327121.48	10363.06	9.95	3.76	145.70	232.04	27.30	189.54	17.99	1057.54	50.76	83.26	6.51	1.37	4.87	2.08	5.63	26.74
CH19C009	CH19C009_gl6	Phase 1	354167.39	10363.06	11.33	3.84	149.00	221.36	27.52	214.36	19.72	1005.44	53.45	75.53	6.83	1.22	4.58	2.38	6.07	22.78
CH19C009	CH19C009_gl7	Phase 1	363926.72	10363.06	10.61	4.04	136.30	235.98	24.78	253.87	20.34	980.40	42.84	73.74	6.16	1.09	4.07	2.48	7.93	27.32
CH19C009	CH19C009_gl8	Phase 1	371336.16	10363.06	10.19	3.18	154.44	221.63	24.37	204.37	19.25	1002.52	42.97	73.08	5.65	1.17	4.41	2.56	6.09	24.79
CH19C009	CH19C009_gl9	Phase 1	367159.25	10363.06	10.57	3.84	159.15	217.57	22.78	160.13	18.40	1093.30	41.30	91.14	5.70	1.02	4.40	1.63	5.72	29.14
CH19C009	CH19C009_gl10	Phase 1	355432.48	10363.06	10.21	3.98	154.28	222.50	22.67	163.81	18.67	1115.46	43.24	93.11	5.61	1.04	5.00	2.45	4.88	26.71
CH19C009	CH19C009_gl14	Phase 1	341757.89	10363.06	10.46	3.03	140.55	239.98	27.60	216.83	19.84	1069.66	45.76	83.57	5.44	1.16	4.17	2.29	7.29	21.67
CH19C009	CH19C009_gl15	Phase 1	346468.06	10363.06	10.24	3.27	151.15	213.17	20.93	151.56	17.18	1097.58	41.63	84.92	5.78	1.16	3.89	2.09	4.51	29.33
CH19C009	CH19C009_gl16	Phase 1	352966.28	10363.06	10.07	3.82	156.96	222.01	22.78	161.55	19.10	1106.22	42.16	90.46	6.59	1.18	3.52	1.95	5.80	28.65
CH19C009	CH19C009_gl17	Phase 1	310533.69	10363.06	9.10	3.53	144.62	241.89	27.83	196.27	17.07	1091.23	48.92	81.38	6.47	1.24	4.28	2.47	6.05	24.61
CH19C009	CH19C009_gl18	Phase 1	314303.98	10363.06	10.22	3.72	142.76	226.79	27.34	195.65	16.47	1045.81	44.84	86.93	6.82	1.16	4.05	2.49	6.37	24.62
CH19C009	CH19C009_gl19	Phase 1	317185.80	10363.06	10.09	3.30	138.98	246.69	27.83	205.66	20.40	1154.96	50.02	88.03	6.78	0.87	5.24	2.36	6.26	25.25
CH19C009	CH19C009_gl20	Phase 1	395768.16	10363.06	12.13	7.97	154.33	222.95	19.90	214.98	23.14	876.95	32.80	61.51	4.81	0.71	2.97	1.60	6.33	27.09
CH19C007	CH19C007_gl2	Andesite	389566.20	24799.89	24.59	51.89	138.55	348.21	46.50	348.17	16.77	983.46	48.05	85.76	7.83	1.55	7.55	3.49	7.44	20.29
CH19C007	CH19C007_gl3	Andesite	373009.74	24799.89	25.88	47.12	145.43	361.42	48.17	352.07	16.45	975.64	48.84	87.84	9.24	1.49	7.56	4.17	8.84	20.85
CH19C007	CH19C007_gl5	Andesite	305303.33	24799.89	20.84	51.11	113.25	349.04	50.69	320.79	12.27	948.45	41.46	89.13	9.56	1.28	7.64	4.19	9.93	18.88
CH19C007	CH19C007_gl12	Andesite	310251.35	24799.89	19.25	45.69	120.82	310.65	32.14	242.77	13.60	805.23	36.71	70.70	5.88	1.29	6.90	3.73	6.22	16.16
CH19C007	CH19C007_gl14	Andesite	423478.10	24799.89	26.36	59.47	155.11	361.53	50.87	452.06	19.02	981.64	53.12	118.90	11.54	1.51	8.17	3.50	11.83	27.72
CH19C007	CH19C007_gl15	Andesite	388133.04	24799.89	29.03	50.27	158.47	362.36	45.63	362.48	16.92	994.36	47.53	87.51	9.21	1.11	8.59	5.07	8.20	19.66
CH12020_1	CH12020_1_gl1	Andesite	308359.41	23513.44	21.26	61.03	114.72	318.88	42.63	263.86	13.71	883.12	37.42	75.28	6.88	1.14	7.06	2.86	7.88	16.86
CH12020_1	CH12020_1_gl2	Andesite	284062.85	23513.44	20.30	54.20	110.47	338.09	39.05	281.73	13.47	863.11	40.73	70.71	7.29	1.28	6.29	3.23	6.81	17.05
CH12020_1	CH12020_1_gl3	Andesite	318652.19	23513.44	20.85	53.94	120.93	333.75	39.87	286.52	14.56	837.88	39.80	70.68	8.63	1.30	6.29	3.39	7.04	16.89
CH12020_1	CH12020_1_gl6	Andesite	299772.78	23513.44	19.91	54.59	110.14	333.45	39.24	276.45	13.61	836.51	39.68	67.76	7.24	1.24	6.66	3.41	6.57	16.44
CH12020_1	CH12020_1_gl7	Andesite	292669.27	23513.44	20.72	52.03	112.67	335.40	39.47	284.06	13.82	819.75	40.50	70.88	7.51	1.03	6.19	2.94	6.21	14.58
CH12020_1	CH12020_1_gl8	Andesite	284178.59	23513.44	20.82	58.30	116.82	326.69	33.30	272.06	13.82	842.21	42.00	75.76	5.26	1.45	3.83	3.03	6.34	16.31
CH12020_1	CH12020_1_gl9	Andesite	295314.55	23513.44	20.66	55.39	105.73	341.02	39.78	281.45	13.10	837.65	41.02	70.14	6.39	1.31	6.68	3.72	6.67	15.22

CH12020_1	CH12020_1_gl10	Andesite	290145.62	23513.44	21.27	56.05	110.73	321.95	40.35	289.12	14.28	841.14	40.37	70.58	7.19	1.16	7.03	3.51	6.94	17.72
CH12020_1	CH12020_1_gl11	Andesite	293685.92	23513.44	19.64	54.91	111.21	322.96	38.88	280.79	13.87	815.06	38.55	69.52	7.48	1.25	6.18	2.92	6.31	17.16
CH12020_1	CH12020_1_gl12	Andesite	302506.80	23513.44	19.61	55.40	112.01	334.70	38.23	286.26	14.90	851.16	40.38	71.28	7.30	1.17	6.94	2.95	7.13	17.81
CH12020_1	CH12020_1_gl13	Andesite	300280.79	23513.44	19.72	56.09	115.80	334.62	37.11	282.19	14.16	818.63	37.64	70.95	6.64	1.13	5.92	2.51	6.77	15.58
CH12020_1	CH12020_1_gl14	Andesite	255157.39	23513.44	18.24	48.60	107.35	336.84	37.19	276.80	12.12	768.39	38.32	65.02	7.21	1.06	6.48	3.00	6.54	17.57
CH12020_1	CH12020_1_gl15	Andesite	356181.58	23513.44	22.62	50.84	144.40	371.85	47.32	312.34	14.44	897.86	48.08	81.38	9.95	0.72	7.20	3.20	7.83	21.47
83069	83069_gl3	Andesite	314228.94	22798.74	21.64	55.79	138.38	342.70	44.16	306.86	15.67	941.75	45.17	80.69	7.89	1.18	6.57	3.56	7.31	30.88
83069	83069_gl4	Andesite	321810.73	22798.74	20.93	53.97	132.59	348.01	41.95	301.87	15.23	934.40	43.06	81.41	7.78	1.28	7.14	3.70	7.00	24.74
83069	83069_gl5	Andesite	380044.26	22798.74	22.50	62.46	164.45	341.82	37.03	317.79	16.93	868.64	45.22	80.90	7.64	1.39	7.18	3.22	7.85	48.44
83069	83069_gl6	Andesite	371535.67	22798.74	22.61	58.76	167.28	399.53	46.23	316.49	16.33	983.05	45.61	80.62	7.57	1.26	6.87	3.59	7.07	33.87
83069	83069_gl7	Andesite	332582.57	22798.74	20.63	50.10	149.43	324.29	43.59	315.69	14.05	898.69	42.00	77.27	2.86	0.96	6.51	3.07	7.24	19.23
83069	83069_gl11	Andesite	333972.57	22798.74	21.74	61.90	160.96	344.83	46.21	328.91	15.99	946.67	45.91	85.66	8.72	1.33	6.21	3.57	7.04	42.65
83069	83069_gl12	Andesite	332204.66	22798.74	17.65	59.72	149.16	333.26	40.51	296.68	15.66	962.20	42.76	77.72	6.85	1.23	5.43	2.49	5.71	18.26
83069	83069_gl14	Andesite	308600.57	22798.74	20.44	54.96	131.60	338.35	44.53	305.84	14.40	921.76	41.49	80.77	8.37	1.29	6.82	3.28	6.96	17.98
83069	83069_gl15	Andesite	260450.19	22798.74	17.79	44.86	109.28	307.08	35.98	257.51	12.77	740.93	35.31	65.95	7.53	1.14	6.41	2.99	6.43	16.54
CH12020_2	CH12020_2_gl1	Andesite	295690.76	23656.38	21.25	55.47	109.84	324.02	40.18	280.36	13.20	808.05	40.24	70.97	7.73	1.11	6.58	2.86	6.61	15.89
CH12020_2	CH12020_2_gl4	Andesite	378933.37	23656.38	23.50	62.81	136.83	321.78	34.95	280.38	14.07	854.15	37.17	71.79	6.41	1.17	6.67	2.49	6.71	21.49
CH12020_2	CH12020_2_gl5	Andesite	313434.64	23656.38	21.73	60.74	126.45	332.16	105.75	283.84	13.40	787.47	51.27	80.14	8.56	1.60	10.63	11.14	7.86	16.86
CH12020_2	CH12020_2_gl7	Andesite	323220.64	23656.38	21.93	58.58	112.48	323.25	38.60	278.68	14.59	831.15	39.77	71.10	7.10	1.29	5.90	3.04	6.72	17.14
CH12020_2	CH12020_2_gl8	Andesite	307363.90	23656.38	21.25	59.11	110.26	317.50	40.20	283.98	14.65	845.44	43.55	74.47	7.78	1.22	6.29	3.20	6.57	17.15
CH12020_2	CH12020_2_gl9	Andesite	235167.74	23656.38	19.93	54.08	101.14	310.77	55.33	271.76	13.82	854.48	45.42	72.53	8.01	1.75	10.71	4.51	6.27	15.02
CH12020_2	CH12020_2_gl11	Andesite	297564.28	23656.38	21.12	57.70	125.89	321.30	43.28	298.78	15.78	909.23	42.20	79.68	7.69	1.43	7.46	3.39	7.23	20.26
CH12020_2	CH12020_2_gl12	Andesite	299027.51	23656.38	21.66	53.94	118.03	320.68	43.49	295.47	14.36	886.25	42.94	79.68	8.60	1.45	6.81	3.78	6.76	18.37
CH12020_2	CH12020_2_gl14	Andesite	316543.65	23656.38	21.89	53.36	124.12	328.64	45.25	312.16	14.33	902.78	43.72	78.67	8.11	1.38	6.46	3.42	7.10	16.61
CH12020_2	CH12020_2_gl15	Andesite	350732.79	23656.38	20.17	67.85	135.94	319.87	34.10	251.21	16.66	946.34	37.28	83.50	7.42	1.33	5.77	2.96	6.26	25.05
CH12020_2	CH12020_2_gl16	Andesite	352634.46	23656.38	20.62	68.22	130.20	313.19	35.51	256.90	14.75	890.67	38.32	78.87	6.72	1.31	5.77	3.04	6.05	20.63
CH12020_2	CH12020_2_gl17	Andesite	364161.75	23656.38	21.75	62.29	137.82	323.93	37.48	282.39	15.33	899.77	40.38	80.43	8.51	1.18	6.55	3.16	6.57	24.08
CH12020_2	CH12020_2_gl18	Andesite	343588.20	23656.38	22.61	54.51	125.44	328.35	41.39	308.13	14.97	962.44	44.29	83.64	8.23	1.39	7.42	3.74	7.73	21.35
CH12020_2	CH12020_2_gl19	Andesite	364619.47	23656.38	22.06	62.97	141.62	320.65	37.24	270.43	17.31	971.77	42.15	86.09	7.43	1.39	6.42	3.41	6.71	23.79
CH12020_2	CH12020_2_gl20	Andesite	341294.52	23656.38	21.37	66.48	133.76	315.32	35.22	253.10	15.82	916.33	38.58	79.46	7.87	1.37	5.58	2.85	6.01	22.77
CH12020_2	CH12020_2_gl21	Andesite	305750.99	23656.38	21.31	54.15	119.93	310.86	41.24	282.49	14.12	921.26	40.99	75.64	8.31	1.24	7.19	3.51	7.98	19.71
CH12020_2	CH12020_2_gl23	Andesite	368112.73	23656.38	22.02	61.24	145.54	330.77	38.03	276.08	16.40	933.21	41.79	80.56	8.04	1.35	6.09	3.02	6.65	24.87
CH12020_2	CH12020_2_gl24	Andesite	334511.84	23656.38	21.24	66.16	134.05	316.77	35.59	252.63	15.80	924.65	38.16	86.39	7.41	1.28	6.55	3.19	6.13	23.39
CH12020_2	CH12020_2_gl25	Andesite	361657.51	23656.38	23.24	52.45	140.14	343.98	45.46	331.80	15.56	973.54	46.18	81.85	9.63	1.41	6.99	4.59	8.25	19.86
CH12020_2	CH12020_2_gl27	Andesite	230413.05	23656.38	16.52	43.35	86.96	340.67	39.52	249.29	11.87	752.21	35.36	60.73	5.59	1.00	4.15	3.52	5.70	17.63

Error (1SD) - Averages LAICPMS

Sample	Spot	Rocktype	Sc	V	Rb	Sr	Y	Zr	Nb	Ba	La	Ce	Sm	Eu	Dy	Yb	Hf	Pb
84014	all	Phase 2	1.35	0.16	8.65	3.70	5.15	10.80	1.30	46.69	1.68	3.55	0.71	0.08	0.54	0.32	0.43	3.85
83070	all	Phase 2	0.85	0.30	10.12	2.15	2.08	9.12	1.93	24.11	1.76	3.67	0.27	0.05	0.19	0.17	0.35	4.22
CH12021	all	Phase 2	1.16	0.16	8.02	3.23	4.36	9.37	1.35	43.92	1.61	3.84	0.49	0.05	0.51	0.30	0.35	4.03
CH19C005	all	Phase 2	1.40	0.22	15.17	5.31	5.07	11.03	1.40	51.39	1.95	3.61	0.57	0.10	0.83	0.40	0.47	4.00
CH19C003	all	Phase 1	0.77	0.28	4.81	6.43	2.28	14.45	1.61	37.80	1.39	2.72	0.37	0.09	0.29	0.18	0.42	3.22
CH19C009	all	Phase 1	0.81	0.32	4.52	5.61	2.41	18.19	1.65	31.57	2.07	2.75	0.44	0.09	0.31	0.16	0.49	2.85
CH19C007	all	Andesite	1.90	3.54	9.49	8.07	4.50	32.66	1.80	39.75	2.31	4.56	0.62	0.13	0.51	0.32	0.86	3.09
CH12020_1	all	Andesite	1.42	3.00	4.17	8.38	3.67	24.29	1.21	22.40	1.16	2.17	0.54	0.10	0.55	0.26	0.63	1.92
83069	all	Andesite	1.56	3.20	6.71	8.24	4.05	27.11	1.36	29.99	1.37	2.20	0.83	0.14	0.58	0.30	0.66	3.53
CH12020_2	all	Andesite	1.44	3.22	4.60	7.86	4.91	24.65	1.29	27.75	1.62	2.57	0.43	0.10	0.45	0.39	0.54	2.24

Error (1SD) Raw LAICPMS

Sample	Spot	Rocktype	Si	Ca	Sc	V	Rb	Sr	Y	Zr	Nb	Ba	La	Ce	Sm	Eu	Dy	Yb	Hf	Pb
84014	84014_gl1	Rhyolite	9298.67	102.50	1.16	0.07	5.24	3.76	4.64	9.91	1.27	31.61	1.27	3.17	0.49	0.04	0.32	0.22	0.32	3.90
84014	84014_gl2	Rhyolite	13871.63	102.50	1.36	0.17	5.38	3.87	4.65	10.36	1.12	44.41	1.43	2.54	0.55	0.08	0.37	0.31	0.52	3.33
84014	84014_gl3	Rhyolite	27279.18	102.50	1.89	0.13	12.29	8.38	5.17	11.88	1.73	79.29	3.56	6.15	0.67	0.23	0.82	0.44	0.56	4.14
84014	84014_gl4	Rhyolite	8067.95	102.50	1.58	No_Data	13.58	4.20	5.28	11.23	1.39	47.68	2.07	4.75	1.11	0.18	0.58	0.41	0.41	3.18
84014	84014_gl5	Rhyolite	20228.62	102.50	1.33	0.21	8.55	4.29	4.96	11.44	1.33	41.43	1.39	2.77	2.03	0.08	0.65	0.56	0.36	3.77
84014	84014_gl6	Rhyolite	6354.23	102.50	1.10	0.03	4.16	2.92	4.77	9.89	1.12	40.80	2.18	4.61	0.34	0.07	0.47	0.17	0.35	3.13
84014	84014_gl7	Rhyolite	5945.26	102.50	1.24	0.15	9.91	3.49	5.35	11.41	1.33	22.31	1.71	2.18	0.68	0.10	0.40	0.38	0.34	3.31
84014	84014_gl8	Rhyolite	7069.82	102.50	1.25	0.08	4.11	2.31	4.71	10.68	1.15	38.54	1.43	4.00	0.31	0.05	0.46	0.36	0.35	2.69
84014	84014_gl9	Rhyolite	8351.40	102.50	1.27	0.43	6.84	2.36	5.44	10.81	1.42	32.69	1.52	3.37	0.47	0.08	0.70	0.30	0.59	3.43
84014	84014_gl10	Rhyolite	7935.81	102.50	1.27	0.08	9.02	2.12	4.64	9.92	1.29	30.99	1.23	3.32	0.46	0.03	0.31	0.24	0.57	4.00
84014	84014_gl11	Rhyolite	11701.51	102.50	1.17	0.16	4.65	2.57	5.26	10.00	1.32	67.59	1.06	3.04	0.48	0.06	0.41	0.23	0.42	4.11
84014	84014_gl12	Rhyolite	16076.30	102.50	1.29	0.15	7.91	2.19	4.58	10.10	1.20	37.26	0.92	3.19	0.99	0.04	0.44	0.30	0.29	4.83
84014	84014_gl13	Rhyolite	13535.61	102.50	1.30	0.08	6.45	2.17	4.46	9.71	1.23	36.48	1.36	3.62	0.33	0.05	1.15	0.20	0.27	4.18
84014	84014_gl13	Rhyolite	8258.17	102.50	1.25	0.08	6.16	2.29	4.52	9.71	1.14	29.33	0.98	2.47	0.48	0.03	0.26	0.22	0.39	3.40
84014	84014_gl14	Rhyolite	25254.61	102.50	1.67	0.35	18.59	6.90	8.00	12.32	1.47	104.19	2.40	4.40	1.14	0.07	0.63	0.46	0.54	5.38
84014	84014_gl15	Rhyolite	13637.13	102.50	1.55	0.28	15.56	5.47	6.02	13.42	1.35	62.45	2.35	3.24	0.85	0.10	0.65	0.29	0.61	4.88
83070	83070_gl2	Rhyolite	5896.89	102.50	0.81	0.41	6.55	1.75	1.89	9.33	1.92	13.50	1.14	3.01	0.22	0.03	0.17	0.10	0.29	4.10
83070	83070_gl3	Rhyolite	19266.77	102.50	1.20	0.27	23.58	1.57	2.51	9.45	2.48	67.30	2.59	8.96	0.24	0.04	0.18	0.27	0.36	4.92
83070	83070_gl4	Rhyolite	13308.95	102.50	0.97	0.37	12.04	1.27	2.03	9.38	2.11	22.97	2.08	4.10	0.34	0.05	0.18	0.18	0.50	4.54
83070	83070_gl5	Rhyolite	9211.18	102.50	0.90	0.26	11.30	1.73	2.19	9.26	2.00	20.17	1.52	2.80	0.36	0.06	0.17	0.20	0.44	4.77
83070	83070_gl6	Rhyolite	13256.11	102.50	0.84	0.22	8.55	2.29	1.90	8.84	2.37	30.35	1.84	4.91	0.19	0.04	0.17	0.11	0.32	5.22
83070	83070_gl7	Rhyolite	9360.51	102.50	0.77	0.29	8.61	2.30	1.79	8.41	1.76	23.84	1.57	3.73	0.24	0.03	0.16	0.17	0.33	3.89
83070	83070_gl10	Rhyolite	7160.26	102.50	0.71	0.23	8.92	2.05	2.29	9.74	1.80	15.75	1.30	3.06	0.37	0.06	0.15	0.09	0.34	3.20
83070	83070_gl11	Rhyolite	11029.89	102.50	0.80	0.25	6.68	1.79	2.03	8.99	1.86	18.10	1.59	1.91	0.16	0.03	0.18	0.10	0.32	4.15
83070	83070_gl12	Rhyolite	12988.27	102.50	0.85	0.35	13.31	1.61	2.09	8.77	1.96	16.60	1.62	2.39	0.16	0.05	0.20	0.18	0.27	4.31
83070	83070_gl14	Rhyolite	8354.54	102.50	0.80	0.27	7.38	3.20	2.40	10.39	1.80	19.10	3.12	3.52	0.24	0.04	0.23	0.20	0.48	4.00
83070	83070_gl15	Rhyolite	10762.26	102.50	0.78	0.21	8.03	2.20	2.18	9.53	1.78	15.54	1.55	2.36	0.44	0.07	0.27	0.30	0.35	3.77
83070	83070_gl16	Rhyolite	7428.95	102.50	0.71	0.45	6.51	4.07	1.71	7.31	1.35	26.10	1.23	3.25	0.24	0.06	0.25	0.15	0.23	3.76
CH12021	CH12021_gl1	Rhyolite	10791.69	104.73	1.16	0.11	6.14	4.99	4.52	9.60	1.18	51.01	1.64	1.83	0.45	0.03	0.73	0.31	0.42	8.82
CH12021	CH12021_gl2	Rhyolite	14838.32	104.73	1.36	0.10	8.25	1.62	4.25	8.94	1.39	39.76	1.25	3.54	0.54	0.05	0.44	0.25	0.33	4.60

CH12021	CH12021_gl3	Rhyolite	14930.19	104.73	1.13	0.24	13.65	3.78	4.62	9.52	1.30	73.20	1.35	7.37	0.43	0.05	0.39	0.32	0.26	3.20
CH12021	CH12021_gl4	Rhyolite	14713.03	104.73	1.22	0.21	18.61	5.23	4.92	10.68	1.37	44.15	1.50	3.26	0.39	0.06	0.52	0.32	0.41	5.23
CH12021	CH12021_gl5	Rhyolite	14802.97	104.73	0.95	0.14	6.81	2.50	4.02	9.10	1.15	79.94	3.57	3.93	0.30	0.04	0.71	0.54	0.40	2.53
CH12021	CH12021_gl6	Rhyolite	29182.41	104.73	1.40	0.44	12.36	4.87	4.89	11.44	1.19	52.53	2.90	3.28	1.11	0.04	1.02	0.49	0.56	2.76
CH12021	CH12021_gl7	Rhyolite	18547.79	104.73	1.22	0.11	7.70	5.01	3.45	7.27	1.29	25.09	1.21	4.39	0.36	0.03	0.45	0.24	0.31	3.74
CH12021	CH12021_gl8	Rhyolite	6082.72	104.73	1.05	0.06	3.41	2.69	4.11	8.75	1.30	28.46	1.69	1.90	0.45	0.02	0.64	0.24	0.30	3.82
CH12021	CH12021_gl9	Rhyolite	8529.44	104.73	1.13	0.05	3.63	1.64	4.38	9.33	1.32	23.24	0.88	2.27	0.44	0.03	0.26	0.11	0.33	3.49
CH12021	CH12021_gl10	Rhyolite	11327.59	104.73	1.11	0.29	5.74	2.22	5.22	10.45	1.69	52.39	1.84	5.56	0.60	0.06	0.49	0.57	0.38	3.09
CH12021	CH12021_gl11	Rhyolite	9685.99	104.73	1.12	0.14	4.98	2.88	4.05	8.70	1.29	35.70	1.19	4.02	0.25	0.15	0.28	0.17	0.31	3.50
CH12021	CH12021_gl12	Rhyolite	8640.38	104.73	1.11	0.11	4.69	2.06	4.13	9.20	1.76	39.02	1.12	5.57	0.54	0.06	0.25	0.23	0.30	3.99
CH12021	CH12021_gl13	Rhyolite	6089.00	104.73	1.17	0.06	8.30	2.50	4.19	8.81	1.33	26.52	0.79	2.94	0.47	0.04	0.45	0.14	0.28	3.60
CH19C005	CH19C005_gl1	Rhyolite	26816.73	111.41	1.34	0.24	22.96	7.58	4.95	11.50	1.42	56.75	2.26	2.18	0.78	0.19	0.68	0.41	0.57	3.51
CH19C005	CH19C005_gl2	Rhyolite	34069.40	111.41	1.41	0.13	17.44	5.03	5.42	10.31	1.74	42.53	1.64	3.62	0.45	0.05	0.25	0.19	0.37	3.73
CH19C005	CH19C005_gl3	Rhyolite	30009.09	111.41	1.33	0.17	7.22	5.06	4.70	9.42	1.51	57.47	2.22	4.22	0.69	0.10	1.07	0.43	0.44	5.14
CH19C005	CH19C005_gl4	Rhyolite	38591.70	111.41	2.21	0.10	34.88	8.63	5.56	11.54	1.26	100.44	2.71	3.91	0.75	0.12	0.79	0.92	0.77	4.58
CH19C005	CH19C005_gl5	Rhyolite	8386.88	111.41	1.11	0.09	19.51	4.11	5.14	10.91	1.35	30.97	1.60	2.79	0.40	0.17	0.34	0.43	0.38	2.99
CH19C005	CH19C005_gl6	Rhyolite	18779.97	111.41	1.39	0.18	6.75	2.74	4.99	10.24	1.24	44.47	1.48	3.72	0.37	0.10	0.45	0.14	0.33	2.80
CH19C005	CH19C005_gl7	Rhyolite	7293.93	111.41	1.78	0.15	8.00	4.32	4.96	10.62	1.43	41.66	1.14	3.61	0.64	0.06	0.43	0.41	0.48	4.74
CH19C005	CH19C005_gl8	Rhyolite	30957.31	111.41	1.89	0.36	10.16	4.56	4.70	10.21	1.27	58.84	3.28	5.39	0.32	0.03	1.67	0.28	0.30	2.55
CH19C005	CH19C005_gl9	Rhyolite	12003.63	111.41	1.18	0.15	12.23	8.78	4.71	10.73	1.26	48.31	1.98	4.36	0.35	0.05	0.41	0.49	0.49	4.02
CH19C005	CH19C005_gl10	Rhyolite	7284.30	111.41	1.25	0.15	8.22	3.81	5.19	10.85	1.31	30.11	1.26	2.12	0.72	0.06	0.60	0.29	0.51	3.37
CH19C005	CH19C005_gl11	Rhyolite	24581.83	111.41	2.11	0.76	17.93	7.39	5.54	18.22	1.41	67.44	1.80	5.19	0.42	0.12	2.31	0.40	0.51	5.53
CH19C005	CH19C005_gl12	Rhyolite	47282.63	111.41	1.20	0.53	46.83	8.11	6.40	11.68	1.66	56.08	3.23	5.40	0.54	0.15	2.14	0.67	0.70	5.32
CH19C005	CH19C005_gl13	Rhyolite	14674.51	111.41	1.12	0.16	8.10	2.45	4.53	9.23	1.69	74.83	1.71	4.47	0.57	0.02	0.49	0.24	0.36	3.96
CH19C005	CH19C005_gl14	Rhyolite	8139.24	111.41	1.26	0.08	7.85	1.97	4.64	9.89	1.49	26.85	1.76	2.15	0.59	0.03	0.34	0.39	0.54	4.57
CH19C005	CH19C005_gl15	Rhyolite	20259.94	111.41	1.12	0.07	9.37	4.73	5.17	10.78	1.49	42.79	2.01	3.11	0.74	0.04	0.84	0.24	0.42	5.69
CH19C005	CH19C005_gl16	Rhyolite	6211.23	111.41	1.12	0.20	8.82	2.03	3.96	10.76	1.08	46.85	1.52	2.89	0.89	0.20	0.25	0.30	0.40	2.37
CH19C005	CH19C005_gl17	Rhyolite	15962.67	111.41	1.04	0.14	11.67	8.99	5.67	10.60	1.18	47.31	1.56	2.31	0.41	0.12	1.12	0.64	0.48	3.09
CH19C003	CH19C003_gl1	Rhyolite	21008.24	160.40	0.73	0.18	3.99	4.49	1.99	12.98	1.66	28.80	1.12	2.53	0.38	0.08	0.20	0.34	0.46	4.88
CH19C003	CH19C003_gl2	Rhyolite	21799.08	160.40	0.87	0.26	4.71	15.37	2.40	14.49	1.79	44.45	2.23	4.58	0.25	0.09	0.43	0.12	0.38	3.91
CH19C003	CH19C003_gl3	Rhyolite	16792.56	160.40	0.77	0.23	4.28	4.96	2.20	14.27	1.77	34.93	1.33	2.63	0.43	0.09	0.19	0.18	0.43	2.73
CH19C003	CH19C003_gl4	Rhyolite	8923.82	160.40	0.74	0.29	5.39	5.95	2.19	14.54	1.58	22.75	2.10	1.54	0.25	0.20	0.17	0.18	0.33	3.43
CH19C003	CH19C003_gl5	Rhyolite	7474.35	160.40	0.68	0.23	4.58	5.08	2.06	13.31	1.72	34.53	0.87	3.34	0.26	0.06	0.17	0.25	0.60	2.79
CH19C003	CH19C003_gl6	Rhyolite	9448.43	160.40	1.12	0.22	9.97	7.66	2.57	13.34	1.76	63.30	1.51	3.57	0.29	0.12	0.22	0.13	0.38	3.04
CH19C003	CH19C003_gl7	Rhyolite	7167.49	160.40	0.68	0.18	3.31	4.28	2.90	16.05	1.38	36.31	1.35	2.06	0.41	0.13	0.34	0.22	0.50	3.32
CH19C003	CH19C003_gl8	Rhyolite	7742.15	160.40	0.67	0.23	4.14	5.28	2.28	14.25	1.54	27.59	0.97	2.09	0.25	0.06	0.48	0.14	0.50	2.78
CH19C003	CH19C003_gl9	Rhyolite	10980.18	160.40	0.90	0.41	4.54	17.38	2.71	18.86	1.40	121.71	2.62	2.73	0.40	0.11	0.41	0.28	0.49	3.08
CH19C003	CH19C003_gl10	Rhyolite	5937.13	160.40	0.61	0.21	4.74	5.68	2.45	16.38	1.53	25.78	1.14	2.50	0.58	0.07	0.54	0.13	0.36	3.38
CH19C003	CH19C003_gl11	Rhyolite	6949.59	160.40	0.79	0.22	4.21	4.27	2.01	12.58	1.55	26.25	1.19	2.28	0.32	0.07	0.44	0.11	0.37	4.05
CH19C003	CH19C003_gl12	Rhyolite	7738.48	160.40	0.66	0.19	2.68	4.00	2.08	13.86	1.51	25.21	1.12	2.21	0.24	0.04	0.14	0.22	0.45	2.53
CH19C003	CH19C003_gl13	Rhyolite	8584.47	160.40	0.72	0.21	4.22	3.74	1.98	13.82	1.55	25.15	0.94	2.11	0.58	0.04	0.20	0.17	0.32	2.79
CH19C003	CH19C003_gl14	Rhyolite	5812.13	160.40	0.74	0.27	3.41	3.77	2.11	12.96	1.79	21.09	0.85	2.72	0.32	0.11	0.15	0.14	0.39	2.79
CH19C003	CH19C003_gl16	Rhyolite	6457.51	160.40	0.89	0.96	8.04	4.55	2.23	14.98	1.62	29.09	1.50	3.99	0.66	0.07	0.27	0.08	0.37	2.80
CH19C009	CH19C009_gl1	Rhyolite	9824.01	161.51	0.74	0.18	5.60	4.10	2.44	17.89	1.53	20.08	1.07	2.24	0.33	0.13	0.22	0.16	0.49	3.09
CH19C009	CH19C009_gl2	Rhyolite	7949.31	161.51	0.85	0.22	3.12	6.38	2.78	19.62	1.83	27.82	4.25	3.01	1.01	0.17	0.34	0.13	0.44	2.69
CH19C009	CH19C009_gl3	Rhyolite	11053.85	161.51	0.78	0.24	2.80	3.80	2.30	15.69	1.53	25.70	1.71	1.95	0.51	0.04	0.28	0.18	0.56	2.87
CH19C009	CH19C009_gl4	Rhyolite	11657.23	161.51	1.40	0.47	6.65	7.41	3.11	34.49	1.95	42.90	4.88	1.96	0.65	0.07	0.32	0.10	0.49	3.94
CH19C009	CH19C009_gl5	Rhyolite	6114.08	161.51	0.70	0.28	2.84	5.04	2.54	15.83	1.50	27.57	1.01	2.53	0.29	0.13	0.31	0.17	0.42	2.79
CH19C009	CH19C009_gl6	Rhyolite	15391.71	161.51	0.79	0.23	3.87	4.74	2.74	17.89	1.61	32.41	3.53	2.80	0.72	0.11	0.40	0.13	0.49	3.28
CH19C009	CH19C009_gl7	Rhyolite	14860.29	161.51	0.84	0.27	8.73	7.79	2.33	26.76	1.71	30.30	1.87	2.84	0.33	0.07	0.16	0.14	0.67	2.75
CH19C009	CH19C009_gl8	Rhyolite	14809.85	161.51	0.94	0.27	5.21	4.82	2.13	17.07	2.00	29.06	1.67	1.74	0.57	0.06	0.27	0.32	0.61	2.74
CH19C009	CH19C009_gl9	Rhyolite	6613.86	161.51	0.70	0.18	3.66	5.99	2.39	13.71	1.58	33.13	1.60	4.41	0.25	0.06	0.33	0.13	0.40	3.04
CH19C009	CH19C009_gl10	Rhyolite	7011.84	161.51	0.68	0.20	3.61	4.77	1.99	13.52	1.54	22.60	1.00	3.63	0.21	0.09	0.27	0.12	0.51	2.58
CH19C009	CH19C009_gl14	Rhyolite	10220.08	161.51	0.92	0.53	5.55	7.39	2.57	18.94	1.73	40.01	2.56	4.04	0.51	0.11	0.43	0.32	0.51	2.11
CH19C009	CH19C009_gl15	Rhyolite	11959.35	161.51	0.69	0.31	3.12	5.65	1.95	12.81	1.41	23.35	0.99	1.81	0.32	0.06	0.29	0.14	0.57	2.94
CH19C009	CH19C009_gl16	Rhyolite	10130.63	161.51	0.64	0.19	5.74	7.05	2.13	14.96	1.56	59.27	1.05	3.15	0.29	0.09	0.47	0.10	0.41	3.42

CH19C009	CH19C009_gl17	Rhyolite	13262.63	161.51	0.72	0.17	2.90	5.37	2.44	16.14	1.38	24.67	1.67	1.76	0.24	0.09	0.21	0.12	0.43	2.45
CH19C009	CH19C009_gl18	Rhyolite	17059.02	161.51	0.66	0.21	4.74	5.53	2.46	16.24	1.51	30.17	1.80	2.74	0.46	0.10	0.36	0.17	0.46	2.60
CH19C009	CH19C009_gl19	Rhyolite	7465.39	161.51	0.90	0.29	3.45	4.49	2.63	19.34	1.81	29.32	1.54	3.64	0.36	0.08	0.38	0.11	0.51	2.47
CH19C009	CH19C009_gl20	Rhyolite	20255.04	161.51	0.87	1.20	5.29	5.14	1.98	18.37	1.91	38.34	2.97	2.47	0.38	0.09	0.23	0.25	0.42	2.64
CH19C007	CH19C007_gl2	Andesite	12837.85	393.04	1.69	2.29	9.90	5.84	4.25	29.19	1.42	25.05	1.35	2.43	0.42	0.19	0.46	0.35	0.58	2.20
CH19C007	CH19C007_gl3	Andesite	15222.25	393.04	1.67	2.13	8.22	7.92	4.20	29.12	1.34	21.29	1.29	2.17	0.42	0.09	0.27	0.15	1.09	2.22
CH19C007	CH19C007_gl5	Andesite	36374.22	393.04	2.59	3.18	14.30	7.59	5.27	31.81	2.53	56.47	3.19	5.24	0.84	0.09	0.61	0.38	0.80	6.15
CH19C007	CH19C007_gl12	Andesite	25798.96	393.04	1.54	5.75	16.04	6.35	4.17	34.41	2.46	71.16	3.53	6.64	0.58	0.07	0.48	0.30	0.99	2.91
CH19C007	CH19C007_gl14	Andesite	6961.60	393.04	1.77	4.66	3.12	10.24	4.52	39.13	1.59	27.04	1.86	7.62	0.98	0.17	0.51	0.36	0.78	2.73
CH19C007	CH19C007_gl15	Andesite	7655.39	393.04	2.11	3.23	5.34	10.48	4.61	32.26	1.44	37.46	2.64	3.28	0.45	0.17	0.75	0.38	0.94	2.33
CH12020_1	CH12020_1_gl1	Andesite	8080.46	372.65	1.79	4.33	3.58	7.72	4.74	25.57	1.13	47.78	1.67	5.82	0.38	0.08	0.96	0.30	1.05	2.17
CH12020_1	CH12020_1_gl2	Andesite	7223.14	372.65	1.25	3.16	2.69	6.13	3.45	23.55	1.13	23.09	0.87	1.79	0.31	0.08	0.40	0.18	0.48	1.69
CH12020_1	CH12020_1_gl3	Andesite	7508.90	372.65	1.47	3.10	2.97	7.77	3.51	23.67	1.20	17.51	0.93	1.61	0.51	0.11	0.31	0.14	0.44	1.74
CH12020_1	CH12020_1_gl6	Andesite	14060.08	372.65	1.39	3.26	5.00	5.43	3.45	23.09	1.17	16.20	0.86	2.07	0.29	0.06	0.31	0.19	0.43	2.23
CH12020_1	CH12020_1_gl7	Andesite	14854.49	372.65	1.36	2.87	3.76	6.00	3.42	23.36	1.17	19.70	1.03	1.91	0.34	0.08	0.27	0.29	0.57	2.81
CH12020_1	CH12020_1_gl8	Andesite	8259.86	372.65	1.46	3.87	2.55	10.64	3.86	23.42	1.25	28.02	1.58	2.09	1.67	0.14	2.08	0.21	0.82	1.62
CH12020_1	CH12020_1_gl9	Andesite	11738.24	372.65	1.35	2.66	6.65	5.44	3.48	23.22	1.33	16.97	0.95	2.09	0.38	0.07	0.63	0.46	0.47	1.65
CH12020_1	CH12020_1_gl10	Andesite	6422.69	372.65	1.69	2.52	2.98	7.44	3.52	23.80	1.17	15.85	1.01	1.50	0.47	0.07	0.21	0.12	0.55	1.80
CH12020_1	CH12020_1_gl11	Andesite	9833.63	372.65	1.25	2.39	5.85	6.40	3.38	23.34	1.16	16.39	0.80	1.57	0.29	0.06	0.19	0.18	0.41	1.73
CH12020_1	CH12020_1_gl12	Andesite	10273.39	372.65	1.24	2.76	3.88	6.75	3.36	23.64	1.26	19.50	0.83	1.92	0.23	0.07	0.47	0.19	0.51	1.82
CH12020_1	CH12020_1_gl13	Andesite	5012.28	372.65	1.37	2.65	2.41	5.45	3.40	23.24	1.23	16.78	0.88	1.61	0.41	0.08	0.25	0.18	0.55	1.57
CH12020_1	CH12020_1_gl14	Andesite	5607.76	372.65	1.19	2.55	3.38	7.64	3.35	22.99	1.02	23.75	1.35	1.41	0.63	0.14	0.44	0.42	0.54	1.77
CH12020_1	CH12020_1_gl15	Andesite	22896.35	372.65	1.58	2.92	8.53	26.17	4.82	32.86	1.50	29.73	2.37	2.81	1.14	0.23	0.62	0.46	1.34	2.35
83069	83069_gl3	Andesite	14077.52	361.32	1.39	2.55	3.78	5.67	3.92	25.36	1.27	23.89	1.39	1.71	0.42	0.07	0.44	0.21	0.55	4.86
83069	83069_gl4	Andesite	13848.11	361.32	1.34	2.83	10.22	8.60	3.75	25.06	1.41	24.14	1.04	1.95	0.30	0.11	0.41	0.17	0.47	2.63
83069	83069_gl5	Andesite	20351.10	361.32	1.63	3.77	6.99	11.53	4.19	26.18	1.55	31.79	1.56	2.26	0.88	0.18	0.81	0.16	0.83	6.61
83069	83069_gl6	Andesite	8659.33	361.32	1.42	2.99	5.85	6.91	4.11	26.71	1.36	27.82	1.58	1.72	0.39	0.12	0.48	0.47	0.55	3.78
83069	83069_gl7	Andesite	12345.49	361.32	1.79	2.51	4.68	6.82	3.96	30.16	1.25	28.72	1.13	1.71	3.14	0.35	0.54	0.45	1.20	1.92
83069	83069_gl11	Andesite	15076.45	361.32	1.52	2.92	3.79	10.08	4.94	29.31	1.41	24.97	1.29	1.91	0.62	0.09	0.40	0.29	0.52	4.21
83069	83069_gl12	Andesite	10522.21	361.32	1.71	3.15	12.08	7.51	3.56	24.81	1.53	18.15	1.16	1.95	0.46	0.14	1.51	0.50	0.84	2.16
83069	83069_gl14	Andesite	6291.82	361.32	1.47	2.48	3.73	10.73	4.26	25.64	1.17	33.53	1.17	2.12	0.92	0.10	0.30	0.21	0.49	1.79
83069	83069_gl15	Andesite	25894.23	361.32	1.76	5.63	9.34	6.28	3.75	30.77	1.29	56.86	2.00	4.45	0.38	0.09	0.29	0.26	0.48	3.84
CH12020_2	CH12020_2_gl1	Andesite	6755.06	437.97	1.39	3.25	3.38	7.82	3.49	23.37	1.27	24.57	1.14	1.58	0.39	0.07	0.20	0.21	0.46	1.54
CH12020_2	CH12020_2_gl4	Andesite	14872.02	437.97	1.78	3.30	7.26	9.65	3.76	24.13	1.19	24.97	1.41	2.06	0.67	0.06	0.41	0.53	0.50	2.33
CH12020_2	CH12020_2_gl5	Andesite	11637.86	437.97	1.54	2.82	3.32	7.67	25.10	24.59	1.18	26.33	2.81	3.78	0.97	0.32	0.85	3.04	0.82	1.71
CH12020_2	CH12020_2_gl7	Andesite	13414.14	437.97	1.41	2.80	3.99	6.08	3.40	23.06	1.22	24.40	0.90	2.32	0.39	0.08	0.35	0.16	0.45	2.03
CH12020_2	CH12020_2_gl8	Andesite	6333.24	437.97	1.40	2.75	3.50	5.91	3.78	27.14	1.22	21.11	1.27	2.01	0.33	0.05	0.27	0.23	0.47	1.79
CH12020_2	CH12020_2_gl9	Andesite	12316.26	437.97	1.32	3.15	6.32	7.41	7.30	23.95	1.26	45.31	3.38	3.29	0.40	0.35	1.67	0.54	0.50	1.64
CH12020_2	CH12020_2_gl11	Andesite	9783.97	437.97	1.36	3.24	3.20	7.01	4.36	26.30	1.31	19.27	1.20	1.92	0.32	0.07	0.23	0.22	0.54	1.98
CH12020_2	CH12020_2_gl12	Andesite	13006.55	437.97	1.37	2.56	5.31	6.77	4.08	24.64	1.20	30.29	1.02	2.11	0.50	0.06	0.23	0.13	0.52	2.07
CH12020_2	CH12020_2_gl14	Andesite	5429.93	437.97	1.39	2.59	2.72	7.91	4.06	25.92	1.17	19.15	1.04	1.96	0.37	0.09	0.35	0.13	0.51	1.75
CH12020_2	CH12020_2_gl15	Andesite	7080.19	437.97	1.27	3.04	2.94	6.83	3.17	21.09	1.37	20.44	1.19	1.95	0.30	0.05	0.21	0.12	0.43	2.44
CH12020_2	CH12020_2_gl16	Andesite	22595.85	437.97	1.42	4.54	6.23	12.13	3.11	21.54	1.31	43.23	1.24	3.33	0.28	0.08	0.21	0.15	0.39	4.62
CH12020_2	CH12020_2_gl17	Andesite	13347.73	437.97	1.63	3.22	6.02	6.11	3.36	23.32	1.46	21.42	0.88	2.29	0.54	0.06	0.34	0.29	0.46	2.89
CH12020_2	CH12020_2_gl18	Andesite	9308.13	437.97	1.46	2.69	3.11	6.61	3.79	26.08	1.37	20.36	0.97	1.82	0.32	0.08	0.26	0.17	0.69	2.19
CH12020_2	CH12020_2_gl19	Andesite	9432.94	437.97	1.38	2.83	4.27	6.58	3.32	24.24	1.41	22.48	1.04	1.93	0.26	0.05	0.27	0.19	0.45	2.34
CH12020_2	CH12020_2_gl20	Andesite	9133.03	437.97	1.41	3.23	2.68	6.09	3.41	21.73	1.31	22.31	1.09	1.66	0.29	0.05	0.20	0.14	0.40	2.19
CH12020_2	CH12020_2_gl21	Andesite	9000.23	437.97	1.45	3.09	2.88	10.47	4.15	25.13	1.15	25.85	2.75	2.76	0.63	0.11	0.35	0.25	0.90	2.04
CH12020_2	CH12020_2_gl23	Andesite	10348.22	437.97	1.43	3.00	4.73	7.18	3.38	23.39	1.35	26.49	1.17	2.32	0.29	0.04	0.22	0.16	0.45	2.61
CH12020_2	CH12020_2_gl24	Andesite	9996.75	437.97	1.38	3.09	6.06	7.02	3.24	21.46	1.46	22.41	0.90	2.31	0.23	0.08	0.27	0.11	0.42	2.30
CH12020_2	CH12020_2_gl25	Andesite	16324.95	437.97	1.52	2.60	5.88	8.13	4.10	27.79	1.38	30.74	2.05	4.02	0.61	0.07	0.51	0.37	0.52	2.14
CH12020_2	CH12020_2_gl27	Andesite	18980.72	437.97	1.53	6.55	8.26	13.87	3.88	34.22	1.12	63.84	5.00	5.92	0.51	0.14	1.70	0.57	0.85	2.26

0.0
0.0
0.0
0.0
0.0
0.0
0.0
0.0
0.0
0.0
0.0
0.0
0.0
0.0
0.0
0.0
0.0
0.0
0.0
0.0
0.0
0.0
0.0
0.0
0.0
0.0
0.0
0.0
0.0
0.0
0.0
0.0
0.0
0.0
0.0
0.0
0.0
0.0
0.0
0.0
0.0
0.0
0.0
0.0
0.0
0.0
0.0
0.0
0.0
0.0
0.0
0.0
0.0
0.0
0.0

Feldspar

Rock Type	Comment	Spot	Cao	K2o	Sio2	Al2o3	Na2o	Mgo	Feo	Total	An	Ab	Or
Phase 1 rhyolit	CH12022_Fspar1_core1	Core	7.9	0.5	58.7	26.6	6.4	0.0	0.2	100.2	0.4	0.6	0.0
Phase 1 rhyolit	CH12022_Fspar1_core2	Core	8.4	0.4	57.3	26.5	6.3	0.0	0.2	99.1	0.4	0.6	0.0
Phase 1 rhyolit	CH12022_Fspar1_core3	Core	8.0	0.5	58.5	26.4	6.4	0.0	0.2	100.0	0.4	0.6	0.0
Phase 1 rhyolit	CH12022_Fspar2_core1	Core	6.5	0.7	59.8	24.5	7.1	0.0	0.2	98.9	0.3	0.6	0.0
Phase 1 rhyolit	CH12022_Fspar2_core2	Core	7.9	0.5	58.6	25.9	6.6	0.0	0.2	99.7	0.4	0.6	0.0
Phase 1 rhyolit	CH12022_Fspar2_core3	Core	7.7	0.6	58.7	26.1	6.5	0.0	0.2	99.7	0.4	0.6	0.0
Phase 1 rhyolit	CH12022_Fspar3_core1	Core	8.4	0.4	57.8	26.5	6.3	0.0	0.2	99.6	0.4	0.6	0.0
Phase 1 rhyolit	CH12022_Fspar3_core2	Core	8.0	0.5	58.3	26.2	6.5	0.0	0.3	99.7	0.4	0.6	0.0
Phase 1 rhyolit	CH12022_Fspar3_core3	Core	8.3	0.4	57.7	26.4	6.3	0.0	0.2	99.4	0.4	0.6	0.0
Phase 1 rhyolit	CH12022_Fspar4_core1	Core	7.0	0.6	59.3	25.5	6.9	0.0	0.2	99.5	0.3	0.6	0.0
Phase 1 rhyolit	CH12022_Fspar4_core2	Core	7.2	0.6	59.2	25.6	6.9	0.0	0.2	99.7	0.4	0.6	0.0
Phase 1 rhyolit	CH12022_Fspar4_core3	Core	7.2	0.5	59.5	25.6	6.9	0.0	0.2	99.9	0.4	0.6	0.0
Phase 1 rhyolit	CH12022_Fspar5_core1	Core	8.1	0.5	57.1	25.9	6.2	0.0	0.2	97.9	0.4	0.6	0.0
Phase 1 rhyolit	CH12022_Fspar5_core3	Core	8.2	0.4	55.9	25.6	6.1	0.0	0.2	96.4	0.4	0.6	0.0
Phase 1 rhyolit	CH19C002_Fspar1_Core1	Core	8.0	0.5	57.8	26.1	6.5	0.0	0.2	99.1	0.4	0.6	0.0
Phase 1 rhyolit	CH19C002_Fspar1_core2	Core	8.1	0.5	57.8	26.3	6.5	0.0	0.2	99.3	0.4	0.6	0.0
Phase 1 rhyolit	CH19C002_Fspar1_Core3	Core	8.2	0.4	57.5	26.3	6.4	0.0	0.2	99.0	0.4	0.6	0.0
Phase 1 rhyolit	CH19C002_Fspar2_Core1	Core	8.0	0.5	58.2	26.3	6.6	0.0	0.2	99.7	0.4	0.6	0.0
Phase 1 rhyolit	CH19C002_Fspar2_Core2	Core	7.8	0.5	58.4	26.0	6.5	0.0	0.2	99.4	0.4	0.6	0.0
Phase 1 rhyolit	CH19C002_Fspar2_Core3	Core	7.9	0.5	58.4	26.2	6.5	0.0	0.2	99.7	0.4	0.6	0.0
Phase 1 rhyolit	CH19C002_Fspar3_core1	Core	8.6	0.4	57.4	26.9	6.2	0.0	0.3	99.8	0.4	0.6	0.0
Phase 1 rhyolit	CH19C002_Fspar3_core2	Core	8.3	0.4	57.4	26.6	6.3	0.0	0.4	99.4	0.4	0.6	0.0
Phase 1 rhyolit	CH19C002_Fspar3_core3	Core	9.0	0.4	56.6	27.1	6.1	0.0	0.3	99.5	0.4	0.5	0.0
Phase 1 rhyolit	CH19C002_Fspar4_Core1	Core	8.3	0.5	58.2	26.4	6.4	0.0	0.2	100.1	0.4	0.6	0.0
Phase 1 rhyolit	CH19C002_Fspar4_Core2	Core	6.8	0.6	59.6	25.1	7.0	0.0	0.2	99.3	0.3	0.6	0.0
Phase 1 rhyolit	CH19C002_Fspar4_Core3	Core	8.0	0.5	58.3	26.3	6.5	0.0	0.2	99.8	0.4	0.6	0.0
Phase 2 Rhyolit	CH12021_Fspar1_core1	Core	6.3	0.8	60.8	24.6	7.2	0.0	0.1	99.8	0.3	0.6	0.0
Phase 2 Rhyolit	CH12021_Fspar1_core2	Core	6.5	0.8	59.3	24.7	7.2	0.0	0.1	98.5	0.3	0.6	0.0
Phase 2 Rhyolit	CH12021_Fspar1_core3	Core	6.4	0.8	60.4	24.9	7.1	0.0	0.1	99.7	0.3	0.6	0.0
Phase 2 Rhyolit	CH12021_Fspar_Kcore1	Core	16.4	0.2	48.5	33.3	2.5	0.0	0.3	101.2	0.8	0.2	0.0
Phase 2 Rhyolit	CH12021_Fspar_Kcore2	Core	16.8	0.1	48.1	33.8	2.2	0.0	0.1	101.1	0.8	0.2	0.0
Phase 2 Rhyolit	CH12021_Fspar_Kcore3	Core	16.8	0.1	48.0	33.6	2.2	0.0	0.2	100.8	0.8	0.2	0.0
Phase 2 Rhyolit	CH12021_Fspar2_core1	Core	6.3	0.8	60.5	24.9	7.4	0.0	0.1	100.0	0.3	0.6	0.0
Phase 2 Rhyolit	CH12021_Fspar2_core2	Core	6.1	0.8	60.9	24.8	7.3	0.0	0.1	100.0	0.3	0.7	0.0
Phase 2 Rhyolit	CH12021_Fspar2_core3	Core	6.2	0.8	60.8	24.9	7.3	0.0	0.1	100.1	0.3	0.7	0.0
Phase 2 Rhyolit	CH12021_Fspar3_core1	Core	8.8	0.5	57.8	27.2	6.2	0.0	0.1	100.6	0.4	0.5	0.0
Phase 2 Rhyolit	CH12021_Fspar3_core2	Core	8.7	0.5	57.7	27.1	6.2	0.0	0.2	100.4	0.4	0.5	0.0
Phase 2 Rhyolit	CH12021_Fspar3_core3	Core	8.8	0.5	57.7	27.0	6.2	0.0	0.2	100.2	0.4	0.5	0.0
Phase 2 Rhyolit	CH12021_Fspar5_core1	Core	5.5	1.0	61.2	24.1	7.2	0.0	0.1	99.3	0.3	0.7	0.1
Phase 2 Rhyolit	CH12021_Fspar5_core2	Core	5.4	1.1	61.5	23.9	7.4	0.0	0.1	99.3	0.3	0.7	0.1
Phase 2 Rhyolit	CH12021_Fspar5_core3	Core	5.4	1.0	61.4	23.9	7.6	0.0	0.1	99.4	0.3	0.7	0.1
Phase 2 Rhyolit	83070_Fspar1_core1	Core	6.2	0.8	60.9	25.2	7.4	0.0	0.1	100.6	0.3	0.7	0.0
Phase 2 Rhyolit	83070_Fspar1_core2	Core	6.6	0.8	60.5	25.4	7.3	0.0	0.1	100.7	0.3	0.6	0.0
Phase 2 Rhyolit	83070_Fspar1_core3	Core	6.8	0.7	60.2	25.5	7.2	0.0	0.1	100.5	0.3	0.6	0.0
Phase 2 Rhyolit	83070_Fspar3_core1	Core	6.9	0.6	59.3	25.5	6.9	0.0	0.1	99.4	0.3	0.6	0.0
Phase 2 Rhyolit	83070_Fspar3_core2	Core	7.0	0.7	59.6	25.4	7.0	0.0	0.1	99.8	0.3	0.6	0.0
Phase 2 Rhyolit	83070_Fspar3_core3	Core	6.9	0.7	59.6	25.6	6.9	0.0	0.1	99.8	0.3	0.6	0.0
Phase 2 Rhyolit	83070_Fspar4_core1	Core	6.0	0.8	61.0	24.8	7.4	0.0	0.1	100.1	0.3	0.7	0.0
Phase 2 Rhyolit	83070_Fspar4_core2	Core	6.3	0.8	61.0	25.0	7.4	0.0	0.1	100.6	0.3	0.6	0.0
Phase 2 Rhyolit	83070_Fspar4_core3	Core	6.7	0.7	60.0	25.2	7.1	0.0	0.1	99.8	0.3	0.6	0.0

		_Fspar5_core1											
0.0	Phase 2 Rhyolit	_Fspar5_core2	Core	6.3	0.8	60.6	25.0	7.3	0.0	0.1	100.0	0.3	0.6
0.0	Phase 2 Rhyolit	_Fspar5_core3	Core	6.2	0.8	60.9	25.1	7.3	0.0	0.1	100.5	0.3	0.6
0.0	Phase 2 Rhyolit 83070	_Fspar7_core1	Core	6.2	0.8	60.5	24.9	7.3	0.0	0.1	99.9	0.3	0.6
0.0	Phase 2 Rhyolit 83070	_Fspar7_core2	Core	6.6	0.8	60.6	25.2	7.1	0.0	0.1	100.4	0.3	0.6
0.0	Phase 2 Rhyolit 83070	_Fspar7_core3	Core	6.5	0.7	59.9	25.0	7.2	0.0	0.1	99.4	0.3	0.6
0.0	Phase 2 Rhyolit 83070		Core	6.3	0.8	60.7	25.1	7.3	0.0	0.1	100.3	0.3	0.6
0.0	Andesite 83070	CH120202_Fspar1_score1	Score	16.0	0.2	48.9	33.1	2.5	0.0	0.3	100.9	0.8	0.2
0.0	Andesite 83070	CH120202_Fspar1_score2	Score	17.2	0.1	47.3	34.2	1.9	0.0	0.2	101.0	0.8	0.2
0.0	Andesite	CH120202_Fspar1_score3	Score	16.4	0.2	48.4	33.3	2.4	0.0	0.2	100.9	0.8	0.2
0.0	Andesite	CH120202_Fspar2_score1	Score	15.9	0.2	49.1	33.1	2.6	0.0	0.2	101.1	0.8	0.2
0.0	Andesite	CH120202_Fspar2_score2	Score	17.4	0.1	47.2	34.3	1.9	0.0	0.2	101.1	0.8	0.2
0.0	Andesite	CH120202_Fspar2_score3	Score	17.2	0.1	47.0	34.0	1.9	0.0	0.2	100.4	0.8	0.2
0.0	Andesite	CH120202_Fspar3_core1	G1core	16.7	0.1	48.1	33.9	2.1	0.0	0.2	101.1	0.8	0.2
0.0	Andesite	CH120202_Fspar3_core2	G1core	16.9	0.1	47.8	33.8	2.1	0.0	0.2	101.0	0.8	0.2
0.0	Andesite	CH120202_Fspar3_core3	G1core	16.4	0.2	48.3	33.3	2.4	0.0	0.2	100.8	0.8	0.2
0.0	Andesite	CH120202_Fspar4_core1	G1core	17.1	0.1	47.8	34.1	2.0	0.0	0.2	101.4	0.8	0.2
0.0	Andesite	CH120202_Fspar4_core2	G1core	17.4	0.1	47.1	34.5	1.9	0.0	0.2	101.2	0.8	0.2
0.0	Andesite	CH120202_Fspar4_core3	G1core	17.2	0.1	47.7	34.1	2.0	0.0	0.2	101.4	0.8	0.2
0.0	Andesite	CH120202_Fspar5_core1	Core	17.1	0.1	47.8	34.1	2.1	0.0	0.2	101.5	0.8	0.2
0.0	Andesite	CH120202_Fspar5_core2	Core	17.1	0.1	47.6	34.4	2.0	0.0	0.3	101.6	0.8	0.2
0.0	Andesite	CH120202_Fspar5_core3	Core	17.3	0.1	47.4	34.4	2.0	0.0	0.3	101.5	0.8	0.2
0.0	Andesite	CH120202_Fspar6_core1	Core	17.1	0.1	47.7	34.1	2.0	0.0	0.2	101.2	0.8	0.2
0.1	Andesite	CH120202_Fspar6_core2	Core	17.2	0.1	47.4	34.3	2.0	0.0	0.2	101.2	0.8	0.2
0.1	Andesite	CH120202_Fspar6_core3	Core	17.3	0.1	47.3	34.2	2.0	0.0	0.2	101.0	0.8	0.2
0.1	Andesite	CH120202_Fspar7_core1	Core	16.9	0.1	48.0	33.8	2.2	0.0	0.2	101.3	0.8	0.2
0.0	Andesite	CH120202_Fspar7_core2	Core	16.9	0.1	47.9	33.8	2.2	0.0	0.2	101.2	0.8	0.2
0.1	Andesite	CH120202_Fspar7_core3	Core	16.3	0.1	48.6	33.4	2.4	0.0	0.2	101.2	0.8	0.2
0.1	Andesite	CH120202_Fspar8_core1	Core	17.5	0.1	47.3	34.4	1.9	0.0	0.2	101.4	0.8	0.2
0.1	Andesite	CH120202_Fspar8_core2	Core	18.2	0.1	46.1	35.0	1.4	0.0	0.2	101.0	0.9	0.1
0.0	Andesite	CH120202_Fspar8_core3	Core	18.1	0.1	46.3	34.9	1.5	0.0	0.2	101.2	0.9	0.1
0.0	Andesite	CH120202_Fspar9_core1	Core	17.2	0.1	47.6	34.1	2.1	0.0	0.3	101.4	0.8	0.2
0.0	Andesite	CH120202_Fspar9_core2	Core	16.3	0.1	48.7	33.6	2.4	0.0	0.2	101.4	0.8	0.2
0.0	Andesite	CH120202_Fspar10_core1	Core	17.0	0.1	47.7	34.1	2.0	0.0	0.3	101.2	0.8	0.2
0.0	Andesite	CH120202_Fspar10_core2	Core	17.0	0.1	47.7	33.8	2.1	0.0	0.2	101.0	0.8	0.2
0.0	Andesite	CH120202_Fspar12_core1	G1core	16.8	0.2	48.2	33.9	2.2	0.0	0.2	101.5	0.8	0.2
0.0	Andesite	CH120202_Fspar13_core1	Core	15.8	0.1	49.4	32.9	2.7	0.0	0.2	101.2	0.8	0.2
0.0	Andesite	CH120202_Fspar13_core2	Core	17.1	0.1	48.1	33.8	2.2	0.0	0.3	101.5	0.8	0.2
0.0	Andesite	CH19C007_Fspar1_score1	Core	16.9	0.1	47.8	33.8	2.0	0.0	0.2	100.9	0.8	0.2
0.0	Andesite	CH19C007_Fspar1_score2	Core	16.9	0.1	47.8	34.0	2.1	0.0	0.3	101.2	0.8	0.2
0.0	Andesite	CH19C007_Fspar2_core1	G1core	15.8	0.2	49.0	33.0	2.6	0.0	0.3	100.9	0.8	0.2
0.0	Andesite	CH19C007_Fspar2_core2	G1core	16.4	0.1	48.4	33.2	2.3	0.0	0.2	100.7	0.8	0.2
0.0	Andesite	CH19C007_Fspar3_core1	Core	16.4	0.1	48.3	33.3	2.3	0.0	0.2	100.7	0.8	0.2
0.0	Andesite	CH19C007_Fspar3_core2	Core	16.2	0.1	48.5	33.0	2.4	0.0	0.2	100.5	0.8	0.2
0.1	Andesite	CH19C007_Fspar5_core1	G1core	17.4	0.1	47.5	34.2	1.9	0.0	0.2	101.3	0.8	0.2
0.1	Andesite	CH19C007_Fspar5_core2	G1core	16.8	0.1	48.0	33.8	2.1	0.0	0.3	101.0	0.8	0.2
0.1	Andesite	CH19C007_Fspar6_core1	Core	17.3	0.1	47.1	34.0	1.9	0.0	0.2	100.7	0.8	0.2
0.0	Andesite	CH19C007_Fspar6_core2	Core	17.4	0.1	47.3	34.0	1.8	0.0	0.2	100.8	0.8	0.2
0.1	Andesite	CH19C007_Fspar7_core1	G1core	16.7	0.1	47.9	33.8	2.2	0.0	0.2	101.0	0.8	0.2
0.0	Andesite	CH19C007_Fspar8_core1	Core	17.2	0.1	47.3	34.2	1.9	0.0	0.2	101.0	0.8	0.2
0.0	Andesite	CH19C007_Fspar9_core1	Core	16.8	0.1	47.5	33.8	2.1	0.0	0.2	100.6	0.8	0.2
0.0	Andesite	CH19C007_Fspar9_core2	Core	16.4	0.1	48.3	33.3	2.4	0.0	0.3	100.8	0.8	0.2
0.0	Andesite	CH19C007_Fspar9_core3	Core	16.3	0.1	48.4	33.2	2.3	0.0	0.3	100.7	0.8	0.2
0.0	Andesite	CH19C007_Fspar10_core1	Core	17.1	0.1	47.6	33.9	2.0	0.0	0.2	100.9	0.8	0.2
0.0	Andesite	CH19C007_Fspar10_core2	Core	17.1	0.1	47.3	34.1	1.9	0.0	0.2	100.8	0.8	0.2
0.0	Andesite	CH19C007_Fspar10_core3	Core	17.3	0.1	47.4	34.3	1.9	0.0	0.2	101.2	0.8	0.2

	Andesite	CH19C007_Fspar11_core3	Core	17.0	0.1	47.4	33.9	2.0	0.0	0.2	100.6	0.8	0.2
0.0	Phase 1 rhyolite	CH12022_Fspar1_rim1	Rim	7.8	0.5	57.7	25.8	6.3	0.0	0.2	98.3	0.4	0.6
0.0	Phase 1 rhyolite	CH12022_Fspar1_rim2	Rim	8.2	0.5	58.0	26.3	6.3	0.0	0.2	99.5	0.4	0.6
0.0	Phase 1 rhyolite	CH12022_Fspar2_rim1	Rim	8.1	0.5	58.0	26.4	6.5	0.0	0.2	99.7	0.4	0.6
0.0	Phase 1 rhyolite	CH12022_Fspar2_rim3	Rim	7.7	0.5	58.4	26.2	6.6	0.0	0.2	99.6	0.4	0.6
0.0	Phase 1 rhyolite	CH12022_Fspar3_rim1	Rim	8.2	0.4	58.3	26.5	6.6	0.0	0.2	100.2	0.4	0.6
0.0	Phase 1 rhyolite	CH12022_Fspar3_rim2	Rim	8.4	0.4	57.7	26.6	6.3	0.0	0.2	99.7	0.4	0.6
0.0	Phase 1 rhyolite	CH12022_Fspar4_rim1	Rim	7.9	0.5	59.0	26.4	6.6	0.0	0.2	100.7	0.4	0.6
0.0	Phase 1 rhyolite	CH12022_Fspar4_rim2	Rim	8.0	0.5	58.5	26.5	6.6	0.0	0.2	100.3	0.4	0.6
0.0	Phase 1 rhyolite	CH12022_Fspar5_rim3	Rim	8.1	0.5	57.7	26.2	6.4	0.0	0.2	99.2	0.4	0.6
0.0	Phase 1 rhyolite	CH19C002_Fspar1_Rim1	Rim	8.2	0.4	58.9	27.0	6.6	0.0	0.2	101.3	0.4	0.6
0.0	Phase 1 rhyolite	CH19C002_Fspar1_Rim2	Rim	8.1	0.6	58.5	26.4	6.7	0.0	0.2	100.4	0.4	0.6
0.0	Phase 1 rhyolite	CH19C002_Fspar1_Rim3	Rim	8.3	0.5	59.4	27.1	6.5	0.0	0.2	102.0	0.4	0.6
0.0	Phase 1 rhyolite	CH19C002_Fspar2_Rim1	Rim	7.9	0.5	59.9	26.6	6.9	0.0	0.2	102.0	0.4	0.6
0.0	Phase 1 rhyolite	CH19C002_Fspar2_Rim2	Rim	7.8	0.6	58.3	26.0	6.5	0.0	0.2	99.4	0.4	0.6
0.0	Phase 1 rhyolite	CH19C002_Fspar2_Rim3	Rim	7.1	0.8	60.0	24.4	6.2	0.0	0.3	98.8	0.4	0.6
0.0	Phase 1 rhyolite	CH19C002_Fspar3_Rim1	Rim	8.1	0.5	59.0	26.6	6.6	0.0	0.2	100.9	0.4	0.6
0.0	Phase 1 rhyolite	CH19C002_Fspar3_Rim2	Rim	8.1	0.5	59.0	26.7	6.6	0.0	0.2	101.0	0.4	0.6
0.0	Phase 1 rhyolite	CH19C002_Fspar3_Rim3	Rim	8.1	0.5	58.9	26.5	6.6	0.0	0.2	100.8	0.4	0.6
0.0	Phase 1 rhyolite	CH19C002_Fspar4_Rim1	Rim	7.8	0.5	58.1	25.7	6.6	0.0	0.2	98.9	0.4	0.6
0.0	Phase 1 rhyolite	CH19C002_Fspar4_Rim2	Rim	7.5	0.6	58.4	25.5	6.7	0.0	0.3	98.9	0.4	0.6
0.0	Phase 1 rhyolite	CH19C002_Fspar4_Rim3	Rim	7.7	0.6	57.8	25.8	6.7	0.0	0.2	98.8	0.4	0.6
0.0	Phase 2 Rhyolit	CH12021_Fspar_rim1	Rim	5.6	1.4	62.2	23.0	6.5	0.0	0.3	99.0	0.3	0.6
0.0	Phase 2 Rhyolit	CH12021_Fspar_rim2	Rim	5.2	1.5	62.7	22.3	6.2	0.0	0.4	98.3	0.3	0.6
0.0	Phase 2 Rhyolit	CH12021_Fspar_rim3	Rim	5.9	1.2	61.4	23.2	6.5	0.0	0.2	98.4	0.3	0.6
0.0	Phase 2 Rhyolit	CH12021_Fspar_Krim3	Rim	16.3	0.1	49.0	33.5	2.5	0.0	0.1	101.5	0.8	0.2
0.0	Phase 2 Rhyolit	CH12021_Fspar5_rim1	Rim	5.0	1.1	61.9	23.6	7.6	0.0	0.2	99.4	0.3	0.7
0.0	Phase 2 Rhyolit	CH12021_Fspar5_rim2	Rim	5.4	1.0	61.1	23.9	7.5	0.0	0.1	99.0	0.3	0.7
0.0	Phase 2 Rhyolit	CH12021_Fspar5_rim4	Rim	5.6	1.2	61.8	23.8	6.9	0.0	0.2	99.5	0.3	0.6
0.0	Phase 2 Rhyolit	CH12021_Fspar6_1	Micropheno	7.8	0.6	58.7	26.3	6.5	0.0	0.2	100.0	0.4	0.6
0.0	Phase 2 Rhyolit	CH12021_Fspar6_2	Micropheno	7.8	0.6	58.4	26.0	6.4	0.0	0.2	99.4	0.4	0.6
0.0	Phase 2 Rhyolit	CH12021_Fspar6_3	Micropheno	7.7	0.6	58.8	26.0	6.6	0.0	0.2	99.9	0.4	0.6
0.0	Phase 2 Rhyolit	CH12021_Fspar6_4	Micropheno	7.4	0.6	59.2	25.7	6.7	0.0	0.2	99.9	0.4	0.6
0.0	Phase 2 Rhyolit	_Fspar1_rim2	Rim	6.6	0.8	60.9	25.5	7.3	0.0	0.1	101.2	0.3	0.6
0.0	Phase 2 Rhyolit	_Fspar1_rim3	Rim	6.2	0.8	61.0	25.2	7.4	0.0	0.1	100.8	0.3	0.7
0.0	Phase 2 Rhyolit 83070	_Fspar2_1	Rim	6.4	0.7	60.0	25.3	7.2	0.0	0.1	99.6	0.3	0.6
0.0	Phase 2 Rhyolit 83070	_Fspar2_2	Micropheno	6.2	0.8	60.2	25.1	7.4	0.0	0.1	99.8	0.3	0.7
0.0	Phase 2 Rhyolit 83070	_Fspar2_3	Micropheno	6.2	0.8	60.5	24.9	7.4	0.0	0.1	99.9	0.3	0.6
0.0	Phase 2 Rhyolit 83070	_Fspar2_4	Micropheno	6.3	0.8	60.4	24.9	7.3	0.0	0.1	99.9	0.3	0.6
0.0	Phase 2 Rhyolit 83070	_Fspar3_rim1	Micropheno	6.3	0.8	60.4	25.0	7.4	0.0	0.1	100.0	0.3	0.7
0.0	Phase 2 Rhyolit 83070	_Fspar3_rim2	Rim	6.5	0.8	59.9	25.1	7.3	0.0	0.1	99.6	0.3	0.6
0.0	Phase 2 Rhyolit 83070	_Fspar3_rim3	Rim	6.2	0.8	60.1	24.7	7.3	0.0	0.1	99.3	0.3	0.6
0.0	Phase 2 Rhyolit 83070	_Fspar4_rim2	Rim	6.2	0.8	60.6	25.1	7.3	0.0	0.1	100.1	0.3	0.6
0.0	Phase 2 Rhyolit 83070	_Fspar5_rim1	Rim	5.9	1.1	60.8	24.0	6.9	0.0	0.2	98.9	0.3	0.6
0.0	Phase 2 Rhyolit 83070	_Fspar5_rim4	Rim	5.9	1.1	61.0	24.2	6.9	0.0	0.2	99.2	0.3	0.6
0.0	Phase 2 Rhyolit 83070	_Fspar6_1	Rim	5.7	1.1	63.2	24.3	6.9	0.0	0.2	101.4	0.3	0.6
0.0	Phase 2 Rhyolit 83070	_Fspar6_2	Micropheno	6.7	0.8	60.1	25.3	7.2	0.0	0.1	100.2	0.3	0.6
0.0	Phase 2 Rhyolit 83070	_Fspar6_3	Micropheno	6.2	0.9	60.9	25.0	7.4	0.0	0.1	100.3	0.3	0.6
0.0	Phase 2 Rhyolit 83070	_Fspar7_rim1	Micropheno	6.5	0.8	60.7	25.2	7.2	0.0	0.1	100.5	0.3	0.6
0.0	Phase 2 Rhyolit 83070	_Fspar7_rim2	Rim	6.5	0.8	60.3	25.1	7.3	0.0	0.1	100.1	0.3	0.6
0.0	Phase 2 Rhyolit 83070		Rim	7.1	0.7	59.8	25.5	7.0	0.0	0.1	100.3	0.3	0.6
0.0	Andesite 83070	CH120202_Fspar1_srim1	Srim	17.3	0.1	46.8	34.0	1.8	0.0	0.2	100.2	0.8	0.2
0.0	Andesite 83070	CH120202_Fspar1_srim2	Srim	16.5	0.1	47.5	33.3	2.1	0.0	0.3	99.8	0.8	0.2
0.0	Andesite	CH120202_Fspar2_srim1	Srim	16.3	0.1	48.8	33.4	2.4	0.0	0.2	101.3	0.8	0.2
	Andesite	CH120202_Fspar2_srim2	Srim	15.7	0.2	49.3	32.5	2.7	0.0	0.2	100.5	0.8	0.2

0.0
0.0
0.0
0.0
0.0
0.0
0.0
0.0
0.0
0.0
0.0
0.0
0.0
0.0
0.0
0.0
0.0
0.0
0.0
0.0

Andesite	CH120202_Fspar3_rim1	G1rim	17.0	0.1	47.4	34.0	2.0	0.0	0.2	100.8	0.8	0.2
Andesite	CH120202_Fspar3_rim2	G1rim	17.2	0.1	47.4	34.0	1.9	0.0	0.2	100.9	0.8	0.2
Andesite	CH120202_Fspar3_rim3	G1rim	17.2	0.1	47.4	34.0	2.0	0.0	0.2	100.9	0.8	0.2
Andesite	CH120202_Fspar4_rim1	G1rim	17.0	0.1	48.3	34.2	2.1	0.0	0.2	102.0	0.8	0.2
Andesite	CH120202_Fspar4_rim2	G1rim	16.4	0.1	49.6	33.9	2.5	0.0	0.3	102.8	0.8	0.2
Andesite	CH120202_Fspar4_rim3	G1rim	17.1	0.1	48.1	34.3	2.1	0.0	0.3	102.1	0.8	0.2
Andesite	CH120202_Fspar5_rim1	Rim	16.9	0.1	48.0	34.2	2.0	0.0	0.3	101.5	0.8	0.2
Andesite	CH120202_Fspar5_rim2	Rim	17.1	0.1	48.1	34.4	2.1	0.0	0.2	102.0	0.8	0.2
Andesite	CH120202_Fspar6_rim1	Rim	17.1	0.1	47.4	33.9	2.0	0.0	0.2	100.8	0.8	0.2
Andesite	CH120202_Fspar6_rim2	Rim	16.8	0.1	47.9	33.8	2.1	0.0	0.2	101.1	0.8	0.2
Andesite	CH120202_Fspar6_rim3	Rim	17.0	0.1	47.5	34.0	2.1	0.0	0.2	100.9	0.8	0.2
Andesite	CH120202_Fspar7_rim1	Rim	17.2	0.1	47.8	34.3	1.9	0.0	0.3	101.6	0.8	0.2
Andesite	CH120202_Fspar7_rim2	Rim	16.8	0.1	47.9	33.9	2.2	0.0	0.2	101.2	0.8	0.2
Andesite	CH120202_Fspar7_rim3	Rim	17.1	0.1	47.6	34.0	2.1	0.0	0.2	101.2	0.8	0.2
Andesite	CH120202_Fspar8_rim1	Rim	18.0	0.1	47.1	35.1	1.6	0.0	0.2	102.1	0.9	0.1
Andesite	CH120202_Fspar8_rim2	Rim	17.8	0.1	47.1	34.7	1.8	0.0	0.3	101.8	0.8	0.2
Andesite	CH120202_Fspar8_rim3	Rim	16.8	0.2	47.1	33.6	2.1	0.0	0.3	100.0	0.8	0.2
Andesite	CH120202_Fspar9_rim1	Rim	17.1	0.1	47.8	34.1	2.1	0.0	0.3	101.4	0.8	0.2
Andesite	CH120202_Fspar9_rim2	Rim	17.1	0.1	47.8	34.2	2.1	0.0	0.3	101.6	0.8	0.2
Andesite	CH120202_Fspar10_rim1	Rim	15.9	0.2	49.1	33.1	2.6	0.1	0.3	101.2	0.8	0.2
Andesite	CH120202_Fspar10_rim2	Rim	17.0	0.1	47.5	33.6	2.0	0.0	0.3	100.6	0.8	0.2
Andesite	CH120202_Fspar11_1	Micropheno	16.6	0.1	48.1	34.0	2.1	0.0	0.2	101.2	0.8	0.2
Andesite	CH120202_Fspar11_2	Micropheno	15.8	0.2	48.8	32.9	2.6	0.0	0.2	100.5	0.8	0.2
Andesite	CH120202_Fspar12_rim1	G1rim	17.4	0.1	47.8	34.6	1.9	0.0	0.2	102.1	0.8	0.2
Andesite	CH120202_Fspar13_rim1	Rim	16.5	0.1	47.8	33.2	2.2	0.0	0.2	100.2	0.8	0.2
Andesite	CH120202_Fspar13_rim2	Rim	16.6	0.1	47.7	33.0	2.3	0.0	0.2	100.0	0.8	0.2
Andesite	CH19C007_Fspar1_srim1	Srim	17.2	0.1	46.8	34.1	1.8	0.0	0.2	100.3	0.8	0.2
Andesite	CH19C007_Fspar1_srim2	Srim	17.0	0.1	46.8	33.7	1.9	0.0	0.2	99.8	0.8	0.2
Andesite	CH19C007_Fspar2_rim1	G1rim	17.2	0.1	46.9	34.2	1.9	0.0	0.3	100.5	0.8	0.2
Andesite	CH19C007_Fspar2_rim2	G1rim	17.2	0.1	47.5	34.1	2.0	0.0	0.2	101.0	0.8	0.2
Andesite	CH19C007_Fspar3_rim1	Rim	17.1	0.1	46.9	33.9	1.9	0.0	0.3	100.2	0.8	0.2
Andesite	CH19C007_Fspar3_rim2	Rim	17.1	0.1	47.2	33.8	2.0	0.0	0.2	100.4	0.8	0.2
Andesite	CH19C007_Fspar4_1	Micropheno	17.2	0.1	47.2	34.1	1.9	0.0	0.3	100.9	0.8	0.2
Andesite	CH19C007_Fspar4_2	Micropheno	16.8	0.1	47.3	33.6	2.0	0.0	0.3	100.1	0.8	0.2
Andesite	CH19C007_Fspar5_rim1	G1rim	15.5	0.2	49.3	32.8	2.7	0.0	0.2	100.7	0.8	0.2
Andesite	CH19C007_Fspar5_rim2	G1rim	17.0	0.1	47.3	33.8	1.9	0.0	0.2	100.3	0.8	0.2
Andesite	CH19C007_Fspar6_rim1	Rim	17.2	0.1	46.9	33.6	1.9	0.0	0.3	100.1	0.8	0.2
Andesite	CH19C007_Fspar6_rim2	Rim	17.1	0.1	47.1	33.8	1.9	0.0	0.3	100.3	0.8	0.2
Andesite	CH19C007_Fspar7_rim1	G1rim	16.5	0.1	48.5	33.7	2.3	0.0	0.2	101.3	0.8	0.2
Andesite	CH19C007_Fspar8_rim1	Rim	16.8	0.1	47.6	33.9	2.1	0.0	0.2	100.8	0.8	0.2
Andesite	CH19C007_Fspar9_rim1	Rim	16.3	0.1	48.7	33.1	2.4	0.0	0.3	100.9	0.8	0.2
Andesite	CH19C007_Fspar9_rim2	Rim	15.8	0.2	49.1	32.7	2.6	0.0	0.2	100.6	0.8	0.2
Andesite	CH19C007_Fspar9_rim3	Rim	15.6	0.1	49.1	32.7	2.7	0.0	0.3	100.6	0.8	0.2
Andesite	CH19C007_Fspar10_rim1	G1rim	16.6	0.1	48.3	33.8	2.1	0.0	0.2	101.1	0.8	0.2
Andesite	CH19C007_Fspar10_rim2	G1rim	16.7	0.1	47.8	33.8	2.1	0.0	0.2	100.8	0.8	0.2
Andesite	CH19C007_Fspar11_rim1	G1rim	17.0	0.1	47.2	34.2	1.9	0.0	0.2	100.8	0.8	0.2
Andesite	CH19C007_Fspar11_rim2	G1rim	17.0	0.1	47.1	33.5	2.1	0.0	0.2	100.0	0.8	0.2
Andesite	CH120202_Gspar1_1	Glom	17.2	0.1	47.6	34.0	1.9	0.0	0.2	101.1	0.8	0.2
Andesite	CH120202_Gspar1_2	Glom	17.7	0.1	47.2	34.6	1.8	0.0	0.3	101.6	0.8	0.2
Andesite	CH120202_Gspar1_3	Glom	17.1	0.1	47.7	34.4	2.1	0.0	0.3	101.7	0.8	0.2
Andesite	CH120202_Gspar1_4	Glom	16.6	0.1	48.6	33.9	2.3	0.0	0.3	101.9	0.8	0.2
Andesite	CH120202_Gspar1_5	Glom	16.4	0.1	48.4	33.2	2.4	0.0	0.4	101.0	0.8	0.2
Andesite	CH120202_Gspar1_6	Glom	16.8	0.1	48.4	33.8	2.2	0.0	0.3	101.6	0.8	0.2

Andesite	CH120202_Gspar1_7	Glom	17.2	0.1	47.4	34.3	1.9	0.0	0.3	101.1	0.8	0.2
Andesite	CH120202_Gspar2_1	Glom	18.6	0.1	46.1	35.3	1.3	0.0	0.3	101.6	0.9	0.1
Andesite	CH120202_Gspar2_2	Glom	17.3	0.1	47.6	34.6	2.0	0.0	0.3	101.9	0.8	0.2
Andesite	CH120202_Gspar2_3	Glom	16.8	0.1	48.2	33.6	2.3	0.0	0.3	101.3	0.8	0.2
Andesite	CH120202_Gspar2_4	Glom	16.9	0.1	47.7	33.8	2.0	0.0	0.3	100.9	0.8	0.2
Andesite	CH120202_Gspar2_5	Glom	17.4	0.1	47.6	34.4	1.9	0.0	0.3	101.8	0.8	0.2
Andesite	CH120202_Gspar2_6	Glom	16.5	0.1	48.3	33.5	2.3	0.0	0.4	101.1	0.8	0.2
Andesite	CH120202_Gspar2_7	Glom	16.7	0.1	48.0	33.9	2.2	0.0	0.3	101.1	0.8	0.2
Andesite	CH120202_Gspar2_8	Glom	17.3	0.1	47.0	34.1	1.9	0.0	0.2	100.7	0.8	0.2
Andesite	CH19C007_GSpar_Core1	Glom	17.1	0.1	47.3	34.2	2.0	0.0	0.3	101.0	0.8	0.2
Andesite	CH19C007_GSpar_Core2	Glom	16.8	0.2	47.7	33.9	2.1	0.0	0.3	100.8	0.8	0.2
Andesite	CH19C007_GSpar_Core3	Glom	17.1	0.1	47.4	34.1	2.0	0.0	0.3	100.9	0.8	0.2
Andesite	CH19C007_GSpar_Core4	Glom	16.4	0.1	48.0	33.4	2.3	0.0	0.3	100.5	0.8	0.2
Andesite	CH19C007_GSpar_Core5	Glom	17.1	0.1	47.3	34.2	1.9	0.0	0.3	100.9	0.8	0.2
Andesite	CH19C007_GSpar_Rim1	Glom	16.5	0.1	48.4	33.8	2.3	0.0	0.2	101.3	0.8	0.2
Andesite	CH19C007_GSpar_Rim2	Glom	16.6	0.1	48.6	33.9	2.2	0.0	0.3	101.7	0.8	0.2
Andesite	CH19C007_GSpar_Rim3	Glom	16.4	0.1	48.7	33.9	2.3	0.0	0.2	101.7	0.8	0.2
Andesite	CH19C007_GSpar_Rim4	Glom	15.9	0.2	48.3	32.9	2.5	0.0	0.3	100.1	0.8	0.2
Andesite	CH19C007_GSpar_Rim5	Glom	15.9	0.1	48.2	32.9	2.5	0.0	0.3	100.0	0.8	0.2
Andesite	CH19C007_GSpar_Rim6	Glom	15.9	0.2	48.6	33.0	2.6	0.0	0.5	100.8	0.8	0.2

Orthopyroxene

No.	Comment	CaO	TiO2	SiO2	Al2O3	MgO	P2O5	FeO	NiO	Cr2O3	MnO	Total	En	Fs	Wo
204	CH12020-2opx1_core1	1.30	0.25	52.19	1.23	19.87	0.00	23.57	-0.01	0.06	0.46	98.94	57.94	39.33	2.73
205	CH12020-2opx1_core2	1.24	0.19	52.27	1.24	20.06	-0.03	23.57	0.04	0.04	0.51	99.15	58.21	39.20	2.59
206	CH12020-2opx1_core3	1.28	0.20	51.94	1.18	19.76	0.10	24.42	0.03	0.00	0.46	99.38	57.05	40.30	2.65
207	CH12020-2opx1_core4	1.35	0.26	51.73	1.21	20.06	-0.01	23.96	-0.01	0.03	0.42	98.99	57.80	39.41	2.79
208	CH12020-2opx1_core5	1.33	0.28	52.06	1.25	19.66	-0.01	23.88	0.03	0.05	0.43	98.96	57.41	39.81	2.78
209	CH12020-2opx1_rim1	1.21	0.19	51.77	1.23	19.64	-0.07	24.39	-0.03	0.03	0.40	98.76	57.07	40.41	2.52
210	CH12020-2opx1_rim2	1.24	0.23	51.56	1.10	19.47	0.00	24.24	-0.02	0.00	0.51	98.34	56.85	40.55	2.60
211	CH12020-2opx1_rim3	1.22	0.22	53.04	1.12	19.69	0.05	23.78	0.04	0.03	0.48	99.67	57.62	39.81	2.57
212	CH12020-2opx1_rim4	1.19	0.26	52.96	1.14	20.16	-0.04	24.26	0.07	0.03	0.52	100.56	57.73	39.82	2.45
213	CH12020-2opx1_rim5	1.22	0.28	52.26	1.08	19.58	-0.04	24.47	0.00	0.02	0.49	99.36	56.82	40.63	2.55
214	CH12020-2opx2_core1	1.15	0.23	51.64	0.97	18.18	0.01	25.94	0.01	0.03	0.47	98.61	53.76	43.81	2.44
215	CH12020-2opx2_core2	1.17	0.23	51.68	1.01	18.37	0.03	26.43	0.02	0.00	0.51	99.46	53.53	44.03	2.44
216	CH12020-2opx2_core3	1.21	0.22	52.11	1.00	18.45	0.04	26.34	0.06	-0.01	0.48	99.91	53.70	43.78	2.52
217	CH12020-2opx2_core4	1.16	0.19	51.63	0.98	18.31	-0.12	26.62	0.02	0.01	0.52	99.31	53.28	44.29	2.42
218	CH12020-2opx2_core5	1.12	0.21	51.84	0.87	18.33	0.04	25.68	0.00	-0.01	0.49	98.57	54.20	43.42	2.38
219	CH12020-2opx2_rim1	1.26	0.24	51.77	1.12	18.69	0.00	25.49	0.08	0.04	0.48	99.16	54.71	42.64	2.65
220	CH12020-2opx2_rim2	1.20	0.18	51.03	1.03	18.30	-0.05	26.00	-0.06	0.04	0.48	98.15	53.80	43.68	2.53
221	CH12020-2opx2_rim3	1.25	0.26	50.70	0.92	17.84	0.08	25.95	-0.01	0.01	0.52	97.52	53.10	44.22	2.68
222	CH12020-2opx2_rim4	1.24	0.24	50.85	0.99	17.61	-0.04	26.31	0.02	-0.02	0.43	97.63	52.57	44.78	2.66
223	CH12020-2opx2_rim5	1.18	0.26	52.09	0.98	19.14	-0.01	25.03	-0.06	0.01	0.51	99.12	55.78	41.74	2.47
224	CH12020-2opx3_core1	1.29	0.37	52.05	1.60	20.64	0.01	22.66	-0.03	0.04	0.38	99.01	59.85	37.46	2.70
225	CH12020-2opx3_core2	1.25	0.27	52.31	1.37	20.54	0.04	23.51	-0.03	0.01	0.51	99.77	58.84	38.60	2.57
226	CH12020-2opx3_core3	1.26	0.26	52.09	1.47	20.73	-0.04	22.50	0.04	-0.01	0.35	98.65	60.16	37.21	2.64
227	CH12020-2opx3_core4	1.33	0.27	52.23	1.48	20.80	0.05	22.55	0.00	0.02	0.42	99.14	60.05	37.20	2.75
228	CH12020-2opx3_core5	1.22	0.24	52.41	1.34	20.33	0.02	22.96	0.06	0.02	0.41	99.00	59.25	38.20	2.55
229	CH12020-2opx3_rim1	1.30	0.26	52.84	1.36	21.11	-0.07	23.64	0.07	0.04	0.43	100.98	59.39	37.98	2.63
230	CH12020-2opx3_rim2	1.14	0.21	51.55	1.14	20.00	0.01	24.13	0.04	0.01	0.40	98.64	57.83	39.79	2.37
231	CH12020-2opx3_rim3	1.28	0.25	52.60	1.17	19.24	-0.08	24.89	-0.08	0.02	0.49	99.79	55.93	41.40	2.67
232	CH12020-2opx3_rim4	1.21	0.27	50.62	1.31	19.84	-0.06	23.86	-0.02	0.00	0.45	97.49	57.76	39.70	2.54
233	CH12020-2opx3_rim5	1.31	0.31	51.55	1.39	20.25	-0.07	22.69	-0.02	0.02	0.35	97.79	59.35	37.88	2.77
234	CH12020-2opx4_core1	1.36	0.23	52.07	1.55	20.33	0.06	23.23	0.05	0.05	0.41	99.32	58.81	38.36	2.83
235	CH12020-2opx4_core2	1.30	0.26	52.45	1.45	21.09	0.03	23.26	0.02	0.06	0.47	100.39	59.68	37.68	2.63
236	CH12020-2opx4_core3	1.36	0.29	52.35	1.35	19.95	-0.07	23.94	-0.04	0.04	0.43	99.61	57.67	39.50	2.83
237	CH12020-2opx4_core4	1.26	0.29	52.57	1.39	20.30	0.12	22.94	-0.05	0.01	0.41	99.25	59.17	38.19	2.65

238 CH12020-2opx4_core5	1.28	0.27	52.09	1.48	20.07	0.04	23.50	0.07	0.03	0.45	99.29	58.30	39.02	2.68
239 CH12020-2opx4_rim1	1.22	0.23	52.18	1.27	19.16	-0.04	24.96	0.03	0.07	0.52	99.60	55.82	41.63	2.55
240 CH12020-2opx4_rim2	1.18	0.20	52.21	1.06	19.51	-0.10	24.94	-0.03	-0.02	0.49	99.43	56.34	41.21	2.45
243 CH12020-2opx4_rim5	1.23	0.25	51.38	1.00	18.73	-0.08	24.64	0.01	0.00	0.42	97.58	55.62	41.75	2.63
244 CH12020-2opx5_core1	1.10	0.23	51.62	1.10	19.16	0.06	24.90	-0.04	0.00	0.45	98.56	56.07	41.62	2.31
245 CH12020-2opx5_core2	0.69	0.26	50.44	3.07	18.79	0.07	25.09	0.04	0.08	0.45	98.98	55.91	42.62	1.47
246 CH12020-2opx5_core3	1.05	0.24	51.48	1.23	19.19	-0.03	25.00	-0.03	0.05	0.47	98.65	56.06	41.73	2.21
247 CH12020-2opx5_core4	0.85	0.27	50.60	2.53	18.73	-0.04	25.20	0.01	0.04	0.47	98.66	55.52	42.68	1.80
248 CH12020-2opx5_core5	0.82	0.26	51.18	1.97	19.67	-0.01	23.94	-0.04	0.13	0.45	98.37	57.94	40.31	1.75
249 CH12020-2opx5_rim1	1.22	0.27	51.97	1.02	19.54	0.01	24.69	0.01	0.01	0.49	99.21	56.56	40.90	2.53
250 CH12020-2opx5_rim2	1.26	0.21	51.20	1.14	19.06	0.12	24.76	0.04	0.03	0.49	98.30	55.84	41.51	2.65
251 CH12020-2opx5_rim3	1.25	0.24	51.96	1.05	18.71	-0.04	24.58	-0.03	0.02	0.40	98.14	55.65	41.68	2.67
252 CH12020-2opx5_rim4	1.19	0.20	51.10	1.06	19.22	0.02	24.47	0.02	0.01	0.44	97.72	56.44	41.05	2.50
253 CH12020-2opx5_rim5	1.21	0.24	51.83	1.09	19.18	-0.01	25.23	0.04	0.01	0.50	99.31	55.62	41.86	2.52
254 CH12020-2opx6_core1	1.16	0.25	51.45	1.05	17.60	-0.01	27.03	-0.05	0.00	0.49	98.98	51.96	45.57	2.47
255 CH12020-2opx6_core2	1.19	0.24	50.93	1.00	18.23	0.03	26.38	0.01	0.03	0.52	98.55	53.34	44.16	2.50
256 CH12020-2opx6_core3	1.19	0.21	51.45	1.00	18.20	0.07	26.67	0.00	0.01	0.46	99.26	53.10	44.41	2.49
257 CH12020-2opx6_core4	1.15	0.26	51.50	1.01	18.50	-0.15	25.70	-0.01	-0.02	0.53	98.46	54.34	43.22	2.44
258 CH12020-2opx6_core5	1.17	0.23	51.35	0.84	17.95	0.02	26.51	0.01	0.02	0.55	98.65	52.83	44.69	2.48
259 CH12020-2opx6_rim1	1.20	0.25	50.58	1.02	17.95	-0.04	26.52	0.01	0.00	0.48	97.95	52.86	44.61	2.53
260 CH12020-2opx6_rim2	1.26	0.20	51.34	0.97	18.55	-0.03	25.11	0.03	-0.02	0.54	97.95	54.81	42.52	2.67
261 CH12020-2opx6_rim3	1.19	0.20	51.66	1.03	18.91	0.07	24.90	0.00	-0.01	0.44	98.39	55.64	41.84	2.52
262 CH12020-2opx6_rim4	1.28	0.23	52.30	0.91	19.28	-0.08	25.08	-0.02	0.03	0.47	99.47	55.83	41.50	2.67
263 CH12020-2opx6_rim5	1.31	0.23	52.04	1.00	19.08	-0.03	25.21	-0.01	0.02	0.50	99.38	55.39	41.87	2.74
264 CH12020-2opx7_core1	1.29	0.22	51.30	1.06	17.70	-0.01	26.67	0.07	0.02	0.49	98.80	52.27	44.99	2.73
265 CH12020-2opx7_core2	1.25	0.22	51.39	1.11	17.77	0.13	26.36	-0.03	0.01	0.51	98.71	52.66	44.67	2.66
266 CH12020-2opx7_core3	1.18	0.23	50.78	0.90	16.84	0.03	28.90	0.02	0.01	0.58	99.47	49.18	48.33	2.48
268 CH12020-2opx7_core5	1.25	0.25	50.70	0.99	17.01	-0.02	28.21	0.00	0.02	0.57	98.97	49.95	47.42	2.63
269 CH12020-2opx7_rim1	1.29	0.25	51.99	0.99	18.97	-0.05	25.28	-0.03	0.00	0.50	99.20	55.20	42.10	2.71
270 CH12020-2opx7_rim2	1.23	0.30	52.12	1.14	19.19	0.03	24.89	0.00	-0.02	0.47	99.37	55.93	41.48	2.59
271 CH12020-2opx7_rim3	1.22	0.37	50.60	0.97	18.83	0.11	24.56	-0.06	0.04	0.51	97.16	55.76	41.65	2.59
273 CH12020-2opx7_rim5	1.26	0.23	51.51	0.97	18.66	0.03	25.63	0.04	-0.03	0.56	98.86	54.47	42.88	2.65
274 CH12020-2opx8_core1	1.19	0.27	52.24	1.47	21.38	-0.07	21.80	-0.01	0.03	0.41	98.70	61.63	35.91	2.46
275 CH12020-2opx8_core2	1.26	0.31	52.03	1.42	20.96	0.03	22.50	-0.03	0.02	0.41	98.91	60.37	37.02	2.61
276 CH12020-2opx8_core3	1.25	0.38	52.91	1.45	21.81	-0.05	21.31	0.05	0.07	0.35	99.53	62.58	34.85	2.57
277 CH12020-2opx8_core4	1.22	0.24	52.08	1.38	20.47	0.02	23.07	-0.02	0.10	0.41	98.97	59.31	38.15	2.54
278 CH12020-2opx8_core5	1.29	0.32	52.63	1.30	21.53	0.00	21.38	0.00	0.03	0.44	98.91	62.05	35.28	2.67
279 CH12020-2opx8_rim1	1.26	0.24	52.51	1.23	19.88	0.04	24.65	0.00	-0.01	0.39	100.18	57.08	40.32	2.60
280 CH12020-2opx8_rim2	1.29	0.22	51.67	1.24	19.64	-0.04	24.13	0.01	0.02	0.47	98.65	57.16	40.15	2.70
281 CH12020-2opx8_rim3	1.23	0.22	52.89	1.69	22.32	0.03	19.83	0.03	0.15	0.36	98.76	64.62	32.81	2.56
282 CH12020-2opx8_rim4	1.30	0.26	51.53	1.33	19.22	0.06	23.81	0.02	0.02	0.45	97.99	56.92	40.31	2.77
283 CH12020-2opx8_rim5	1.20	0.30	51.54	1.47	21.31	0.04	22.00	0.02	0.06	0.36	98.30	61.38	36.13	2.49
284 CH12020-2opx9_core1	1.79	0.24	50.68	1.36	20.25	-0.08	21.25	0.00	0.04	0.42	95.96	60.10	36.08	3.82
285 CH12020-2opx9_core2	1.34	0.28	52.85	1.42	21.59	0.06	21.53	0.00	0.03	0.40	99.50	61.93	35.30	2.76
286 CH12020-2opx9_core3	1.36	0.28	52.24	1.44	20.45	0.00	22.66	0.01	0.01	0.39	98.84	59.52	37.64	2.84
287 CH12020-2opx9_core4	1.38	0.30	52.20	1.66	21.32	0.04	21.80	0.02	0.05	0.36	99.12	61.36	35.79	2.85
288 CH12020-2opx9_core5	1.32	0.30	51.64	1.41	19.91	0.04	23.38	0.05	0.02	0.49	98.55	58.14	39.10	2.76
289 CH12020-2opx9_rim1	1.26	0.25	51.47	1.05	19.05	-0.04	24.59	0.07	-0.01	0.49	98.17	56.00	41.35	2.65
290 CH12020-2opx9_rim2	1.22	0.29	51.85	1.12	19.42	0.02	24.89	-0.03	0.06	0.43	99.28	56.28	41.18	2.54
291 CH12020-2opx9_rim3	1.24	0.19	52.43	1.07	19.52	-0.08	24.43	0.05	-0.01	0.52	99.36	56.73	40.69	2.59

292 CH12020-2opx9_rim4	1.28	0.25	52.38	1.05	19.12	0.03	24.80	-0.07	0.01	0.42	99.27	55.92	41.39	2.69
293 CH12020-2opx9_rim5	1.33	0.28	52.15	1.31	19.58	0.04	23.44	0.01	0.04	0.49	98.68	57.64	39.54	2.82
294 CH12020-2opx10_core1	1.33	0.29	52.51	1.38	21.63	0.01	21.22	-0.02	0.04	0.42	98.83	62.29	34.96	2.75
295 CH12020-2opx10_core2	1.27	0.22	52.44	1.25	21.66	-0.03	21.76	-0.01	0.13	0.47	99.17	61.80	35.59	2.61
296 CH12020-2opx10_core3	1.40	0.32	52.56	1.32	21.47	0.05	21.48	0.03	0.05	0.40	99.09	61.78	35.33	2.89
297 CH12020-2opx10_core4	1.38	0.20	52.86	1.28	21.65	-0.02	21.67	0.01	0.01	0.42	99.45	61.81	35.36	2.83
298 CH12020-2opx10_core5	1.44	0.32	52.28	1.73	21.52	0.09	21.38	0.00	0.08	0.41	99.25	61.88	35.15	2.97
299 CH12020-2opx10_rim1	1.35	0.24	52.23	0.80	21.31	-0.08	22.34	0.05	0.02	0.45	98.70	60.77	36.47	2.76
300 CH12020-2opx10_rim2	1.30	0.26	53.24	0.95	21.65	-0.09	22.07	0.00	0.02	0.45	99.85	61.47	35.88	2.65
301 CH12020-2opx10_rim3	1.31	0.29	52.97	1.39	21.67	-0.02	21.31	0.04	0.02	0.42	99.40	62.27	35.03	2.71
302 CH12020-2opx10_rim4	1.34	0.29	52.91	1.53	21.73	-0.03	21.35	-0.03	0.03	0.42	99.53	62.25	34.99	2.76
303 CH12020-2opx10_rim5	1.41	0.31	53.40	1.64	22.26	0.01	20.23	-0.01	0.03	0.38	99.66	63.90	33.19	2.91
304 CH12020-2opx11_core1	1.15	0.26	51.93	1.27	20.07	0.05	23.41	-0.04	0.11	0.44	98.65	58.56	39.03	2.40
305 CH12020-2opx11_core2	1.23	0.29	51.97	1.40	19.91	-0.06	23.75	0.02	0.12	0.48	99.11	57.89	39.53	2.58
306 CH12020-2opx11_core3	1.26	0.30	51.87	1.61	20.20	0.01	23.72	0.04	0.19	0.37	99.57	58.35	39.03	2.62
307 CH12020-2opx11_core4	1.21	0.29	52.18	1.33	19.83	0.03	23.61	-0.01	0.15	0.42	99.05	58.01	39.44	2.55
308 CH12020-2opx11_core5	1.22	0.28	52.13	1.38	20.09	0.03	23.67	0.08	0.14	0.42	99.41	58.28	39.19	2.53
309 CH12020-2opx11_rim1	1.28	0.23	51.65	0.98	20.32	0.12	23.85	0.03	0.03	0.42	98.91	58.29	39.07	2.64
310 CH12020-2opx11_rim2	1.24	0.24	51.28	1.05	19.38	0.02	25.02	-0.04	0.00	0.39	98.59	56.13	41.28	2.59
311 CH12020-2opx11_rim3	1.37	0.26	52.23	1.24	19.83	-0.12	24.04	0.04	0.04	0.47	99.39	57.38	39.77	2.85
312 CH12020-2opx11_rim4	1.27	0.25	51.60	1.19	19.14	-0.02	24.24	-0.02	0.00	0.48	98.13	56.44	40.88	2.68
313 CH12020-2opx11_rim5	1.32	0.28	51.54	1.25	18.97	0.02	24.33	-0.02	0.04	0.52	98.22	56.04	41.17	2.79
314 CH12020-2opx12_core1	1.23	0.25	51.29	1.08	18.95	-0.02	26.13	-0.11	-0.02	0.54	99.32	54.47	42.99	2.55
315 CH12020-2opx12_core2	1.27	0.20	51.26	0.93	18.63	-0.03	25.25	-0.04	0.02	0.46	97.96	54.85	42.47	2.68
316 CH12020-2opx12_core3	1.18	0.27	51.41	0.92	18.41	0.03	25.85	-0.05	0.02	0.54	98.56	54.05	43.47	2.49
317 CH12020-2opx12_core4	1.32	0.23	52.28	1.34	21.35	-0.06	21.99	0.01	0.05	0.43	98.95	61.22	36.05	2.73
318 CH12020-2opx12_core5	1.28	0.31	51.99	1.41	19.80	0.01	23.71	-0.06	0.07	0.46	98.98	57.77	39.55	2.68
319 CH12020-2opx12_rim1	1.27	0.30	51.58	1.28	19.36	-0.04	24.35	0.03	0.02	0.41	98.56	56.67	40.67	2.66
320 CH12020-2opx12_rim2	1.26	0.27	51.46	1.31	19.89	0.05	23.31	-0.03	0.02	0.46	98.00	58.28	39.07	2.65
321 CH12020-2opx12_rim3	1.26	0.20	51.06	0.97	18.32	-0.01	25.71	0.02	0.00	0.45	97.99	54.03	43.29	2.68
322 CH12020-2opx12_rim4	1.26	0.24	50.91	1.04	18.93	-0.09	24.62	0.02	0.01	0.51	97.43	55.79	41.55	2.67
323 CH12020-2opx12_rim5	1.26	0.29	52.41	1.15	19.48	0.01	25.42	-0.03	-0.04	0.51	100.47	55.76	41.65	2.59
324 CH12020-2opx13_core1	1.22	0.23	52.05	1.05	19.21	-0.05	24.72	0.00	-0.02	0.47	98.89	56.14	41.31	2.55
325 CH12020-2opx13_core2	1.27	0.29	52.41	1.01	19.48	-0.01	24.54	0.05	0.01	0.50	99.56	56.55	40.80	2.65
326 CH12020-2opx13_core3	1.20	0.25	52.35	1.03	19.35	0.07	24.91	-0.02	-0.03	0.47	99.59	56.16	41.33	2.51
327 CH12020-2opx13_core4	1.19	0.27	52.07	1.00	19.42	0.08	24.78	0.05	0.03	0.43	99.31	56.42	41.10	2.48
328 CH12020-2opx13_core5	1.27	0.22	52.05	0.97	19.45	-0.04	24.53	-0.04	0.02	0.47	98.90	56.57	40.78	2.65
329 CH12020-2opx13_rim1	1.20	0.20	52.91	1.34	19.80	0.03	23.84	0.07	0.01	0.48	99.88	57.71	39.77	2.52
330 CH12020-2opx13_rim2	1.32	0.26	52.52	1.09	20.12	-0.03	24.43	-0.01	0.00	0.49	100.20	57.39	39.89	2.72
331 CH12020-2opx13_rim3	1.21	0.26	51.43	1.04	19.84	-0.05	24.27	0.03	-0.02	0.48	98.50	57.35	40.13	2.52
332 CH12020-2opx13_rim4	1.30	0.23	51.38	0.84	19.23	-0.07	24.05	-0.04	0.01	0.48	97.42	56.69	40.56	2.76
333 CH12020-2opx13_rim5	1.3187	0.2751	51.4489	1.1808	19.3319	-0.0185	23.9204	0	0.041	0.441	97.9394	56.95	40.26	2.79

Ilmenite																		
Rock Type	Spot	Comment	SiO2	TiO2	Al2O3	FeO	MnO	MgO	CaO	K2O	Cr2O3	ZnO	V2O3	NiO	Total	Fe2O3*	FeO*	Total	%Ilm*
Andesite	Rim	007_ox1_tp1	0.01	49.69	0.16	43.96	0.46	2.53	0.13	0.02	0.02	0.01	0.70	0.01	97.69	4.88	39.57	98.18	0.95
Andesite	Rim	007_ox1_tp2	0.01	49.65	0.16	43.67	0.42	2.57	0.10	0.02	0.01	0.10	0.70	0.02	97.44	4.69	39.45	97.91	0.95
Andesite	Rim	007_ox1_tp3	0.02	49.72	0.16	43.93	0.49	2.48	0.13	0.02	0.02	0.07	0.73	0.00	97.75	4.82	39.59	98.26	0.95
Andesite	Core	007_ox1_tp4	0.02	49.79	0.17	43.92	0.42	2.40	0.08	0.02	0.01	0.04	0.75	0.02	97.64	4.38	39.97	98.08	0.96
Andesite	Core	007_ox1_tp5	0.01	49.77	0.18	43.95	0.43	2.49	0.04	0.00	0.01	0.02	0.73	0.03	97.67	4.57	39.84	98.13	0.95
Andesite	Core	007_ox1_tp6	0.01	49.68	0.18	43.55	0.44	2.57	0.09	0.02	0.00	0.00	0.75	0.00	97.22	4.41	39.58	97.72	0.95
Andesite	Rim	007_ox2_rim1	0.02	49.89	0.19	43.80	0.48	2.59	0.03	0.02	0.00	0.04	0.75	0.00	97.80	4.54	39.72	98.28	0.95
Andesite	NA	007_ox4_1	0.03	49.70	0.18	43.85	0.42	2.35	0.03	0.02	0.04	0.00	0.73	0.00	97.26	4.19	40.08	97.78	0.96
Andesite	NA	007_ox4_1	0.00	49.59	0.17	43.82	0.48	2.25	0.04	0.01	0.01	0.00	0.67	0.02	97.03	4.18	40.05	97.50	0.96
Andesite	Core	007_ox6_cr1	0.03	48.57	0.14	42.45	0.50	2.61	0.13	0.03	0.01	0.03	0.78	0.00	95.26	4.53	38.38	95.74	0.95
Andesite	Rim	007_ox6_rm2	0.03	49.93	0.16	43.39	0.46	2.59	0.03	0.03	0.00	0.09	0.77	0.00	97.46	4.04	39.76	97.88	0.96
Andesite	Core	007_ox8_1	0.02	49.94	0.17	43.39	0.46	2.60	0.08	0.01	0.04	0.05	0.73	0.01	97.51	4.11	39.69	97.92	0.96
Andesite	Rim	007_ox8_3	0.05	49.57	0.17	43.32	0.45	2.64	0.09	0.03	0.00	0.07	0.71	0.01	97.11	4.45	39.31	97.56	0.95
Andesite	Rim	007_ox8_4	0.05	49.89	0.17	43.24	0.46	2.53	0.04	0.02	0.02	0.03	0.72	0.00	97.16	3.74	39.87	97.55	0.96
Andesite	NA	007_ox10_1	0.03	49.81	0.15	43.31	0.44	2.70	0.09	0.03	0.02	0.06	0.79	0.00	97.43	4.32	39.42	97.86	0.96
Andesite	NA	007_ox10_2	0.04	49.86	0.16	43.31	0.43	2.65	0.12	0.02	0.03	0.05	0.77	0.00	97.43	4.20	39.53	97.86	0.96
Andesite	NA	007_ox10_3	0.03	49.96	0.16	43.53	0.45	2.67	0.09	0.03	0.02	0.02	0.79	0.00	97.74	4.32	39.64	98.18	0.96
Andesite	NA	007_ox10_4	0.06	49.81	0.16	43.12	0.44	2.72	0.06	0.04	0.01	0.00	0.75	0.01	97.15	4.00	39.52	97.57	0.96
Andesite	Core	007_ox10_1	0.01	50.21	0.17	43.47	0.49	2.64	0.02	0.01	0.01	0.09	0.81	0.00	97.91	3.99	39.87	98.32	0.96
Andesite	Core	007_ox10_2	0.00	50.16	0.18	43.37	0.47	2.60	0.00	0.01	0.00	0.00	0.78	0.00	97.55	3.72	40.02	97.94	0.96
Andesite	Rim	007_ox10_3	0.05	47.06	0.17	45.65	0.40	2.43	0.05	0.03	0.02	0.07	0.75	0.00	96.68	9.02	37.54	97.59	0.91
Andesite	Rim	007_ox10_4	0.15	48.57	0.17	44.26	0.49	2.61	0.05	0.01	0.02	0.00	0.77	0.00	97.08	6.23	38.66	97.72	0.94
Andesite	Incl	007_ox14_1	0.03	49.80	0.18	43.56	0.44	2.53	0.05	0.01	0.01	0.06	0.79	0.00	97.45	4.22	39.77	97.88	0.96
Andesite	Incl	007_ox14_2	0.04	49.80	0.17	43.61	0.48	2.58	0.05	0.01	0.04	0.00	0.81	0.00	97.56	4.34	39.71	98.03	0.96
Andesite	Incl	007_ox14_3	0.03	49.75	0.18	43.51	0.43	2.60	0.03	0.01	0.02	0.00	0.80	0.00	97.38	4.25	39.69	97.80	0.96
Andesite	Rim	007_ox15_1	0.01	50.05	0.17	43.08	0.50	2.88	0.01	0.02	0.03	0.01	0.77	0.01	97.55	4.12	39.37	97.96	0.96
Andesite	Rim	007_ox15_2	0.02	50.11	0.17	43.14	0.49	2.85	0.02	0.02	0.01	0.00	0.78	0.00	97.59	4.06	39.49	98.02	0.96
Andesite	Rim	007_ox15_3	0.01	49.84	0.15	43.36	0.48	2.86	0.01	0.02	0.01	0.00	0.79	0.00	97.53	4.58	39.24	98.00	0.95
Andesite	NA	007_ox17_1	0.02	49.78	0.16	43.36	0.46	2.63	0.04	0.03	0.14	0.03	0.78	0.00	97.42	4.21	39.58	97.85	0.96
Andesite	NA	007_ox17_2	0.04	49.77	0.17	43.26	0.46	2.61	0.03	0.01	0.15	0.05	0.77	0.00	97.33	4.07	39.61	97.74	0.96
Andesite	NA	007_ox17_3	0.03	49.69	0.16	43.33	0.44	2.64	0.04	0.04	0.18	0.00	0.80	0.02	97.31	4.22	39.53	97.79	0.96
Andesite	NA	007_ox17_4	0.03	49.48	0.17	43.63	0.49	2.58	0.04	0.03	0.14	0.00	0.76	0.00	97.35	4.71	39.39	97.83	0.95
Andesite	Core	007_ox20_1	0.01	50.16	0.17	43.62	0.43	2.59	0.02	0.01	0.01	0.03	0.76	0.00	97.79	3.99	40.03	98.22	0.96
Andesite	Core	007_ox20_2	0.00	50.22	0.17	43.43	0.45	2.69	0.02	0.02	0.02	0.05	0.77	0.00	97.83	3.95	39.88	98.23	0.96
Andesite	Core	007_ox20_3	0.01	50.08	0.18	43.32	0.43	2.66	0.02	0.00	0.01	0.10	0.78	0.00	97.56	3.92	39.79	97.98	0.96
Andesite	Core	007_ox20_4	0.00	50.82	0.17	44.07	0.45	2.73	0.01	0.01	0.01	0.06	0.75	0.00	99.08	4.17	40.33	99.50	0.96
Andesite	Core	007_ox20_5	0.00	50.83	0.17	44.13	0.50	2.64	0.01	0.02	0.00	0.08	0.77	0.00	99.16	4.13	40.42	99.58	0.96
Andesite	NA	007_ox21_1	0.00	50.24	0.17	43.51	0.50	2.63	0.02	0.02	0.01	0.01	0.83	0.02	97.94	3.94	39.96	98.34	0.96
Andesite	NA	007_ox21_2	0.02	50.12	0.17	43.44	0.49	2.56	0.03	0.02	0.02	0.09	0.79	0.01	97.76	3.90	39.94	98.15	0.96
Andesite	NA	007_ox22_1	0.04	49.50	0.18	43.34	0.43	2.75	0.04	0.02	0.00	0.09	0.82	0.00	97.18	4.71	39.10	97.68	0.95
Andesite	Rim	007_ox23_1	0.02	50.21	0.18	43.30	0.47	2.57	0.08	0.01	0.02	0.09	0.80	0.01	97.75	3.71	39.96	98.12	0.96
Andesite	Rim	007_ox23_2	0.02	49.61	0.15	43.67	0.42	2.60	0.07	0.01	0.01	0.00	0.78	0.00	97.29	4.64	39.50	97.80	0.95
Andesite	Rim	007_ox23_3	0.03	49.54	0.17	43.84	0.42	2.63	0.12	0.02	0.00	0.16	0.78	0.00	97.69	5.17	39.19	98.22	0.95
Andesite	Rim	007_ox25_1	0.04	49.56	0.17	43.09	0.45	2.73	0.16	0.03	0.01	0.00	0.79	0.00	97.02	4.42	39.12	97.49	0.95
Andesite	Rim	007_ox25_2	0.02	49.80	0.17	43.10	0.40	2.69	0.09	0.02	0.02	0.06	0.81	0.00	97.17	4.06	39.45	97.58	0.96
Andesite	Incl	007_ox27_1	0.02	50.01	0.17	42.85	0.45	2.82	0.05	0.01	0.00	0.00	0.82	0.00	97.17	3.76	39.46	97.59	0.96

Andesite	Incl	007_ox27_2	0.05	49.61	0.16	42.76	0.40	2.74	0.13	0.03	0.03	0.04	0.81	0.01	96.77	3.96	39.19	97.17	0.96
Andesite	Rim	007_ox29_1	0.02	49.95	0.17	43.50	0.45	2.46	0.02	0.03	0.02	0.04	0.77	0.00	97.41	3.82	40.06	97.80	0.96
Andesite	Rim	007_ox29_2	0.07	49.70	0.19	43.49	0.43	2.63	0.03	0.02	0.02	0.04	0.74	0.00	97.36	4.35	39.58	97.79	0.96
Andesite	Rim	0202_tp1	0.00	50.81	0.19	43.16	0.47	3.19	0.04	0.03	0.07	0.05	0.86	0.00	98.88	4.14	39.44	99.31	0.96
Andesite	Rim	0202_tp2	0.01	50.34	0.21	42.40	0.46	3.28	0.05	0.01	0.06	0.15	0.91	0.01	97.89	4.02	38.78	98.29	0.96
Andesite	Rim	0202_tp3	0.02	50.24	0.19	42.70	0.44	3.19	0.06	0.02	0.08	0.06	0.87	0.00	97.86	4.17	38.95	98.28	0.96
Andesite	Incl	0202_ox1	0.00	50.50	0.16	42.75	0.45	3.19	0.01	0.01	0.08	0.04	0.84	0.00	98.03	3.89	39.25	98.43	0.96
Andesite	Incl	0202_ox2	0.00	50.56	0.17	42.63	0.43	3.24	0.01	0.00	0.05	0.03	0.81	0.01	97.93	3.77	39.23	98.31	0.96
Andesite	Incl	0202_tp1	0.03	50.23	0.19	42.57	0.42	3.29	0.05	0.02	0.11	0.06	0.64	0.01	97.61	4.17	38.81	98.02	0.96
Andesite	Lrg glom	0202_bg_tp1	0.01	49.69	0.16	42.94	0.55	3.11	0.03	0.02	0.06	0.02	0.78	0.00	97.36	4.86	38.56	97.86	0.95
Andesite	Lrg glom	0202_bg_tp2	0.00	49.67	0.17	43.23	0.67	3.12	0.03	0.01	0.06	0.00	0.79	0.00	97.74	5.37	38.40	98.31	0.94
Andesite	Sml glom	0202_tp3_1	0.00	50.50	0.19	42.61	0.46	3.03	0.04	0.02	0.06	0.00	0.84	0.00	97.70	3.43	39.53	98.09	0.96
Andesite	Sml glom	0202_tp3_2	0.01	50.62	0.19	42.50	0.45	3.10	0.02	0.02	0.05	0.08	0.86	0.00	97.89	3.37	39.46	98.23	0.97
Andesite	Sml glom	0202_tp4_1	0.00	50.42	0.19	42.78	0.46	3.18	0.04	0.02	0.03	0.00	0.85	0.03	97.92	4.00	39.18	98.38	0.96
Andesite	Sml glom	0202_tp4_2	0.00	50.53	0.17	42.84	0.40	3.10	0.03	0.02	0.10	0.00	0.82	0.01	98.01	3.72	39.50	98.38	0.96
Andesite	Core	015_ox1_cr1	0.00	50.60	0.19	43.22	0.42	3.12	0.01	0.00	0.04	0.05	0.82	0.00	98.44	4.16	39.48	98.88	0.96
Andesite	Core	015_ox1_cr2	0.00	50.65	0.22	43.37	0.43	3.10	0.02	0.01	0.04	0.00	0.81	0.00	98.62	4.20	39.59	99.06	0.96
Andesite	Rim	015_ox1_rm1	0.02	50.54	0.17	42.98	0.43	3.17	0.04	0.02	0.06	0.13	0.83	0.00	98.38	4.18	39.22	98.82	0.96
Andesite	Rim	015_ox1_rm2	0.04	50.35	0.17	42.96	0.43	3.09	0.02	0.02	0.05	0.07	0.85	0.00	98.03	4.06	39.30	98.46	0.96
Andesite	Rim	015_ox1_rm3	0.02	50.79	0.17	43.20	0.49	3.08	0.02	0.01	0.06	0.00	0.86	0.00	98.67	3.88	39.71	99.09	0.96
Andesite	Core	015_ox2_cr1	0.12	50.63	0.26	43.08	0.45	3.00	0.04	0.02	0.03	0.02	0.81	0.03	98.50	3.63	39.81	98.86	0.96
Andesite	Core	015_ox2_cr2	0.00	50.60	0.19	43.19	0.51	3.07	0.07	0.01	0.07	0.03	0.81	0.00	98.56	4.20	39.41	98.99	0.96
Andesite	Core	015_ox2_cr3	0.02	50.82	0.20	43.20	0.47	2.96	0.01	0.02	0.06	0.02	0.84	0.00	98.58	3.59	39.96	98.96	0.96
Andesite	Rim	015_ox2_rm1	0.03	50.35	0.19	43.16	0.48	3.20	0.03	0.04	0.05	0.00	0.92	0.00	98.44	4.52	39.10	98.90	0.95
Andesite	Rim	015_ox4_tp1	0.01	50.74	0.19	43.16	0.43	3.11	0.02	0.02	0.07	0.04	0.84	0.00	98.62	3.94	39.62	99.03	0.96
Andesite	Rim	015_ox4_tp2	0.00	50.47	0.19	43.38	0.41	3.15	0.03	0.02	0.07	0.00	0.82	0.00	98.52	4.48	39.35	98.98	0.95
Andesite	Rim	015_ox4_tp3	0.00	50.63	0.18	43.50	0.46	2.94	0.02	0.02	0.06	0.00	0.86	0.00	98.67	4.09	39.82	99.09	0.96
Andesite	Core	015_ox4_tp9	0.01	50.66	0.19	42.88	0.43	3.36	0.04	0.03	0.04	0.00	0.81	0.00	98.42	4.18	39.11	98.87	0.96
Andesite	Core	015_ox4_tp10	0.02	50.67	0.20	42.65	0.53	3.31	0.03	0.03	0.06	0.01	0.82	0.00	98.30	3.90	39.13	98.71	0.96
Andesite	Core	015_ox4_tp11	0.03	50.60	0.20	42.66	0.46	3.27	0.05	0.03	0.03	0.00	0.80	0.00	98.08	3.84	39.20	98.52	0.96
Andesite	Core	015_ox5_cr1	0.00	50.86	0.20	42.92	0.44	3.11	0.00	0.01	0.08	0.00	0.86	0.01	98.45	3.50	39.77	98.84	0.96
Andesite	Core	015_ox5_cr2	0.00	50.78	0.19	43.00	0.43	3.15	0.02	0.01	0.05	0.15	0.87	0.01	98.66	3.92	39.47	99.05	0.96
Andesite	Core	015_ox5_cr3	0.00	50.84	0.28	43.19	0.43	3.11	0.01	0.01	0.05	0.07	0.87	0.00	98.84	3.90	39.68	99.24	0.96
Andesite	Rim	015_ox5_tp1	0.02	49.95	0.16	43.77	0.44	3.11	0.04	0.03	0.08	0.04	0.84	0.03	98.52	5.44	38.87	99.07	0.94
Andesite	Rim	015_ox5_tp2	0.00	50.44	0.20	43.27	0.42	3.07	0.03	0.04	0.08	0.00	0.90	0.00	98.35	4.27	39.43	98.88	0.96
Andesite	Incl	015_ox7_1	0.04	50.61	0.23	42.47	0.44	3.70	0.02	0.01	0.10	0.00	0.88	0.01	98.46	4.39	38.51	98.94	0.95
Andesite	Incl	015_ox7_2	0.04	50.60	0.22	42.35	0.41	3.57	0.02	0.02	0.12	0.06	0.89	0.02	98.33	4.07	38.69	98.74	0.96
Andesite	Core	015_ox8_1	0.02	51.14	0.19	42.35	0.40	3.59	0.03	0.02	0.05	0.03	0.87	0.02	98.71	3.54	39.17	99.07	0.96
Andesite	Core	015_ox8_2	0.02	51.12	0.19	42.72	0.45	3.63	0.03	0.03	0.07	0.00	0.88	0.01	99.12	4.08	39.05	99.56	0.96
Andesite	Core	015_ox8_3	0.03	51.23	0.19	42.06	0.44	3.61	0.01	0.02	0.09	0.03	0.86	0.00	98.57	3.18	39.20	98.89	0.97
Andesite	Rim	015_ox8_rm2	0.07	50.87	0.16	42.48	0.46	3.53	0.05	0.04	0.06	0.00	0.85	0.01	98.58	3.85	39.02	98.97	0.96
Andesite	Core	015_ox9_cr1	0.00	50.99	0.20	42.86	0.45	3.27	0.02	0.01	0.06	0.00	0.88	0.02	98.74	3.68	39.55	99.12	0.96
Andesite	Core	015_ox9_cr2	0.00	51.05	0.19	42.77	0.46	3.32	0.00	0.01	0.10	0.01	0.84	0.00	98.75	3.60	39.53	99.12	0.96
Andesite	Rim	015_ox9_rm1	0.05	50.45	0.19	42.23	0.48	3.52	0.03	0.03	0.10	0.00	0.83	0.00	97.92	4.00	38.63	98.32	0.96
Andesite	Rim	015_ox9_rm2	0.03	50.70	0.20	42.98	0.43	3.49	0.03	0.04	0.10	0.00	0.84	0.00	98.82	4.50	38.93	99.29	0.95
Andesite	Rim	015_ox10_tp1	0.01	51.10	0.18	43.00	0.47	3.04	0.02	0.02	0.08	0.05	0.83	0.01	98.81	3.31	40.02	99.14	0.97
Andesite	Rim	015_ox10_tp2	0.01	51.01	0.20	43.35	0.42	2.93	0.01	0.00	0.07	0.00	0.84	0.01	98.80	3.45	40.24	99.17	0.97
Andesite	Rim	015_ox10_tp3	0.00	50.92	0.18	42.97	0.45	2.94	0.02	0.02	0.06	0.00	0.81	0.01	98.37	3.22	40.08	98.70	0.97
Andesite	Core	015_ox10_tp5	0.01	50.92	0.19	43.09	0.42	3.08	0.01	0.02	0.08	0.06	0.82	0.00	98.69	3.61	39.84	99.05	0.96
Andesite	Core	015_ox10_tp6	0.01	50.89	0.19	42.82	0.47	3.07	0.01	0.00	0.04	0.00	0.83	0.03	98.34	3.31	39.84	98.69	0.97
Andesite	Core	015_ox10_tp7	0.02	51.07	0.19	42.85	0.43	3.09	0.02	0.02	0.06	0.00	0.81	0.01	98.50	3.18	39.99	98.87	0.97
Andesite	Core	015_ox10_tp11	0.01	50.91	0.18	43.16	0.41	3.14	0.00	0.02	0.06	0.00	0.83	0.00	98.69	3.75	39.79	99.11	0.96
Andesite	Core	015_ox10_tp12	0.01	51.08	0.18	42.86	0.48	3.24	0.01	0.01	0.05	0.04	0.84	0.00	98.79	3.57	39.65	99.17	0.96
Andesite	Rim	015_ox10_tp15	0.00	51.00	0.20	42.85	0.42	3.16	0.03	0.02	0.07	0.06	0.83	0.01	98.63	3.46	39.74	98.98	0.96
Andesite	Rim	015_ox10_tp17	0.00	50.83	0.19	42.72	0.49	3.12	0.01	0.01	0.09	0.09	0.85	0.02	98.42	3.49	39.57	98.77	0.96
Andesite	Rim	015_ox11_tp1	0.00	50.76	0.19	43.35	0.47	3.03	0.06	0.01	0.05	0.00	0.83	0.00	98.68	4.04	39.71	99.17	0.96
Andesite	Rim	015_ox11_tp2	0.02	50.78	0.18	42.94	0.49	3.08	0.05	0.01	0.08	0.00	0.85	0.01	98.48	3.65	39.65	98.85	0.96
Andesite	Core	015_ox12_cr1	0.03	50.57	0.18	42.03	0.44	3.19	0.03	0.01	0.08	0.00	0.85	0.02	97.38	2.96	39.37	97.74	0.97
Andesite	Core	015_ox12_cr2	0.01	50.87	0.21	42.74	0.44	3.12	0.03	0.00	0.07	0.00	0.81	0.01	98.20	3.34	39.73	98.63	0.97
Andesite	Rim	015_ox12_rm1	0.40	49.48	0.22	42.27	0.45	2.99	0.10	0.11	0.07	0.08	0.79	0.00	96.96	3.63	39.00	97.33	0.96
Andesite	Rim	015_ox12_rm2	0.08	50.66	0.20	43.04	0.49	3.02	0.03	0.01	0.07	0.05	0.81	0.01	98.46	3.71	39.70	98.83	0.96

Andesite	Core	0202plug_tp2	0.00	50.39	0.20	41.91	0.43	3.36	0.07	0.01	0.13	0.00	0.84	0.00	97.24	3.44	38.81	97.68	0.96
Andesite	Rim	0202plug_tp5	0.01	50.48	0.21	42.17	0.42	3.58	0.07	0.01	0.05	0.00	0.89	0.00	97.84	4.04	38.53	98.28	0.96
Andesite	NA	0202plug2_tp1	0.00	50.72	0.20	42.37	0.45	3.35	0.01	0.00	0.09	0.06	0.83	0.00	98.09	3.61	39.12	98.45	0.96
Andesite	Core	0202plug2_cr1	0.00	50.74	0.20	42.45	0.46	3.33	0.02	0.00	0.08	0.00	0.83	0.00	98.07	3.59	39.22	98.47	0.96
Andesite	Rim	0202plug2_rm1	0.01	50.78	0.21	42.16	0.45	3.31	0.01	0.01	0.09	0.00	0.82	0.00	97.82	3.15	39.33	98.16	0.97
Andesite	Rim	0202plug2_rm2	0.00	50.23	0.20	42.07	0.50	3.49	0.09	0.01	0.08	0.04	0.84	0.01	97.56	4.18	38.31	97.98	0.96
Andesite	Rim	0202plug3_tp1	0.00	50.63	0.18	42.54	0.42	3.22	0.02	0.01	0.08	0.00	0.83	0.03	97.91	3.54	39.36	98.31	0.96
Andesite	Rim	0202plug3_tp2	0.00	50.72	0.20	42.53	0.44	3.35	0.00	0.01	0.09	0.00	0.82	0.01	98.13	3.68	39.22	98.53	0.96
Andesite	Core	0202plug3_cr1	0.01	50.79	0.17	42.23	0.45	3.46	0.01	0.00	0.07	0.05	0.83	0.00	98.07	3.56	39.03	98.44	0.96
Andesite	Core	0202plug3_cr2	0.00	50.52	0.17	42.01	0.46	3.21	0.07	0.01	0.09	0.00	0.83	0.00	97.36	3.15	39.17	97.69	0.97
Andesite	Core	0202plug4_tp1	0.02	50.58	0.21	42.57	0.46	3.17	0.04	0.02	0.10	0.00	0.85	0.01	97.99	3.58	39.34	98.39	0.96
Andesite	Core	0202plug4_tp2	0.17	48.39	0.20	43.45	0.42	2.77	0.09	0.03	0.09	0.00	0.82	0.00	96.39	5.78	38.25	97.01	0.94
Andesite	Rim	0202plug4_rm1	0.01	50.65	0.18	42.20	0.44	2.95	0.08	0.02	0.09	0.00	0.87	0.00	97.44	2.70	39.77	97.75	0.97
Andesite	Rim	0202plug4_tp2	0.00	50.44	0.20	42.62	0.42	3.20	0.21	0.03	0.07	0.00	0.81	0.00	97.94	4.06	38.97	98.42	0.96
Andesite	Core	0202plug6_cr1	0.00	50.65	0.21	42.05	0.45	3.11	0.02	0.02	0.08	0.03	0.87	0.01	97.50	2.82	39.51	97.78	0.97
Andesite	Rim	0202plug6_rm1	0.00	50.69	0.20	42.48	0.52	3.31	0.00	0.01	0.09	0.10	0.87	0.00	98.25	3.77	39.09	98.65	0.96
Andesite	Core	0202plug7_cr1	0.02	50.40	0.19	42.20	0.48	3.31	0.03	0.01	0.05	0.03	0.86	0.01	97.57	3.66	38.91	97.93	0.96
Andesite	Rim	0202plug7_rm1	0.00	50.71	0.17	42.33	0.45	3.22	0.01	0.01	0.05	0.14	0.84	0.01	97.94	3.38	39.28	98.28	0.97
Andesite	Core	0202plug8_cr1	0.00	50.59	0.20	42.53	0.48	3.35	0.00	0.01	0.09	0.00	0.87	0.00	98.07	3.88	39.04	98.51	0.96
Andesite	Rim	0202plug8_rm1	0.01	50.16	0.19	42.06	0.52	3.29	0.02	0.01	0.06	0.00	0.86	0.02	97.19	3.71	38.72	97.57	0.96
Andesite	NA	0202plug8_tp1	0.16	49.25	0.26	43.34	0.42	3.05	0.19	0.03	0.07	0.02	0.83	0.00	97.61	5.51	38.38	98.17	0.94
Andesite	Rim	0202plug8_rm1	0.01	50.49	0.22	42.24	0.45	3.58	0.01	0.02	0.08	0.00	0.85	0.00	97.88	4.08	38.57	98.36	0.96
Andesite	Rim	0202plug8_rm2	0.00	50.37	0.19	42.03	0.43	3.46	0.02	0.02	0.08	0.16	0.81	0.00	97.57	3.87	38.55	97.96	0.96
Andesite	Core	0202plug10_tp1	0.04	47.84	0.29	42.33	0.39	4.79	0.05	0.02	0.07	0.00	0.88	0.00	96.66	9.16	34.09	97.63	0.90
Andesite	Core	0202plug10_tp2	0.00	50.89	0.19	42.48	0.47	3.40	0.06	0.01	0.08	0.00	0.82	0.02	98.42	3.69	39.16	98.79	0.96
Andesite	Rim	0202plug10_rm1	0.00	50.72	0.19	42.21	0.47	3.53	0.01	0.02	0.07	0.05	0.80	0.00	98.08	3.79	38.80	98.46	0.96
Andesite	Core	0202plug11_cr1	0.00	50.60	0.19	43.05	0.49	3.01	0.01	0.02	0.04	0.00	0.85	0.00	98.22	3.77	39.65	98.64	0.96
Andesite	Rim	0202plug11_rm1	0.02	50.44	0.18	42.83	0.45	3.05	0.02	0.02	0.06	0.01	0.85	0.02	97.95	3.74	39.47	98.33	0.96
Andesite	Rim	0202plug12_tp1	0.01	50.78	0.20	42.62	0.41	3.15	0.01	0.02	0.07	0.00	0.89	0.00	98.10	3.29	39.66	98.48	0.97
Andesite	NA	0202plug12_tp3	0.00	50.23	0.20	42.26	0.43	3.41	0.01	0.01	0.08	0.06	0.82	0.00	97.49	4.05	38.62	97.91	0.96
Andesite	Core	0202plug12_cr1	0.01	50.62	0.19	42.57	0.55	3.32	0.01	0.01	0.07	0.00	0.87	0.01	98.16	3.89	39.06	98.63	0.96
Andesite	Core	0202plug13_cr1	0.00	50.60	0.20	42.68	0.43	3.18	0.01	0.02	0.07	0.08	0.86	0.00	98.13	3.70	39.34	98.50	0.96
Andesite	Rim	0202plug13_rm1	0.02	50.57	0.20	42.09	0.43	3.56	0.02	0.02	0.07	0.02	0.86	0.00	97.82	3.77	38.69	98.23	0.96
Andesite	Core	0202plug14_cr1	0.01	50.82	0.20	42.41	0.48	3.39	0.02	0.01	0.06	0.05	0.88	0.00	98.31	3.64	39.13	98.69	0.96
Andesite	NA	0202plug14_tp1	0.00	50.64	0.19	42.36	0.48	3.26	0.01	0.03	0.06	0.00	0.86	0.00	97.86	3.46	39.25	98.24	0.96
Andesite	Core	0202plug14_cr1	0.02	51.13	0.23	42.42	0.43	3.16	0.00	0.02	0.08	0.14	0.85	0.02	98.48	2.89	39.82	98.77	0.97
Andesite	Rim	0202plug14_rm1	0.01	51.07	0.21	41.97	0.42	3.23	0.03	0.01	0.07	0.00	0.84	0.00	97.84	2.50	39.72	98.11	0.97
Andesite	Core	0202plug16_tp1	0.00	50.79	0.18	42.62	0.46	3.34	0.03	0.00	0.04	0.00	0.84	0.00	98.26	3.76	39.23	98.67	0.96
Andesite	Core	0202plug16_tp3	0.00	50.77	0.20	42.67	0.47	3.14	0.03	0.01	0.08	0.03	0.84	0.00	98.24	3.49	39.53	98.59	0.96
Andesite	Core	0202plug16_tp6	0.00	50.63	0.19	42.77	0.44	3.00	0.03	0.00	0.07	0.00	0.84	0.00	97.95	3.39	39.71	98.32	0.97
Andesite	NA	0201plug1_tp1	0.00	50.43	0.18	42.50	0.48	3.22	0.08	0.01	0.07	0.09	0.86	0.00	97.89	3.95	38.95	98.32	0.96
Andesite	Core	0201plug1_cr1	0.01	50.12	0.30	42.26	0.46	3.44	0.03	0.02	0.02	0.04	0.87	0.00	97.55	4.26	38.42	97.99	0.96
Andesite	Core	0201plug2_cr1	0.00	50.70	0.20	42.55	0.43	3.24	0.05	0.01	0.07	0.16	0.86	0.00	98.27	3.71	39.21	98.64	0.96
Andesite	Rim	0201plug2_rm1	0.00	50.40	0.19	42.49	0.45	3.36	0.02	0.01	0.06	0.05	0.87	0.00	97.89	4.07	38.83	98.30	0.96
Andesite	Core	0201plug2_cr1	0.00	50.58	0.20	42.46	0.42	3.23	0.03	0.01	0.09	0.03	0.89	0.00	97.92	3.54	39.27	98.28	0.96
Andesite	Core	0201plug2_cr2	0.01	50.73	0.22	42.59	0.43	3.31	0.01	0.02	0.06	0.00	0.84	0.02	98.23	3.65	39.31	98.61	0.96
Andesite	Rim	0201plug2_rm1	0.00	50.52	0.20	42.27	0.48	3.21	0.06	0.03	0.07	0.04	0.85	0.02	97.75	3.50	39.12	98.10	0.96
Andesite	Rim	0201plug2_rm2	0.00	50.78	0.20	42.59	0.42	3.46	0.01	0.00	0.06	0.00	0.89	0.01	98.43	3.91	39.07	98.82	0.96
Andesite	Core	0201plug4_cr1	0.01	50.66	0.20	42.44	0.42	3.39	0.03	0.02	0.09	0.05	0.89	0.00	98.20	3.79	39.04	98.59	0.96
Andesite	Rim	0201plug4_rm1	0.01	50.63	0.20	42.43	0.45	3.35	0.02	0.02	0.10	0.03	0.91	0.00	98.15	3.73	39.08	98.53	0.96

Phase 2	Core	021plug1_cr1	0.01	49.18	0.09	47.26	0.52	0.51	0.00	0.01	0.00	0.00	0.21	0.00	97.76	4.95	42.80	98.29	0.95
Phase 2	Core	021plug1_cr2	0.00	49.12	0.08	46.91	0.53	0.51	0.00	0.02	0.00	0.03	0.21	0.01	97.40	4.65	42.72	97.87	0.95
Phase 2	Core	021plug1_cr3	0.00	49.17	0.08	47.35	0.47	0.50	0.02	0.01	0.00	0.00	0.20	0.01	97.80	5.00	42.85	98.31	0.95
Phase 2	Rim	021plug1_rm1	0.00	49.36	0.08	47.16	0.48	0.51	0.01	0.01	0.00	0.05	0.24	0.00	97.91	4.69	42.94	98.40	0.95
Phase 2	Rim	021plug1_rm2	0.00	49.51	0.09	47.28	0.51	0.47	0.01	0.02	0.00	0.00	0.28	0.00	98.13	4.56	43.17	98.63	0.96
Phase 2	Rim	021plug1_rm3	0.00	49.50	0.07	47.03	0.52	0.46	0.01	0.02	0.01	0.00	0.23	0.00	97.67	4.28	43.19	98.28	0.96
Phase 2	NA	021plug1_tp1	0.00	49.04	0.07	47.51	0.52	0.51	0.05	0.02	0.00	0.04	0.24	0.00	97.98	5.46	42.59	98.54	0.95
Phase 2	NA	021plug1_tp2	0.00	48.88	0.08	46.99	0.51	0.56	0.04	0.02	0.00	0.00	0.23	0.00	97.22	5.09	42.41	97.83	0.95
Phase 2	Rim	021plug1_rm1	0.01	48.66	0.09	47.17	0.52	0.56	0.01	0.01	0.00	0.01	0.29	0.02	97.32	5.48	42.24	97.88	0.95
Phase 2	Rim	021plug1_rm3	0.01	49.72	0.07	47.29	0.54	0.51	0.01	0.03	0.01	0.10	0.31	0.00	98.59	4.56	43.18	99.05	0.96
Phase 2	Core	021plug3_cr1	0.00	49.20	0.08	47.05	0.55	0.51	0.00	0.01	0.00	0.03	0.27	0.00	97.69	4.75	42.78	98.18	0.95
Phase 2	Core	021plug3_cr2	0.00	49.26	0.09	47.58	0.53	0.55	0.00	0.01	0.02	0.09	0.24	0.00	98.34	5.40	42.72	98.91	0.95
Phase 2	Rim	021plug3_rm1	0.02	48.58	0.09	47.18	0.56	0.56	0.02	0.02	0.02	0.00	0.36	0.00	97.21	5.58	42.15	97.97	0.94
Phase 2	Rim	021plug3_rm2	0.02	48.34	0.08	46.95	0.51	0.54	0.01	0.02	0.00	0.03	0.39	0.00	96.88	5.53	41.98	97.44	0.95
Phase 2	Rim	021plug3_rm3	0.01	48.82	0.08	46.90	0.49	0.54	0.01	0.01	0.00	0.00	0.45	0.00	97.30	4.93	42.46	97.81	0.95
Phase 2	Core	021plug3_cr1	0.00	49.21	0.08	47.24	0.49	0.50	0.00	0.01	0.03	0.00	0.23	0.02	97.76	4.85	42.87	98.30	0.95
Phase 2	Core	021plug4_cr1	0.00	49.04	0.08	46.91	0.50	0.49	0.02	0.02	0.00	0.16	0.26	0.01	97.46	4.82	42.57	97.97	0.95
Phase 2	Core	021plug4_cr2	0.01	49.20	0.08	47.34	0.51	0.49	0.00	0.01	0.00	0.04	0.26	0.00	97.93	5.00	42.84	98.45	0.95
Phase 2	Core	021plug4_cr3	0.01	49.06	0.09	46.95	0.58	0.52	0.01	0.01	0.01	0.06	0.24	0.00	97.54	4.88	42.56	98.03	0.95
Phase 2	Rim	021plug4_rm2	0.00	48.78	0.08	46.57	0.53	0.59	0.01	0.01	0.02	0.03	0.46	0.00	97.05	4.79	42.26	97.55	0.95
Phase 2	Core	021plug6_cr1	0.01	49.19	0.07	47.11	0.51	0.51	0.01	0.01	0.00	0.08	0.21	0.00	97.67	4.84	42.75	98.19	0.95
Phase 2	Core	021plug6_cr2	0.00	49.32	0.09	47.33	0.55	0.53	0.01	0.02	0.00	0.00	0.22	0.03	98.04	4.98	42.85	98.59	0.95
Phase 2	Rim	021plug6_rm1	0.02	48.86	0.11	46.62	0.55	0.50	0.01	0.02	0.00	0.02	0.24	0.00	96.94	4.58	42.50	97.40	0.95
Phase 2	Rim	021plug6_rm2	0.01	49.38	0.08	46.96	0.46	0.48	0.04	0.02	0.00	0.00	0.25	0.03	97.64	4.35	43.05	98.14	0.96
Phase 2	Rim	021plug6_rm3	0.48	48.86	0.11	46.42	0.52	0.58	0.03	0.02	0.00	0.12	0.30	0.00	97.42	3.99	42.82	97.83	0.96
Phase 2	Core	021plug9_cr1	0.00	49.18	0.09	47.55	0.50	0.50	0.01	0.02	0.00	0.02	0.22	0.00	98.09	5.26	42.82	98.62	0.95
Phase 2	Core	021plug9_cr2	0.00	49.12	0.08	47.64	0.54	0.51	0.00	0.01	0.01	0.00	0.24	0.00	98.14	5.46	42.73	98.70	0.95
Phase 2	Rim	021plug9_rm2	0.00	48.33	0.09	46.86	0.57	0.62	0.02	0.01	0.00	0.00	0.37	0.00	96.83	5.65	41.78	97.43	0.94

Magnetite																			
Rock Type	**Spot**	**Comment**	**SiO2**	**TiO2**	**Al2O3**	**FeO**	**MnO**	**MgO**	**CaO**	**K2O**	**Cr2O3**	**ZnO**	**V2O3**	**NiO**	**Total**	**Fe2O3***	**FeO***	**Total***	**%Usp***
Plinian	NA	009plug1_tp1	0.03	4.98	2.83	82.37	0.94	1.26	0.00	0.02	0.00	0.25	0.05	0.00	92.70	55.36	32.55	98.27	0.14
Plinian	Core	009plug1_cr1	0.04	5.34	3.10	82.53	0.88	1.30	0.00	0.01	0.00	0.24	0.06	0.00	93.46	54.85	33.18	99.00	0.16
Plinian	Core	009plug2_cr1	0.02	4.46	2.39	83.80	0.82	1.15	0.00	0.01	0.01	0.09	0.18	0.03	92.94	56.99	32.51	98.65	0.13
Plinian	Rim	009plug2_rm2	0.02	4.38	2.04	83.07	0.83	0.94	0.00	0.02	0.02	0.31	0.14	0.01	91.78	56.62	32.13	97.45	0.13
Plinian	Rim	009plug2_rm3	0.02	4.43	2.02	82.55	0.92	0.98	0.00	0.02	0.03	0.24	0.17	0.03	91.41	56.23	31.96	97.05	0.13
Plinian	Core	009plug2_cr2	0.03	4.44	2.42	83.58	0.87	1.23	0.00	0.00	0.00	0.18	0.17	0.00	92.91	57.03	32.27	98.65	0.13
Plinian	Core	009plug3_1	0.03	3.70	2.45	83.27	0.81	1.24	0.00	0.02	0.81	0.23	0.11	0.01	92.67	57.51	31.52	98.44	0.11
Plinian	Core	009plug4_tp1	0.04	6.87	3.73	79.51	0.70	1.96	0.01	0.02	0.00	0.20	0.09	0.03	93.14	50.93	33.68	98.25	0.20
Plinian	Rim	009plug4_rm1	0.05	6.86	4.19	77.88	0.68	2.22	0.01	0.04	0.00	0.07	0.13	0.00	92.13	49.73	33.13	97.11	0.20
Plinian	Rim	009plug4_rm2	0.04	7.06	4.18	78.58	0.63	2.25	0.00	0.03	0.03	0.00	0.15	0.00	92.89	49.93	33.65	97.95	0.21
Plinian	Core	009plug5_cr2	0.04	5.82	2.94	81.70	0.81	1.40	0.00	0.02	0.00	0.21	0.10	0.05	93.04	53.73	33.35	98.45	0.17
Plinian	Rim	009plug5_rm1	0.04	5.79	3.17	80.15	0.76	1.58	0.00	0.02	0.02	0.11	0.12	0.02	91.79	52.61	32.82	97.06	0.17
Rhyolite	NA	021plug5_tp4	0.09	16.68	1.95	74.46	0.31	0.25	0.00	0.01	0.01	0.15	1.39	0.03	95.32	31.93	45.73	98.52	0.52
Rhyolite	NA	021plug5_tp5	0.09	16.66	1.97	74.23	0.34	0.26	0.02	0.01	0.00	0.22	1.37	0.02	95.16	31.87	45.55	98.39	0.52
Rhyolite	NA	021plug5_tp6	0.08	16.48	1.96	74.67	0.36	0.24	0.01	0.01	0.02	0.36	1.34	0.00	95.53	32.53	45.40	98.79	0.51

*Recalculatiof Stormer (1983)

Fayalite															
No.	Comment	CaO	TiO2	SiO2	Al2O3	MgO	P2O5	FeO	NiO	Cr2O3	MnO	Total	Fo	Fa	Tp
53	83070fay1_core2	0.07	-0.02	30.10	0.00	3.59	0.04	64.58	-0.03	-0.01	1.38	99.69	0.09	0.89	0.02
54	83070fay1_core2	0.05	-0.01	30.03	0.00	3.53	0.04	65.12	-0.02	-0.02	1.31	100.03	0.09	0.90	0.02
55	83070fay1_core3	0.06	0.03	30.07	0.01	3.52	-0.01	65.09	-0.06	-0.03	1.36	100.03	0.09	0.89	0.02
56	83070fay1_core4	0.07	0.03	30.18	0.00	3.50	0.06	64.47	-0.06	0.00	1.32	99.58	0.09	0.89	0.02
57	83070fay1_core5	0.09	0.01	30.03	-0.01	3.57	0.06	64.90	-0.01	-0.01	1.27	99.90	0.09	0.89	0.02
58	83070fay1_rim1	0.05	-0.01	29.89	0.00	3.53	-0.11	64.67	0.03	0.01	1.43	99.49	0.09	0.89	0.02
59	83070fay1_rim2	0.09	0.05	31.14	-0.02	3.74	-0.03	62.08	0.01	0.01	1.34	98.41	0.10	0.89	0.02
61	83070fay1_rim4	0.08	0.01	31.11	0.18	3.46	-0.01	62.77	0.05	0.00	1.21	98.86	0.09	0.89	0.02
62	83070fay1_rim5	0.10	0.06	30.25	0.01	3.58	-0.02	62.99	-0.01	-0.02	1.34	98.28	0.09	0.89	0.02
63	83070fay2_core1	0.07	0.01	29.96	-0.01	3.58	-0.03	64.99	-0.04	-0.04	1.34	99.84	0.09	0.89	0.02
65	83070fay2_core3	0.08	0.03	30.39	-0.02	3.45	-0.04	64.03	0.02	-0.01	1.31	99.24	0.09	0.90	0.02
66	83070fay2_core4	0.06	0.04	29.92	0.01	3.56	-0.03	64.29	-0.01	-0.01	1.35	99.19	0.09	0.89	0.02
69	83070fay2_rim2	0.08	-0.01	30.04	-0.01	3.80	-0.01	64.12	-0.08	-0.01	1.36	99.29	0.09	0.89	0.02
70	83070fay2_rim3	0.08	0.04	30.03	-0.01	3.81	-0.06	63.86	0.04	0.01	1.39	99.20	0.09	0.89	0.02
71	83070fay2_rim4	0.09	0.04	29.83	0.00	3.66	0.03	64.24	0.01	-0.02	1.31	99.21	0.09	0.89	0.02
73	CH12021fay1_core1	0.08	0.00	30.14	0.00	3.55	0.00	64.47	-0.06	-0.01	1.31	99.48	0.09	0.89	0.02
74	CH12021fay1_core2	0.08	0.02	30.33	-0.01	3.57	0.07	63.78	-0.02	-0.01	1.30	99.11	0.09	0.89	0.02
75	CH12021fay1_core3	0.09	0.03	30.38	0.01	3.52	-0.05	64.20	0.06	0.01	1.36	99.61	0.09	0.89	0.02
76	CH12021fay1_core4	0.15	0.01	30.43	0.00	3.56	0.05	64.41	-0.05	0.02	1.28	99.86	0.09	0.89	0.02
77	CH12021fay1_core5	0.08	0.03	30.17	-0.01	3.51	0.04	64.34	0.03	-0.03	1.37	99.53	0.09	0.89	0.02
78	CH12021fay1_rim1	0.09	0.01	31.70	0.02	3.93	0.04	64.39	0.02	0.01	1.36	101.57	0.10	0.88	0.02
81	CH12021fay1_rim4	0.09	0.02	30.36	-0.01	3.53	0.06	63.76	-0.01	-0.02	1.26	99.05	0.09	0.89	0.02
82	CH12021fay1_rim5	0.10	-0.02	30.83	0.13	3.51	-0.02	63.81	-0.03	-0.01	1.31	99.63	0.09	0.89	0.02

Biotite

No.	CaO	K2O	SiO2	Al2O3	MgO	Na2O	FeO	MnO	Cr2O3	TiO2	Cl	Total	Comment
4	-0.01	9.02	33.42	14.29	4.23	0.55	29.22	0.19	0.00	5.29	0.27	96.38	CH12021_bio1.1
5	0.02	9.07	33.43	14.21	4.29	0.57	29.44	0.16	0.00	5.29	0.27	96.68	CH12021_bio1.2
6	0.02	9.12	33.72	14.26	4.24	0.63	29.50	0.15	0.05	5.27	0.27	97.16	CH12021_bio1.3
7	0.01	9.15	33.80	14.42	4.20	0.58	29.28	0.16	-0.01	5.26	0.26	97.04	CH12021_bio1.4
8	0.02	9.07	33.39	14.34	4.27	0.54	29.08	0.13	0.04	5.24	0.24	96.32	CH12021_bio1.5
9	0.02	8.98	33.91	14.17	4.18	0.56	29.21	0.22	0.04	5.34	0.26	96.84	CH12021_bio2.1
10	0.05	9.01	33.64	14.13	4.17	0.54	29.51	0.15	0.04	5.32	0.25	96.75	CH12021_bio2.2
11	0.02	8.96	33.44	14.24	4.30	0.60	29.37	0.16	-0.03	5.28	0.26	96.54	CH12021_bio2.3
12	0.04	8.92	33.60	14.24	4.17	0.59	29.79	0.14	0.00	5.35	0.26	97.04	CH12021_bio2.4
13	0.05	8.90	33.63	14.15	4.28	0.60	29.81	0.14	0.02	5.34	0.26	97.13	CH12021_bio3.1
14	0.01	8.98	33.84	14.29	4.29	0.62	29.76	0.14	0.01	5.36	0.26	97.48	CH12021_bio3.2
15	0.04	8.98	33.63	14.16	4.21	0.53	29.35	0.15	0.01	5.26	0.24	96.52	CH12021_bio3.3
16	0.04	8.92	33.37	14.14	4.25	0.59	29.24	0.14	0.00	5.32	0.25	96.21	CH12021_bio3.4
17	0.01	9.20	33.42	14.05	4.27	0.57	29.42	0.16	-0.01	5.25	0.26	96.55	CH12021_bio3.5
18	0.00	9.05	33.66	14.15	4.20	0.56	29.56	0.17	-0.02	5.31	0.24	96.83	CH12021_bio5.1
19	0.04	9.14	33.41	14.25	4.22	0.54	30.05	0.16	0.02	5.27	0.26	97.31	CH12021_bio5.2
20	0.07	8.91	33.40	13.98	4.17	0.56	28.41	0.16	0.00	5.25	0.25	95.08	CH12021_bio5.3
21	0.05	8.97	33.62	14.12	4.27	0.58	28.99	0.18	0.03	5.29	0.25	96.30	CH12021_bio5.4
22	0.03	9.00	33.93	14.48	4.26	0.53	29.16	0.14	0.01	5.25	0.25	96.99	CH12021_bio5.5
23	0.02	9.02	33.65	14.11	4.22	0.54	29.29	0.13	0.01	5.34	0.25	96.52	CH12021_bio5.6
24	0.03	9.06	33.75	14.35	4.25	0.49	29.27	0.16	0.01	5.23	0.25	96.77	CH12021_bio6.1
25	0.04	9.04	33.62	14.21	4.17	0.57	29.43	0.15	0.03	5.26	0.27	96.73	CH12021_bio6.2
26	0.03	9.13	33.65	14.17	4.19	0.54	29.34	0.13	-0.01	5.28	0.27	96.65	CH12021_bio6.3
27	0.01	9.09	33.82	14.24	4.14	0.60	29.69	0.16	-0.01	5.31	0.26	97.24	CH12021_bio8.1
28	0.02	9.05	33.85	14.29	4.24	0.60	29.58	0.13	0.01	5.31	0.24	97.25	CH12021_bio8.2
29	0.00	9.06	33.54	14.18	4.09	0.57	29.72	0.19	-0.01	5.30	0.26	96.84	CH12021_bio8.3
30	0.11	8.88	33.42	14.14	4.14	0.55	28.92	0.17	0.00	5.21	0.28	95.76	CH12021_bio8.4
31	0.01	9.06	34.03	14.46	4.50	0.52	29.79	0.17	0.04	4.55	0.26	97.36	CH12021_bio8.5
32	0.05	9.16	33.79	14.18	4.34	0.59	29.63	0.12	-0.02	5.15	0.30	97.22	CH12021_bio8.6
33	0.03	9.02	33.94	14.21	4.21	0.57	29.38	0.16	-0.01	5.22	0.25	96.93	83070_bio1.1
34	0.04	8.89	33.53	14.25	4.19	0.56	29.52	0.14	0.02	5.32	0.25	96.66	83070_bio1.2
35	0.03	9.07	33.78	14.30	4.26	0.56	29.25	0.16	0.00	5.26	0.25	96.87	83070_bio1.3
36	0.03	9.08	33.86	14.27	4.21	0.54	29.31	0.13	0.00	5.29	0.26	96.93	83070_bio1.4
37	0.03	9.01	33.66	14.30	4.15	0.63	29.59	0.16	0.03	5.35	0.25	97.10	83070_bio2.1
38	0.02	9.14	33.81	14.48	4.27	0.57	29.64	0.16	0.00	5.32	0.24	97.58	83070_bio2.2
39	0.01	9.15	33.71	14.39	4.18	0.58	29.48	0.15	-0.03	5.36	0.26	97.17	83070_bio2.3
40	0.00	8.91	33.64	14.40	4.24	0.60	29.54	0.16	0.04	5.35	0.26	97.09	83070_bio2.4
41	0.04	9.07	33.31	14.17	4.19	0.57	29.31	0.15	0.04	5.27	0.25	96.33	83070_bio2.5
42	0.03	9.12	32.77	13.80	4.07	0.61	28.86	0.17	0.00	5.33	0.26	94.97	83070_bio2.6
43	0.06	9.09	33.23	14.18	4.19	0.59	29.09	0.15	0.03	5.32	0.25	96.12	83070_bio2.7

Fig. 7 Model

Sample	87Sr/86Sr	143Nd/144Nd	[Sr]	[Nd]
Sierra de Moreno*	0.719532	0.512087	116	36.63
Mantle Values'	0.7033	0.513	711	13

r	0.6
zsr	-1.5
Dsr	1
Dnd	0.9
znd	-1.25

F	87Sr/86 result^	143/144 result^	1/Sr
1	0.70330	0.51300	0.00
0.9	0.70374	0.51271	0.00
0.8	0.70428	0.51252	0.00
0.7	0.70497	0.51240	0.00
0.6	0.70586	0.51231	0.00
0.5	0.70702	0.51225	0.00
0.4	0.70856	0.51220	0.00
0.3	0.71064	0.51216	0.00
0.2	0.71342	0.51213	0.01
0.1	0.71682	0.51210	0.01
0	0.71953	0.51209	0.01

**Compositions for Sierra de Moreno taken from Lucassen et al. (2001)*
^Equation 15b of DePaolo (1981)
'Sr compositions from van Alderwerelt et al. (2021). Nd compositions from Mamani et al. (2010)

Supplementary Figure

Sample		87Sr/86Sr	[Sr]
Sierra de Moreno*		0.713811	114
Caspana	CH19C006	0.711168	524.1

r	0.05
zsr	-1.42
Dsr	2.30

F	87Sr/86Sr result^	[Sr] mix
1	0.71117	524.09
0.9	0.71117	483.08
0.8	0.71118	442.07
0.7	0.71118	401.06
0.6	0.71119	360.05
0.5	0.71120	319.04
0.4	0.71122	278.03
0.3	0.71126	237.03
0.2	0.71134	196.02
0.1	0.71162	155.01
0	0.71381	114.00

**Compositions for Sierra de Moreno taken from Lucassen et al. (2001)*
^Equation 15b of DePaolo (1981)

Aitcheson and Forrest Models

All models below from Aitcheson and Forrest (1994)

		Sample	$^{87}Sr/^{86}Sr$	$^{143}Nd/^{144}Nd$	$^{206}Pb/^{204}Pb$	[Sr]	[Nd]	[Pb]
Assimilant	Sierra de Moreno*		0.719532	0.512128	19.781	115.53	36.63	12.3
	Parent^		0.7033	0.513	18.221	711	13	4
Daughter	Caspana	CH19C006	0.711168	0.51214	18.745	524.0872	23.8	14

				r = 0.1	0.2	0.3	0.4	0.5	0.6	0.7	0.8	0.9
Sr			Eqn 5	0.111111107	0.249882336	0.423661	0.6289813	0.852709	1.081648075	1.306545566	1.521984985	1.725258
	lambda	0.940698231										
	gamma	0.162489451										
	Dsr	1										
			Eqn 6	0.107367472	0.194599743	0.250631	0.2877897	0.313891	0.333136951	0.347880954	0.359523542	0.3689437
			Eqn 7	0.111092833	0.244797122	0.383797	0.5106135	0.620182	0.713301117	0.79236032	0.85982415	0.9178162
Nd			Eqn 5	#NUM!	0.25	0.428569	0.665913	0.984877	1.395730325	1.889782124	2.447420268	3.0469342
	lambda	71.66666667										
	gamma	2.817692308										
	D Nd	0.85										
			Eqn 6	0.097818739	0.185159796	0.258065	0.3181368	0.367855	0.409410469	0.44453076	0.474534876	0.5004269
			Eqn 7	-6.64335E+27	0.25	0.428571	0.6665696	0.994798	1.443111676	2.020035269	2.711300096	3.4908792
206 Pb			Eqn 5	0.101168804	0.132561036	0.143158	0.1484745	#DIV/0!	0.153801668	0.155325578	0.15646903	0.1573587
	lambda	0.505791506										
	gamma	3.075										
	D Pb	0.5										
			Eqn 6	0.095806215	0.199344692	0.310531	0.4294878	#DIV/0!	0.691882885	0.836186372	0.989974101	1.153936
			Eqn 7	0.094454936	0.223628704	0.406186	0.6624391	#DIV/0!	-42.28285369	-5.935259133	-3.018788011	-2.1126672

**Compositions for Sierra de Moreno taken from Lucassen et al. (2001)*

'Sr compositions from van Alderwerelt et al. (2021). Nd and Pb compositions from Mamani et al. (2010)